Escola Tècnica Superior
d'Enginyeria ETSE-UV

DOCTORADO EN INGENIERÍA ELECTRÓNICA

Universitat de València

MEJORA DE LA EFICIENCIA EN CONVERTIDORES RESONANTES DE ALTA FRECUENCIA MEDIANTE EL CONTROL DE LOS ELEMENTOS REACTIVOS

TESIS PRESENTADA POR COMPENDIO DE PUBLICACIONES PARA OBTENER EL TÍTULO DE DOCTOR EN INGENIERÍA ELECTRÓNICA CON MENCIÓN INDUSTRIAL

AUTOR:
JUAN LUIS BELLIDO RUIZ

DIRECTOR:
DR. VICENTE ESTEVE GÓMEZ

MARZO, 2025

El Dr. D. Vicente Esteve Gómez, Profesor Titular de Universidad del Departamento de Ingeniería Electrónica de la Universitat de València.

HACE CONSTAR: Que el Graduado en Ingeniería Electrónica Industrial D. Juan Luis Bellido Ruiz ha realizado bajo su dirección el trabajo titulado "Mejora de la eficiencia en convertidores resonantes de alta frecuencia mediante el control de los elementos reactivos", que se presenta en esta memoria para optar al grado de Doctor en Ingeniería Electrónica.

Y para que así conste, firmo el presente documento en Valencia a de de 2025.

Fdo. D. Vicente Esteve Gómez.

UNIVERSITAT DE VALÈNCIA
ESCUELA TÉCNICA SUPERIOR DE INGENIERÍA
Departamento de Ingeniería Electrónica

Avd. de la Universitat s/n, 46100 Burjassot (Valencia)

VNIVERSITAT
DE VALÈNCIA

Acta de calificación de tesis doctoral

Autor: Juan Luis Bellido Ruiz.

Título: **Mejora de la eficiencia en convertidores resonantes de alta frecuencia mediante el control de los elementos reactivos.**

Director: Vicente Esteve Gómez.

El tribunal nombrado para juzgar la citada Tesis Doctoral, compuesta por:

Secretario	*Presidente*	*Vocal*
Fdo: D/Da	*Fdo: D/Da*	*Fdo: D/Da*

Acuerda otorgarle la calificación de: ___________________________

En Burjassot, a de de 2025

Agradecimientos

Deseo expresar mi agradecimiento a todas las personas que, con su ayuda, han hecho posible la realización de esta tesis.

En primer lugar, al director y tutor de la tesis, Dr. Vicente Esteve, y también al Dr. José Jordán, compañeros del grupo de investigación LEII. Gracias por aportarme todos los conocimientos que tengo en el ámbito de la electrónica de potencia y de los componentes magnéticos, por haberme guiado durante todas las fases del proceso de la investigación y por asesorarme en los aspectos técnicos que han ido surgiendo.

En segundo lugar, a los integrantes de la empresa Smart Induction Converter Technologies S.L. en especial a los excompañeros del departamento de I+D el Dr. Pedro J. Martínez y Kevil J. Ferrara por haberme introducido en el mundo de la investigación, y al gerente Dr. Enrique J. Dede por incentivar el conocimiento y aprendizaje dentro de la empresa.

Por último, quería agradecer a mi familia, mis padres y mi hermana, por apoyarme y comprenderme en todo momento y por estar siempre a mi lado.

Resumen

El presente trabajo de tesis presenta las aportaciones realizadas al diseño, análisis y validación experimental de inversores resonantes de potencia y alta frecuencia para aplicaciones de calentamiento por inducción, con un enfoque innovador en el control de elementos reactivos. La técnica de modulación en frecuencia permite que los inversores resonantes puedan regular su potencia de salida variando la frecuencia de conmutación en relación con la frecuencia de resonancia lo cual presenta inconvenientes en cuanto a su eficiencia y la calidad del tratamiento térmico. Sin embargo, es posible operar a frecuencia constante, si se controlar la frecuencia de resonancia mediante el control de los elementos reactivos, lo que mejora la eficiencia y el comportamiento del inversor. La investigación llevada a cabo proporcionó como resultado la mejora en tres topologías de estos convertidores.

La primera consiste en un convertidor resonante LLC donde se sustituye el inductor serie por un inductor variable controlado por corriente además de utilizar la modulación por desplazamiento de fase. Esta estrategia busca mantener la frecuencia de conmutación fija y reducir la corriente reactiva del inversor, minimizando las pérdidas de conducción y conmutación, mientras se mantiene la conmutación a tensión cero en todo el rango de potencia. Se presenta una metodología de diseño para el inductor variable, validada mediante modelado matemático y experimentalmente. Los resultados experimentales, demuestran una eficiencia máxima del 98,5 % en un amplio rango de potencia de salida, representando una mejora significativa respecto a topologías previas.

La segunda consiste en mejorar la eficiencia de un convertidor basado en un inversor resonante LC serie. Para ello se emplea un transformador variable controlado por corriente junto con regulación por desplazamiento de fase para operar a una frecuencia fija cercana a la de resonancia. Este enfoque permite mantener un ángulo de conmutación reducido, logrando adaptarse a variaciones significativas de carga sin comprometer la conmutación a tensión cero en los transistores, mejorando así el rendimiento del inversor en todo su rango operativo. Además, se analiza un nuevo diseño de transformador con relación variable, validado mediante modelado matemático. Tanto el diseño del inversor como el del transformador variable fueron validados experimentalmente obteniendo un rendimiento superior al 99 %.

La tercera se basa un inversor resonante en serie tipo LC con control de los dos elementos reactivos. El método propuesto utiliza un transformador variable controlado por corriente para ajustar la inductancia reflejada del inductor en el circuito resonante, y un interruptor de recuperación de energía magnética para modificar la influencia del condensador como elemento de compensación de potencia reactiva. Esta topología permite ajustar el factor de calidad o la frecuencia de operación, facilitando el tratamiento térmico de piezas de diferentes geometrías y materiales con un único convertidor. Los resultados experimentales realizados operando entre 60 kHz y 100 kHz con un factor de calidad de 6 a 10, muestran eficiencias superiores al 95 %.

Para las tres topologías se utilizaron inversores de puente completo con transistores MOSFET de SiC operando en rangos de potencia de hasta 20 kW y con frecuencias de conmutación de hasta 200 kHz. En conjunto, los tres trabajos destacan avances significativos en la eficiencia y versatilidad de inversores resonantes para aplicaciones de calentamiento por inducción.

Abstract

This thesis presents contributions to the design, analysis, and experimental validation of high frequency resonant power inverters for induction heating applications, with an innovative approach to reactive element control. Frequency modulation techniques allow resonant inverters to regulate their output power by varying the switching frequency relative to the resonant frequency. However, this approach has drawbacks in terms of efficiency and thermal treatment quality. Nevertheless, constant frequency operation is possible if the resonant frequency is controlled through reactive element control, which enhances both inverter efficiency and performance. The research conducted resulted in improvements to three topologies of these converters.

The first topology consists of an LLC resonant converter in which the series inductor is replaced by a current-controlled variable inductor, in addition to employing phase shift modulation. This strategy aims to maintain a fixed switching frequency and reduce the inverter reactive current, thereby minimizing conduction and switching losses while ensuring zero voltage switching across the entire power range. A design methodology for the variable inductor is presented and validated through mathematical modelling and experimental testing. Experimental results demonstrate a maximum efficiency of 98,5 % over a wide output power range, representing a significant improvement compared to previous topologies.

The second topology focuses on improving the efficiency of a converter based on a series LC resonant inverter. This is achieved by employing a current controlled variable transformer along with phase shift regulation to operate at a fixed frequency close to resonance. This approach maintains a reduced switching angle, allowing adaptation to significant load variations without compromising zero voltage switching in the transistors, thereby enhancing the inverter performance across its entire operating range. Additionally, a novel transformer design with a variable turns ratio is analysed and validated through mathematical modelling. Both the inverter and the variable transformer designs were experimentally validated, achieving an efficiency exceeding 99 %.

The third topology is based on a series LC resonant inverter with control of both reactive elements. The proposed method utilizes a current controlled variable transformer to adjust the reflected inductance of the inductor in the resonant circuit, and a magnetic energy recovery switch to modify the influence of the capacitor as a reactive power compensation element. This topology allows for the adjustment of the quality factor or operating frequency, facilitating thermal treatment of workpieces with different geometries and materials using a single converter. Experimental results, obtained in the frequency range of 60 kHz to 100 kHz with a quality factor of 6 to 10, demonstrate efficiencies exceeding 95 %.

For all three topologies, full bridge inverters with SiC MOSFET transistors were used, operating at power levels of up to 20 kW and switching frequencies of up to 200 kHz. Collectively, these three studies highlight significant advancements in the efficiency and versatility of resonant inverters for induction heating applications.

Resum

El present treball de tesi presenta les aportacions realitzades al disseny, anàlisi i validació experimental d'inversors ressonants de potència i alta freqüència per a aplicacions de calfament per inducció, amb un enfocament innovador en el control d'elements reactius. La tècnica de modulació en freqüència permet que els inversors ressonants puguen regular la seua potència d’eixida variant la freqüència de commutació en relació amb la freqüència de ressonància, la qual cosa presenta inconvenients quant a l'eficiència i la qualitat del tractament tèrmic. No obstant això, és possible operar a freqüència constant si es controla la freqüència de ressonància mitjançant el control dels elements reactius, cosa que millora tant l'eficiència com el comportament de l'inversor. La investigació realitzada ha donat lloc a millores en tres topologies d’aquests convertidors.

La primera consisteix en un convertidor ressonant LLC on es substitueix l'inductor en sèrie per un inductor variable controlat per corrent, a més d'utilitzar la modulació per desplaçament de fase. Aquesta estratègia busca mantenir la freqüència de commutació fixa i reduir el corrent reactiu de l'inversor, minimitzant les pèrdues de conducció i commutació, alhora que es manté la commutació a tensió zero en tot el rang de potència. Es presenta una metodologia de disseny per a l'inductor variable, validada mitjançant modelatge matemàtic i experimentalment. Els resultats experimentals mostren una eficiència màxima del 98,5 % en un ampli rang de potència d’eixida, cosa que representa una millora significativa respecte a topologies prèvies.

La segona consisteix a millorar l'eficiència d'un convertidor basat en un inversor ressonant LC en sèrie. Per a això, s'empra un transformador variable controlat per corrent junt amb una regulació per desplaçament de fase per operar a una freqüència fixa pròxima a la de ressonància. Aquest enfocament permet mantenir un angle de commutació reduït, aconseguint adaptar-se a variacions significatives de càrrega sense comprometre la commutació a tensió zero en els transistors, millorant així el rendiment de l'inversor en tot el seu rang operatiu. A més, s'analitza un nou disseny de transformador amb relació variable, validat mitjançant modelatge matemàtic. Tant el disseny de l'inversor com el del transformador variable han sigut validats experimentalment, obtenint un rendiment superior al 99 %.

La tercera es basa en un inversor ressonant en sèrie tipus LC amb control dels dos elements reactius. El mètode proposat utilitza un transformador variable controlat per corrent per a ajustar la inductància reflectida de l'inductor en el circuit ressonant i un interruptor de recuperació d'energia magnètica per a modificar la influència del condensador com a element de compensació de potència reactiva. Aquesta topologia permet ajustar el factor de qualitat o la freqüència d'operació, facilitant el tractament tèrmic de peces de diferents geometries i materials amb un únic convertidor. Els resultats experimentals obtinguts, operant entre 60 kHz i 100 kHz amb un factor de qualitat de 6 a 10, mostren eficiències superiors al 95 %.

Per a les tres topologies s'han utilitzat inversors de pont complet amb transistors MOSFET de SiC, operant en rangs de potència de fins a 20 kW i amb freqüències de commutació de fins a 200 kHz. En conjunt, els tres treballs destaquen avanços significatius en l'eficiència i versatilitat dels inversors ressonants per a aplicacions de calfament per inducció.

Tabla de contenido

Índice de abreviaturas

AC	Corriente alterna
A_{dc}	Área efectiva de la sección transversal de la rama de DC bias
A_e	Área efectiva de la sección transversal del núcleo
A_{ext}	Área efectiva de la sección transversal de la rama externa
A_{gap}	Área efectiva de la sección transversal del entrehierro
A_{int}	Área efectiva de la sección transversal de la rama central
A_p	Área efectiva de la sección transversal de primario
A_s	Área efectiva de la sección transversal de secundario
A_w	Área de bobinado
B	Densidad de flujo magnético
BJT	Transistor de Unión Bipolar
B_{pk}	Valor de pico de la densidad de flujo magnético
C	Condensador
c	Velocidad de la luz en el vacío
C_P	Condensador paralelo
C_p	Condensador en primario
C_S	Condensador serie
C_s	Condensador en secundario
CSI	Inversor fuente de corriente
DAB	Convertidor activo dual
DC	Corriente directa
dI/dt	Magnitud de la tasa de cambio de la corriente con respecto al tiempo
DSO	Osciloscopio digital
dV/dt	Magnitud de la tasa de cambio de la tensión con respecto al tiempo
D-MOS	MOS de doble difusión
EMI	Interferencia electromagnética
E_{off}	Energía de conmutación a OFF del MOSFET
ESR	Resistencia serie equivalente
f	Frecuencia de trabajo
FET	Transistor de efecto de campo
FM	Modulación de la frecuencia
FM-PS	Modulación de la frecuencia y desplazamiento de fase
f_o	Frecuencia de resonancia
f_{sw}	Frecuencia de conmutación
GaN	Nitruro de Galio
GCSC	Condensador serie con control de puerta
H	Campo magnético
H_{bias}	Campo magnético continuo
HEMT	Transistor de alta movilidad de electrones
HF	Alta frecuencia
H_v	Ganancia de la tensión
I_{bias}	Corriente de bias
I_{C_Q}	Corriente conmutada por el MOSFET
I_{eff}	Corriente efectiva
i_F	Corrientes de Foucault
IGBT	Transistor bipolar de puerta aislada
i_o	Corriente de salida del puente completo

I_L	Corriente por el inductor
J	Densidad de corriente
JFET	Transistores de efecto de campo de unión
K	Factor de llenado
K_M	Coeficiente de acoplamiento mutuo
K_p	Coeficiente de acoplamiento en primario
K_s	Coeficiente de acoplamiento en secundario
l	Longitud del circuito magnético
L	Inductor
L_{ac}	Inductor principal del inductor variable controlado por corriente
$L_{ac_{max}}$	Valor máximo de L_{ac}
$L_{ac_{min}}$	Valor mínimo de L_{ac}
L_{bias}	Inductor de control de la saturación
l_{dc}	Longitud del camino magnético de la rama de saturación
l_{dc_p}	Longitud del camino magnético de la rama de saturación a primario
L_{dc_p}	Inductancia de la rama de saturación desde primario
l_{dc_s}	Longitud del camino magnético de la rama de saturación a secundario
L_{dc_s}	Inductancia de la rama de saturación desde secundario
l_{ext}	Longitud magnética de la rama externa
L_{ext}	Inductancia de la rama externa
l_{gap}	Longitud del gap de aire
L_{gap}	Inductancia del gap de aire
L_{gap_p}	Inductancia del gap de aire desde primario
L_{gap_s}	Inductancia del gap de aire desde secundario
l_{int}	Longitud magnética de la rama central
L_{int}	Inductancia de la rama central
$L_{leakage}$	Inductancia de fugas
L_{lk_p}	Inductancia de fugas de primario
L_{lk_s}	Inductancia de fugas de secundario
L_M	Inductancia mutua
L_P	Inductor paralelo
L_p	Inductor en primario
$L_{p_{max}}$	Inductancia máxima de primario
$L_{p_{min_{cc}}}$	Inductancia mínima de primario en corto circuito
$L_{p_{min_{oc}}}$	Inductancia mínima de primario en circuito abierto
l_{p_p}	Longitud del camino magnético de la rama de primario
L_{p_p}	Inductancia de primario reflejada por el primario
l_{p_s}	Longitud del camino magnético de primario a secundario
L_{p_s}	Inductancia de primario reflejada por el secundario
L_S	Inductor serie
L_s	Inductor en secundario
$L_{sec_{max}}$	Inductancia máxima de secundario reflejada en primario
$L_{s_{max}}$	Inductancia máxima de secundario
$L_{s_{min_{cc}}}$	Inductancia mínima de secundario en cortocircuito
$L_{s_{min_{oc}}}$	Inductancia mínima de secundario en circuito abierto
l_{s_p}	Longitud del camino magnético de secundario a primario
L_{s_p}	Inductancia de secundario reflejada por el primario

l_{s_s}	Longitud del camino magnético de la rama de secundario
L_{s_s}	Inductancia de secundario reflejada por el secundario
MERS	Interruptor magnético de recuperación de energía
MF	Frecuencia media
MIMO	Sistema de múltiples entradas y múltiples salidas
MOSFET	Transistor de efecto de campo metal-óxido-semiconductor
n	Numero de vueltas en primario, expresado con $n{:}\,1$
n_{ext}	Número de vueltas de la bobina de L_{bias}
n_{int}	Número de vueltas de la bobina de L_{ac}
n_p	Número de vueltas de primario
n_s	Número de vueltas de secundario
P	Potencia térmica
P_{cd}	Pérdidas por la conducción de corriente por el canal del MOSFET
P_{core}	Pérdidas en el núcleo
P_{gate}	Pérdidas en la puerta del MOSFET
PID	Proporcional, integral y derivativo
P_o	Potencia de salida
PS	Desplazamiento de fase
P_{sw}	Pérdidas de conmutación
P_{tot}	Pérdidas totales
P_v	Densidad de pérdidas en el núcleo
P_{wire}	Pérdidas en el bobinado de cobre
PWM	Modulación por ancho de pulso
Q	Factor de calidad serie
Q_G	Carga total de la puerta del transistor
Q_p	Factor de calidad paralelo
R_{copper}	Resistencia efectiva del bobinado
$R_{DS_{on}}$	Resistencia del canal en estado de ON del MOSFET
RMS	Raíz cuadrática media
R_p	Resistentica en primario
R_s	Resistencia en secundario
R_1	Resistencia efectiva del devanado primario
R_2	Resistencia efectiva del devanado de secundario desde primario
Si	Silicio
SiC	Carburo de Silicio
SPWM	Modulación por ancho de pulso sinusoidal
T	Periodo de la forma de onda de salida
T_c	Temperatura crítica o de Curie
TR	Relación de transformación para el transformador variable controlado por corriente
TR_{max}	Relación de transformación máxima
TR_{min}	Relación de transformación mínima
TPS	Desplazamiento de fase triple
$V_{C_{Eq}}$	Tensión equivalente de los condensadores del MERS
V_d	Tensión de entrada
V_e	Volumen del núcleo
V_{eff}	Tensión efectiva
V_G	Tensión puerta a surtidor
VI	Inductor variable
VI-PS	Inductor variable y desplazamiento de fase

V_{L_s}	Tensión del inductor L_s
V_o	Tensión de salida
V_p	Tensión del condensador paralelo en el LLC
VSI	Inversor fuente de tensión
V2G	Vehículo a red
V2L	Vehículo a carga
WBG	Semiconductores de banda prohibida ancha
X_C	Reactancia del condensador utilizado para el MERS
X_{MERS}	Reactancia del MERS
α	Ángulo entre la conmutación a ON del transistor y el cruce por cero de la corriente
β	Ángulo entre el inicio de cambio de estado de la tensión de salida y el cruce por cero de la corriente
β_o	Ángulo entre el inicio del cambio de estado de la tensión de salida y el alcance del valor de V_d
γ	Ángulo de conducción del condensador del MERS
δ	Profundidad de penetración
ε	Fuerza electromotriz
λ	Longitud de onda
μ	Permeabilidad magnética
$\tilde{\mu}$	Permeabilidad relativa sometida a DC bias
μ_e	Permeabilidad efectiva para un núcleo con gap
μ_i	Permeabilidad inicial
μ_o	Permeabilidad del vacío
μ_r	Permeabilidad magnética relativa del material
ρ	Resistividad
ϕ	Fase entre V_d y V_o
ω	Frecuencia angular
ω_o	Frecuencia angular de resonancia serie
ω_{op}	Frecuencia angular de resonancia paralelo

Índice de figuras

Índice de tablas

Capítulo 1. Introducción y objetivos

1.1 Introducción

La transición hacia fuentes de energía sostenibles y el auge de dispositivos electrónicos cada vez más compactos y de alto rendimiento, unido a la necesidad de reducir el consumo eléctrico, han impulsado una demanda creciente de convertidores de potencia más eficientes y con mayor densidad de potencia. En aplicaciones como cargadores de vehículos eléctricos, equipos de tratamiento térmico por inducción, excitadores de lámparas de gas para iluminación o fuentes de alimentación inalámbrica, los convertidores resonantes han emergido como una solución clave. Estos convertidores se componen de combinaciones en serie o paralelo de por lo menos dos elementos reactivos, un condensador (C) y un inductor (L). Su capacidad para operar a altas frecuencias permite utilizar componentes más pequeños y ligeros, lo que resulta en sistemas de mayor densidad de potencia. Además, su diseño facilita la integración de estrategias de control avanzadas para mantener un rendimiento óptimo bajo diversas condiciones de carga.

En los últimos años, la investigación en electrónica de potencia ha mostrado un enfoque creciente hacia los convertidores resonantes debido a su capacidad para minimizar las pérdidas de conmutación mediante la utilización de técnicas como la conmutación con tensión cero (ZVS) o corriente cero (ZCS). Estas técnicas permiten que los dispositivos semiconductores operen en condiciones más ideales, reduciendo considerablemente las pérdidas de energía y el estrés térmico. A pesar de estas ventajas, los convertidores resonantes presentan complejidades inherentes en su diseño y control, especialmente cuando se busca optimizar simultáneamente la eficiencia, la densidad de potencia y la estabilidad operativa.

La mejora de la eficiencia en convertidores resonantes de alta frecuencia y potencia representa un desafío crítico en el diseño de sistemas electrónicos modernos. Estos convertidores destacan por su capacidad para operar a altas frecuencias, reduciendo así el tamaño y el peso de los componentes pasivos. Sin embargo, estas altas frecuencias también conllevan pérdidas significativas, tanto en los dispositivos semiconductores como en los elementos pasivos, lo que puede comprometer el rendimiento y la fiabilidad del sistema. No obstante, operar a altas frecuencias plantea una serie de desafíos técnicos, entre los que destacan las pérdidas por conducción y conmutación en los semiconductores, que, aunque se han reducido gracias a tecnologías como el carburo de silicio (SiC) y el nitruro de galio (GaN), requieren un diseño cuidadoso del circuito y una gestión eficiente del calor. Otro aspecto para considerar son las pérdidas en elementos pasivos, ya que los condensadores y bobinas utilizados en circuitos resonantes sufren pérdidas adicionales debido a la resistencia equivalente en serie (ESR) y los efectos de histéresis y corrientes de Foucault, entre otros. Por último, las interferencias electromagnéticas (EMI), dado que las altas frecuencias pueden generar perturbaciones que afectan tanto al correcto funcionamiento de otros dispositivos cercanos como a la estabilidad del propio sistema.

Actualmente para combatir los desafíos técnicos que presentan los convertidores resonantes y mejorar la eficiencia, se implica abordar una serie de consideraciones. La primera es la optimización de las topologías, el convertidor LLC y el resonante serie LC han destacado por su eficiencia y capacidad para adaptarse a diferentes rangos de carga. Sin embargo, su comportamiento dinámico puede ser complejo, requiriendo métodos de control avanzados para prever su respuesta en condiciones reales. La selección y diseño de los componentes del convertidor, y el uso de materiales avanzados como núcleos magnéticos de baja pérdida y semiconductores de banda prohibida ancha (WBG) han mostrado un impacto positivo en la eficiencia general del sistema. Estos avances requieren un equilibrio entre el costo y el rendimiento para ser viables comercialmente. El diseño del control, los esquemas de control deben ser capaces de adaptarse rápidamente a variaciones en la carga y diferentes parámetros como las tensiones, corrientes o potencias, garantizando una operación eficiente y estable. Las estrategias basadas en control digital y algoritmos de optimización en tiempo real están ganando popularidad en este campo. Por último, la distribución de las pérdidas y la gestión térmica, debido a que a medida que la densidad de potencia aumenta, también lo hace la necesidad de gestionar eficientemente el calor generado para evitar fallos prematuros, garantizar una larga vida útil del sistema y mejorar la eficiencia.

1.2 Objetivos

Actualmente la mejora de la eficiencia de los convertidores resonantes se basa en los siguientes puntos.

El primero es mantener una frecuencia de conmutación fija o permitir únicamente pequeñas variaciones de la frecuencia de conmutación. Dependiendo de la aplicación a la que se destine el convertidor, el barrido en frecuencia se utiliza para cambiar la consigna de salida del convertidor, como puede ser la corriente, la tensión o la potencia. Este punto se está logrando con la implementación de sistemas de control que varían otros parámetros del convertidor como es el caso de la tensión aplicada al resonante, o también mediante modelos matemáticos complejos que permiten predecir el comportamiento del convertidor. Este punto es necesario puesto que para la comercialización de los convertidores estos deben cumplir con la normativa de compatibilidad electromagnética. Para cumplirla se precisará de filtros en el convertidor que serán más complejos y costosos cuanto mayor sea el rango de frecuencias a filtrar.

El segundo trata de garantizar el comportamiento eficiente del convertidor en todo el rango de aplicación y ante cambios bruscos de carga. Los convertidores resonantes presentan la ventaja de poder funcionar con conmutaciones suaves en una de las transiciones de encendido o apagado de los semiconductores, pero este estado es muy sensible a cambios en el punto de operación, haciendo que si se pierden las conmutaciones suaves el convertidor reduzca drásticamente su eficiencia o incluso se puedan generar roturas. En la actualidad se han diseñado controles que combinan la variación de la frecuencia con otros parámetros para garantizar las conmutaciones suaves del convertidor, pero si se requiere conmutar a frecuencias fijas, esta debe incrementarse sustancialmente con respecto a la frecuencia de resonancia para poder variar el rango de aplicación.

El tercero consiste en conmutar a una frecuencia cercana a la frecuencia de resonancia, al conmutar a una frecuencia cercana a la de resonancia se consigue optimizar los elementos reactivos del circuito resonante. Un convertidor resonante, como puede ser el resonante serie LC, tiene su punto óptimo de trabajo justo en la frecuencia de resonancia, en este punto el condensador y el inductor se anulan entre ellos dejando solo la resistencia de la carga enfrentada a la tensión de entrada del convertidor, es decir en este punto se consigue obtener la mayor potencia del convertidor, pero no es posible trabajar en estas condiciones debido a las grandes corrientes que tendrían que circular por los semiconductores del inversor. Por ello, se considera que el punto óptimo real es el más cercano posible a la frecuencia de resonancia, debido a que con ello se mejora la eficiencia de la conversión energética y además se optimiza el coste y tamaño del convertidor. Para poder conmutar en este punto y no variarlo dependiendo de la consigna es importante que la frecuencia de conmutación sea fija o tenga un rango de variación estrecho, de lo contrario la optimización de los elementos reactivos se pierde.

El cuarto concierne al número de elementos reactivos del convertidor, anteriormente en la literatura se podía observar cómo se incrementaban el número de elementos reactivos en los convertidores resonantes para poder cumplir con los requerimientos citados anteriormente. Es habitual encontrarse con diseños de tres, cuatro o cinco elementos reactivos. Pero este incremento genera un sobrecoste en el convertidor, además de aumentar su tamaño, con lo que se reduce la densidad de potencia y se complica el control debido a que hay que lidiar con más de una frecuencia de resonancia. Un ejemplo muy utilizado actualmente es el convertidor LLC utilizando la inductancia magnetizante del transformador para lograr tener las dos frecuencias de resonancia típicas de un resonante de tres elementos, con ello se logra reducir los elementos reactivos, presentando un rendimiento elevado y una buena respuesta dinámica. Por tanto, es un ejemplo del enfoque actual a reducir el número de elementos reactivos.

Como se ha podido observar en los distintos puntos, todos ellos están interrelacionados, por tanto, en esta tesis se propone una novedosa técnica de control que combinada con modulaciones actuales pretende mantener la frecuencia de conmutación fija, además de mejorar la eficiencia en todo el rango de trabajo y mantener las conmutaciones suaves ante cambios de carga sin incrementar el número de elementos reactivos de los convertidores. Para lograrlo se basa en el control de los elementos reactivos del resonante, lo que permite variar las consignas de trabajo del convertidor sin realizar barridos de frecuencia, enfocándolo en aplicaciones para calentamiento por inducción. Los elementos que se variarán serán el inductor serie para un convertidor LLC, la relación del transformador en un convertidor LC serie en posición de activa y por último se estudiará la ventaja añadida en cuanto al rango de aplicación de la combinación de la variación de dos elementos, como son el condensador del resonante serie LC y la influencia de la inductancia del inductor de calentamiento mediante la relación del transformador variable en posición de reactiva.

1.3 Entorno de la tesis

La presente tesis se ha desarrollado en colaboración con el grupo de investigación del Laboratorio de Electrónica Industrial e Instrumentación (LEII) de la Universidad de Valencia, que tiene como principales líneas de investigación el diseño de convertidores DC/DC y AC/DC de alta eficiencia, el diseño de nuevas técnicas de conversión de energía y el desarrollo de sistemas electrónicos de instrumentación industrial. Por otra parte, también se ha desarrollado en el departamento de investigación y desarrollo de la empresa Smart Induction Converter Technologies S.L. esta empresa tiene por objeto la investigación, desarrollo, ingeniería, fabricación y comercialización de convertidores avanzados de potencia y sistemas completos de alimentación para aplicaciones de calentamiento por inducción industrial entre otros.

1.3.1 Proyecto

Durante el desarrollo de la tesis doctoral se ha colaborado con el proyecto *"Vertical GaN on Silicon: Wide Band Gap Power at Silicon Cost"* con Grant Agreement Number: 101007229, el cual tiene como objetivo el desarrollo de transistores de GaN verticales con alta eficiencia y bajo coste. El proyecto ha recibido financiación de la Empresa Común de Sistemas de Componentes Electrónicos para el Liderazgo Europeo (ECSEL JU) que cuenta con el apoyo del Programa de Investigación e Innovación Horizonte 2020 de la Unión Europea.

El proyecto presenta los siguientes objetivos:

- Desarrollo de una oblea de GaN vertical de hasta 1200 V de bloqueo utilizando un sustrato de bajo coste como el silicio o el zafiro.
- Desarrollo de un transistor de potencia de GaN vertical de bajo coste con un rendimiento superior a los MOSFET de SiC más avanzados y a un coste de chip competitivo como el IGBT de Si.
- Desarrollo de una membrana para transistores de potencia verticales de GaN con una contribución de resistencia ultra baja del contacto trasero.
- Desarrollo de una tecnología de interconexión avanzada compatible con los transistores verticales de potencia de GaN de membrana y evaluación de su fiabilidad basada en la directriz AQG324 de ECPE.

- Comprensión de las limitaciones de rendimiento, degradación y mecanismos de fallo de los transistores de potencia verticales de GaN de membrana desde el chip hasta el dispositivo.
- Entrega de una hoja de datos para transistores de potencia GaN verticales de membrana con comportamiento estático y dinámico completo. Mejorar la eficiencia del sistema reduciendo las pérdidas hasta un 50 % y aumentando la densidad de potencia en un 15 % en comparación con el silicio para los demostradores tecnológicos elegidos de convertidores de alta potencia con el fin de aumentar su rentabilidad.

En cuanto a las contribuciones remarcables del proyecto, cabe destacar la publicación de tres artículos de revista:

- Esteve, V.; Jordán, J.; Dede, E.J.; **Bellido, J.L.**: Enhanced asymmetrical modulation for half-bridge series resonant inverters in induction heating applications. IET Power Electron. 16, 2482–2491 (2023). https://doi.org/10.1049/pel2.12573
- Esteve, V.; **Bellido, J.L.**; Jordán, J.; Dede, E.J.: Improving the Efficiency of an Isolated Bidirectional Dual Active Bridge DC–DC Converter Using Variable Frequency. Electronics 2024, 13, 294. https://doi.org/10.3390/electronics13020294
- Esteve, V.; **Bellido, J.L.**; Jordán, J.: Optimal Design of a Single-Phase Bidirectional Rectifier. Energies 2024, 17, 1280. https://doi.org/10.3390/en17061280

1.3.2 Mención industrial

Debido a la existencia de un contrato laboral entre el doctorando y la empresa Smart Induction Converter Technologies S.L. y que el doctorando participa en un proyecto de investigación industrial y de desarrollo experimental que mantiene relación con la tesis realizada, se firmó un convenio de colaboración entre la empresa y la Universidad de Valencia para la realización del doctorado con mención industrial.

1.3.3 Ayudas

Dada la resolución de 25 de septiembre de 2024 del Vicerrectorado de Estudios de la Universidad de Valencia, por la que se convocan ayudas para la financiación de actuaciones que favorezcan la realización de doctorados con mención industrial, publicado en el Diari Oficial de la Generalitat Valenciana número 9964 de fecha 24.10.2024. Esta tesis cuenta con el beneficio de la concesión de la ayuda dirigida a financiar los precios públicos devengados en estudios de doctorado con mención industrial durante el año 2024. La financiación procede de la Conselleria de Educación, Cultura, Universidades y Empleo de la Generalitat Valenciana y del Fondo Social Europeo Plus (FSE+).

Capítulo 2. Convertidor resonante

2.1 Convertidores resonantes

Los convertidores conmutados, ya sean convertidores DC-DC, inversores DC-AC o rectificadores AC-DC, utilizan interruptores controlables que permiten conducir o interrumpir la amplitud de la corriente que circula por la carga durante los ciclos de conmutación. Estas topologías se utilizan para suministrar energía regulada y para aplicaciones de accionamiento de motores. La entrada del convertidor es, en la mayoría de las ocasiones, una tensión continua no regulada, que se obtiene mediante la rectificación de la tensión de la línea.

Por una parte, los convertidores DC-DC se utilizan para convertir la tensión no regulada de la red en un nivel de tensión deseado, y las topologías básicas que conforman estos convertidores son el Buck, utilizado como reductor del nivel de tensión, y el Boost, utilizado como elevador del nivel de tensión. Otras topologías como el Buck-Boost, el Ćuk o el puente completo son adaptaciones de las topologías básicas.

Por otra parte, los inversores DC-AC tienen como objetivo generar una salida de tensión alterna a partir de la tensión continua de la entrada. Esta tensión alterna suele ser controlada en amplitud y frecuencia. Estos se utilizan en aplicaciones de tracción eléctrica con motores de alterna o para fuente de alimentación ininterrumpida. Estos inversores se pueden diferenciar por inversores de fuente de tensión (VSI), cuando su entrada es una fuente de tensión de DC, o inversores fuente de corriente (CSI), donde su entrada es una fuente de corriente DC. Estos últimos son menos utilizados en la actualidad debido a las escasas aplicaciones donde se implementan. En cuanto a la topología base se parte del inversor de medido puente, de la que derivan el inversor de puente completo y el inversor trifásico.

Los rectificadores AC-DC con diodos que operan a frecuencia de línea se utilizan cada vez más en la entrada de sistemas de electrónica de potencia en modo conmutado, permitiendo la conversión de una entrada de AC en un voltaje de salida de DC no regulado. No obstante, en ciertas aplicaciones, como cargadores de baterías y algunos tipos de accionamientos de motores de DC y AC, es fundamental contar con un voltaje de DC ajustable. Para lograr esta conversión de AC a DC controlada, se emplean convertidores de frecuencia de línea controlados por fases mediante tiristores.

Los convertidores, en su diseño básico, solo pueden transferir energía en un único sentido, ya que generan un voltaje y una corriente de dirección única. Sin embargo, un convertidor de puente completo permite el flujo de potencia en ambas direcciones, lo que significa que tanto el voltaje de salida como la corriente pueden invertirse de manera independiente. Gracias a esta capacidad de operar en los cuatro cuadrantes del plano $V_O - I_O$, un convertidor puede funcionar tanto como inversor de DC a AC como rectificador de AC a DC. De manera similar, es posible diseñar topologías bidireccionales para conversión DC-DC mediante la combinación de dos convertidores que se alternan entre los modos de rectificación e inversión de corriente.

Para poder realizar la transformación de la energía, los convertidores conmutados utilizan semiconductores como interruptores controlables. Estos se ven sometidos a grandes pérdidas en la conmutación, que incrementan con razón a la frecuencia de conmutación. Además, presentan inconvenientes como la EMI, que se produce debido a los *dI/dt* y *dV/dt* causados por la conmutación brusca de los semiconductores. Este efecto se puede atenuar si las conmutaciones en el convertidor se hacen cuando la tensión o corriente a través del semiconductor es cero, dando lugar a las conmutaciones ZVS o ZCS. Para lograr esto, la gran mayoría de topologías utilizan combinaciones de L y C dando lugar a resonancias entre ellas. Esto se conoce como convertidores resonantes.

Dentro de los considerados convertidores resonantes se pueden diferenciar en cuatro grupos [1]:

El primero integra a los convertidores resonantes a la carga [2], estos convertidores se caracterizan por tener un circuito o tanque resonante como carga, que se compone por elementos L y C. En ellos, la carga recibe una tensión y corriente oscilantes generadas por la resonancia del circuito. Los interruptores del convertidor realizan su conmutación en condiciones de tensiones o corriente nulas, optimizando la eficiencia del sistema. Es posible implementar un circuito LC tanto en configuración serie como paralelo, o con combinaciones de ambos. En estos diseños, el flujo de potencia hacia la carga está determinado por la impedancia resonante del circuito tanque, la cual, a su vez, depende de la relación entre la frecuencia de conmutación (f_{sw}) y la frecuencia de resonancia (f_o). Este tipo de convertidores se tratarán en mayor profundidad más adelante, debido a que son los utilizados para la aplicación de esta tesis.

El segundo grupo son los convertidores cuasirresonantes [3], estos hacen uso de la resonancia LC, principalmente para modelar la forma de la tensión y la corriente en los interruptores. Esto permite que las conmutaciones se realicen con tensión o corriente nula, optimizando su funcionamiento. En este tipo de convertidores, cada ciclo de conmutación incluye tramos en los que ocurre la resonancia como tramos en los que no es así.

El tercer grupo concierne a los convertidores resonantes de enlace de DC [4], en los inversores de corriente continua a corriente alterna convencionales con modulación por ancho de pulso (PWM) en modo conmutado, la tensión de entrada (V_d) es de magnitud constante. La salida senoidal se genera a través de conmutaciones PWM. Por otro lado, en los convertidores resonantes con enlace de DC, la tensión de entrada se hace oscilar mediante la resonancia de un circuito LC. Este diseño permite que la tensión de entrada alcance valores de cero durante ciertos intervalos, lo que facilita cambiar el estado de los interruptores del inversor bajo condiciones de conmutación de tensión nula.

Por último, el cuarto grupo son los convertidores de enlace de alta frecuencia y semiciclo integral [5], en estos se utilizan interruptores bidireccionales que se activan y desactivan en los puntos donde la tensión de entrada cruza por cero, logrando que cuando un inversor recibe una señal de entrada de corriente alterna sinusoidal de alta frecuencia, sea posible generar una salida de baja frecuencia con magnitud y frecuencia ajustables, o una corriente continua de magnitud variable.

2.1.1 Aplicación

La optimización en la eficiencia de los convertidores resonantes estudiados en este trabajo se destina a aplicaciones industriales de calentamiento por inducción [6]. Este proceso consiste en calentar materiales conductores mediante un campo magnético variable, eliminando la necesidad de contacto físico entre la fuente de energía y el material a calentar. La energía se transfiere por medio de un campo magnético, lo que hace posible que el calentamiento se realice de manera eficiente y sin contacto directo. El material conductor actúa como la carga del sistema, mientras que el campo magnético es generado por el inductor o bobina de calentamiento. Al circular una corriente alterna a través de la bobina, se crea un campo magnético alterno que induce corrientes en un material conductor ubicado cerca de la bobina. Este enfoque permite calentar materiales de cualquier tamaño o forma, además de concentrar el calentamiento en áreas específicas del material según sea necesario. En la Figura 1 se presenta un esquema del sistema, donde la carga es un material conductor de cierta geometría y el inductor es una bobina que la rodea.

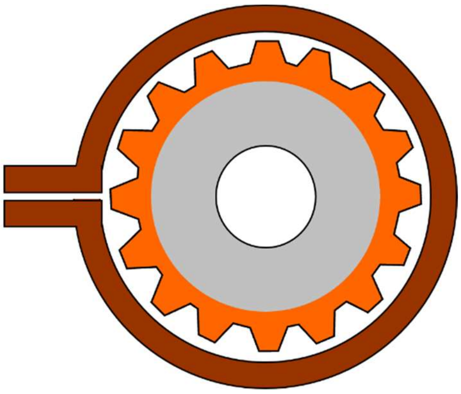

Figura 1. Esquema inductor y pieza de calentamiento.

El calentamiento por inducción tiene su actividad en sectores industriales como el automotriz, aeroespacial, la industria alimentaria y las acerías. Dentro de estos sectores tiene una gran presencia en el procesamiento de piezas metálicas, con aplicaciones que incluyen soldadura, endurecimiento, revenido, fusión de metales y sellado.

El sistema básico para este tipo de calentamiento incluye un convertidor resonante, una bobina de calentamiento, los condensadores y la pieza que se desea calentar, la cual se coloca dentro de la bobina. Cuando la corriente alterna pasa a través de la bobina, genera un campo magnético de igual frecuencia que interactúa con la pieza, produciendo calor mediante dos fenómenos principales. El primero son las pérdidas por efecto Joule, este es el principal mecanismo de disipación de energía en el calentamiento por inducción. El campo magnético induce corrientes en la superficie del material, corrientes de Foucault, generando calor debido al efecto Joule. Este fenómeno ocurre tanto en materiales ferromagnéticos como en no ferromagnéticos. La diferencia entre ambos materiales es la permeabilidad (μ), en los materiales ferromagnéticos la permeabilidad es mayor que la permeabilidad del vacío (μ_o), $4\pi 10^{-7}$, mientras que en los no ferromagnéticos es igual. El segundo son las pérdidas por histéresis, en los materiales ferromagnéticos, un campo magnético alterno (H) provoca que su respuesta magnética (B) se desfase respecto al campo aplicado. Este fenómeno, conocido como histéresis magnética, se debe al tiempo que tardan los dipolos magnéticos en alinearse con el campo. La energía liberada durante este proceso genera calor, aunque su contribución es menor en comparación con el efecto Joule y se limita a materiales ferromagnéticos.

El principio físico del calentamiento por inducción consiste en el campo generado por hacer pasar una corriente eléctrica por un bobinado conductor. Este campo magnético tendrá una amplitud y distribución que se definen por la ley de Ampère [7].

$$Ni = \oint \vec{H}\vec{dl} = Hl \tag{1}$$

En esta expresión, *N* representa el número de vueltas del inductor, i la corriente que circula por él, *H* el campo magnético resultante y l la longitud del circuito magnético. Cuando la corriente aplicada al inductor es alterna, el campo magnético generado varía con el tiempo, produciendo un flujo magnético oscilante en el área especificada. La ley de Faraday establece que un campo magnético en cambio constante induce una fuerza electromotriz (ε) en cualquier material conductor dentro de su alcance, según la siguiente relación.

$$\varepsilon = -N\frac{d\phi}{dt} \tag{2}$$

donde en esta fórmula, *N* el número de espiras de la bobina y ϕ el flujo magnético a través del área.

Las corrientes inducidas dentro del material conductor, conocidas como corrientes de Foucault (i_F), son generadas por esta fuerza electromotriz. Estas corrientes son responsables del calentamiento del material debido al efecto Joule, que se describe mediante la siguiente expresión:

$$P = {i_F}^2 R_{eq} \qquad (3)$$

P es la potencia térmica generada y R_{eq} la resistencia equivalente del material conductor. Estas corrientes obedecen al campo eléctrico y la conductividad del material debido a que la longitud de onda (λ) dada la frecuencia de trabajo es superior a las dimensiones de la pieza a calentar dando lugar a que se deprecie el efecto de la radiación del campo,

$$\lambda = c\frac{2\pi}{\omega} \qquad (4)$$

donde c es la velocidad de la luz en el vacío y ω es la frecuencia angular de trabajo.

Uno de los aspectos fundamentales en el calentamiento por inducción es la frecuencia de trabajo (f), debido a que de esta depende la profundidad de penetración (*δ*). En la pieza a calentar la mayor densidad de corrientes se obtiene en la superficie del material y estas van decreciendo conforme se recorre el interior del material. Además, la profundidad de penetración tiene relación con otros parámetros debido a que esta se reduce cuando se incrementa la frecuencia, aumenta la permeabilidad magnética del material o disminuye su resistividad. Por el contrario, esta profundidad se incrementa si la resistividad aumenta, la frecuencia disminuye o si la permeabilidad magnética del material conductor es menor. Por tanto, la profundidad de penetración cumple con la siguiente expresión.

$$\delta = \sqrt{\frac{\rho}{\pi f \mu_o \mu_r}} \qquad (5)$$

donde ρ es la resistividad del material y μ_r la permeabilidad magnética relativa del material.

Por otra parte, la Figura 2 muestra como varía la profundidad de penetración en función de la frecuencia en una pieza de acero al carbono 1040.

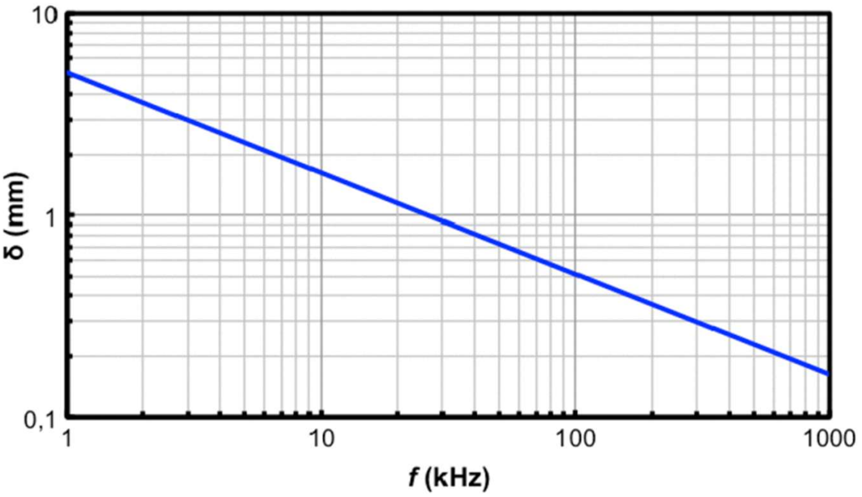

Figura 2. Profundidad de penetración en acero al carbono 1040 frente a la frecuencia.

Por consiguiente, la selección de la frecuencia de operación depende de la pieza a calentar. Las aplicaciones típicas de muy baja frecuencia, 50 Hz, son por ejemplo la fusión de metales en crisoles. En el caso de la forja de metales con geometría cilíndrica, donde se busca un calentamiento uniforme en toda la sección transversal de la pieza, se requiere una frecuencia que permita una profundidad de penetración comparable al radio de la pieza. Estas frecuencias se encuentran en el rango de 1 a 5 kHz, permitiendo que el calor generado en la superficie se propague hacia el interior por conducción térmica. Para tratamientos como el temple, en los que se necesita una profundidad de calentamiento reducida, se eligen frecuencias más altas, normalmente en torno a los 10 kHz. Por otro lado, materiales con baja permeabilidad magnética, como el aluminio, el cobre o ciertos aceros, requieren frecuencias más elevadas, del orden de 50 kHz. Otras aplicaciones más específicas, como el temple de coronas donde el calentamiento debe concentrarse en la superficie exterior, se utilizan frecuencias del rango de los 100 kHz a 200 kHz.

Otro de los aspectos a tener en cuenta con la profundidad de penetración es la temperatura de Curie (T_c). Al inicio del ciclo de calentamiento de un material ferromagnético, la profundidad de penetración de la corriente incrementa lentamente a medida que la temperatura sube, debido al aumento progresivo de la resistividad eléctrica del material. Esto produce que la profundidad de penetración crezca de manera gradual porque la permeabilidad magnética relativa del material se mantiene prácticamente constante, dejando que el cambio en la resistividad sea el factor predominante. Sin embargo, al acercarse a una temperatura de aproximadamente 550 °C, la permeabilidad magnética comienza a reducirse de forma notable, lo que causa un aumento más rápido en la profundidad de penetración. Cuando el material alcanza una temperatura crítica conocida como temperatura de Curie, la permeabilidad magnética cae abruptamente a un valor cercano a uno, ya que el material deja de comportarse como ferromagnético y pasa a ser paramagnético. Este cambio genera un incremento drástico en la profundidad de penetración. Más allá del punto de Curie, la profundidad continúa aumentando, aunque de forma más gradual, debido al incremento continuo de la resistividad del material con la temperatura. Es importante destacar que el cambio más significativo en la profundidad de penetración está asociado al comportamiento magnético del material al alcanzar el punto de Curie, más que al aumento de su resistividad eléctrica. Este fenómeno es crucial al trabajar con procesos como el temple de materiales ferromagnéticos, ya que la profundidad de penetración varía considerablemente durante el ciclo de calentamiento.

2.1.2 Topología

El puente completo como convertidor en modo conmutado tiene cuatro aplicaciones fundamentales. Los accionamientos motrices de DC. La conversión de DC a AC generando una onda sinusoidal para fuentes no interrumpibles monofásicas o rectificadores bidireccionales y la conversión de DC a AC de frecuencia alta para fuentes de potencia [1].

La topología del puente completo se representa en la Figura 3. La entrada es una fuente de tensión constante (V_d), mientras que la salida $(V_o = V_a - V_b)$ se controla en magnitud, polaridad y frecuencia. En cuanto a la corriente de salida (i_o) se controla en magnitud y sentido. Es por lo que este convertidor presenta la ventaja de situarse en los cuatro cuadrantes del plano $i_o - V_o$, es decir permite la bidireccionalidad del flujo de potencia.

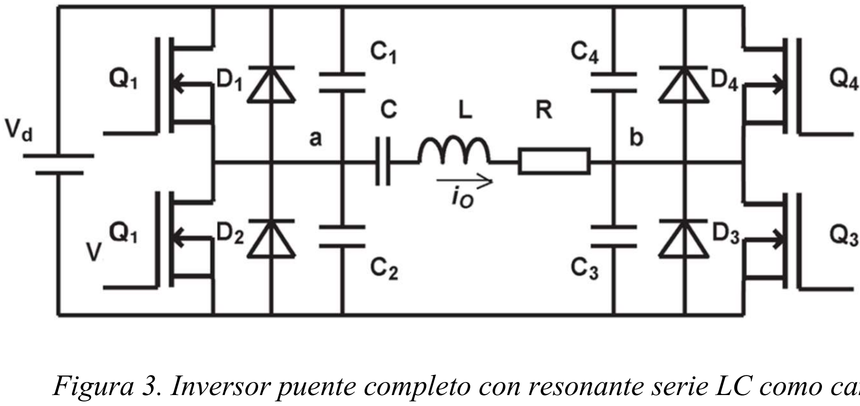

Figura 3. Inversor puente completo con resonante serie LC como carga.

En la configuración del convertidor los diodos se encuentran conectados en antiparalelo con los interruptores, es importante diferenciar entre el estado activo y el estado de conducción del interruptor. Debido a la conexión antiparalela de los diodos, al activarse un interruptor, la circulación de corriente dependerá del sentido de la corriente de salida (i_o). Si el interruptor efectivamente permite el paso de corriente, se considera que está en estado de conducción. Esta distinción resulta irrelevante en los casos en que el interruptor permanece apagado, ya que no fluye corriente a través de él y solo podrá conducirse en sentido opuesto por el diodo.

El convertidor de puente completo está compuesto por dos ramas, denominadas a y b, y cada una contiene de dos interruptores con sus respectivos diodos antiparalelos. La conmutación de los interruptores en cada rama se realiza de forma complementaria. Cuando un interruptor está apagado, el otro se encuentra encendido, evitando que ambos permanezcan encendidos simultáneamente. En la práctica, existe un breve intervalo denominado tiempo muerto, durante el cual ambos interruptores de una misma rama están apagados momentáneamente. Este intervalo se implementa para prevenir un cortocircuito en la entrada de corriente continua. Es importante destacar que, si la conmutación se realiza adecuadamente la corriente de salida fluirá de manera continua. En consecuencia, el voltaje de salida dependerá únicamente del estado de los interruptores.

2.2 Resonante LC serie con transformador de activa

El circuito resonante serie LC, como se muestra en la Figura 4, está compuesto por un inductor de calentamiento (L_S) en serie con un condensador (C_S) para compensar la energía reactiva. La resistencia en serie equivalente (R_S) representa la impedancia impuesta por la pieza a calentar. Este circuito se conecta al inversor de alta frecuencia a través de un transformador, proporcionando aislamiento galvánico y adaptando la impedancia del circuito mediante la relación de transformación.

Esta topología ofrece ventajas sobre el circuito LC en paralelo, como la eliminación de la inductancia de entrada al inversor, un transformador de aislamiento más económico y de menor tamaño, ya que está ubicado en la salida de alta frecuencia del inversor, en lugar de en la red de alimentación del inversor. Además, el circuito resonante serie también presenta ventajas sobre el LLC, ya que su diseño es más simple, utilizando solo dos elementos reactivos y simplificando el control al eliminar la necesidad de gestionar dos frecuencias de resonancia [8].

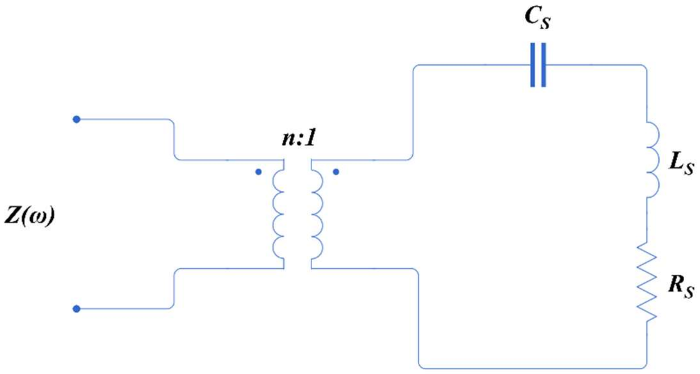

Figura 4. Resonante LC serie con transformador de activa.

El efecto teórico del transformador como adaptador de impedancias se expresa como:

$$R_p = R_s n^2 \tag{6}$$

donde la resistencia de secundario del transformador se refleja en primario (R_p) multiplicada por el cuadrado de la relación de transformación (n), siendo el número de vueltas en primario $n{:}1$. Este efecto también ocurre para la inductancia equivalente reflejada en primario.

$$L_p = L_s n^2 \tag{7}$$

Y tiene el efecto contrario con la capacidad equivalente reflejada en primario.

$$C_p = \frac{C_s}{n^2} \tag{8}$$

Esto hace que cambiar la relación del transformador de activa no implique un cambio en la frecuencia de resonancia del circuito.

$$\omega_o = \omega_p = \frac{1}{\sqrt{L_p C_p}} = \frac{1}{\sqrt{L_s n^2 \frac{C_s}{n^2}}} = \frac{1}{\sqrt{L_s C_s}} \tag{9}$$

Sucediendo lo mismo con el factor de calidad.

$$Q = Q_p = \frac{L_p \omega_p}{R_p} = \frac{L_s n^2 \omega_o}{R_s n^2} = \frac{L_s \omega_o}{R_s} \tag{10}$$

Sin embargo, tiene implicaciones en la magnitud de la impedancia, donde se refleja en primario del transformador como:

$$|Z(\omega)| = n^2 \left| R_s + j\omega L_s + \frac{1}{j\omega C_s} \right| = \frac{n^2 R_s}{\cos\alpha} \tag{11}$$

Siendo α el argumento de la impedancia, representando la fase entre la tensión de salida y la corriente en resonancia, expresándose como:

$$\alpha = \arg\big(Z(\omega)\big) = \arctan\left(\frac{\omega L_p - \frac{1}{\omega C_p}}{n^2 R_p}\right) \tag{12}$$

Por tanto, el efecto de variar la relación del transformador se puede observar en la Figura 5. La magnitud y fase de la impedancia se han representado en función de la frecuencia para diferentes relaciones de transformación, en un resonante LC serie para un factor de calidad superior a 6. Como se observa en la figura, para una frecuencia dada, la magnitud de la impedancia se incrementa con la relación del transformador, comportándose al contrario con la fase. Este efecto permite obtener más potencia para la misma frecuencia únicamente incrementando la relación del trasformador.

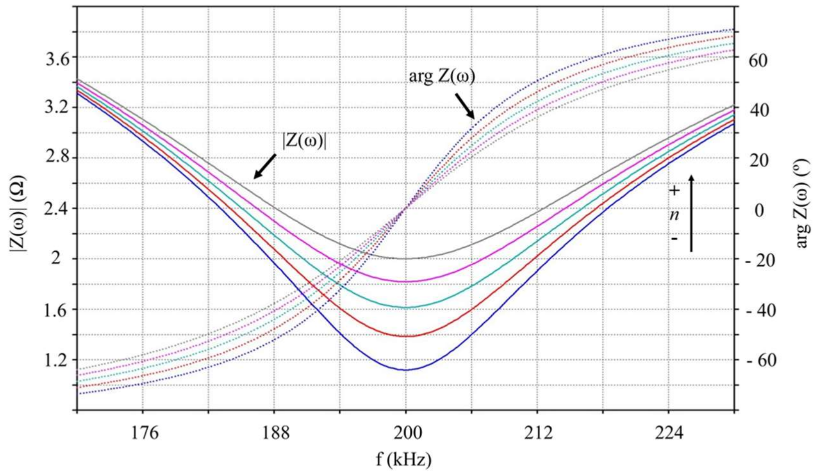

Figura 5. Magnitud de la impedancia (azul, rojo, azul claro, magenta y gris líneas continuas) y fase de la impedancia (azul, rojo, azul claro, magenta y gris líneas discontinuas) en orden creciente de la relación del transformador de activa para el resonante LC.

2.3 Resonante LC serie con transformador de reactiva

El resonante LC serie con transformador de reactiva es una topología similar a la presentada anteriormente. La diferencia radica en la posición y efecto del transformador. Por consiguiente, se compone de un inductor de calentamiento (L_s) en secundario del transformador y que está en serie con un condensador (C_p) ubicado en primario del transformador que compensa la potencia reactiva del circuito. Como se puede observar, se utiliza el transformador para adaptar el inductor al tanque resonante, amplificando la inductancia. Junto con estos componentes, se representa una resistencia en secundario (R_s), la cual corresponde al valor de la resistencia equivalente de la pieza a calentar.

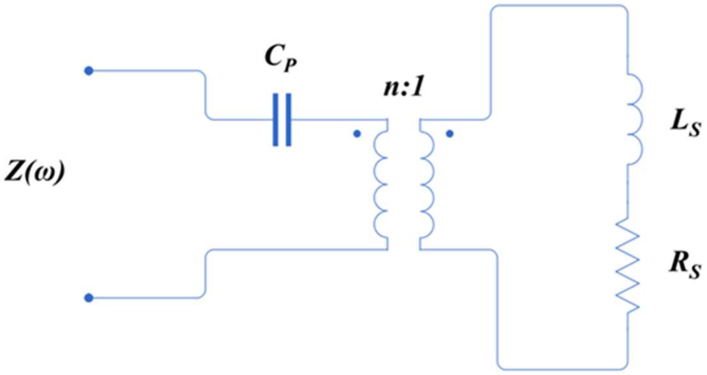

Figura 6. Resonante LC serie con transformador de reactiva.

El comportamiento del transformador consiste en adaptar la inductancia al condensador deseado y a la frecuencia de operación, de manera que la inductancia reflejada en el primario del transformador se expresa como:

$$L_p = L_s n^2 \tag{13}$$

Se puede observar que la inductancia serie en secundario del transformador se refleja en el primario multiplicada por el cuadrado de la relación del número de vueltas del transformador. Este efecto también ocurre con la resistencia equivalente reflejada desde el primario (R_p).

$$R_p = R_s n^2 \tag{14}$$

En contraste con el efecto de variar la relación del transformador en posición de activa, la frecuencia de resonancia si se verá afectada por la relación de transformación.

$$\omega_o = \omega_p = \frac{1}{\sqrt{L_p C_p}} = \frac{1}{\sqrt{n^2 L_s C_p}} \tag{15}$$

Y también afecta al factor de calidad del tanque resonante considerando una potencia activa fija.

$$Q = \frac{L_p \omega_o {I_o}^2}{P_o} = \frac{n^2 L_s \omega_o {I_o}^2}{P_o} \tag{16}$$

Por tanto, el efecto de variar la relación del transformador se puede observar en la Figura 7. En esta figura se ha representado el factor de calidad para un resonante serie en función de la frecuencia, donde se limita la potencia activa manteniendo fija la resistencia equivalente de la pieza a calentar en primario. En este resonante se varía la inductancia serie para simular el efecto de variar la relación del transformador de reactiva. Como se puede observar en la figura, el factor de calidad se incrementa cuando se incrementa la relación del transformado, es decir la inductancia reflejada en primario, pese a que la frecuencia de resonancia baja.

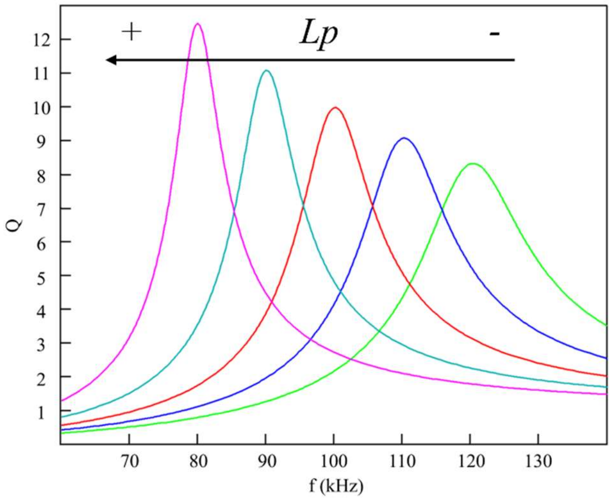

Figura 7. Comportamiento del factor de calidad para R_p contante donde se varía la relación de transformador de reactiva. El pico de la curva se corresponde con el factor de calidad de esta.

2.4 Resonante LLC

El circuito resonante LLC consta de dos inductores y un condensador, junto con la resistencia equivalente de la carga, forma una topología híbrida serie-paralelo, como se muestra en la Figura 8. El circuito está configurado con el inductor de calentamiento (L_P) en paralelo con el condensador (C_P) para compensar la energía reactiva, mientras que el inductor en serie (L_S) está conectado en serie con ellos.

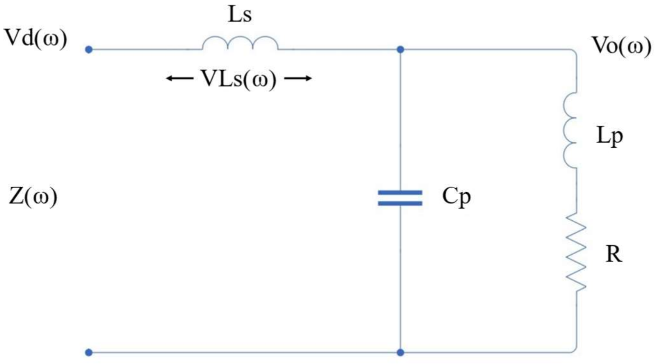

Figura 8. Circuito resonante LLC.

Esta configuración permite que el circuito LLC paralelo exhiba características ventajosas tanto de circuitos resonantes en serie como en paralelo. Cuando se conecta a un inversor como fuente de tensión, simplifica la sección de entrada del convertidor, como ocurre en un inversor resonante serie, donde la inductancia de entrada en el circuito resonante actúa como una fuente de corriente. Además, a través del inductor de salida cercano a la resonancia en paralelo, la corriente amplificada funciona como en un inversor resonante paralelo, eliminando la necesidad de transformadores elevadores de corriente.

Dado que el circuito está compuesto por tres elementos reactivos, existen dos frecuencias de resonancia entre ellos. La frecuencia angular de resonancia paralelo, definida entre el inductor paralelo y el condensador paralelo, se expresa como:

$$\omega_{op} = \frac{1}{\sqrt{L_P C_P}} \tag{17}$$

Mientras que la frecuencia angular de resonancia serie, entre el inductor serie y el condensador paralelo, se expresa como:

$$\omega_o = \frac{1}{\sqrt{\left(\frac{L_P L_S}{L_P + L_S}\right) C_P}} \tag{18}$$

Sus respectivos factores de calidad se expresan como:

$$Q_p = \frac{L_P \omega_{op}}{R} \tag{19}$$

y como:

$$Q = \frac{L_P \omega_o}{R} \tag{20}$$

El ratio entre los dos inductores viene dado por:

$$\beta = \frac{L_S}{L_P} \tag{21}$$

La expresión de la impedancia de entrada del circuito en función de la frecuencia angular se define como:

$$Z(\omega) = L_P \omega_o (\beta + 1) \frac{\frac{1}{Q}\left(\frac{1}{\beta + 1} - \left(\frac{\omega}{\omega_o}\right)^2\right) + j\frac{\omega}{\omega_o}\left(1 - \left(\frac{\omega}{\omega_o}\right)^2\right)}{\left(1 - \left(\frac{\omega}{\omega_{op}}\right)^2\right) + j\frac{\omega}{Q_p \omega_{op}}} \tag{22}$$

Si se sustituye (17) y (18) en (22), se obtiene la expresión de la impedancia de entra en la frecuencia de resonancia serie.

$$Z(\omega_o) = \frac{L_p \omega_o \beta^2}{Q - j(\beta + 1)} \tag{23}$$

Mientras que la fase entre la tensión y corriente de salida se obtiene por su argumento.

$$\alpha = \arg\big(Z(\omega_o)\big) = \arctan\left(\frac{\beta + 1}{Q}\right) \tag{24}$$

La magnitud y la fase de la impedancia de entrada del circuito se muestran en función de la frecuencia angular para un factor de calidad alto (Q > 6), típico de los circuitos LLC [8], en la Figura 9. En esta figura se puede observar el efecto de las dos frecuencias de resonancia del circuito. La frecuencia de resonancia paralela se encuentra en el pico de la magnitud de la impedancia, mientras que la frecuencia de resonancia serie se ubica en el punto de mínima impedancia. En cuanto al comportamiento de la fase respecto a estos puntos, se observa que, al operar por encima de la frecuencia de resonancia serie y por debajo de la frecuencia de resonancia paralela, la fase es positiva. Sin embargo, entre estas dos frecuencias de resonancia, la fase es negativa. Dado que el circuito debe operar con conmutaciones en ZVS, el punto de operación debe tener una fase positiva, situándose ligeramente por encima de la frecuencia de resonancia serie. Esto se debe a que la impedancia del circuito se minimiza, optimizando así los elementos reactivos del circuito resonante LLC al operar con un inversor fuente de tensión.

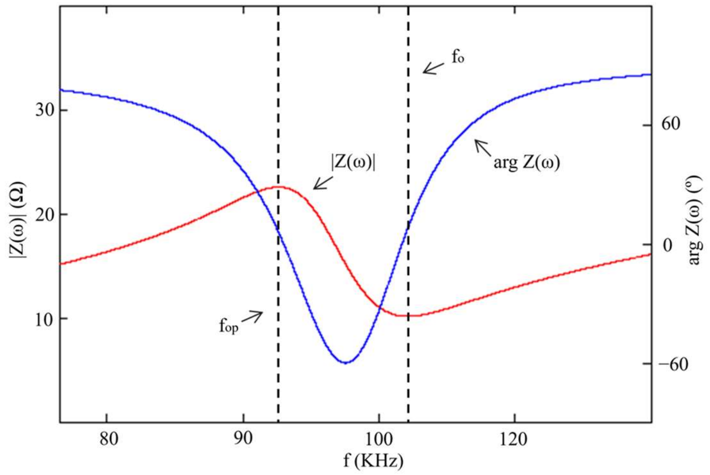

Figura 9. Magnitud de la impedancia (rojo) y fase de la impedancia (azul) del circuito resonante LLC.

2.5 Modulaciones

En este apartado se estudiarán brevemente las tres modulaciones más utilizadas que tienen relación con el contenido de la investigación desarrollada en esta tesis. Estas modulaciones son típicas en los convertidores resonantes para aplicaciones de calentamiento por inducción. Las tres modulaciones tienen en común que son aplicables al puente completo como topología del inversor.

La modulación es un aspecto fundamental para asegurar que el inversor genere la forma de onda de salida requerida. La función esencial del inversor es producir una forma de onda alterna con una forma específica, esta puede ser sinusoidal, cuadrada o cuasi-cuadrada y variar en su fase o frecuencia. Para lograrlo, se emplea un sistema de modulación que ajusta la amplitud, frecuencia y fase mediante el control de los dispositivos de conmutación.

Uno de los aspectos fundamentales es la reducción de armónicos, esto se debe a que las señales generadas por el inversor pueden incluir armónicos de alta frecuencia, los cuales pueden provocar interferencias en los dispositivos conectados y afectar la eficiencia general del sistema. Para mitigar estos efectos, el sistema de modulación optimiza el funcionamiento de los interruptores, minimizando las distorsiones armónicas. Esto permite obtener una forma de onda más limpia, favoreciendo la eficiencia y la compatibilidad electromagnética del sistema. Este requisito es típico de aplicaciones donde se requiere una inyección a red, como por ejemplo en el trabajo desarrollado en [9] y [10].

Dependiendo de la aplicación, se pueden requerir diferentes niveles de tensión y frecuencias de salida. Este es un requerimiento típico de las aplicaciones de calentamiento por inducción donde la frecuencia se relaciona con las consigas de potencia y corriente de salida, además de la profundidad de penetración en la pieza a calentar, mientras que la tensión se relaciona con la potencia y corriente de salida. Gracias al control de modulación, es posible adaptar estas variables según las necesidades de la aplicación ajustándose a las distintas demandas de carga.

El sistema de modulación también contribuye a optimizar el rendimiento del inversor bajo diversas condiciones de carga. Al adaptar su operación a cada escenario, el inversor trabaja de manera más eficiente, reduciendo las pérdidas de energía, especialmente cuando se enfrenta a cargas ligeras. Esto se traduce en un menor consumo y una mayor sostenibilidad operativa. Por ejemplo en [11] se combina la modulación asimétrica con la modulación en frecuencia para incrementar la eficiencia de un inversor medio puente para aplicaciones de calentamiento por inducción.

2.5.1 Modulación en frecuencia

La modulación de la potencia o corriente de salida del inversor variando la frecuencia de conmutación (FM) consiste en aplicar al resonante una onda cuadrada de frecuencia variable, tal y como se muestra en la Figura 10. La forma de onda de la corriente de salida es sinusoidal siempre que el factor de calidad del circuito sea elevado, como corresponde a las aplicaciones de calentamiento por inducción utilizando un resonante serie LC.

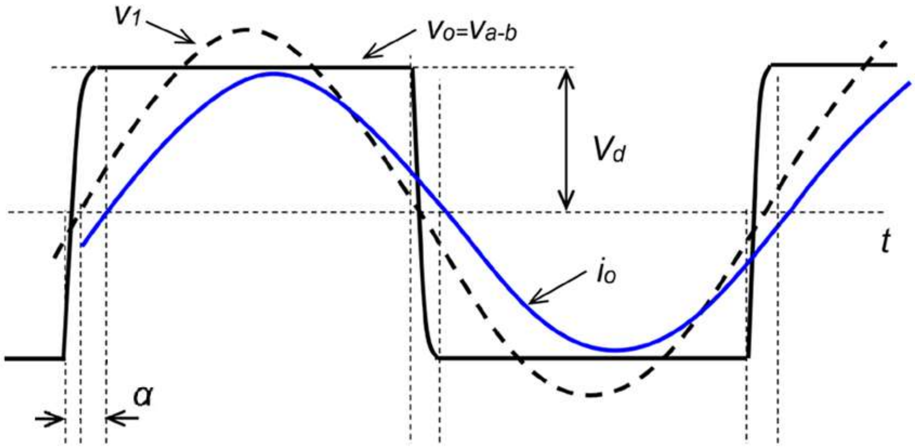

Figura 10. Formas de onda de salida simplificadas para la modulación en frecuencia.

La potencia de salida se define mediante la siguiente expresión:

$$P_o = \frac{1}{T}\int_0^T i_o V_o dt \tag{25}$$

Suponiendo que la forma de onda de la tensión de salida es puramente cuadrada esta puede expresarse por la siguiente función:

$$V_o(t) = \begin{cases} V_d, & 0 < t < T/2 \\ -V_d, & T/2 < t < T \end{cases} \tag{26}$$

Mientras que, si se supone una corriente sinusoidal debido al factor de calidad elevado del circuito, la corriente de salida se define mediante:

$$i_o(t) = i_{pk} \sin(\omega t - \alpha) \tag{27}$$

Por tanto, integrando (25) y sustituyendo el resultado con (27) se obtiene la potencia de salida en función de la tensión de entrada, la corriente de salida y el desfase entre ambas:

$$P_o = \frac{2}{\pi} V_d i_{pk} \cos(\alpha) \tag{28}$$

De la expresión anterior se deduce que la potencia de salida depende de la corriente de salida, del valor de la tensión de entrada, de la frecuencia y de la fase entre la tensión y la corriente de salida. Por tanto, con esta modulación únicamente se variará la frecuencia lo que involucrará cambios en la fase, la corriente de salida y por tanto en la potencia de salida.

2.5.2 Modulación por desplazamiento de fase

La modulación por desplazamiento de fase (PS) permite variar la tensión aplicada al resonante dejando tramos de tensión cero, por tanto, la forma de onda de la tensión aplicada será cuasi-cuadrada. La Figura 11 muestra la forma de onda de la tensión de salida y la corriente de salida sinusoidal.

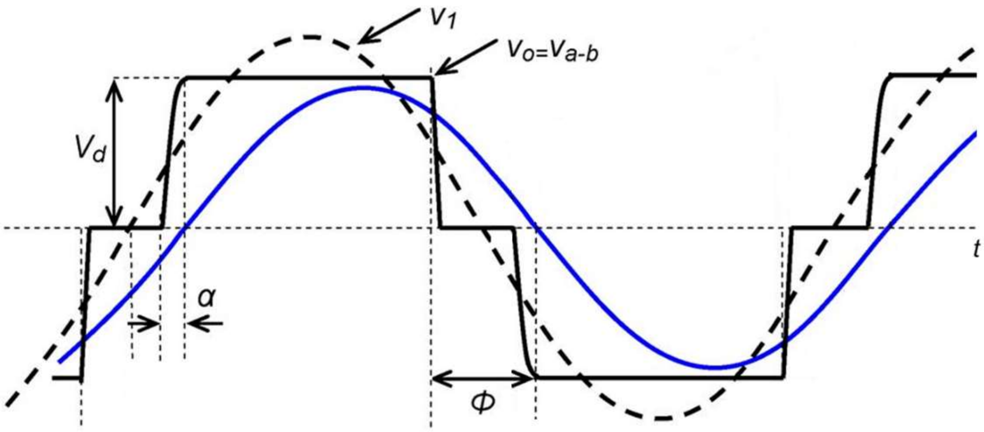

Figura 11. Formas de onda de salida simplificadas para la modulación por desplazamiento de fase.

El ángulo φ, define el desplazamiento de fase y está definido entre 0 y 180 grados, siendo 0 cuando se aplica la máxima tensión al resonante y 180 cuando no se aplica tensión. Por tanto, la tensión de salida se verá definida por los siguientes intervalos,

$$V_o(t) = \begin{cases} V_d, & 0 < t < \varphi \\ 0, & \varphi < t < T/2 \\ -V_d, & T/2 < t < T/2 + \varphi \\ 0, & T/2 + \varphi < t < T \end{cases} \tag{29}$$

Por consiguiente, la expresión de la potencia de salida contempla ahora el ángulo del desplazamiento de fase:

$$P_o = \frac{2}{\pi} V_d i_{pk} \cos\left(\frac{\varphi}{2}\right) \cos(\alpha) \tag{30}$$

De esta expresión podemos concluir que con esta modulación la variación de la potencia vendrá dada por la variación del ángulo del desplazamiento de fase, es decir la tensión aplicada al resonante, con ella se variará también la corriente de salida y la fase entre la tensión y corriente de salida.

2.5.3 Modulación en frecuencia con desplazamiento de fase

La modulación en frecuencia con desplazamiento de fase (FM-PS) es el resultado de la combinación de ambas técnicas de modulación, es decir la forma de onda de la tensión de salida varía tanto en frecuencia como en el ángulo del desplazamiento de fase, lo que permite generar tramos de tensión cero en el resonante.

Esta modulación es la más utilizada en la actualidad y se ha estudiado en numerosos trabajos, [8] y [12]. El éxito de esta modulación radica en que, al poder actuar sobre dos variables, como son la tensión de salida y la frecuencia, se puede obtener por ejemplo la potencia deseada variando la tensión de salida mientras se mantiene un ángulo α fijo por la modulación en frecuencia. Esto hace que el sistema sea multivariable.

Las ventajas de esta modulación frente a las otras dos se deben por un lado a que, al poder aplicar una tensión menor en el resonante, el incremento de la frecuencia se reduce para obtener una potencia menor. Esto proporciona una eficiencia mayor debido a que la frecuencia de conmutación se reduce, además de mejorar las EMI. Por otra parte, poder mantener un desfase reducido entre la tensión y corriente de salida del inversor permite conmutar un nivel de corriente inferior, lo que reducirá las pérdidas de conmutación a OFF de los transistores.

2.6 Transistor MOSFET

Para los diseños de los inversores estudiados en esta tesis se utilizaron transistores como conmutadores en el puente completo. A continuación, se introducen los transistores de potencia y se justifica el uso de transistores de efecto de campo metal-óxido semiconductor (MOSFET) de SiC.

Existen dos tipos principales de transistores, el transistor de unión bipolar (BJT) y el transistor de efecto de campo (FET). Los BJT se utilizan generalmente para corrientes eléctricas inferiores a un amperio, mientras que los MOSFET, que son un tipo de FET, se emplean en aplicaciones de corriente más alta.

El MOSFET es un semiconductor ampliamente utilizado en circuitos digitales y analógicos, además de ser un dispositivo de potencia útil. Su popularidad frente al BJT radica en su requerimiento de corriente mínima para el control de la corriente de carga. Entre sus ventajas adicionales se encuentran su rápida conmutación, bajo consumo de energía y alta densidad, lo que los hace ideales para la integración a gran escala. El MOSFET cuenta con cuatro terminales: surtidor (S), puerta (G), drenador (D) y sustrato (B). El sustrato suele estar conectado al surtidor para que el MOSFET funcione como un transistor de efecto de campo.

El MOSFET de potencia tiene una estructura vertical en lugar de planar, lo que le permite mantener un alto voltaje de bloqueo y una corriente elevada simultáneamente. Además, opera principalmente con portadores mayoritarios, evitando los problemas generados por los portadores minoritarios en los transistores bipolares. Su impedancia de entrada es generalmente mayor que la de los transistores de efecto de campo de unión (JFET) [13].

Inicialmente, se creía que lograr una baja resistencia en estado de conducción, un alto voltaje de ruptura y una gran capacidad de potencia en los MOSFET de potencia sería complicado. Sin embargo, en los últimos años, han surgido mejoras significativas en su rendimiento gracias a sus estructuras [13]. La Figura 12 ilustra las tres estructuras más comunes utilizadas en la actualidad. En el apartado (a) se muestra la estructura de MOS de doble difusión (D-MOS). En esta los canales se forman mediante un proceso de doble difusión que proporciona un alto voltaje de ruptura. Este proceso es ideal para aumentar la densidad del dispositivo, permitiendo la creación de MOSFET de potencia de alto rendimiento con baja resistencia en estado de conducción y baja pérdida de energía. En cambio, el apartado (b) muestra la estructura de puerta en trinchera. Esta forma un canal de puerta vertical en forma de ranura en U, lo que aumenta la densidad del dispositivo y reduce aún más la resistencia en estado de conducción. Esta estructura se emplea para fabricar MOSFET de potencia de bajo voltaje. Por último, en el apartado (c) se puede observar la estructura de superunión (SJ). En esta estructura, el "*drift layer*" está compuesto por capas alternas de semiconductores tipo P- y N-. Este proceso supera las limitaciones inherentes al proceso de silicio vertical utilizado en los MOSFET de potencia convencionales y ofrece una resistencia en estado de conducción extremadamente baja.

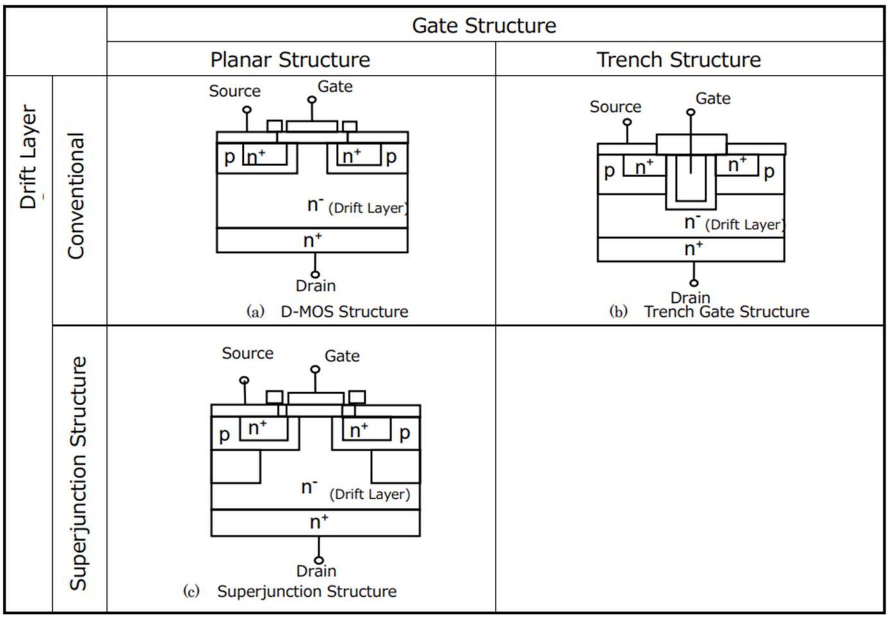

Figura 12. Estructura de los MOSFET de potencia [13].

Actualmente, la tecnología de silicio (Si) domina el mercado de la electrónica de potencia debido a su fiabilidad y bajo costo. Sin embargo, la constante necesidad de mejorar la eficiencia, reducir el tamaño y aumentar la capacidad de tensión ha llevado esta tecnología a su límite. En este contexto, han surgido nuevas alternativas, como los semiconductores de banda prohibida ancha (WBG), que ofrecen un mejor desempeño.

Entre estos materiales, el GaN destaca por su idoneidad en aplicaciones de alta potencia y frecuencia, pero como se estudió en el proyecto descrito en el apartado 1.3.1 su desarrollo ha sido más lento debido a la falta de sustratos de alta calidad. Por otro lado, el SiC ha avanzado más rápidamente y ya cuenta con dispositivos comerciales robustos y confiables, superando al silicio en muchas aplicaciones.

En términos de aplicación el GaN es adecuado para sistemas de tensión media y alta frecuencia de conmutación, aunque su eficiencia disminuye a altas temperaturas. Mientras que el SiC es más apropiado para condiciones de alta tensión y temperatura.

A pesar de que el interés industrial en GaN ha aumentado debido a su capacidad de formar heteroestructuras, lo que permite desarrollar transistores de alta movilidad de electrones (HEMTs) con mayor concentración de portadores y alta movilidad en el canal, su uso en dispositivos de alta tensión sigue siendo limitado por la falta de transistores verticales.

Los inversores estudiados en esta tesis operan con potencias inferiores a 20 kW y frecuencias de hasta 200 kHz. Aunque cualquiera de las tres tecnologías (Si, GaN o SiC) podría ser utilizada, la búsqueda de una mayor eficiencia descarta el silicio. La elección entre SiC y GaN se basa en dos factores clave, el primero es la tensión de ruptura, la ausencia de transistores verticales en GaN limita las tensiones máximas de los dispositivos laterales a 600 V. El segundo es la capacidad de avalancha, la robustez eléctrica de los dispositivos depende de su capacidad para soportar sobretensiones de manera segura. En los MOSFET de silicio y SiC, esto se debe a su capacidad intrínseca de avalancha, un fenómeno de ionización por impacto y multiplicación que permite disipar internamente la energía de sobretensión, evitando daños. La energía de avalancha es la máxima cantidad de energía que un dispositivo puede disipar sin provocar fugas catastróficas que resulten en un embalamiento térmico. En contraste, los dispositivos GaN HEMT tienen una capacidad de avalancha muy limitada o nula [14].

Finalmente se puede concluir que cada tecnología tiene aplicaciones específicas determinadas por la frecuencia y la tensión de operación. En la Figura 13 se ilustran las aplicaciones de cada material en función de la potencia y la frecuencia. La elección del SiC en los inversores de esta tesis se debe a su superioridad en términos de tensión de ruptura y robustez eléctrica frente al GaN, lo que lo convierte en la mejor opción para las condiciones de operación establecidas.

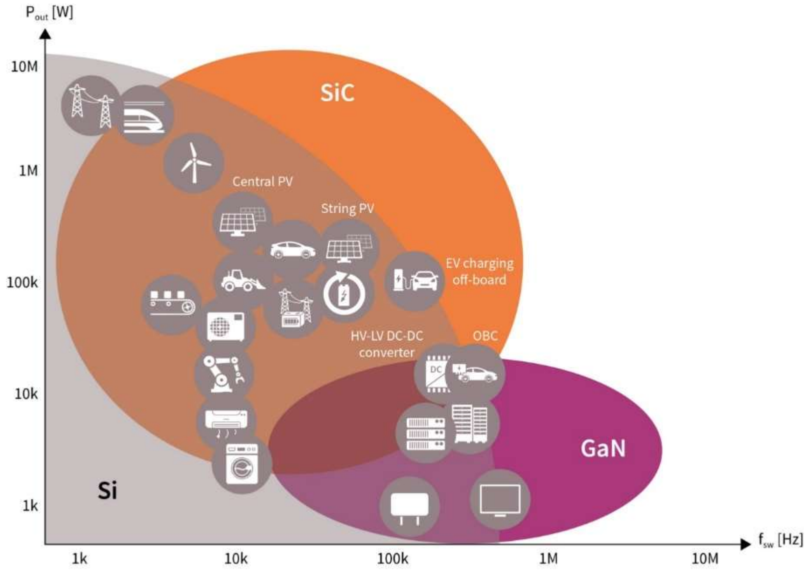

Figura 13. Aplicaciones de los dispositivos de banda ancha prohibida [15].

2.7 Conmutación ZVS

Para comprender la importancia de las conmutaciones suaves con relación a las regiones de funcionamiento en la topología del inversor propuesta para este trabajo, se ha representado en la Figura 14 la transición de la conmutación de OFF del transistor Q4 a la conmutación a ON del transistor Q3. En esta figura se está conmutando una carga resonante serie LC a una frecuencia superior a la frecuencia de resonancia, por tanto, la tensión de salida está adelantada a la corriente de salida y el inversor trabaja en ZVS debió a estar trabajando en la zona inductiva. Como se puede observar en la figura, la topología del inversor es un puente completo con transistores MOSFET, y la modulación utilizada es el desplazamiento de fase.

En el primer punto se está trabajando en el modo de recirculación de la corriente por la parte superior del inversor, para poder llegar al cuarto punto, que es conmutar la diagonal positiva del inversor, primero debe conmutarse a OFF el transistor Q4. Tanto el punto dos como el punto tres se corresponden con el tiempo muerto, necesarios para no cortocircuitar la rama de Q4 y Q3. Durante el punto dos, se descarga la capacidad parásita del transistor Q3 y se carga la capacidad parásita del transistor Q4. Entiéndase descargar el condensador cuando la diferencia de tensión de este se corresponde a cero voltios y cargarlo cuando se alcanza V_d. A continuación, tercer punto, la corriente circulará por el diodo en antiparalelo del transistor Q3, para posteriormente, punto cuatro, conmutar a ON el transistor Q3. Por tanto, la conmutación a ON del transistor Q3 se está dando a cero tensión, debido que la tensión que soporta el transistor durante la conmutación es la caída de tensión del diodo intrínseco del dispositivo.

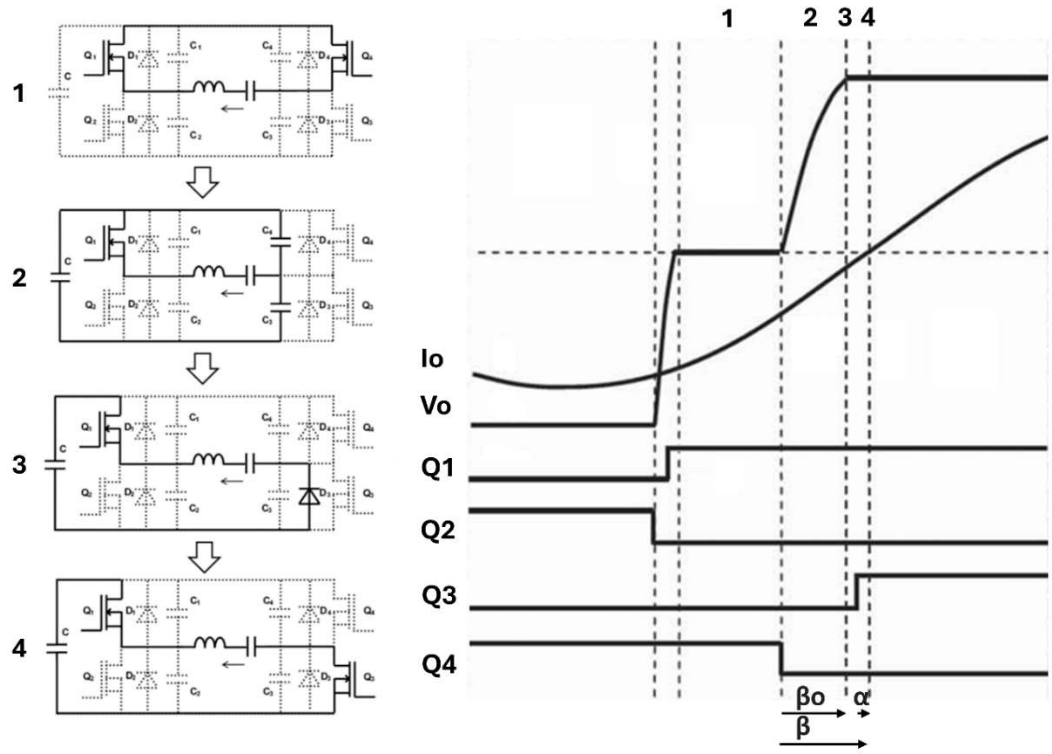

Figura 14. Secuencia conmutación en ZVS.

Para conmutar óptimamente los transistores, evitando por tanto pérdidas en los dispositivos, es importante tener en cuenta el valor del tiempo muerto. Si el tiempo muerto es muy pequeño o se omite, se producirá un solapamiento de los transistores de la misma rama, lo que equivaldrá a un cortocircuito de la alimentación V_d a través del canal de los transistores. Por otra parte, si el tiempo muerto no es lo suficientemente grande para descargar y cargar las capacidades parásitas de los transistores antes de conmutar Q3 a ON, se descargará la capacidad de este mismo bruscamente a través del canal del transistor incrementando las pérdidas en el dispositivo, al igual que se cargará bruscamente la capacidad parásita del transistor Q4. Por último, si el tiempo muerto es superior al tiempo muerto necesario, circulará la corriente más tiempo del óptimo por el diodo intrínseco del dispositivo, incrementando también las pérdidas del dispositivo.

Para obtener un tiempo muerto óptimo se tienen que considerar tres ángulos, el primero es β que se corresponde con el ángulo entre el inicio de cambio de estado de la tensión de salida y el cruce por cero de la corriente, el segundo es β_o que atañe al ángulo entre el inicio del cambio de estado de la tensión de salida y el alcance del valor de V_d, por último, el ángulo α que se vincula al ángulo entre la conmutación a ON del transistor y el cruce por cero de corriente. El ángulo α juega un papel fundamental en la determinación del tipo de conmutación y las pérdidas asociadas. Este ángulo puede ser positivo, negativo o igual a cero. Sin embargo, el tipo de conmutación no depende directamente del valor de este ángulo, se corresponde con el nivel de tensión que presenten los condensadores parásitos en el momento de la conmutación hacia conducción. Debido a esto, determinar los procesos de conmutación puede ser complejo. Las posibles casuísticas para α en relación con las pérdidas de conmutación son, si es negativo la conmutación hacia conducción siempre se producirá con los condensadores parásitos a una tensión inferior a V_d, siendo este caso el que producirá pérdidas asociadas en la conmutación. Si α es cero la conmutación hacia conducción será sin pérdidas únicamente si el ángulo β es mayor o igual a β_o, que corresponde al ángulo en el que los condensadores parásitos se cargan a V_d. Por último, si α es positivo la conmutación hacia conducción será sin pérdidas solo si α es menor que la diferencia entre el ángulo β y β_o.

Estas condiciones pueden resumirse matemáticamente con la fórmula (31) y deben considerarse cuidadosamente para optimizar el rendimiento del inversor resonante con componentes reales y minimizar así las pérdidas durante las conmutaciones [7].

$$\beta - \beta_o \geq \alpha \geq 0 \tag{31}$$

Nótese que se ha fijado como punto óptimo un valor de α siempre superior o igual a 0, lo que descarta trabajar en la zona capacitiva, es decir por debajo de la frecuencia de resonancia serie, este hecho hace que solo se puedan considerar la operación del inversor con conmutaciones en ZVS y no en ZCS. Esto se debe a que las conmutaciones en ZCS evitan tener pérdidas de conmutación a OFF en el transistor, pero no en la conmutación a ON. Lo que presenta dos inconvenientes, el primero como se ha mencionado con anterioridad, es que al conmutar con valores de α pequeños y menores a cero, se estarán cargando y descargando las capacidades parásitas bruscamente a través del canal del transistor, lo que elevará las pérdidas de conmutación a ON, por otra parte si los valores de α son grandes y menores que cero, dando lugar a que la corriente se adelante a la tensión, se estará conmutando en la zona capacitiva, lo que provocará pérdidas en la conmutación debido a la recuperación inversa del diodo de uno de los MOSFET y la conducción a ON del otro MOSFET de la misma rama. El segundo inconveniente concierne al propio comportamiento de las pérdidas de los transistores MOSFET en cuanto a las pérdidas de conmutación de ON y de OFF, como se puede observar en la Figura 15 para una conmutación brusca a un mismo nivel de corriente, se obtienen una menor energía de pérdidas en la conmutación a OFF que en la conmutación a ON, lo que hace favorable trabajar en una situación donde no se tengan pérdidas en la conmutación a ON, como es la conmutación en ZVS.

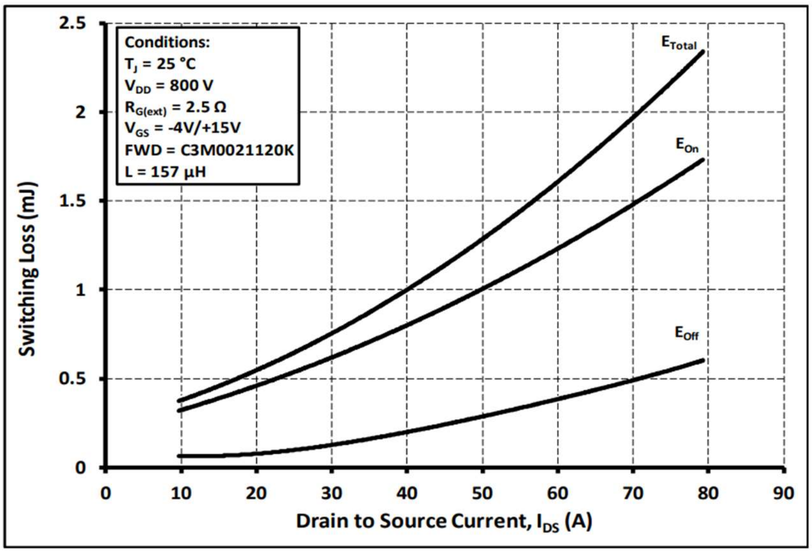

Figura 15. Energía de conmutación inductiva frente a la corriente de drenador [16].

Capítulo 3. Control de los elementos reactivos

3.1 Inductor variable controlado por corriente

El inductor variable controlado por corriente tiene sus orígenes en estudios previos [18] y [19]. Su principio de funcionamiento se basa en saturar la parte externa del núcleo del inductor con corriente continua para variar la permeabilidad efectiva. Como se muestra en la Figura 17, este inductor está compuesto por dos núcleos de ferrita con forma de "E" superpuestos. La rama central tiene un entrehierro y está bobinada para formar el inductor principal (L_{ac}). Por otro lado, los dos brazos laterales forman el inductor de control de saturación (L_{bias}), que está bobinado en serie con polaridad opuesta para desacoplar L_{ac} de L_{bias}, anulando la influencia del flujo magnético de la bobina de L_{ac} y evitando tensiones inducidas.

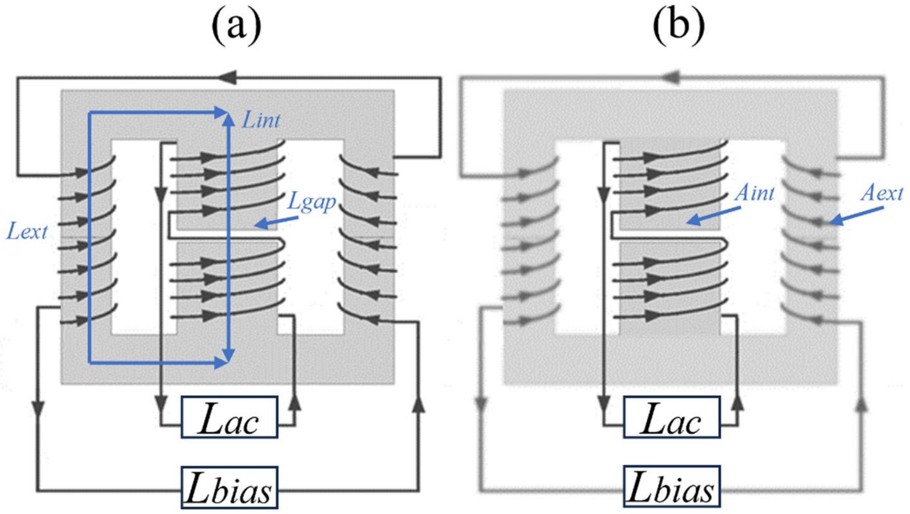

Figura 16. Estructura del inductor variable controlado por corriente: (a) con cero corriente de bias y (b) con la máxima corriente de bias.

Como se puede observar en la figura, cuando la corriente de bias es cero, el flujo magnético de L_{ac} se distribuye entre la parte centrar del núcleo y las ramas exteriores, haciendo por tanto que la inductancia sea máxima. En cambio, cuando se va inyectando corriente continua de bias por el bobinado de L_{bias}, el flujo magnético continuo se cierra por la parte exterior del núcleo, decrementando la permeabilidad relativa de la parte exterior, únicamente se cierra por la parte exterior debido a que la rama central tiene un gap de aire. Esto produce un decremento de la permeabilidad, reduciendo por tanto el valor de la inductancia de L_{ac}. La variación de la permeabilidad relativa para un núcleo de ferrita en función del campo magnético continuo se puede observar en la Figura 17.

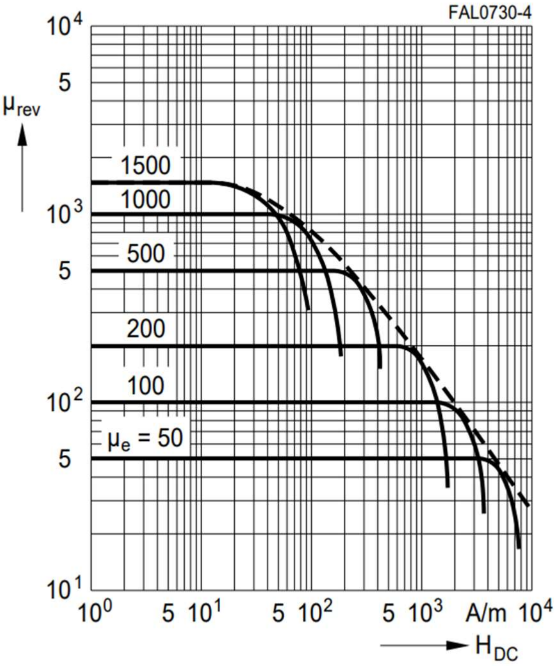

Figura 17. Permeabilidad relativa frente a el campo magnético continuo [17].

El análisis matemático del inductor variable controlado por corriente se basa en las relaciones fundamentales que equilibran los amperios vuelta y los flujos magnéticos. Pudiendo obtener el circuito de la Figura 18, que muestra el circuito equivalente del cual se expresará la relación de inductancias.

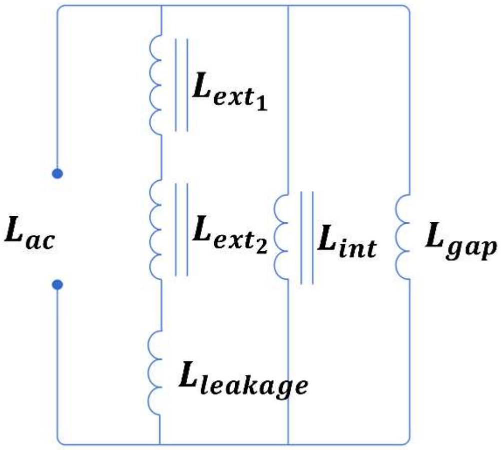

Figura 18. Circuito equivalente de las inductancias.

Primero se obtiene la expresión de cada una de las inductancias que intervienen en el sistema. Utilizando la fórmula de inductancia basada en su geometría para un inductor con núcleo de ferrita, el valor de la inductancia de la rama central se expresa de la siguiente manera:

$$L_{int} = \frac{\mu_0 \mu_i A_{int} (n_{int})^2}{l_{int}} \tag{32}$$

donde μ_i es la permeabilidad inicial del núcleo, μ_0 es la permeabilidad del aire, A_{int} es el área efectiva de la sección transversal de la rama central, n_{int} es el número de vueltas de la bobina de L_{ac}, y l_{int} es la longitud de la rama central.

El valor de la inductancia debido al gap de aire se expresa como:

$$L_{gap} = \frac{\mu_0 A_{int}(n_{int})^2}{l_{gap}} \tag{33}$$

donde l_{gap} es la longitud del gap de aire.

La inductancia de dispersión representa el flujo magnético que se cierra a través del aire y no a través del cuerpo central de la ferrita,

$$L_{leakage} = \frac{\mu_0 16 A_{int}(n_{int})^2}{l_{int}} \tag{34}$$

y la inductancia de las dos ramas externas se expresa como:

$$L_{ext} = \frac{2\mu_0 \tilde{\mu} A_{ext}(n_{int})^2}{l_{ext}} \tag{35}$$

donde $\tilde{\mu}$ es la permeabilidad relativa sin ser sometida a DC bias, A_{ext} es él es el área efectiva de la sección transversal de la rama externa y l_{ext} es la longitud de la rama externa.

Por tanto, mediante la siguiente expresión se obtiene el valor máximo de L_{ac}.

$$\frac{1}{L_{ac_{max}}} = \left(\frac{1}{L_{ext} + L_{leakage}} + \frac{1}{L_{int}} + \frac{1}{L_{gap}}\right) \tag{36}$$

Dado que $\tilde{\mu}$ disminuye cuando se expone a una intensidad de campo magnético continuo (H_{bias}), a la que está sometida la bobina de L_{bias}, la relación entre $L_{ac_{max}}$ y $L_{ac_{min}}$, siendo esta última el valor mínimo de L_{ac} debido al valor mínimo de $\tilde{\mu}$ causado por el valor máximo de H_{bias}, puede obtenerse utilizando la siguiente expresión:

$$\frac{L_{ac_{max}}}{L_{ac_{min}}} = \left(\frac{\dfrac{2\mu_e \dfrac{c}{l_{ext} + l_{int}}}{\tilde{\mu} + 32} + \dfrac{\mu_e \dfrac{l_{int}}{l_{ext} + l_{int}}}{\mu_i} + 1}{\dfrac{2\mu_e \dfrac{l_{int}}{l_{ext} + l_{int}}}{\mu_i + 32} + \dfrac{\mu_e \dfrac{l_{int}}{l_{ext} + l_{int}}}{\mu_i} + 1}\right) \tag{37}$$

donde μ_e es la permeabilidad relativa efectiva de un núcleo con gap, obtenida de la ecuación fundamental de un inductor.

$$L = \frac{\mu_0 \mu_e A_e n^2}{l} \tag{38}$$

Hasta ahora se ha obtenido la expresión que relaciona la variación de las inductancias (37), el diseño final del inductor variable con los parámetros necesario para la aplicación se estudia en el apartado 4.1.2.

3.2 Transformador variable controlado por corriente

El análisis del transformador variable controlado por corriente tiene sus orígenes en artículos previos [20] y [21]. Su funcionamiento básico se basa en el modelo del inductor variable ya presentado en otros trabajos [18] y [19]. Su principio operativo se fundamenta en distribuir el flujo magnético generado por el primario hacia el secundario, variando la permeabilidad efectiva del núcleo mediante un camino que reduce su reluctancia al conectarse a una fuente de corriente continua. Como en el inductor variable, la variación de la permeabilidad relativa frente a la exposición a H_{bias} se muestra en la Figura 17. Esto aumenta la influencia de la reluctancia del camino secundario, el cual incluye un entrehierro. Para lograr esto, numerosos artículos han propuesto diferentes topologías de núcleos magnéticos para diversas aplicaciones. Se han fabricado núcleos personalizados no comerciales, lo que incrementa los costos y complica el proceso de diseño [22] y [23]. Este problema se ha abordado parcialmente utilizando dos núcleos comerciales con forma de "E" [24] y [25], pero, aunque estos núcleos son comerciales, aún requieren modificaciones debido a la posición del entrehierro. Además, presentan una estructura compleja que requiere un proceso de medición experimental para el diseño del transformador y sus relaciones.

La estructura presentada en este trabajo, [26] y [27], como se muestra en la Figura 19, aborda estas limitaciones utilizando cuatro núcleos comerciales con forma de "E" y un entrehierro central, que, distribuidos simétricamente como se describe a continuación, permiten que el modelo de inductancia sea fácilmente analizado. El devanado primario está enrollado entre las dos ramas externas de ambos núcleos, que están unidas entre sí. El devanado secundario está dividido entre las ramas centrales de los núcleos, y sus bobinados están conectados en paralelo. Los dos brazos laterales exteriores forman el inductor de control de saturación sometido a polarización de corriente continua, que está bobinado en serie con polaridad opuesta para desacoplar el primario y el secundario de la polarización de corriente continua, neutralizando la influencia del flujo magnético y evitando tensiones inducidas.

Por lo tanto, cuando el núcleo no está sometido a polarización de corriente continua, la reluctancia del secundario será menor que la del núcleo, ya que incluye un entrehierro, causando que el flujo magnético se cierre en menor medida a través del secundario. Sin embargo, cuando el núcleo está sometido a polarización de corriente continua, la permeabilidad efectiva del núcleo disminuye al saturarse y, por lo tanto, su reluctancia aumenta, haciendo que la reluctancia del secundario sea mayor en relación con la del núcleo, lo que provoca que el flujo magnético se cierre a través de este camino.

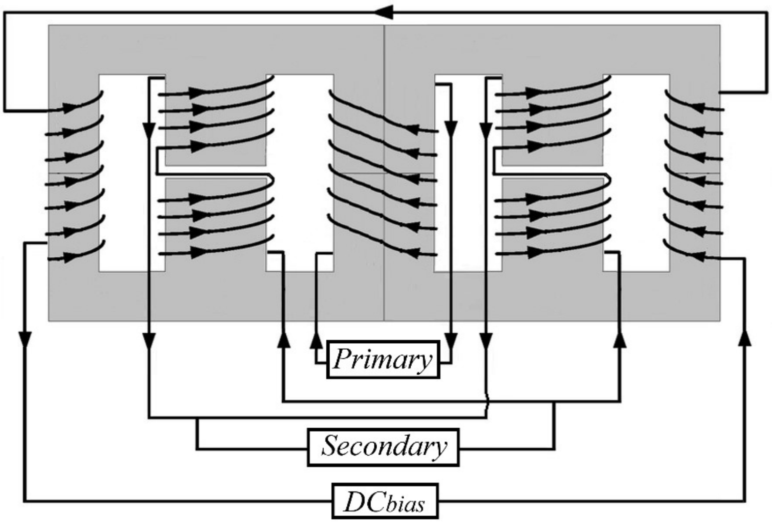

Figura 19. Estructura del transformador variable controlado por corriente.

El análisis del circuito magnético se basa en las relaciones que equilibran los amperios vuelta y los flujos magnéticos de la estructura propuesta dado su carácter simétrico. Esto permite analizar el transformador definiendo las inductancias que lo componen [18], [28] y [29]. Para mantener la simetría y facilitar el diseño, las inductancias reflejadas desde el primario se analizarán como un solo núcleo, mientras que las del secundario se considerarán como dos núcleos en paralelo. Esto conduce a la representación de los circuitos de inductancia equivalentes mostrados en la Figura 20.

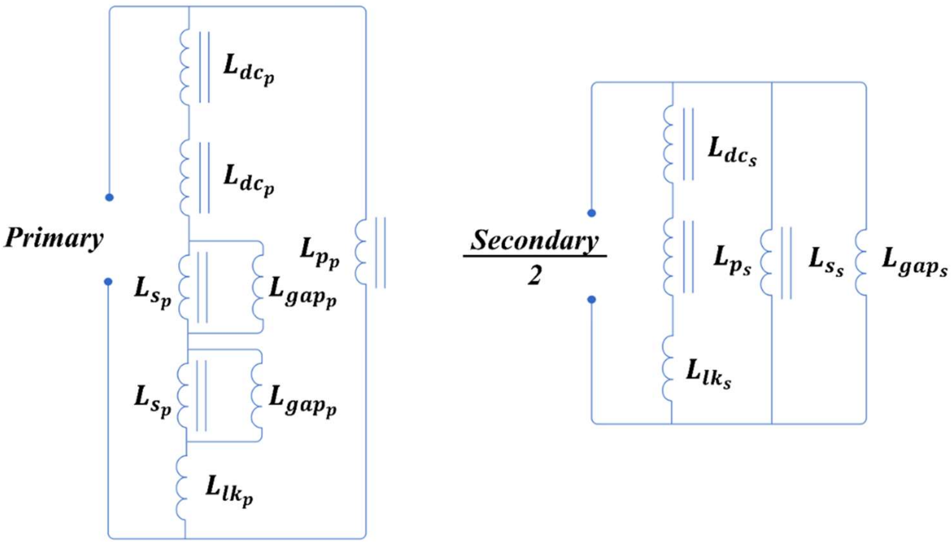

Figura 20. Circuito equivalente de las inductancias en primario a la izquierda y en secundario a la derecha.

Por lo tanto, la inductancia reflejada desde el primario debido a la rama de primario y la inductancia de la rama de primario reflejada desde el secundario se expresan, respectivamente, de la siguiente manera:

$$L_{p_p} = \frac{\mu_0 \mu_i A_p (n_p)^2}{l_{p_p}} \text{ y } L_{p_s} = \frac{\mu_0 \mu_i A_p (n_s)^2}{l_{p_s}} \tag{39}$$

donde A_p es el área efectiva de la rama de primario, n_p y n_s el número de vueltas de primario y de secundario, l_{p_p} es la longitud del camino magnético de la rama de primario y l_{p_s} es la longitud del camino magnético de la rama desde primario a secundario.

Con respecto a las inductancias de las ramas de secundario reflejadas desde el primario y secundario, estas se expresan, respectivamente, como:

$$L_{s_p} = \frac{\mu_0 \mu_i A_s (n_p)^2}{l_{s_p}} \text{ y } L_{s_s} = \frac{\mu_0 \mu_i A_s (n_s)^2}{l_{s_s}} \tag{40}$$

donde A_s es el área efectiva de la rama de secundario, l_{s_s} es la longitud del camino magnético de la rama de secundario, y l_{s_p} es la longitud del camino magnético del brazo secundario hacia el primario.

La inductancia de dispersión, que se cierra a través del aire en lugar de hacerlo a través del núcleo de ferrita, se expresa tanto para el primario como para el secundario de la siguiente manera:

$$L_{lk_p} = \frac{\mu_0 16 A_p (n_p)^2}{l_{p_p}} \text{ y } L_{lk_s} = \frac{\mu_0 16 A_s (n_s)^2}{l_{s_s}} \tag{41}$$

La inductancia debida a las ramas de saturación, tanto para el primario como para el secundario, cumplen con las siguientes expresiones:

$$L_{dc_p} = \frac{\mu_0 \tilde{\mu} A_{dc} (n_p)^2}{l_{dc_p}} \text{ y } L_{dc_s} = \frac{\mu_0 \tilde{\mu} A_{dc} (n_s)^2}{l_{dc_s}} \tag{42}$$

donde A_{dc} es el área efectiva de la rama de la polarización de corriente continua, y l_{dc} es la longitud del camino magnético de la misma rama.

Finalmente, las inductancias debidas al entrehierro ubicado en las ramas secundarias se expresan, cuando se observan desde el primario y el secundario, como:

$$L_{gap_p} = \frac{\mu_0 A_{gap} (n_p)^2}{l_{gap}} \text{ y } L_{gap_s} = \frac{\mu_0 A_{gap} (n_s)^2}{l_{gap}} \tag{43}$$

donde A_{gap} y l_{gap} corresponden, respectivamente, al área efectiva y a la longitud del camino magnético del entrehierro.

La distribución de las longitudes del camino magnético se muestra en la Figura 21.

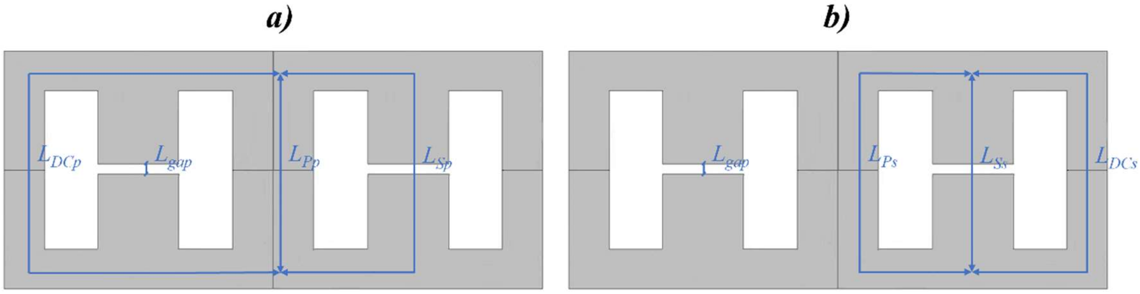

Figura 21. Distribución de la longitud de los caminos magnéticos. (a) desde el lado de primario y (b) desde el lado de secundario.

Por lo tanto, como se muestra en el circuito equivalente de la Figura 20, la inductancia máxima del primario puede expresarse como:

$$\frac{1}{L_{p_{max}}} = \left(\frac{1}{L_{P_p}} + \frac{1}{L_{lk_p} + 2L_{dc_p} + \dfrac{2}{L_{s_p} + L_{gap_p}}} \right) \tag{44}$$

Mientras que la inductancia máxima de secundario se expresa mediante:

$$\frac{1}{2L_{s_{max}}} = \left(\frac{1}{L_{p_s} + L_{dc_s} + L_{lk_s}} + \frac{1}{L_{s_s}} + \frac{1}{L_{gap_s}} \right) \tag{45}$$

Dado que $\tilde{\mu}$ disminuye cuando se expone a una intensidad de campo magnético continuo, a la cual está sometido el bobinado de L_{dc}, la relación entre L_{max} y L_{min}, siendo este último el valor mínimo de inductancia debido al valor mínimo de $\tilde{\mu}$ resultante de la máxima exposición a H_{bias}, puede obtenerse utilizando la siguiente expresión para el primario.

$$\frac{L_{p_{max}}}{L_{p_{min}}} = \left(\frac{\dfrac{1}{2\mu_i} + \dfrac{6l_{gap}}{2l_{gap}(74 + 6\mu_i) + 3l_{p_s}}}{\dfrac{1}{2\mu_i} + \dfrac{24(l_{gap} + l_{p_s})}{2\mu_e l_{gap} l_{p_s}(74 + 4\mu_i + \tilde{\mu}) + 1}} \right) \tag{46}$$

y para el secundario como:

$$\frac{L_{s_{max}}}{L_{s_{min}}} = \left(\frac{\dfrac{2\mu_e \dfrac{l_{s_s}}{l_{s_p} + l_{s_s}}}{\tilde{\mu} + 32} + \dfrac{\mu_e \dfrac{l_{s_s}}{l_{s_p} + l_{s_s}}}{\mu_i} + 1}{\dfrac{2\mu_e \dfrac{l_{s_s}}{l_{s_p} + l_{s_s}}}{\mu_i + 32} + \dfrac{\mu_e \dfrac{l_{s_s}}{l_{s_p} + l_{s_s}}}{\mu_i} + 1} \right) \tag{47}$$

Hasta ahora se han obtenido las relaciones de las inductancias máximas y mínimas de primario (46) y secundario (47). Como se trató en 2.2 y 2.3, el transformador puede situarse en activa o en reactiva, lo que hace que el diseño final dependa de la aplicación y de la posición del transformador, por ello este diseño se estudia en el apartado 4.2.2 para la posición de activa y en el apartado 4.3.2 para la posición de reactiva del transformador.

3.3 Interruptor magnético de recuperación de energía

El control electrónico del condensador de un tanque resonante ya ha sido estudiado en trabajos previos. En [30], se utiliza el interruptor magnético de recuperación de energía (MERS) en un convertidor LC paralelo para variar la frecuencia de trabajo del resonante. Sin embargo, el uso de una topología en paralelo presenta el problema de requerir un rectificador controlado con una inductancia en serie que actúe como fuente de corriente para el condensador en paralelo. Además, para implementar MERS se utilizan cuatro transistores bipolares de puerta aislada (IGBT), lo que limita la frecuencia máxima a 30 kHz, insuficiente para profundidades de penetración pequeñas. Por otro lado, aumentar el ciclo de trabajo del condensador incrementa su influencia en el resonante, disminuyendo la frecuencia, lo que implica una pérdida del factor de calidad, es decir, la capacidad de entregar potencia a la pieza a calentar. En [31], la topología se simplifica utilizando un convertidor LC serie, pero en este caso se emplean cuatro IGBT para formar el puente completo y otros cuatro para el MERS, y la frecuencia sigue estando limitada a 30 kHz. Además, como en el anterior caso se pierde el factor de calidad a medida que disminuye la frecuencia. La topología de condensador controlable también ha sido publicada en otros trabajos como condensador serie con control de puerta (GCSC) [32] y [33], donde se aplica al fenómeno de resonancia subsincrónica de un generador-turbina de vapor. Sin embargo, las frecuencias de aplicación son bajas, lo que permite el uso de tiristores para controlar el condensador. Por lo tanto, y dado que las frecuencias deseadas para aplicaciones de inducción como es el endurecimiento suelen estar en el rango de 50 kHz a 200 kHz [34], se presenta un nuevo diseño de MERS [27], que utiliza solo dos transistores MOSFET de carburo de silicio para controlar la influencia del condensador. La topología propuesta se puede observar en la Figura 22.

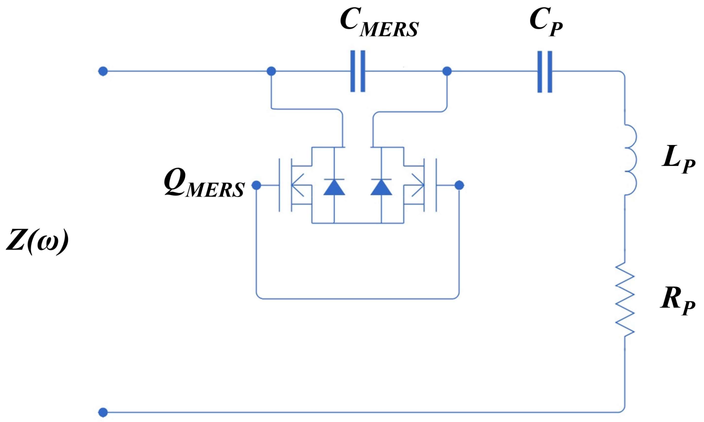

Figura 22. Topología del MERS en un resonante serie LC.

El principio de funcionamiento consiste en cortocircuitar el condensador durante una cierta fase para reducir la compensación de energía reactiva del mismo, de modo que durante ese instante la tensión proporcionada por el condensador MERS al inductor será nula, debido a que no circula corriente a través de él. Para evitar intervalos en los que la energía compensada sea nula, la topología incluye otro condensador en serie que mantiene el valor mínimo, ya que la corriente circula continuamente a través de este. Este efecto permite variar la potencia aplicada a la carga sin modificar la frecuencia de entrada del tanque resonante en serie, o disminuir la frecuencia de resonancia del tanque LC, al variar la capacidad efectiva del condensador.

El ángulo de conducción del condensador (γ) está entre 0 y π radianes, y la reactancia del condensador MERS puede expresarse mediante la siguiente ecuación.

$$X_{MERS}(\gamma) = \frac{V_{eff(\gamma)}}{I_{eff(\gamma)}} = X_C \sqrt{\frac{4\pi - 4\gamma + 3\sin(2\gamma) - 2\,\gamma\cos(2\gamma) + 2\,\pi\cos(2\gamma)}{2\pi - 2\gamma + \sin(2\gamma)}} \tag{48}$$

donde la corriente efectiva del condensador se define como:

$$I_{eff(\gamma)} = \frac{I}{\sqrt{\pi}} \sqrt{\int_{\gamma}^{\pi} \sin(\phi)^2 \, d\phi} \qquad (49)$$

y la tensión efectiva mediante:

$$V_{eff(\gamma)} = \frac{IX}{\sqrt{\pi}} \sqrt{\int_{\gamma}^{\pi} (-\cos(\phi) + \cos(\gamma))^2 \, d\phi} \qquad (50)$$

donde X_C es la reactancia del condensador utilizado para el MERS, I es la corriente de pico del condensador y ϕ es el ángulo que se comprende entre 0 y 2π radianes.

La Figura 23 muestra las formas de onda típicas del circuito cuando se excita con una onda de tensión cuadrada y el MERS interviene para reducir la influencia del condensador. Como puede observarse, durante el período de conducción del MERS, la tensión de este condensador se anula, observándose así un cambio en la tendencia de la corriente de salida, la cual está influenciada únicamente por el condensador en serie.

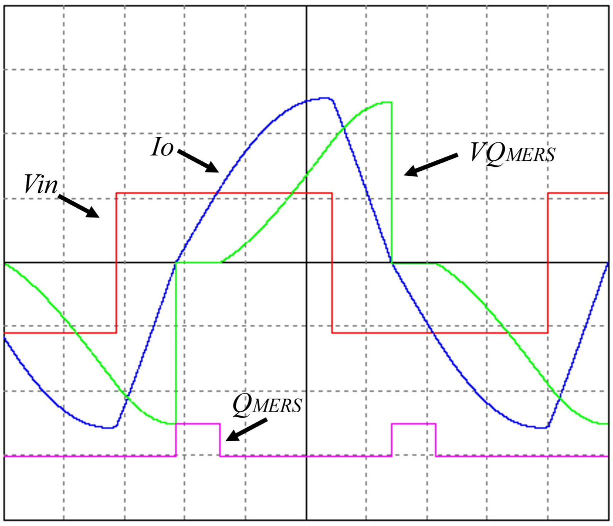

Figura 23. Ejemplo de las formas de onda de la influencia del MERS en un resonante serie LC. La forma de onda azul se corresponde con la corriente de salida, la roja la tensión de entrada, la verde la tensión del condensador y magenta la señal de puerta del MERS.

El dimensionamiento correcto del MERS dependerá de la aplicación, es por ello por lo que su análisis se estudiará en la sección 4.3.2.

Capítulo 4. Metodología

4.1 Resonante LLC con inductor variable

4.1.1 Introducción

En este capítulo se estudia el análisis exhaustivo de un novedoso enfoque de control para mejorar la eficiencia de inversores resonantes LLC, utilizando una combinación de un inductor variable controlado por corriente (VI) presentado en el apartado 3.1 y el desplazamiento de fase, presentado en 2.5.2. El control propuesto tiene como objetivo reducir la corriente eficaz o corriente cuadrática media (RMS), disminuyendo así las pérdidas por conducción y conmutación, y mejorando la eficiencia en la transferencia de potencia, considerando además la operación con conmutación ZVS, variaciones en la potencia de salida y cambios en la carga. La efectividad del enfoque propuesto se evalúa mediante modelado matemático y resultados experimentales.

El motivo de este nuevo enfoque es reducir las desventajas que presentan los métodos tradicionales de control de la corriente o la potencia de salida. Como se describió en el apartado 1.2, cuando se varía la frecuencia de conmutación, se presentan varias desventajas, como un amplio espectro de ruido, filtrado complejo y un uso ineficiente de los componentes reactivos. Las técnicas de control de frecuencia fija o de rango estrecho de frecuencia, como el PDM [35] y [36], el PS o la combinación de PS con FM (FM-PS), pueden abordar algunos de estos problemas. Sin embargo, estas técnicas no garantizan la operación de conmutación suave del convertidor resonante para grandes variaciones de carga o potencia de salida. Por lo tanto, es necesario aumentar la frecuencia de conmutación para lograr la operación en ZVS, lo que resulta en un rendimiento inferior en todo el rango de potencia [37]. Incluso con un análisis complejo del plano de estados, el uso de una frecuencia fija con desplazamiento de fase en convertidores resonantes LLC requiere limitaciones en la corriente de salida para evitar la pérdida de la conmutación suave [38]. Otros modelos de convertidores utilizan inductores saturados o cuasi-saturados que operan en regiones no lineales, lo que mejora la densidad de potencia, pero estas técnicas no resuelven el problema de trabajar con frecuencias fijas ni amplían el rango de operación en ZVS [39] y [40].

Para superar estas limitaciones, se ha propuesto una nueva técnica de control que combina el desplazamiento de fase y el control de inductor variable (VI-PS), [19]. El uso combinado de ambas técnicas en un inversor resonante LLC se investiga a fondo para lograr un rendimiento mejorado. El efecto combinado del PS y del VI como inductor en serie, a lo largo de todo el rango de potencia de salida, es reducir la corriente eficaz de salida, manteniendo la eficiencia del inversor y lograr un buen desempeño ante cambios de carga, asegurando además la operación en ZVS. Se analiza el impacto de estas técnicas de control tanto en las pérdidas por conducción como en las pérdidas por conmutación. Los resultados experimentales muestran que el uso combinado del control por PS y VI puede proporcionar un rendimiento mejorado en comparación con las técnicas tradicionales de control de frecuencia fija o estrecha.

El efecto de utilizar el inductor variable como inductor L_s del circuito LLC puede observarse en la Figura 24. Si el punto de operación del circuito se establece cerca y por encima de la frecuencia de resonancia serie, en el valor de impedancia mínima, se puede observar cómo tanto la magnitud como la fase de la impedancia aumentan a medida que se incrementa el valor de la inductancia serie. Este efecto conlleva dos ventajas sustanciales.

La primera ventaja es que, para una frecuencia fija, la máxima corriente y potencia de salida del inversor se producirán en el punto de inductancia serie mínima, donde tanto la magnitud como la fase de la impedancia están minimizadas. Sin embargo, cuando no se requiere la máxima potencia de salida, el valor de la inductancia serie puede incrementarse para aumentar la magnitud de la impedancia, reduciendo así la corriente de salida.

La segunda ventaja es que, al variar tanto la magnitud como la fase, se logra una mejor respuesta ante los cambios de carga, lo que permite mantener la conmutación ZVS incluso cuando se trabaja muy cerca de la frecuencia de resonancia serie. Esto mejora el comportamiento descrito en otros trabajos, donde al operar con una frecuencia fija cerca de la frecuencia de resonancia serie se mostró un bajo rendimiento del inversor ante cambios de carga, lo que llevó a la pérdida de las conmutaciones en ZVS [41]. En otro estudio [8], se logró una buena respuesta a los cambios de carga al trabajar cerca de la frecuencia de resonancia paralela, ya que la impedancia de entrada era mayor. Sin embargo, esto resultó en una menor optimización de los elementos reactivos.

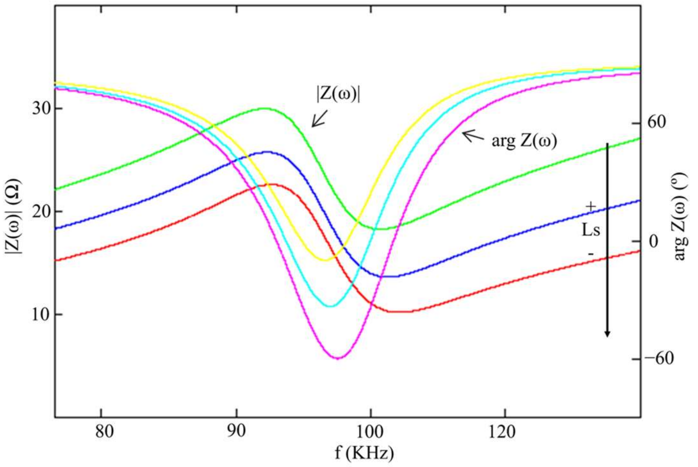

Figura 24. Magnitud simulada de la impedancia (verde, azul y rojo) y la fase de la impedancia (amarillo, azul claro y magenta) ordenadas en orden descendente según los valores de L_s del circuito resonante LLC.

Por lo tanto, trabajar con una inductancia variable añade un grado de libertad al circuito que, combinado con el control PS, permite optimizar la corriente de salida del inversor.

Estas observaciones serán demostradas tanto teórica como experimentalmente en el apartado 4.1.3 y 4.1.4

4.1.2 Diseño

En el procedimiento de diseño del inversor LLC, el valor de la inductancia del inductor de calentamiento (L_P) se determina típicamente a partir de los parámetros geométricos. La potencia requerida (P_o), la frecuencia y el factor de calidad se obtienen del tiempo de calentamiento, la profundidad de penetración en la pieza de trabajo y el tratamiento térmico. Con estos datos, la capacidad del condensador se ajusta a los valores disponibles, considerando su tensión máxima (V_p), utilizando:

$$C_P = \frac{2Q_pP_o}{\omega {V_p}^2} \tag{51}$$

Con la tensión de entrada de del inversor, el valor mínimo de la inductancia serie se calcula como:

$$L_{S_{min}} = L_{ac_{min}} = \frac{2{V_d}^2}{\pi P_o \omega} \tag{52}$$

Y con este valor se ajusta la frecuencia de conmutación a un valor que permita conmutar con desfases entre la tensión y corriente de salida pequeños,

$$\alpha = \arctan\left(\frac{2Q_p\omega_{sw}}{\omega_o} - \sqrt{4{Q_p}^2}\right) \tag{53}$$

Con el nuevo valor de la frecuencia, la tensión máxima a través del condensador se recalcula utilizando la ecuación (51) y, asimismo, se determina nuevamente el valor mínimo de la inductancia en serie empleando la ecuación (52).

La corriente de salida del inversor se obtiene de la siguiente expresión,

$$Irms = \frac{V_d\sqrt{8 + (\pi n)^2 + 2\pi n\big(2\cos(\gamma)\big)}}{\pi L_S \omega_{sw}} \tag{54}$$

donde la fase γ representa la fase entre la conmutación del inversor con la tensión de salida.

$$\gamma = \pi - arc\sin\left(\frac{1}{n}\right) \tag{55}$$

Dado que se utilizará un núcleo de ferrita para el inductor serie de alta frecuencia, y considerando que las aplicaciones de calentamiento por inducción operan con altas tensiones de entrada y salida, es necesario determinar la tensión a través de la inductancia en serie (V_{L_s}) para calcular la densidad de flujo magnético y evitar operar cerca del punto de saturación del núcleo L_{ac}.

A partir del análisis del circuito, Figura 8, se obtiene la siguiente ecuación:

$$V_{L_s}(\omega) = V_d(\omega) - V_o(\omega) \tag{56}$$

Aquí, $V_d(\omega)$ y $V_o(\omega)$ representan las tensiones de entrada y salida del circuito LLC, respectivamente, con $V_d(\omega)$ dentro del rango de:

$$V_d(\omega) = \begin{cases} V_d, & 0 \le \omega < \pi \\ -V_d, & \pi \le \omega < 2\pi \end{cases} \tag{57}$$

La ganancia de la tensión se expresa como:

$$H_v(\omega) = \frac{V_o(\omega)}{V_d(\omega)} = \frac{Z(\omega) - jL_S\omega}{Z(\omega)} \tag{58}$$

Y la diferencia de fase entre las tensiones como:

$$\phi = \arg\big(H_v(\omega)\big) \tag{59}$$

Por lo tanto, a través de la integración de la ecuación (56) y la posterior resolución de esta, se formula la expresión para la tensión a través del inductor en serie como:

$$V_{L_s}(\omega) = \begin{cases} V_d\left(\dfrac{\omega}{2} + n cos(\omega - \phi)\right), & 0 \le \omega < \pi \\ -V_d\left(-\dfrac{\omega}{2} - n cos(\omega - \phi)\right), & \pi \le \omega < 2\pi \end{cases} \tag{60}$$

donde n representa la relación entre las tensiones.

$$n = \frac{V_p}{V_d} \tag{61}$$

Para valores suficientemente grandes de Q_p, el valor de $V_o(\omega)$ es el seno del valor de pico de V_p,

$$V_o(\omega) = V_p sin(\omega) \tag{62}$$

Por tanto, el valor de la tensión máxima del inductor serie se expresa como:

$$V_{L_s} = V_d \left(\frac{\pi}{2} + \frac{V_p}{V_d} cos(\pi - \phi) \right) \tag{63}$$

Y la densidad de flujo magnético viene dado por:

$$B_{pk} = \frac{\sqrt{3} V_{L_s}}{8 n_{int} A_e f} \tag{64}$$

donde A_e es el área efectiva.

Como se mencionó con anterioridad, el punto de operación donde la potencia de salida se maximiza ocurre cuando el valor de la inductancia serie es mínimo, saturando así las ramas externas del inductor. En este punto, la tensión del inductor alcanza su valor máximo, por lo tanto, se obtiene la densidad de flujo máximo que el núcleo puede soportar bajo esta suposición.

Considerando la relación $B = \mu H$ y teniendo en cuenta que la permeabilidad relativa del núcleo cambiará con la exposición a H_{bias} a la que estará sometido el núcleo, se obtiene la relación entre el flujo magnético máximo y la permeabilidad relativa para un campo magnético constante [42].

Teniendo definidos los dos parámetros que intervienen en la selección del núcleo de ferrita, se selecciona un material y se obtiene el valor más restrictivo de la densidad de flujo magnético. Para ello, se comparan las curvas de pérdidas del núcleo a la frecuencia de operación con el valor obtenido de $B = \mu H$, utilizando la variación máxima de la permeabilidad obtenida a partir de las curvas de variación de permeabilidad relativa bajo polarización DC.

Aplicando la relación de área efectiva (A_e) para la densidad de flujo magnético máxima (64) al área del bobinado (A_w), se obtiene la expresión para el producto de área como:

$$A_p = A_e A_w = \frac{\sqrt{3} V_{L_s} Irms}{8 B_{pk} f_{sw} J K} \tag{65}$$

donde:

J representa la densidad de corriente (A/m^2), y en este caso, al trabajar con corrientes de salida elevadas desde el inversor y con el objetivo de minimizar las pérdidas debido a la corriente conducida en L_{bias} solo L_{ac} se considera para el diseño, ya que el bobinado de L_{bias} será despreciable. K es el factor de llenado, que se asumirá con un valor entre 0,5 y 0,9.

Usando el valor obtenido para el producto de área, se selecciona un tamaño de núcleo que mantenga una relación más alta, y el número de vueltas para L_{ac} se calcula mediante:

$$n_{int} = \frac{\sqrt{3} V_{L_s}}{8 A_e f_{sw} B_{pk}} \tag{66}$$

Con el número de espiras y las características del núcleo seleccionado, utilizando la ecuación (36), se calcula $L_{ac_{max}}$, y con el valor previo de $L_{ac_{min}}$, se determina la relación entre las inductancias para obtener la permeabilidad necesaria $\tilde{\mu}$ a partir de la Ecuación (37). Con este valor y la curva proporcionada en la hoja de datos relativa a la permeabilidad relativa sometida a polarización de DC bias, se determina el valor de H_{bias} necesario para alcanzar el valor de $L_{ac_{min}}$. Si no se alcanza el valor de $L_{ac_{min}}$ se realiza una itera utilizando un material ferrítico diferente. En caso de obtener un valor dentro del rango, se procede a la optimización para reducir el valor máximo de corriente en DC (I_{bias}) de L_{bias} mediante la relación dada por:

$$I_{bias} 2 n_{ext} = H_{bias} 2 l_{ext} \tag{67}$$

donde n_{ext} es el número de vueltas de L_{bias}.

La Tabla 1 presenta los requisitos iniciales para una aplicación de calentamiento por inducción para recocido [43], así como los resultados de aplicar el procedimiento de diseño discutido anteriormente, donde finalmente se seleccionó un núcleo de ferrita del material N27 con la referencia E 70/33/32 de TDK Electronics.

Tabla 1. Requerimientos iniciales y resultados del diseño del LLC

Magnitud	Símbolo	Ec.	Valor	Unidad
Potencia de salida	P_o	(71)	20	kW
Factor de calidad	Q_p	(19)	10	
Frecuencia de conmutación	f_{sw}	(53)	157	kHz
Tensión de entrada	V_d	(57)	500	V
Inductor paralelo	L_P	(17)	2	µH
Condensador paralelo	C_P	(51)	0,66	µF
Inductancia serie mínima	$L_{s_{min}}$ $L_{ac_{min}}$	(52)	8	µH
Inductancia serie máxima	$L_{s_{max}}$ $L_{ac_{max}}$	(36)	14,5	µH

Como se trató en 2.5.2, la técnica de control por desplazamiento de fase implica desplazar las fases de conmutación de las dos diagonales del inversor con un ángulo de fase (φ) que varía entre 0 y π. En consecuencia, esto modifica la tensión aplicada al circuito resonante LLC, afectando así la corriente de salida y la potencia del inversor. Por lo tanto, al introducir este factor, la relación entre las tensiones de entrada y salida del circuito se expresa ahora como:

$$n(\varphi) = n\,cos\left(\frac{\varphi}{2}\right) \tag{68}$$

Consecuentemente, la fase entre la tensión de salida del inversor y la tensión de salida del resonante se obtienen de:

$$\gamma(\varphi) = \left| \begin{array}{ll} \pi - arc\sin\left(\frac{1}{n(\varphi)}\right) & \text{if} \quad n(\varphi) > 1 \\ arc\cos\left(\frac{\varphi - \pi}{2n(\varphi)}\right) - \varphi & \text{if} \quad n(\varphi) \le 1 \end{array} \right. \tag{69}$$

Donde se ha considerado que γ depende de φ para mantener la conmutación suave, [41], mediante la siguiente desigualdad.

$$\gamma(\varphi) \ge \arccos\left(\frac{\varphi - \pi}{2n(\varphi)}\right) - \varphi \tag{70}$$

Para controlar la potencia de salida del inversor, se considera que al combinar el ángulo de desplazamiento de fase mediante el control PS y la capacidad de variar la inductancia serie del circuito resonante, se puede optimizar la potencia ajustando tanto la tensión aplicada al circuito resonante como su inductancia serie. Por tanto, la ecuación para la potencia de salida se expresa como una función de estas dos variables de la siguiente manera:

$$P_o(\varphi, L_S) = \frac{{V_d}^2 n(\varphi)\left(\sin(\gamma(\varphi) + \varphi) + \sin\big(\gamma(\varphi)\big)\right)}{L_S\omega_{sw}} \tag{71}$$

Lo mismo sucede con el valor RMS de la corriente de salida del inversor.

$$\begin{aligned} I_{RMS}(\varphi, L_S) = {} & \frac{V_d}{\pi L_S \omega_{sw}} \\ & \sqrt{4\cos(\varphi) + (\pi n(\varphi))^2 + 2\pi n(\varphi)(\cos(\gamma(\varphi) + \varphi) + \cos(\gamma(\varphi))) + 4}\,I_{RMS}(\varphi, L_S) \end{aligned} \tag{72}$$

De estas dos ecuaciones se obtiene un sistema de dos ecuaciones con dos variables. Este sistema se utiliza para encontrar el punto de operación óptimo del inversor, asegurando que la corriente de salida se mantenga minimizada a lo largo de todo el rango de potencia, lo que reduce las pérdidas por conducción y conmutación en los transistores.

La Figura 25 representa todo el rango de operación posible, tanto para la variación del desplazamiento de fase como de la inductancia serie, expresado en función de la potencia de salida del inversor. En la figura, hay una curva de puntos rojos que resulta de optimizar la corriente de salida del inversor. Por lo tanto, este es el punto de operación óptimo para el control, donde se minimizarán las pérdidas en el inversor. Siguiendo la trayectoria de la curva, se puede observar que, en potencias de salida altas, se da prioridad al aumento del valor de la inductancia serie en lugar de al aumento del desplazamiento de fase. Esto se debe a que la reducción de la corriente de salida se logra aumentando la impedancia del circuito de entrada y, al conmutar con un pequeño desplazamiento de fase, para la misma corriente de salida, la corriente de conmutación es menor. Sin embargo, cuando se requiere una potencia de salida más baja, trabajar con un valor de inductancia serie más alto, implica una mayor impedancia de entrada, resulta en la aplicación de una tensión más baja mediante un mayor desplazamiento de fase. Esto permite conmutar con ángulos más pequeños y contrarresta el efecto del aumento de la fase entre la tensión y la corriente de salida debido al elevado valor de inductancia serie.

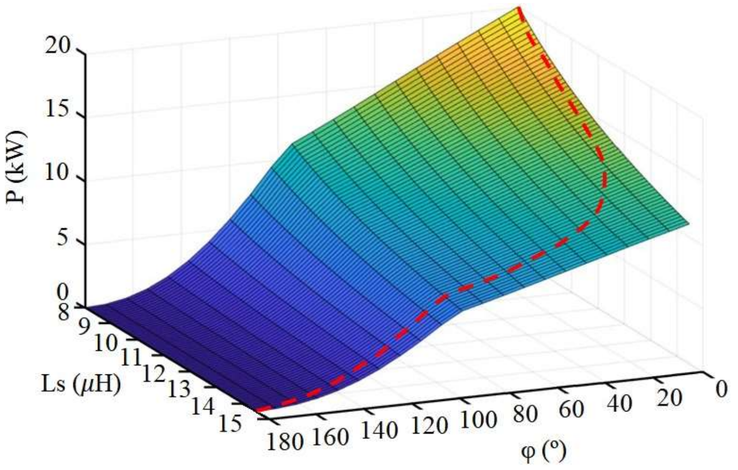

Figura 25. Desplazamiento de fase e inductancia variable en función de la potencia de salida. La curva punteada roja corresponde a la estrategia de control óptima.

El esquema simplificado de control VI-PS se muestra en la Figura 26. Debido a su naturaleza multivariable, se emplea un sistema de Entradas Múltiples y Salidas Múltiples (MIMO). Se resuelve utilizando un control proporcional, integral y derivativo (PID) y una red de diagonalización [44]. Esta configuración permite manipular una variable para afectar a la otra y viceversa, generando un bucle de control que itera entre ellas. Las entradas del sistema incluyen la potencia de entrada del inversor comparada con la referencia seleccionada, y el ángulo de fase entre la tensión y la corriente de salida del inversor, el cual se fija en 15°, según se define en la ecuación (55). En consecuencia, las variables de salida son el ángulo de fase φ del control por desplazamiento de fase y la corriente continua del devanado L_{bias}.

Además, se emplea un observador digital con un optimizador dinámico para reducir el valor RMS de la corriente de salida del inversor [45]. En este bloque, al medir la corriente de salida del inversor y compararla con los valores del ángulo de desplazamiento de fase y de I_{bias}, se realizan intervenciones en las salidas para optimizar ambos valores. Esto asegura que el inversor opere dentro del rango de operación óptimo, representado por la línea roja discontinua en la Figura 25. El bloque de acondicionamiento de señales y lógica de disparo, además de generar las señales de disparo de los transistores con los tiempos muertos correspondientes basados en el valor del ángulo de desplazamiento de fase recibido del sistema, compara los cruces por cero de la corriente en cada ciclo para asegurar la conmutación ZVS.

Si, durante el proceso de calentamiento, el ángulo α cambia significativamente, acercándose a la región capacitiva debido a cambios en la inductancia L_P, modificada debido a cambios en la permeabilidad, conductividad eléctrica del material o debido a un salto de carga causado por el acoplamiento y desacoplamiento de la pieza en el inductor, el sistema de control disminuye directamente la corriente I_{bias} para aumentar el valor de L_S. Este ajuste mantiene la conmutación suave, evitando sobretensiones o sobrecorrientes en la salida del inversor. Aunque el inductor variable ha sido diseñado para trabajar lejos de los límites de saturación, en caso de que el inductor se sature, el ángulo α se reduciría, como se observa en la Figura 24 esto también será detectado en esta parte del control, disminuyendo la corriente de bias para evitar la saturación.

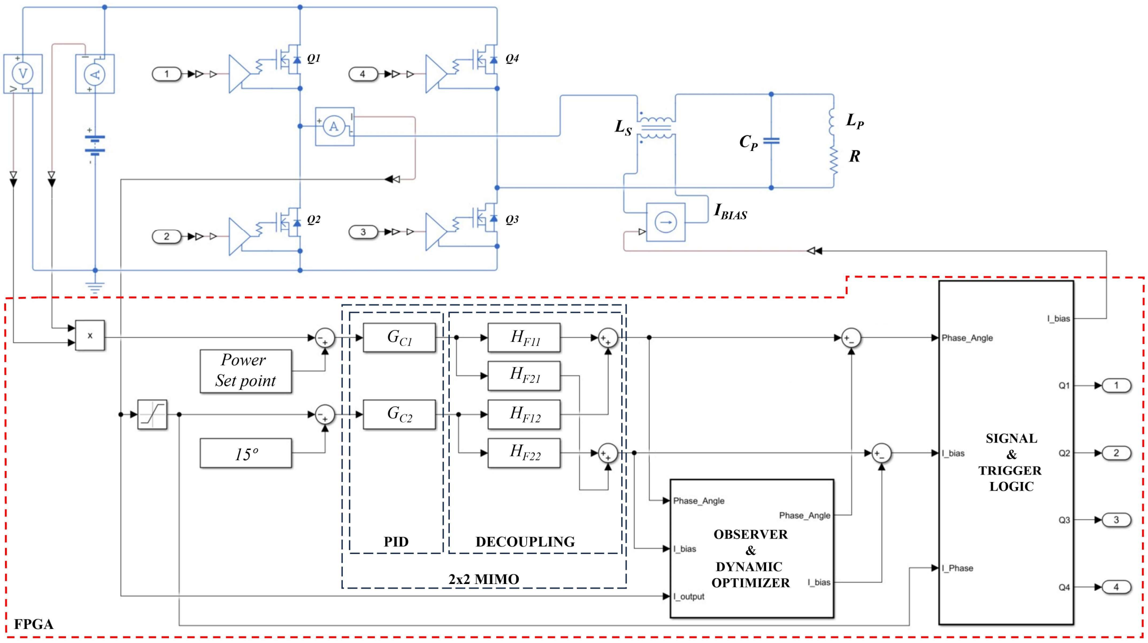

Figura 26. Esquema del sistema propuesto, detallando la topología del inversor, la carga resonante LLC con el inductor variable y el diagrama de control.

4.1.3 Análisis de la eficiencia

Para verificar las ventajas de esta optimización, se analizan matemáticamente las pérdidas de los transistores del inversor con el fin de obtener la eficiencia en todo el rango operativo, considerando la conmutación adecuada para mejorar la distribución de potencia entre los transistores [11].

Las pérdidas debidas a la corriente de conducción en cada canal de los transistores están dadas por:

$$P_{cd}(\varphi, L_S) = \left(\frac{Irms(\varphi, L_S)}{\sqrt{2}}\right)^2 R_{DS_{on}} \tag{73}$$

donde $R_{DS_{on}}$ es la resistencia del canal en estado de ON del MOSFET.

Para las pérdidas de energía por conmutación, solo se considera la conmutación a OFF, ya que la conmutación a ON serán despreciable al opera en ZVS en todo el rango operativo. Para calcular estas pérdidas, se obtiene la ecuación polinómica de las curvas de pérdidas por conmutación de OFF proporcionadas por el fabricante, considerando la tensión de drenador igual a V_d y la resistencia de puerta utilizada. Esta se expresa como:

$$E_{off}(\varphi, L_S) = \mathrm{a}I_c(\varphi, L_S)^2 + bI_c(\varphi, L_S) + c \tag{74}$$

donde I_c es la corriente conmutada, definida para los transistores de la parte superior (Q1 y Q4) como:

$$I_{C_{Q1}}(\varphi, L_S) = \frac{V_d}{L_S\omega_{sw}}\left(n(\varphi)\cos(\gamma) + \frac{\pi - \varphi}{2}\right) \tag{75}$$

y para los transistores de la parte inferior (Q2 y Q3) como:

$$I_{C_{Q3}}(\varphi, L_S) = \frac{V_d}{L_S\omega_{sw}}\left(n(\varphi)\cos(\gamma + \varphi) + \frac{\pi - \varphi}{2}\right) \tag{76}$$

Por tanto, las pérdidas de conmutación para cada transistor se obtienen de la siguiente expresión:

$$P_{sw}(\varphi, L_S) = E_{off}(\varphi, L_S)\frac{\omega_{sw}}{2\pi} \tag{77}$$

Las pérdidas debidas a la puerta del transistor dependen de la carga total de puerta Q_G y de la tensión puerta a surtidor V_G, relacionadas mediante la siguiente expresión:

$$P_{gate} = Q_G V_G \frac{\omega_{sw}}{2\pi} \tag{78}$$

Por otro lado, las pérdidas en el núcleo del inductor se deben a la densidad de flujo magnético, debido a que la influencia de la corriente continua de DC bias es despreciable [18] y [46], por lo tanto, pueden obtenerse utilizando la siguiente ecuación.

$$P_{core}(\varphi, L_S) = P_v V_e \tag{79}$$

donde P_v es la densidad de pérdidas en el núcleo del inductor proporcionada por el fabricante para la frecuencia de operación y la densidad de flujo magnético, y V_e es su volumen.

Como consideración final, para las pérdidas en el bobinado de cobre del inductor (P_{wire}), es necesario conocer la resistencia efectiva del bobinado (R_{copper}), teniendo en cuenta la conductividad, la longitud total y el efecto pelicular, utilizando la siguiente expresión.

$$P_{wire}(\varphi, L_S) = {I_{RMS}}^2 R_{copper} \tag{80}$$

Para concluir, las pérdidas totales se determinan mediante la siguiente ecuación:

$$\begin{aligned} P_{tot}(\varphi, L_S) = {} & 4P_{cd}(\varphi, L_S) + 2\left(P_{sw_{Q1}}(\varphi, L_S) + P_{sw_{Q3}}(\varphi, L_S)\right) + 4P_{gate} + P_{core}(\varphi, L_S) \\ & + P_{wire}(\varphi, L_S) \end{aligned} \tag{81}$$

Mientras que la eficiencia se expresa como:

$$\eta(\varphi, L_s) = \frac{P_o(\varphi, L_S)}{P_o(\varphi, L_S) + P_{tot}(\varphi, L_S)} \tag{82}$$

Para el análisis de pérdidas, se utilizó el MOSFET de SiC G320MT12K como transistor para cada uno de los transistores del inversor. La Tabla 2 presenta las características obtenidas de la hoja de datos para el análisis de la eficiencia del inversor.

Tabla 2. Características del transistor G320MT12K.

Magnitud	Símbolo	Ec.	Valor	Unidad
Resistencia de ON	$R_{DS_{on}}$	(73)	17	mΩ
Pérdidas de conmutación a OFF	a	(74)	0,0268	$\mu J/A^2$
	b		0,2679	µJ/A
	c		18,929	µJ
Carga de la puerta	Q_G	(78)	180	nC

Para ilustrar la diferencia en eficiencia al operar en todo el rango de potencia utilizando solo el control PS, en comparación con la inclusión de la inductancia variable VI-PS, se ha comparado la eficiencia y la corriente de salida de ambos enfoques en función de la potencia en la Figura 27. El punto de partida para ambos controles es el mismo y corresponde al valor máximo de potencia, ya que, en ambos casos, en ese punto, el desplazamiento de fase es el mínimo, y en el control con inductor variable, la inductancia se establece en su valor mínimo, que es el mismo valor mantenido por el control PS en todo su rango de potencia. Como se observa en la figura, la mejora en la eficiencia del sistema propuesto se produce a medida que la potencia de salida del inversor disminuye, debido a la reducción de la corriente RMS de salida. Esto permite mantener un rendimiento superior al 98,5 % en todo el rango de operación, alcanzando incluso el 99 % cuando la corriente de salida se reduce significativamente.

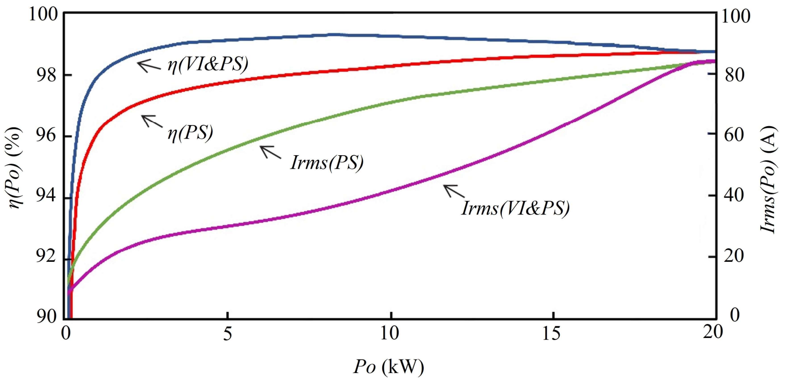

Figura 27. Evolución calculada de la eficiencia y corriente de salida en función de la potencia para el inversor resonante LLC para dos modulaciones.

En la Tabla 3 se muestra la contribución de las pérdidas para ambos convertidores.

Tabla 3. Resultado de las pérdidas del inversor LLC operando a 12 kW.

Magnitud	Símbolo	Ec.	PS	VI&PS	Unidad
Pérdidas de conducción	P_{cd}	(73)	45,61	18,478	W
Pérdidas de conmutación Q1	$P_{sw_{Q1}}$	(77)	3,465	7,783	W
Pérdidas de conmutación Q3	$P_{sw_{Q3}}$		3,238	6,075	W
Pérdidas en la puerta	P_{gate}	(78)	0,508	0,508	W
Pérdidas en el núcleo	P_{core}	(79)	3,57	6,12	W
Pérdidas en el bobinado	P_{wire}	(80)	15,499	6,279	W
Pérdidas totales	P_{tot}	(81)	216,952	116,065	W

4.1.4 Resultados experimentales

Para llevar a cabo las pruebas experimentales discutidas en esta sección, primero se evaluó el diseño de la inductancia variable. El resultado se muestra en la Figura 28, donde se presentan los valores calculados y medidos experimentalmente de la inductancia en función de la corriente de bias. Como se observa en la figura, existe una dispersión entre el valor calculado y el valor medido experimentalmente. Esta desviación se debe principalmente al rango de dispersión de la permeabilidad inicial proporcionada por los fabricantes y a su dependencia con la temperatura. No obstante, se puede apreciar que el modelo matemático describe adecuadamente el comportamiento del inductor variable en función de la corriente de polarización.

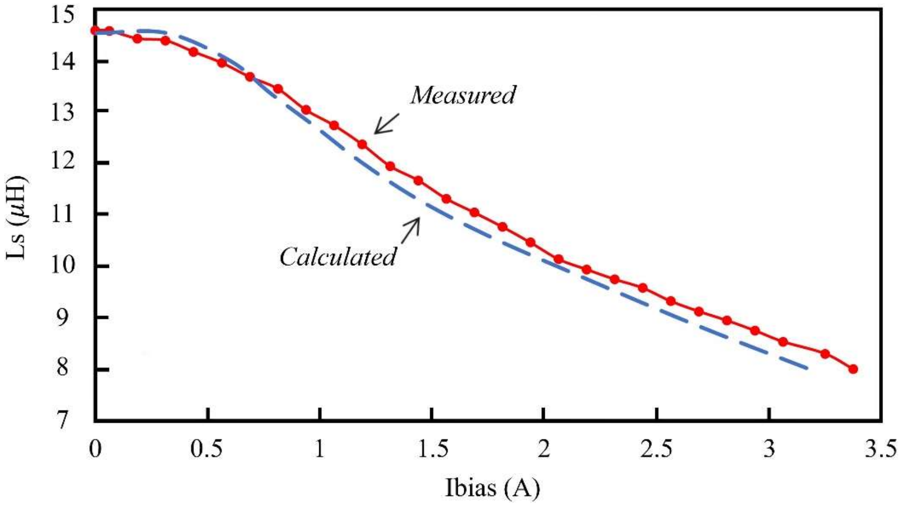

Figura 28. Comportamiento calculado y medido de la inductancia del inductor variable en función de la corriente de bias.

Para comprobar el diseño completo, se utilizó un módulo inversor de calentamiento por inducción de 20 kW. Este módulo incluye control basado en FPGA, etapas de sensado con moduladores sigma-delta, fuentes de alimentación aisladas, una fuente de corriente controlable basada en la bomba de corriente de Howland con un OPA548 como amplificador operacional de alta corriente, drivers de disparo, transistores y un disipador térmico con refrigeración por agua. El inversor es alimentado con una fuente de 500 V_{DC}.

El banco de pruebas utilizado para verificar el diseño del resonante LLC con el inductor variable y realizar la comparativa con las otras modulaciones se muestra en la Figura 29. Este está ensamblado con los componentes diseñados en la sección 4.1.2.

Cada número corresponde con:

(1) Inversor de calentamiento por inducción con cuatro SiC G3R20MT12K
(2) DSO de 300 MHz de ancho de banda
(3) Sonda diferencial de tensión y sonda de corriente Rogowski
(4) Sonda de efecto Hall para la corriente de polarización DC
(5) Inductor serie controlable (L_S)
(6) Condensador en paralelo (C_P)
(7) Inductor en paralelo (L_P)
(8) Carga con refrigeración por agua

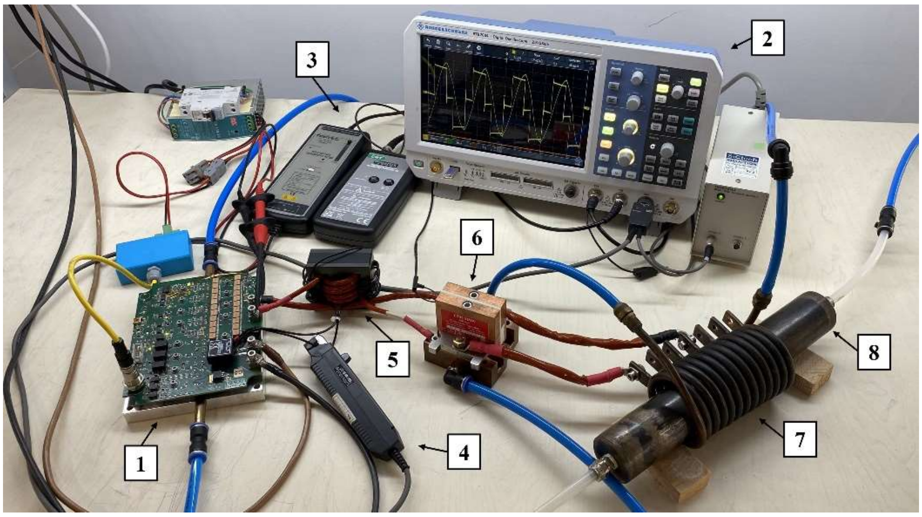

Figura 29. Banco de pruebas del inversor con carga resonante LLC. Las etiquetas numeradas describen los componentes en la parte superior.

Para validar el diseño, los valores teóricos obtenidos a partir de las ecuaciones se compararon con las mediciones realizadas en el inversor a dos niveles de potencia. El resultado se muestra en la Tabla 4, donde se observa una pequeña dispersión debido al método de modelado utilizado y a la existencia de elementos parásitos y pérdidas en otros componentes que no se toman en cuenta en el cálculo, como conductores, conexiones, dependencia de la temperatura de los componentes y errores del sistema de medición, sensores de tensión y corriente.

Tabla 4. Comparación de los resultados teóricos y medidos del funcionamiento del inversor LLC

Magnitud	**Símbolo**	**12 kW**		**20 kW**		**Unidad**
		Teórico	**Medido**	**Teórico**	**Medido**	
Fase de la corriente	α	15	15,1	15	14,8	°
Fase de la tensión	γ	52,4	51,8	39,4	40,7	°
Corriente de salida	I_{RMS}	46,6	49,5	83,5	85,1	A
Corriente conmutada	$I_{C_{Q1}}$	39,2	40	55,1	55,6	A
Corriente conmutada	$I_{C_{Q3}}$	38,6	38,3	54,3	53,7	A

La Figura 30 muestra los oscilogramas capturados por el osciloscopio digital (DSO) para el inversor operando al 60 % de su potencia con tres técnicas de modulación diferentes y su respuesta a cambios de carga. La primera estrategia de modulación es de frecuencia fija, utilizando el control PS. La segunda estrategia de modulación emplea un rango de frecuencia estrecho, combinando modulación de frecuencia con el desplazamiento de fase (FM-PS). La tercera estrategia es el control VI-PS de frecuencia fija. En los tres casos, el circuito resonante LLC permanece igual, manteniendo el valor mínimo de inductancia en serie para las primeras estrategias de modulación. En términos de rendimiento con el mismo punto de ajuste de potencia, como se muestra en la figura, el control PS se ha configurado a una frecuencia más alta que la de diseño resonante. Este ajuste es necesario para incrementar la fase entre tensión y corriente α, permitiendo por tanto mantener la conmutación ZVS en todo el rango de operación. En consecuencia, para el mismo nivel de potencia, la corriente de salida del inversor es mayor con el control PS, alcanzando 64 A_{RMS}, en comparación con las otras modulaciones. En el caso del control FM-PS, la corriente de salida es de 56 A_{RMS}, ligeramente mayor que en el control VI-PS. A pesar de mantener el mismo ángulo α de 15°, la frecuencia es más alta debido a la regulación, y la conmutación se realiza con un desplazamiento de fase más amplio, lo que genera mayores pérdidas de conmutación debido a la mayor amplitud de corriente durante la conmutación a OFF en comparación con el control VI-PS. Por otro lado, el control VI-PS mantiene un desplazamiento de fase cerrado al desaturar la inductancia en serie, permitiendo una corriente de salida más baja de 50 A_{RMS} y conmutando con menos corriente debido a un ángulo φ más estrecho, mientras mantiene el ángulo de fase α de 15° y una frecuencia más baja, más cercana a la frecuencia de resonancia en serie.

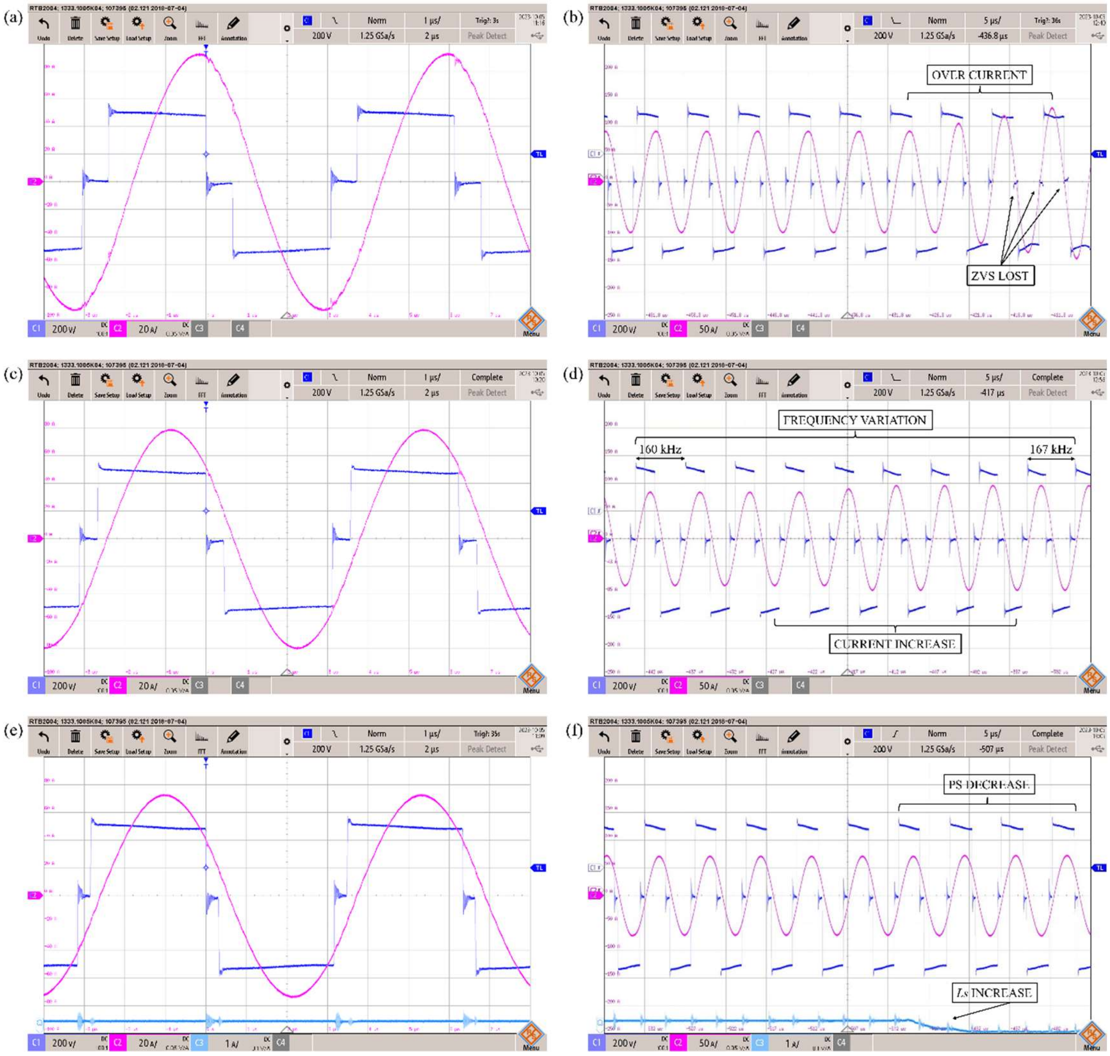

Figura 30. Oscilogramas de pruebas experimentales del inversor LLC con diferentes estrategias de control. (a,b) con PS, (c,d) con FM-PS, y (e,f) con VI-PS. Las figuras (a,c,e) corresponden a la operación al 60 % de potencia, y (b,d,f) muestran la respuesta a un cambio de carga a ese nivel de potencia. C1 (azul oscuro) representa la tensión de salida (200 V/div), C2 (magenta) muestra la corriente de salida (20 A/div) en las figuras (a,c,e) y (50 A/div) en (b,d,f). C3 (azul claro) muestra la corriente de polarización DC (1 A/div) del inductor Ls en (e,f). La base de tiempo es de 1 µs/div en (a,c,e) y 5 µs/div en (b,d,f).

Como se observa en el comportamiento ante cambios de carga, el control PS, a pesar de operar a una frecuencia más alta no logra mantener el comportamiento ZVS ni controlar la sobrecorriente, a pesar de aumentar el ángulo del desplazamiento de fase. El control FM-PS logra mantener el comportamiento ZVS, pero a costa de una variación brusca de la frecuencia de 8 kHz, lo que complicaría el filtrado de armónicos. Además, se observa que la corriente aumenta ligeramente a pesar de la corrección del control de aumentar el desplazamiento de fase. Este efecto podría mitigarse permitiendo que el control aumente aún más la frecuencia. Por último, como se muestra en el oscilograma del control VI-PS, se preserva la conmutación suave y se controla la sobrecorriente causada por el cambio de carga. Esto se logra al desaturar rápidamente las ramas externas del inductor L_s, haciendo que la diferencia de impedancia generada por el cambio de carga se atenúe debido al aumento de la impedancia generada por una inductancia en serie más alta. Se observa que el cambio de impedancia al aumentar L_s, es tan efectivo que el control tiene que disminuir el desplazamiento de fase para mantener el nivel de corriente.

Finalmente, para concluir la comparación entre los tres tipos de control y validar el diseño discutido en el artículo, se midió la eficiencia del inversor en todo el rango de potencia cuando se parte desde el mismo punto a potencia máxima. Esto se hizo comparando la diferencia entre la potencia de entrada, medida directamente en la fuente de alimentación de DC, y la potencia de salida, medida con el DSO a partir del valor de la multiplicación instantánea de la tensión y la corriente de salida del puente del inversor. Como se muestra en la Figura 31, en el punto de inicio, los tres controles logran el mismo rendimiento. Sin embargo, a medida que la potencia disminuye, el control VI-PS incrementa gradualmente su eficiencia, como se explicó anteriormente en la 4.1.3. En esta figura, en comparación con el cálculo teórico en la Figura 27, se ha añadido la medición del control FM-PS. A pesar de mantener un rendimiento similar al control de inductancia variable, el control FM-PS tiene la desventaja de perder la optimización de los elementos reactivos. Esto ocurre porque la frecuencia aumenta con una menor demanda de potencia, lo que resulta en una menor eficiencia y un filtrado armónico más complejo. Es importante destacar que en el control PS, para manejar cambios de carga o variaciones en la permeabilidad del inductor de calentamiento, se debe aumentar la frecuencia, lo que reduce la eficiencia. Como se observa en la figura, las mediciones se alinean estrechamente con los valores teóricamente calculados, a pesar de la dispersión en los componentes reales y de las pérdidas por componentes parásitos que no se consideraron en el cálculo teórico.

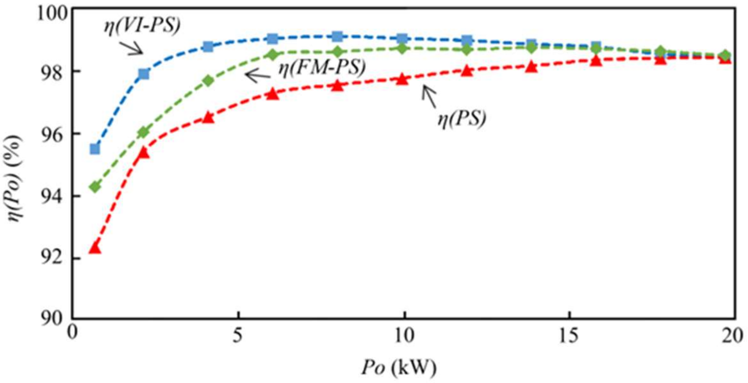

Figura 31. Resultados experimentales de las medidas de la eficiencia del inversor resonante LLC en todo el rango de potencia.

4.2 Resonante LC serie con transformador variable de activa

4.2.1 Introducción

Este capítulo presenta el análisis de un convertidor basado en un inversor resonante LC para aplicaciones de calentamiento por inducción. Emplea un transformador variable (VT) controlado por corriente, presentado en 3.2, junto con una regulación por desplazamiento de fase (PS), 2.5.2 para operar a una frecuencia fija cercana a la frecuencia de resonancia. El convertidor mantiene un fijo el ángulo de conmutación, lo que permite variaciones significativas de carga sin comprometer la conmutación en ZVS de los transistores. Este método innovador mejora el rendimiento del inversor en todo el rango de operación.

Como ya se introdujo en el capítulo 1.2, el inversor resonante en serie se prioriza a otras topologías. Una de las razones es que utiliza un transformador compacto ubicado en la salida del inversor de alta frecuencia, proporcionando aislamiento galvánico y permitiendo la adaptación de la impedancia del circuito resonante a través de la relación de transformación del transformador [47]. En cuanto a la regulación de la potencia, la modulación por frecuencia es comúnmente utilizada, ofreciendo un amplio rango de operación a costa de una menor eficiencia debido al aumento de la frecuencia y a un filtrado más complejo causado por un espectro de ruido más amplio. Además, se pierde la optimización en los componentes reactivos cuando la frecuencia de operación se aleja de la resonancia. Otras técnicas, como la modulación por densidad de pulsos o la modulación por desplazamiento de fase, mejoran la eficiencia y el filtrado, ya que operan a una frecuencia fija cercana a la de resonancia [48]. Sin embargo, carecen de un amplio rango de operación, lo que provoca la pérdida de la conmutación en ZVS. Técnicas de control más sofisticadas, denominadas métodos de rango de frecuencia estrecho, combinan dos de estas técnicas, como la modulación por desplazamiento de fase con modulación de frecuencia. Esta combinación mejora la eficiencia y el rendimiento frente a cambios en la carga. Sin embargo, cuando se requiere un amplio rango de operación, es necesario aumentar la frecuencia, lo que degrada la optimización [49].

Las publicaciones más recientes sobre el mantenimiento de una frecuencia fija solo se centran en convertidores tipo LLC, donde en [50] se emplea un complejo análisis de plano de estados para mantener la conmutación suave, y en [19], que es la publicación tratada en el apartado 4.1, se utiliza un inductor variable controlado por corriente para ampliar el rango de operación y mantener el ZVS. Sin embargo, estos convertidores presentan la desventaja de que deben considerar ambas frecuencias de resonancia en su diseño, lo que los hace más complejos de controlar y no adecuados para todas las aplicaciones.

Por consiguiente, en este apartado, se ha propuesto una nueva técnica de control para mejorar el rendimiento, que combina la modulación por desplazamiento de fase con el control por corriente de la relación de transformación del transformador (VT-PS) [26]. El uso de un inversor resonante serie con una relación de transformación variable electrónicamente controlable permite adaptar dinámicamente la impedancia del circuito. Esto posibilita el control de potencia a una frecuencia fija mediante modulación PS, mientras se mantiene un ángulo de conmutación bajo y fijo en un amplio rango de operación, reduciendo la corriente de salida del inversor. El principio de este control es el efecto mostrado en la Figura 5, donde de manera constante, mediante el uso de un transformador variable controlado por corriente y la modulación por desplazamiento de fase se puede controlar tanto la potencia aplicada a la carga como el ángulo de conmutación mientras se mantiene una frecuencia fija.

4.2.2 Diseño

Como sucedía en el diseño del LLC, los parámetros de partida del diseño provienen de la aplicación de calentamiento por inducción, estos son el rango de potencia, la frecuencia, el factor de calidad y la inductancia del inductor obtenida a partir de su geometría. A partir de estos parámetros y con la ecuación (9), se obtiene el valor del condensador para la frecuencia de trabajo [51]. Utilizando la siguiente expresión, se ajusta la frecuencia de conmutación para lograr un pequeño ángulo (α) entre la tensión de salida del inversor y la corriente de salida.

$$\omega_{sw} = \omega_o \frac{\tan\alpha + \sqrt{\tan^2\alpha + 4\mathrm{Q}^2}}{2Q} \qquad (83)$$

El valor de la corriente de salida RMS se obtiene mediante la potencia de salida y el ángulo seleccionado mediante la siguiente expresión

$$I_o = \frac{P_o}{\frac{2}{\pi}\sqrt{2}V_d \cos\alpha} \tag{84}$$

y la resistencia equivalente en primario se obtiene de:

$$R_p = \frac{P_o}{(I_o)^2} \tag{85}$$

La relación de transformación mínima (TR_{min}) se obtiene a partir de las ecuaciones (84), (85), (10) y (6) para la potencia máxima a la frecuencia de conmutación. Por otro lado, la relación de transformación máxima (TR_{max}) se define por la potencia mínima y se obtiene recalculando las ecuaciones (84), (85) y (6) para este valor. Como el transformador no varía el número de vueltas en primario (n), si no que varía la relación de inductancias expresadas en (46) y (47) mediante la corriente de bias, la relación de transformación se expresa como TR y no como n. En la Tabla 5 se registran los valores iniciales y los obtenidos tras aplicar el diseño para el circuito resonante serie LC.

Tabla 5. Requerimientos iniciales y resultados del diseño del LC serie con transformador de activa.

Magnitud	Símbolo	Ec.	Valor		Unidad
Rango de potencia de salida	P_o		15	4	kW
Factor de calidad	Q		10		
Frecuencia	f_o		200		kHz
Tensión entrada DC	V_d		500		V
Inductor	L_s		1		μH
Condensador	C_s	(9)	0,63		μF
Ángulo de conmutación	α		15		°
Frecuencia de conmutación	f_{sw}	(83)	203		kHz
Corriente de salida RMS	I_o	(84)	32	8,5	A
Resistencia en primario	R_p	(85)	14,7	55,1	Ω
Relación de transformación	TR	(6)	10,7	20	

Para el diseño y la selección del núcleo magnético, el primer paso es aplicar la relación del área efectiva para la densidad de flujo máxima al área del devanado, lo que da como resultado la siguiente expresión del producto de área.

$$A_p = A_e A_w = \frac{V_d I_o}{2F_{sw}B_{max}JK} \tag{86}$$

Con el valor obtenido, se selecciona un núcleo con dimensiones mayores a las calculadas y se comparan las curvas de pérdidas en el núcleo a la frecuencia de operación con el valor obtenido de $B = \mu H$, utilizando la variación máxima de permeabilidad obtenida a partir de las curvas de variación de permeabilidad relativa bajo polarización de corriente continua. Esto garantiza que el valor obtenido sea menos restrictivo que el utilizado para el cálculo del producto de área. Luego, se calcula el número mínimo de vueltas que debe tener el primario del transformador utilizando la siguiente expresión:

$$n_p = \frac{V_d}{4F_{sw}B_{max}A_e} \tag{87}$$

Con el número de vueltas del primario se calcula el valor de la inductancia mínima del primario del transformador, es decir, cuando está sujeto la corriente de bias, [42], a través de las expresiones (44) y (46). Este valor corresponde a la inductancia mínima del primario en circuito abierto $L_{p_{min_{oc}}}$, y se asume que el 20 % de este valor será la inductancia mínima del primario en cortocircuito $L_{p_{min_{cc}}}$. Como resultado, el coeficiente de acoplamiento del primario (K_p) tendrá un valor típico de 0,8.

$$K_p = 1 - \frac{L_{p_{min_{cc}}}}{L_{p_{min_{oc}}}} \tag{88}$$

Por tanto, la inductancia mutua se obtiene de:

$$L_M = \frac{L_{p_{min_{oc}}} K_p}{1 - K_p} \tag{89}$$

Y la inductancia máxima de secundario reflejada desde primario del transformador se expresa como:

$$L_{sec_{max}} = \frac{(L_M/K_p)^2}{2L_{p_{min}}} \tag{90}$$

En cuanto a la inductancia de secundario cuando el primario se cortocircuita, se obtiene para el valor deseado de la relación de transformación máxima.

$$L_{s_{min_{cc}}} = \frac{L_{sec_{max}}}{{TR_{max}}^2} \tag{91}$$

Para obtener el valor de la inductancia de secundario mínima en circuito abierto, se considera un factor de acoplamiento de secundario (K_s) como un valor típico de 0,8, lo que permite obtenerse mediante la siguiente expresión:

$$L_{s_{min_{oc}}} = \frac{L_{s_{min_{cc}}}}{1 - K_s} \tag{92}$$

Con el valor obtenido y las fórmulas (45) y (47) se obtiene el número de vueltas de secundario.

Para obtener el valor de la relación de transformación mínima, se considera que los coeficientes de acoplamiento del primario y secundario son mínimos. Esto se debe a que, cuando el núcleo no está expuesto a corriente de bias, el flujo se cierra en mayor medida a través de las ramas externas del núcleo. Por lo tanto, el coeficiente de acoplamiento mutuo (K) se aproxima a 0,05. Las tres aproximaciones utilizadas para el diseño serán verificadas experimentalmente en la sección 4.2.4.

$$K_M = \sqrt{K_p K_s} \tag{93}$$

Por lo tanto, la relación de transformación mínima se obtiene utilizando las inductancias máximas del primario y del secundario obtenidas de la siguiente manera:

$$TR_{min} = \frac{1}{K_M} \sqrt{L_{s_{max}} / L_{p_{max}}} \tag{94}$$

Si la relación mínima obtenida es menor o igual a la deseada, el diseño puede considerarse correcto. El paso final implica usar el valor de $\tilde{\mu}$ empleado en las ecuaciones para determinar la corriente de polarización necesaria para alcanzar los valores mínimos de inductancia. Para ello, se consulta la curva de la hoja de datos sobre la permeabilidad relativa sometida a polarización de DC, optimizando el equilibrio entre la corriente de polarización (I_{bias}) y el número de vueltas del devanado de saturación (n_{dc}), dado por la siguiente expresión:

$$I_{bias} 2 n_{dc} = H_{bias} 2 l_{dc} \tag{95}$$

donde l_{dc} es la longitud del camino magnético de la rama de saturación.

En combinación con el control de la relación de transformación, se utilizará el control por desplazamiento de fase. El factor de ángulo de desplazamiento de fase modifica la tensión de salida del inversor aplicada al circuito resonante mediante la siguiente expresión:

$$V_{ab}(\varphi) = \frac{2\sqrt{2}}{\pi} V_d \, cos\frac{\varphi}{2} \tag{96}$$

Por lo tanto, la corriente de salida del inversor en función del ángulo de desplazamiento de fase y la relación de transformación se expresa mediante la siguiente ecuación:

$$I_o(\varphi, TR) = \frac{2\sqrt{2}}{\pi R_s TR^2} V_d \cos\frac{\varphi}{2} \cos\left(\alpha + \frac{\varphi}{2}\right) \tag{97}$$

Y la potencia de salida como función de estas dos variables se expresa de la siguiente manera:

$$P_o(\varphi, TR) = \left(\frac{2\sqrt{2}V_d}{\pi}\right)^2 \frac{1}{R_s TR^2} \cos^2\frac{\varphi}{2} \cos^2\left(\alpha + \frac{\varphi}{2}\right) \tag{98}$$

En la Figura 32, se muestra todo el rango operativo permitido en la potencia de salida de la ecuación (98), con la combinación de la variación de la relación de transformación y el desplazamiento de fase, para el diseño realizado. Como se observa en la figura, la línea roja discontinua se corresponde al punto de operación de máxima eficiencia para todo el rango de potencia de salida. Este punto de máxima eficiencia se obtiene al optimizar la ecuación (97), manteniendo un ángulo de conmutación (α) de 15 grados.

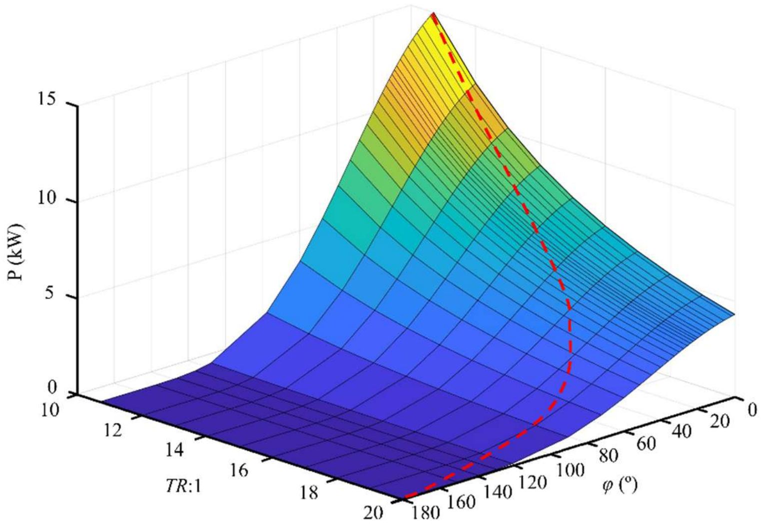

Figura 32. Desplazamiento de fase y transformador variable en función de la potencia de salida calculada. La línea puenteada roja se corresponde con la estrategia de control óptima.

En la Figura 33, se muestra el diagrama simplificado del esquema de control VT-PS. Las entradas del sistema de control son la potencia y el ángulo entre la tensión y la corriente de salida. Debido a las dos variables de control, se utiliza un sistema MIMO, actuando con control PID y una red de diagonalización [44]. Las salidas de este sistema serán, por lo tanto, la corriente de polarización y el ángulo de fase. Para optimizar el sistema y operar en el punto de máxima eficiencia, representado en la Figura 32 por la línea roja discontinua, se utiliza la ecuación (97) para reducir el valor efectivo de la corriente de salida del inversor con un observador digital [45].

Finalmente, en el bloque de las señales lógicas y de disparo, se generan las señales de puerta del transistor con los tiempos muertos, asegurando que el sistema opere en ZVS. En caso de un salto de carga debido a una extracción rápida de carga o un cambio en la permeabilidad de la pieza de trabajo que cause un cambio en el valor del inductor, el sistema actúa rápidamente cambiando la relación de transformación, logrando acoplamiento o desacoplamiento entre la carga y el inversor.

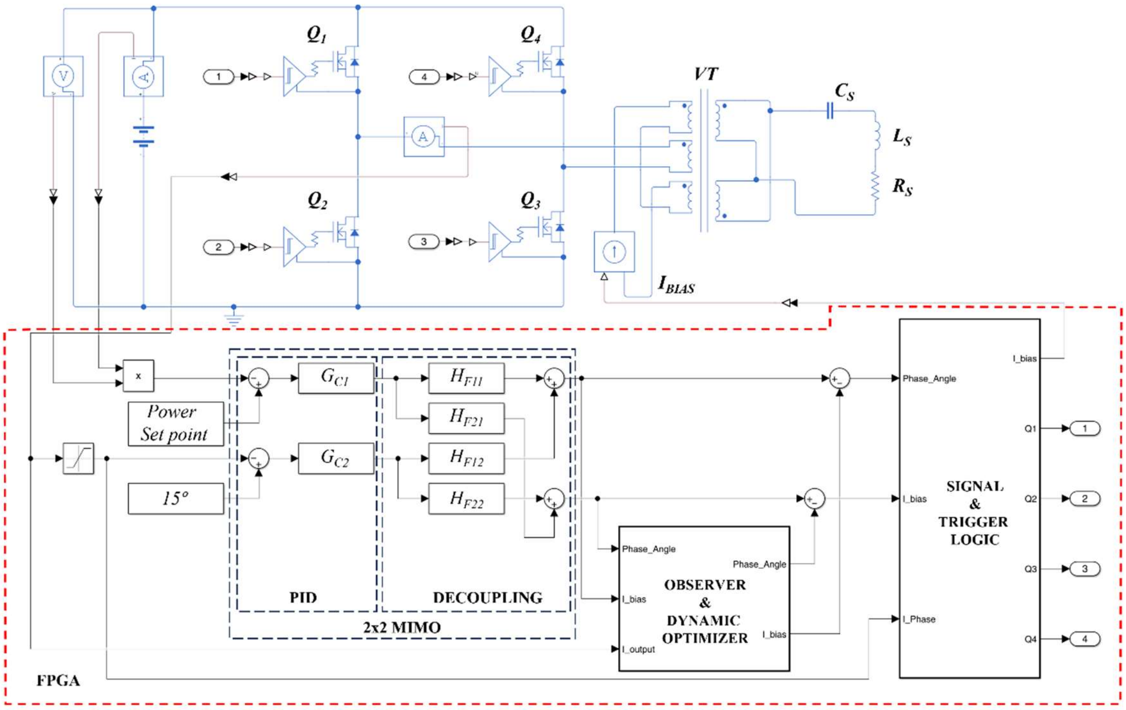

Figura 33. Esquema del sistema propuesto, detallando la topología del inversor, la carga resonante LC con el transformador de activa variable y el diagrama de control.

4.2.3 Análisis de la eficiencia

En este apartado se proporciona un análisis matemático de las pérdidas del inversor y del transformador para verificar las mejoras introducidas por este diseño en todo el rango de operación. Para este propósito, se considera la secuencia de conmutación óptima de desplazamiento de fase [11], combinado con el transformador variable.

Primero se analizan las pérdidas de los transistores MOSFET utilizados en el inversor, las pérdidas de conducción por el canal vienen expresadas por la siguiente fórmula,

$$P_{cd}(\varphi, TR) = \left(\frac{I_o(\varphi, TR)}{\sqrt{2}}\right)^2 R_{DS_{on}} \tag{99}$$

Para las pérdidas de conmutación, solo se han considerado las pérdidas de conmutación a OFF de los MOSFET, ya que el inversor opera en conmutación con tensión cero en todo el rango de operación, lo que hace que las pérdidas de conmutación a ON sean despreciables. La energía se obtiene a partir de la ecuación polinómica de las curvas de pérdidas de conmutación a OFF proporcionadas por el fabricante, considerando una tensión de drenador igual a V_d y la resistencia de puerta utilizada.

$$E_{off}(\varphi, TR) = aI_c(\varphi, TR)^2 + bI_c(\varphi, TR) + c \tag{100}$$

Siendo I_c la amplitud de la corriente que conmuta cada transistor, obtenidas mediante la siguiente expresión:

$$I_c(\varphi,TR)=\frac{2\sqrt{2}}{\pi R_s TR^2}V_d\cos\frac{\varphi}{2}\cos\left(\alpha+\frac{\varphi}{2}\right)\sin(\alpha) \qquad (101)$$

Por consiguiente, las pérdidas de conmutación de cada transistor se obtienen de:

$$P_{sw}(\varphi,TR)=E_{off}(\varphi,TR)\frac{\omega_{sw}}{2\pi} \qquad (102)$$

Y las pérdidas en la puerta del transistor se expresan como:

$$P_{gate}=Q_G V_G\frac{\omega_{sw}}{2\pi} \qquad (103)$$

En cuanto a las pérdidas del transformador se consideran las pérdidas del núcleo, siendo despreciables las pérdidas por la saturación del bobinado de corriente continua.

$$P_{TC}=P_v V_e \qquad (104)$$

Para las pérdidas en el cobre P_{TW} de los bobinados del transformador, es necesario determinar la resistencia efectiva del devanado primario R_1 y del devanado secundario desde primario R_2, teniendo en cuenta la conductividad, la longitud total, el efecto pelicular y la relación de transformación.

$$P_{TW}=I_o(\varphi,TR)^2(R_1+R_2) \qquad (105)$$

Finalmente, la contribución total de las pérdidas viene dada por la siguiente expresión:

$$P_{tot}(\varphi,TR)=\ 4P_{cd}(\varphi,TR)+4P_{sw}(\varphi,TR)+4P_{gate}+P_{TC}+P_{TW} \qquad (106)$$

Dando lugar a la siguiente expresión del rendimiento.

$$\eta(\varphi,TR)=\frac{P_o(\varphi,TR)}{P_o(\varphi,TR)+P_{tot}(\varphi,TR)} \qquad (107)$$

Para el análisis de pérdidas, se utilizó el modelo C3M065100K como MOSFET para cada uno de los transistores del inversor, ya que no solo cumplía con las especificaciones para operar en el área segura, sino que también ofrecía el mejor rendimiento al calcular las pérdidas.

Tabla 6. Características del transistor C3M065100K

Magnitud	Símbolo	Ecuación	Valor	Unidad
Resistencia de ON	$R_{DS_{on}}$	(99)	65	mΩ
Pérdidas conmutación a OFF	a	(100)	0,0213	µJ/A^2
	b		0,436	µJ/A
	c		18,991	µJ
Carga de la puerta	Q_G	(103)	37	nC

La mejora en eficiencia resultante de este nuevo control en comparación con los convencionales se ve representada en la Figura 34 donde se registran las variaciones de eficiencia y corriente de salida con respecto a la potencia de operación. Como se observa al comparar los controles VT-PS y FM-PS, el punto de partida a máxima potencia es similar, pero el control VT-PS aumenta la eficiencia a medida que la corriente disminuye, ya que el transformador incrementa su relación, adaptando la carga al punto óptimo de operación. El control FM-PS muestra un comportamiento similar, pero el aumento de la frecuencia a medida que la potencia disminuye no reduce las pérdidas de manera tan efectiva. Por otro lado, el control PS mantiene una eficiencia más baja desde el inicio, ya que la corriente de salida es mayor debido a la necesidad de operar con un ángulo de conmutación más grande.

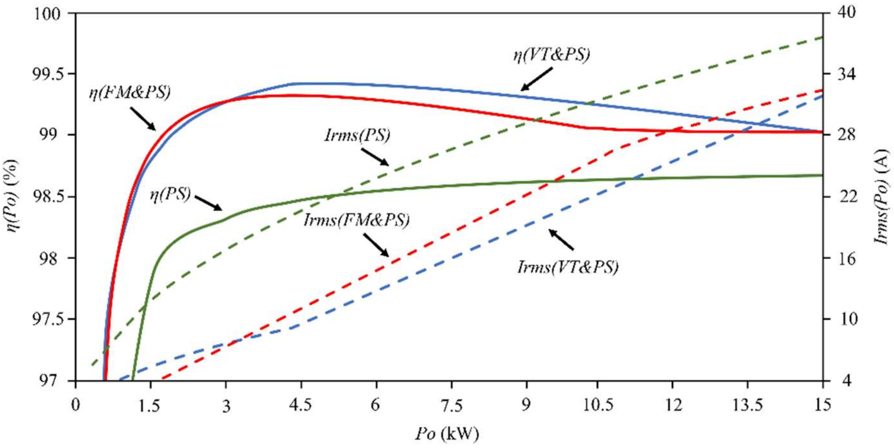

Figura 34. Evolución calculada de la eficiencia y corriente de salida en función de la potencia para el inversor LC con transformador de activa y para tres modulaciones.

En la Tabla 7, se muestra la contribución de las pérdidas para los tres controles trabajando a una misma potencia.

Tabla 7. Resultado de las pérdidas del inversor LC con transformador de activa a 10 kW.

Magnitud	**Símbolo**	**PS**	**FM-PS**	**VT-PS**	**Unidad**
Pérdidas de conducción	P_{cd}	30,92	19,78	16,72	W
Pérdidas de conmutación	P_{sw}	3,83	4,26	3,75	W
Pérdidas en la puerta	P_{gate}	0,115	0,128	0,112	W
Pérdidas en el núcleo	P_{TC}	10,2	11,22	10,2	W
Pérdidas en el bobinado	P_{TW}	9,8	9,28	10,03	W
Pérdidas totales	P_{tot}	159,47	117,16	102,57	W

4.2.4 Resultados experimentales

Para obtener los resultados experimentales del sistema, primero se evaluó el diseño del transformador variable. La Tabla 8 compara los valores teóricos utilizados en el diseño del transformador con los valores medidos en las pruebas de cortocircuito y circuito abierto para el primario y el secundario del transformador. Estas mediciones se realizaron para verificar las suposiciones sobre los factores de acoplamiento tanto en el primario como en el secundario para los transformadores en estado saturado y no saturado. Por otro lado, la Tabla 9 verifica las relaciones de transformación para diferentes niveles de polarización de corriente continua y cómo esto influye en la inductancia del primario y del secundario. Como se puede observar en ambas tablas, existen desviaciones en los valores debido a dispersiones en los componentes y posibles errores de medición.

Tabla 8. Valores teóricos y medidos de las inductancias del trasformador de activa.

Corriente	**Inductancia teórica (µH)**				**Inductancia medida (µH)**			
de bias	**Circuito abierto**		**Corto circuito**		**Circuito abierto**		**Cortocircuito**	
I_{dc} (A)	$L_{p_{oc}}$	$L_{s_{oc}}$	$L_{p_{cc}}$	$L_{s_{cc}}$	$L_{p_{oc}}$	$L_{s_{oc}}$	$L_{p_{cc}}$	$L_{s_{cc}}$
0	1198	85,5	1018	84,2	1222	90,5	1100	89,6
1	244,4	38,18	48,9	7,64	254	40,5	54,1	7,99

Tabla 9. Valores teóricos y medidos de las relaciones del transformador de activa.

Corriente de bias	**Teórico**			**Medido**		
I_{dc} (A)	L_p (μH)	L_s (μH)	**TR**	L_p (μH)	L_s (μH)	**TR**
0	1198	85,5	5,6	1222	90,51	7,02
0,25	820,9	65,2	9,5	767,2	60,854	10,7
0,5	425,6	44,9	13,2	435,5	41,281	12,9
0,75	296,52	39,5	16,3	300,2	42,613	16,1
1	244,4	38,18	20	254,16	40,49	20,8

Para realizar las mediciones que verifican el diseño completo, se utilizó un módulo inversor de 15 kW, que integra la FPGA para implementar el control, sensores, drivers, transistores y una fuente de corriente controlable basada en la bomba de corriente Howland con un OPA548 como amplificador operacional de alta corriente. El inversor se refrigera mediante un radiador por agua y la alimentación proviene de una fuente controlable. El banco de pruebas utilizado se muestra en la Figura 35, donde cada número se corresponde con el siguiente material:

(1) Inversor de calentamiento por inducción con cuatro SiC C3M065100K.
(2) DSO de 300 MHz de ancho de banda.
(3) Sonda diferencial de tensión y sonda de corriente Rogowski.
(4) Sonda de efecto Hall para la corriente de polarización DC.
(5) Transformador variable controlado por corriente.
(6) Condensador en secundario (C_s).
(7) Inductor en secundario (L_s).
(8) Carga.

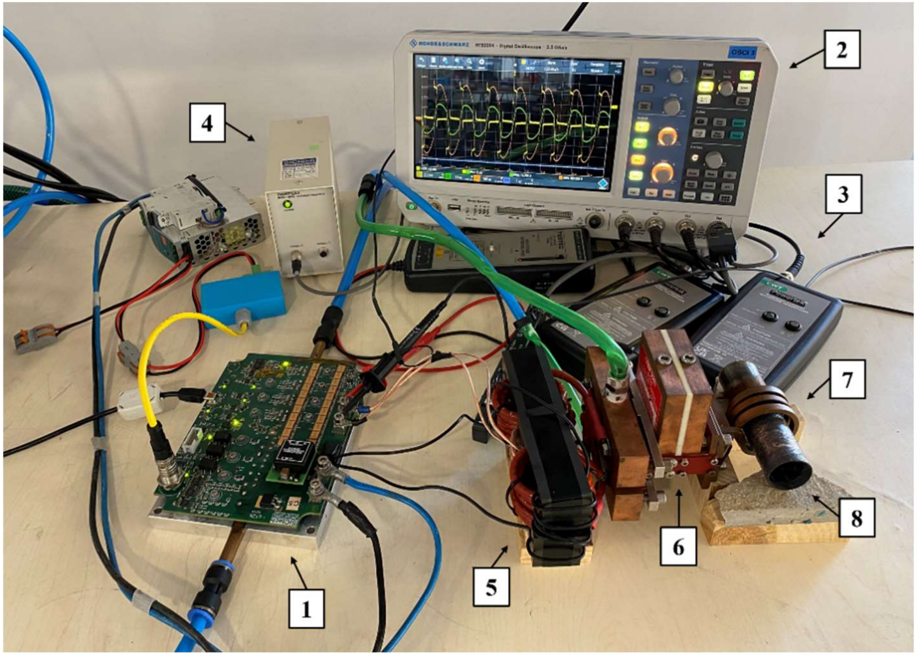

Figura 35. Banco de pruebas del inversor con carga resonante LC y transformador de activa. Las etiquetas numeradas describen los componentes en la parte superior.

En la Tabla 10 se comparan los valores medidos de las principales magnitudes involucradas en el diseño con los valores teóricos a dos niveles de potencia. Como se puede observar, no hay una variación considerable, sin embargo, existen desviaciones debido a los elementos parásitos del sistema que no fueron considerados en el diseño.

Tabla 10. Resultados teóricos y medidos del resonante LC con transformador de activa.

Magnitud	**Símbolo**	**10 kW**		**15 kW**		**Unidad**
		Teórico	**Medido**	**Teórico**	**Medido**	
Ángulo de conmutación	α	15	15,04	15	14,9	°
Relación de trasformación	TR	12,5	12,51	10,7	10,82	
Corriente de salida	I_{RMS}	22,7	22,85	31,9	32,25	A

La Figura 36 muestra los oscilogramas capturados por el DSO para el inversor operando a 10 kW de potencia con tres técnicas de control diferentes y sus respuestas a cambios en la carga. Como se observa en la columna izquierda, el control PS de frecuencia fija requiere operar a una frecuencia más alta, lo que resulta en un ángulo de conmutación de 33° a ese nivel de potencia. Por otro lado, los otros dos controles, al contar con dos variables, pueden mantener un ángulo de 15°. En el caso de FM-PS, esto se debe al aumento de la frecuencia a 229,8 kHz, mientras que en el caso de VT-PS, se debe a la adaptación de la impedancia de la carga mediante el aumento de la relación del transformador. Además, esta adaptación de carga permite una corriente de salida del inversor más baja en comparación con los otros dos controles, siendo de 22,85 A_{RMS}. Asimismo, se observa que, con una carga mejor adaptada debido a la mayor relación del transformador, el ángulo del desplazamiento de desfase de fase es menor, reduciendo las pérdidas por conmutación OFF de los transistores, ya que conmutan un nivel de corriente inferior.

Por otro lado, en respuesta a los cambios de carga, el control PS, al carecer de una regulación directa con la fase entre la tensión y la corriente de salida, pierde ZVS en cinco conmutaciones, y se observa una sobrecorriente en el inversor. Ambas consecuencias provocan un aumento en las pérdidas del inversor. En el caso del control FM-PS, el ángulo se mantiene, pero a costa de cambiar la frecuencia de 230 a 267 kHz, lo que complica el filtrado de armónicos y reduce la optimización de los elementos reactivos del circuito resonante. Finalmente, el control VT-PS es capaz de mantener el ángulo adaptando la impedancia del circuito con un aumento de la relación del transformador de 12,5 a 14,3, permitiendo una frecuencia fija con conmutaciones en ZVS.

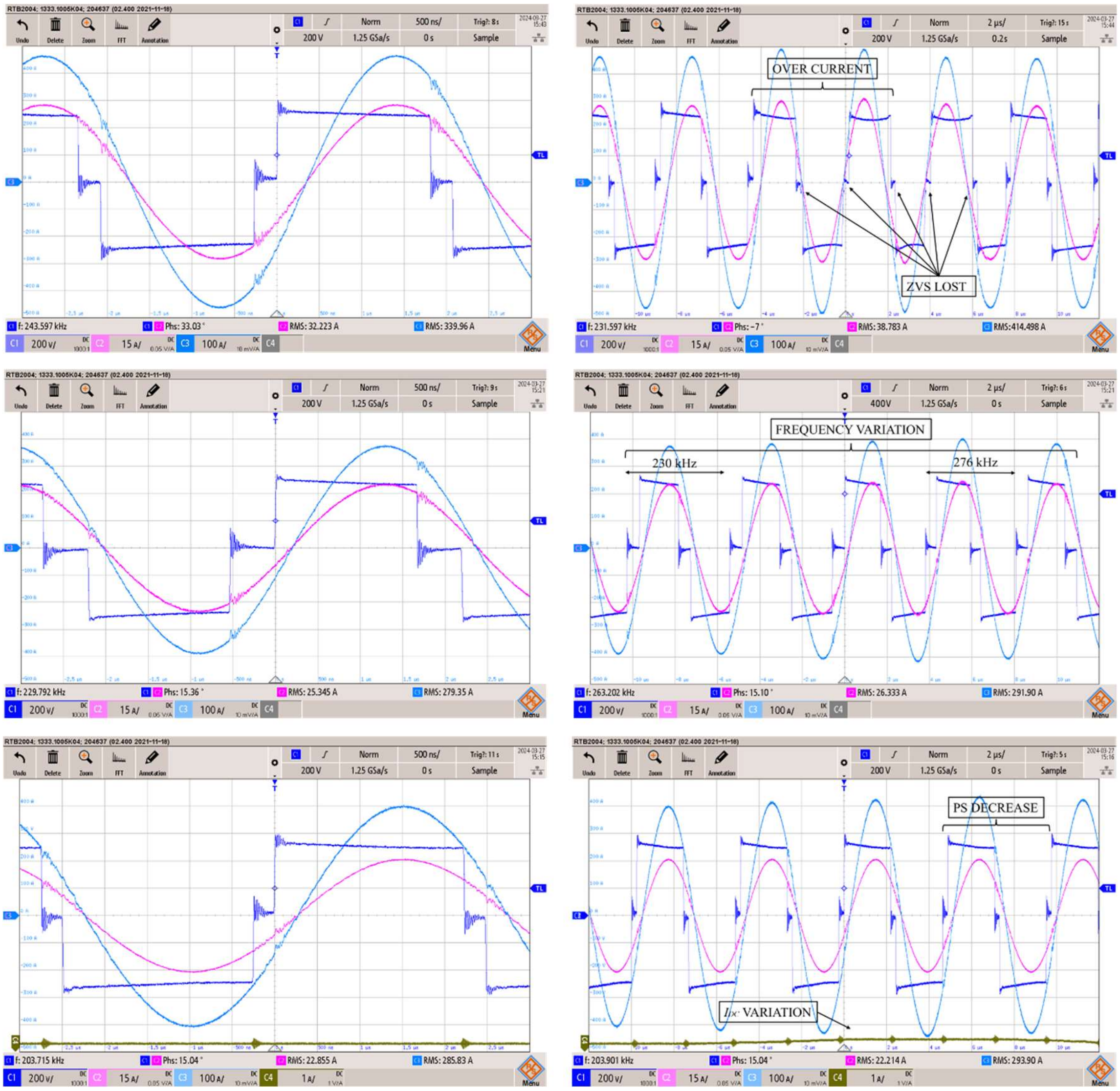

Figura 36. Oscilogramas de pruebas experimentales del inversor LC con transformador de activa y diferentes estrategias de control. Primera fila con PS, segunda fila con FM-PS, y tercera fila con VT-PS. La columna izquierda se corresponde a la operación a 10 kW de potencia, y columna derecha muestra la respuesta a un cambio de carga a ese nivel de potencia. C1 (azul oscuro) representa la tensión de salida (200 V/div), C2 (magenta) muestra la corriente de salida (15 A/div), C3 (azul claro) muestra la corriente en secundario del transformador (100 A/div) y C4 (marrón) muestra la corriente de bias del transformador (1 A/div) en la tercera fila. La base de tiempo es de 500 ns/div en la columna izquierda y 2 µs/div en la derecha.

Finalmente, para concluir la comparación entre los tres tipos de control y validar el diseño discutido en la sección, se midió la eficiencia del inversor en todo el rango de potencia. Esto se realizó calculando la diferencia entre la potencia de entrada medida directamente en la fuente de tensión de DC y la potencia de salida obtenida al multiplicar instantáneamente la tensión y la corriente de salida del puente inversor utilizando el DSO. Los resultados muestran que, a partir de la potencia máxima, Figura 37, tanto los controles FM-PS como VT-PS logran la misma eficiencia, ya que la relación del transformador y la frecuencia son idénticas. Por otro lado, el control PS comienza con una eficiencia más baja debido a su mayor ángulo de desfase entre la tensión y la corriente. Sin embargo, a medida que la potencia disminuye, el control VT-PS aumenta gradualmente su eficiencia gracias a la adaptación de impedancia mediante el incremento de la relación del transformador. En cambio, el control FM-PS obtiene una menor eficiencia debido al aumento de la corriente de salida y la frecuencia. Esto demuestra un rendimiento superior de más del 99 % en todo el rango de operación, siendo mayor con el control VT-PS en comparación con FM-PS. Como se observa en la figura, las mediciones se alinean estrechamente con los valores teóricos calculados, a pesar de la dispersión en los componentes reales y las pérdidas no consideradas en el cálculo teórico.

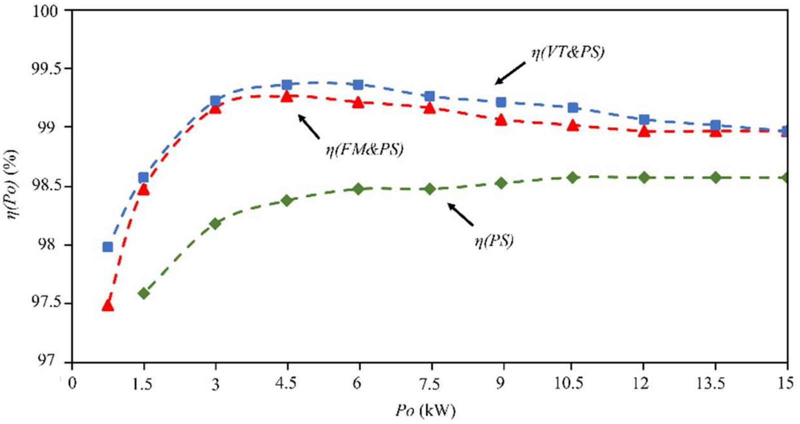

Figura 37. Resultados experimentales de las medidas de la eficiencia del inversor resonante LC con transformador de activa en todo el rango de potencia.

4.3 Resonante LC serie con transformador variable de reactiva y MERS

4.3.1 Introducción

El diseño planteado en este apartado surge a partir del auge que ha impulsado el vehículo eléctrico al desarrollo de nuevos sistemas de temple por escaneo debido a la necesidad de templar piezas con geometrías complejas que deben soportar el par de los motores eléctricos, como ruedas dentadas, engranajes y bujes estriados. Además, estas piezas presentan la dificultad añadida de estar combinadas en una única pieza con forma de eje, que debe ser endurecida a diferentes frecuencias.

Los sistemas de calentamiento más básicos basan su funcionamiento en el ajuste del tanque resonante mediante el cambio de tomas en el transformador o la combinación de condensadores en serie y en paralelo para alcanzar el punto óptimo de operación. El problema es que estos cambios manuales no pueden realizarse durante el proceso de calentamiento, por lo que solo son óptimos si la carga de trabajo no cambia físicamente ni modifica sus propiedades eléctricas resistivas durante el calentamiento, lo cual no ocurre en un proceso real de calentamiento por inducción. Hasta ahora, se ha considerado el uso secuencial de frecuencias duales, [52], una frecuencia media (MF) para calentar la zona casi cilíndrica cercana a la superficie de la pieza y una frecuencia alta (HF) para calentar las superficies más próximas al inductor, como la punta y la cara de los dientes. Sin embargo, este proceso requiere dos tanques resonantes con dos inductores diferentes y dos fuentes de alimentación, lo que implica tener cuatro elementos reactivos ajustados a dos frecuencias de trabajo, además de necesitar un sistema de transferencia mecánica rápida de la pieza entre los dos inductores Figura 38 a).

Como alternativa a esta topología, varios autores han propuesto diferentes combinaciones de tanques resonantes y fuentes de alimentación. En [53], se propone un inductor común para ambos tanques resonantes, pero sigue siendo necesario contar con cuatro elementos reactivos y dos fuentes de alimentación, Figura 38 b). Otra mejora fue introducida en [54], donde, utilizando el mismo inductor y una modulación por ancho de pulso sinusoidal (SPWM), esta variante permite prescindir de una de las fuentes de alimentación, a costa de mantener los cuatro elementos reactivos y perder la conmutación suave a tensión cero, Figura 38 c). Estas propuestas se utilizan actualmente en la industria, pero presentan inconvenientes, como la limitación de diseño a solo dos frecuencias de temple, lo que las hace inviables para piezas con geometrías variables. Además, todas emplean modulación FM o combinaciones de FM con PS.

Como se ha demostrado, el calor generado por las corrientes inducidas en la pieza de trabajo se concentra en una capa superficial de espesor δ, que corresponde a la profundidad de penetración de la ecuación (5), y depende de la frecuencia de trabajo, esto significa que, si la frecuencia varía durante el calentamiento debido a la modulación, la profundidad de penetración también cambia, lo que puede comprometer la calidad del templado. Este problema se ha abordado en esta tesis, centrándose en sistemas de inducción de frecuencia fija.

En [19], se utiliza una topología LLC con tres elementos reactivos demostrando que si potencia de salida del inversor se regula únicamente mediante el PS el sistema pierde la conmutación suave ZVS, en cambio sí se utiliza la combinación de la modulación PS-FM no se pierden las conmutaciones suaves, pero se varía la frecuencia. Proponiendo como solución la modulación VI-PS donde la inductancia en serie es un inductor variable controlado por corriente, lo que, junto con el PS, permite regular la potencia de salida sin variar la frecuencia, aumentando la eficiencia del convertidor en todo el rango de operación y manteniendo la conmutación en ZVS incluso con cambios en la carga. Sin embargo, esta topología tiene la desventaja de requerir tres elementos reactivos para una única frecuencia.

Finalmente, en [26], se propone otra solución para mantener la frecuencia fija y mejorar la eficiencia mediante el uso de un transformador variable controlado por corriente, lo que permite adaptar la impedancia de la carga en cualquier momento. No obstante, a pesar de la disponibilidad de estas soluciones para regular la potencia a una frecuencia fija, solo permiten calentar la pieza a una única frecuencia, lo que las hace inadecuadas para el endurecimiento de geometrías complejas o piezas con diferentes materiales.

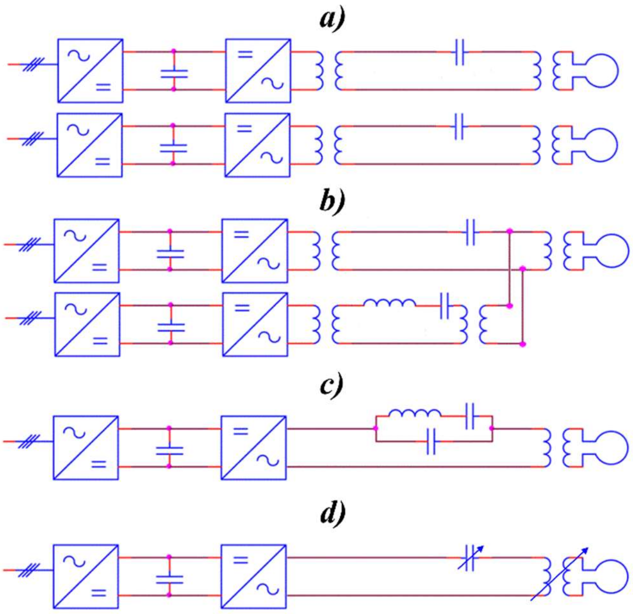

Figura 38. Convertidores multifrecuencia. a) Doble frecuencia independiente, b) Doble frecuencia con único inductor, c) Doble frecuencia con único convertidor y d) Frecuencia variable control de los elementos reactivos.

A diferencia de las topologías presentadas anteriormente en la Figura 38 a), b) y c), en este apartado se propone el control de los elementos reactivos del tanque resonante, [27]. Para ello, se utiliza un transformador variable controlado por corriente (VT), presentado en el capítulo 3.2, con el fin de variar la relación del transformador acoplado al inductor de calentamiento, permitiendo así controlar la inductancia reflejada del inductor en el tanque resonante. Además, se emplea un interruptor de recuperación de energía magnética (MERS), presentado en 3.3, para modificar la influencia del condensador como elemento de compensación de energía reactiva, tal como se muestra en la Figura 38 d). Como se estudiará a continuación, la combinación de estos elementos junto con la regulación PS para variar la potencia de salida del inversor permite conmutar a la frecuencia óptima requerida para el endurecimiento, considerando la profundidad de penetración y la posición de la pieza de trabajo y el inductor en el proceso de escaneo.

Para lograr el comportamiento descrito hay que tener en cuenta el factor de calidad del resonante, debido a que es un parámetro decisivo en el calentamiento por inducción, ya que mide la cantidad de potencia reactiva en el inductor en relación con la potencia activa que puede aplicarse. La elección del factor de calidad está determinada por aspectos como el material de la pieza a calentar, su geometría, el tipo de tratamiento térmico y el acoplamiento entre la pieza y el inductor [55].

En los sistemas de calentamiento por inducción, el inductor tiene dimensiones físicas que no pueden variarse durante el calentamiento. Por lo tanto, en el caso de piezas con dimensiones irregulares o combinaciones de diferentes materiales, es crucial elegir un valor del factor de calidad que permita un acoplamiento adecuado de la pieza a lo largo de todo el proceso de calentamiento para entregar la potencia deseada. Este parámetro es fundamental porque la impedancia reflejada de la pieza de trabajo en el inductor varía durante el calentamiento, ya sea por la geometría variable de la pieza, por la composición de diferentes materiales, por cambios en la permeabilidad dependientes de la temperatura, por la profundidad de penetración y la resistencia eléctrica de la pieza, o por el propio factor de calidad del circuito.

La Figura 39 a) muestra cómo varía la forma del factor de calidad de un circuito resonante LC en serie en función de la frecuencia, manteniendo constantes los dos elementos reactivos. La curva presenta en su punto máximo el valor de Q que define su forma. Como se observa, la máxima entrega de potencia ocurre en la frecuencia de resonancia.

Por otro lado, la Figura 39 b) muestra el efecto de variar únicamente la inductancia reflejada en primario del inductor de calentamiento mediante la variación de la relación de transformación. Debido a la relación entre la inductancia y la frecuencia en el factor de calidad, este aumenta a medida que la inductancia se incrementa. Se debe considerar que la resistencia en serie equivalente (R_p) se ajusta a un valor que no supere la potencia activa máxima del equipo. Para lograr esto, se considera que la resistencia de la pieza de trabajo no es fija, ya que varía durante el proceso de calentamiento para mantener constante R_p.

El caso opuesto se representa en la Figura 39 c), donde el aumento de la capacitancia del condensador provoca una disminución en la frecuencia de resonancia, sin que esto sea compensado por un aumento en la inductancia, lo que causa una reducción en el factor de calidad.

Por lo tanto, como se muestra en la Figura 39 d), el efecto de poder controlar ambos elementos reactivos del sistema permite mantener el factor de calidad en todo un rango de frecuencias, o bien disminuirlo o aumentarlo variando solo uno de los dos elementos y la frecuencia de trabajo.

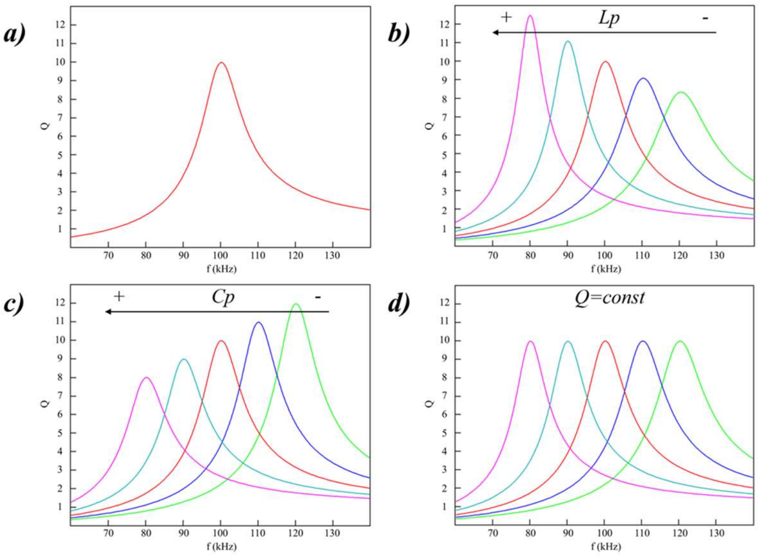

Figura 39. Comportamiento del factor de calidad para R_p constante. a) Resonante de dos elementos, b) Resonante con transformador variable c) Resonante con condensador variable y d) Resonante con control de los elementos reactivos. El pico de la curva se corresponde con el factor de calidad de esta.

4.3.2 Diseño

En aplicaciones reales de endurecimiento, se utilizan inductores de una sola espira estrechamente acoplados a la pieza de trabajo. Como se mencionó anteriormente, el propósito de este diseño es emplear un único circuito resonante con solo un inductor. Por lo tanto, la geometría del inductor, que se determinará con un diámetro mayor al del mayor diámetro de la pieza a calentar, definirá el valor de la inductancia del inductor. El diámetro de la pieza de trabajo también determinará el factor de calidad, ya que este debe aumentar a medida que la pieza se desacopla del inductor para seguir aplicando la potencia deseada a la pieza [43]. Otra característica establecida por la pieza a calentar es la profundidad de penetración, la cual se usa para determinar la frecuencia a la que debe conmutar el inversor. La Tabla 11 muestra los parámetros de ejemplo para el endurecimiento por escaneo de una pieza de geometría variable fabricada en acero al carbono 1040, utilizando un inductor de una sola espira con un diámetro de 40 mm.

Tabla 11. Parámetros iniciales del diseño del inversor LC serie con transformador de reactiva y MERS.

CICLO DE ESCANEO	DIAMETRO DE LA PIEZA (mm)	PENETRACIÓN (mm)	FRECUENCIA (kHz)	FACTOR DE CALIDAD	POTENCIA MÁXIMA (kW)
1	23,5	0,7	67	10	6
2	30,2	0,6	77,5	8	9
3	25,5	0,55	89	9	10
4	35	0,5	100	6	10
5	32	0,65	72	7	10

A partir de los requisitos iniciales, se pueden obtener los parámetros de diseño de las etapas individuales de calentamiento. Para ello, la frecuencia de resonancia del tanque LC se determina mediante la siguiente ecuación:

$$\omega_o = \frac{2Q\omega_{sw}}{tan\,\alpha + \sqrt{\tan^2\alpha + 4Q^2}} \tag{108}$$

Con el requisito de potencia y el factor de calidad, la corriente que debe circular por el inductor se puede obtener utilizando la siguiente expresión:

$$I_L = \sqrt{\frac{P_o Q}{\omega_{sw} L_s}} \tag{109}$$

Mientras que la corriente de salida del inversor se define utilizando la presente ecuación:

$$I_o = \frac{P_o}{\frac{2}{\pi}\sqrt{2}V_d \cos\alpha} \tag{110}$$

Dando lugar a poder calcular la relación del transformador para cada uno de los ciclos de escaneo,

$$TR = \frac{I_L}{I_o} \tag{111}$$

Y la inductancia reflejada en primario:

$$L_p = TR^2 L_s \tag{112}$$

Por lo tanto, el valor de la capacidad equivalente de la combinación entre el condensador en serie C_S y el condensador del C_{MERS} se expresa como:

$$C_{Eq} = \frac{\left(\frac{1}{\omega_o}\right)^2}{L_p} \tag{113}$$

Mediante el valor de la tensión a distribuir entre los dos condensadores,

$$V_{C_{Eq}} = \frac{I_o}{\omega_{sw} C_{Eq}} \tag{114}$$

El valor de los dos condensadores que componen el circuito resonante se selecciona, de manera que el valor equivalente del MERS se obtiene mediante la siguiente expresión:

$$C_{MERS} = \frac{1}{\frac{1}{C_{Eq}} - \frac{1}{C_S}} \tag{115}$$

En la Tabla 12, se muestran los valores resultantes del diseño donde se ha utilizado dos condensadores de 0,66 μF.

Tabla 12. Resultados del diseño del inversor LC serie con transformador de reactiva y MERS.

CICLO DE ESCANEO	**DIAMETRO DE LA PIEZA (mm)**	**CORRIENTE EN EL INDUCTOR (Arms)**	**RELACIÓN DE TRANSFORMACIÓN**	**CONDESADOR EQUIVALENTE (μF)**	**CAPACIDAD DEL MERS (μF)**
1	23,5	567	4,7	0,65	3,58
2	30,2	608	4,77	0,48	1,73
3	25,5	634	4,98	0,33	0,66
4	35	488	3,84	0,45	1,4
5	32	622	4,88	0,53	2,73

En cuanto al diseño del transformador variable, se sigue el mismo procedimiento realizado en el apartado 4.2.2, ecuaciones (86) a (95) donde solo hay que considerar que en las ecuaciones (86) y (87) la tensión V_d se sustituye por la tensión de los condensadores ($V_{C_{Eq}}$).

Al igual que sucedía con los anteriores diseños, para regular la potencia del convertidor, una vez que el circuito resonante está ajustado con el transformador variable y el MERS, se utiliza el control por desplazamiento de fase. La siguiente expresión define la tensión de salida eficaz del armónico fundamental del inversor.

$$V_o(\varphi) = \frac{2\sqrt{2}}{\pi} V_d \, cos\frac{\varphi}{2} \tag{116}$$

Y, por lo tanto, la corriente de salida del inversor se puede expresar como una función del desplazamiento de fase, la relación de transformación y la capacidad equivalente debido a la influencia del MERS mediante la siguiente ecuación:

$$I_o(\varphi, TR, C_{Eq}) = \frac{2V_d Q\sqrt{2C_{Eq}L_s}}{\pi\,\mathrm{TR}\,L_s}\cos\frac{\varphi}{2}\cos(\alpha) \tag{117}$$

De la misma manera, la potencia de salida del convertidor se expresa mediante:

$$P_o\left(\varphi, TR, C_{Eq}\right) = \frac{8{V_d}^2 Q}{\pi^2 TR}\sqrt{\frac{C_{Eq}}{L_s}}\cos^2\frac{\varphi}{2}\cos^2(\alpha) \tag{118}$$

En cuanto al diseño del control del sistema completo se tiene que considerar que el control de los elementos reactivos debe actuar sobre el condensador MERS para variar la capacidad efectiva del resonante, sobre la relación de transformación del transformador variable para aumentar o disminuir la inductancia reflejada del inductor en el primario, y sobre el ángulo de fase para variar la tensión aplicada a la carga. Y estos actúan sobre los parámetros de calentamiento, es decir, la potencia del inversor y la frecuencia de conmutación, los cuales son establecidos por la pieza a calentar en cada punto del proceso de escaneo.

La Figura 40 muestra el esquema simplificado del control propuesto. En la primera etapa, cada entrada actúa de manera independiente con su punto de ajuste mediante un control proporcional, integral y derivativo (PID), donde el primer lazo de control tiene como entrada la potencia de entrada del inversor, con la cual se obtiene el error al compararla con el punto de ajuste. El control PID obtiene el porcentaje de desplazamiento de fase que, en el bloque final, resultará en las señales de puerta de los transistores a la frecuencia de conmutación. Su comportamiento se expresa mediante la ecuación (128). El segundo lazo de control es la corriente de salida del convertidor, que se compara con la corriente óptima, ecuación (117). Esto se debe a que la corriente del inductor puede variar por la relación de transformación o por la corriente de salida del inversor, siendo óptimo obtener la corriente por la relación de transformación que, por la corriente de salida del inversor, considerando que la frecuencia de resonancia variará con la relación de transformación. El último bloque será responsable de controlar la corriente de bias inyectada al transformador. El tercer lazo de control es el ángulo de conmutación óptimo, es decir, el ángulo entre la tensión de salida del inversor y la corriente de salida, el cual se expresa mediante la siguiente ecuación.

$$\omega_{sw} = \omega_o \frac{\tan\frac{\varphi}{2} + \sqrt{\tan^2\frac{\varphi}{2} + 4\mathrm{Q}^2}}{2Q} \tag{119}$$

Donde la frecuencia de conmutación debe ser variada para que el ángulo α sea aproximadamente igual a $\varphi/2$, manteniendo así un ángulo óptimo constante [56]. Como se muestra en la ecuación y considerando la frecuencia de conmutación fija como el parámetro de calentamiento, el sistema debe variar la frecuencia de resonancia mediante el MERS para obtener el valor óptimo, ecuaciones (15) y (115). Por lo tanto, este lazo regula el ciclo de trabajo del MERS, adaptándose a la frecuencia de conmutación y al cruce por cero de la corriente en el último bloque.

Como se ha observado, las ecuaciones del sistema están todas relacionadas entre sí y, por lo tanto, siendo un sistema 3x3, con múltiples entradas y múltiples salidas, donde cada regulación interviene con las demás mediante una red de diagonalización [44].

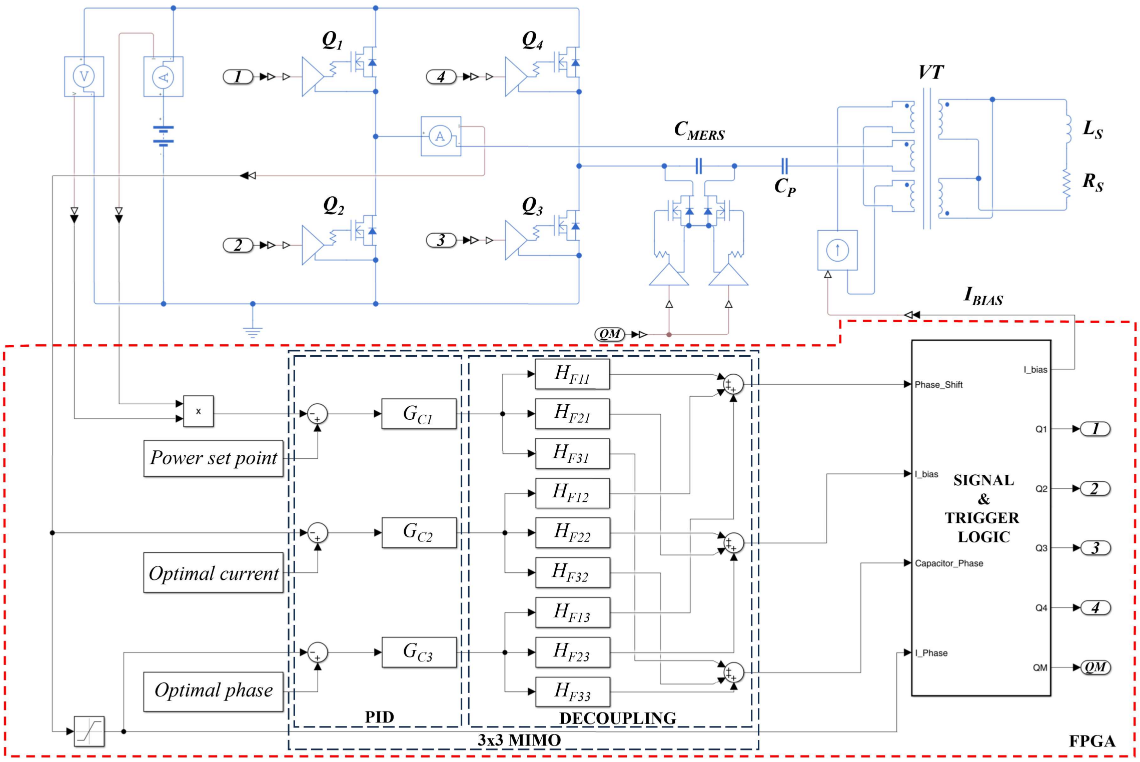

Figura 40. Esquema del sistema propuesto, detallando la topología del inversor, la carga resonante LC con el transformador de reactiva variable, el MERS y el diagrama de control.

4.3.3 Análisis de la eficiencia

En esta sección se analizan las pérdidas teóricas del inversor, el MERS y el transformador variable.

En cuanto a las pérdidas del inversor, las pérdidas debidas a la corriente conducida a través del canal de los MOSFET están dadas por la siguiente expresión:

$$P_{cd}(\varphi,TR,C_{Eq}) = \left(\frac{I_o(\varphi,TR,C_{Eq})}{\sqrt{2}}\right)^2 R_{DS_{on}} \tag{120}$$

Las pérdidas de conmutación se deben a las pérdidas de conmutación a OFF de los MOSFET, debido a la operación en ZVS del convertidor, ya que conmutan por encima de la frecuencia de resonancia, lo que hace que las pérdidas de conmutación a ON sean despreciables. Para su análisis, la energía se obtiene a partir de la ecuación polinómica de las curvas de pérdidas de conmutación a OFF proporcionadas por el fabricante, para una tensión de drenador a surtidor igual a V_d y la resistencia de la puerta utilizada, lo que da como resultado:

$$E_{off}(\varphi,TR,C_{Eq}) = aI_c(\varphi,TR,C_{Eq})^2 + bI_c(\varphi,TR,C_{Eq}) + c \tag{121}$$

Y la corriente de conmutación por cada transistor viene expresada por la siguiente fórmula:

$$I_c(\varphi,TR,C_{Eq}) = \frac{2V_dQ\sqrt{2C_{Eq}L}}{\pi\,\mathrm{TR}\,L}\cos\frac{\varphi}{2}\cos(\alpha)\sin(\alpha) \tag{122}$$

Por lo tanto, las pérdidas de potencia para cada transistor se obtienen de la siguiente manera:

$$P_{sw}(\varphi, TR, C_{Eq}) = E_{off}(\varphi, TR)\frac{\omega_{sw}}{2\pi} \quad (123)$$

De la misma manera, las pérdidas por conducción de los MOSFET utilizados en el MERS se calculan utilizando la siguiente ecuación:

$$P_{MERS_{cd}}(\varphi, TR, C_{Eq}) = \left(I_o(\varphi, TR, C_{Eq})\sin(\gamma)\right)^2 R_{DS_{on}} \quad (124)$$

Y la energía de pérdidas por conmutación OFF del transistor.

$$E_{MERS_{off}}(\varphi, TR, C_{Eq}) = aI_{MERS_c}(\varphi, TR, C_{Eq})^2 + bI_{MERS_c}(\varphi, TR, C_{Eq}) + c \quad (125)$$

Donde la amplitud de la corriente conmutada proviene de la siguiente expresión.

$$I_{MERS_c}(\varphi, TR, C_{Eq}) = \frac{2V_d Q\sqrt{2C_{Eq}L}}{\pi\,\mathrm{TR}\,L}\cos\frac{\varphi}{2}\cos(\alpha)\sin(\gamma) \quad (126)$$

Esto da como resultado la siguiente expresión para las pérdidas por conmutación:

$$P_{MERS_{sw}}(\varphi, TR, C_{Eq}) = E_{off}(\varphi, TR)\frac{\omega_{sw}}{2\pi} \quad (127)$$

En cuanto a las pérdidas del transformador, deben considerarse las pérdidas del núcleo debido a la densidad de flujo magnético, ya que la influencia de corriente continua de bias son despreciables. Por lo tanto, estas pérdidas pueden obtenerse mediante la siguiente ecuación:

$$P_{TC} = P_v V_e \quad (128)$$

Para las pérdidas en el bobinado del transformador, es necesario determinar la resistencia efectiva del devanado primario y del devanado secundario, teniendo en cuenta la conductividad, la longitud total, el efecto pelicular y la relación de transformación. Las pérdidas se obtienen mediante la siguiente ecuación:

$$P_{TW} = I_o(\varphi, TR, C_{Eq})^2 (R_1 + R_2) \quad (129)$$

Finalmente, las pérdidas totales se expresan como:

$$\begin{aligned} P_{tot}(\varphi, TR, C_{Eq}) = {} & 4P_{cd}(\varphi, TR, C_{Eq}) + 4P_{sw}(\varphi, TR, C_{Eq}) + 2P_{MERS_{cd}}(\varphi, TR, C_{Eq}) \\ & + 2P_{MERS_{sw}}(\varphi, TR, C_{Eq}) + P_{TC} + P_{TW} \end{aligned} \quad (130)$$

Y el rendimiento viene dado por:

$$\eta(\varphi, TR) = \frac{P_o(\varphi, TR, C_{Eq})}{P_o(\varphi, TR, C_{Eq}) + P_{tot}(\varphi, TR, C_{Eq})} \quad (131)$$

La Figura 41 muestra la evolución de la eficiencia en función de la potencia para los rangos de potencia de cada ciclo de escaneo del calentamiento. Los transistores seleccionados para el diseño final fueron MOSFET de SiC de Onsemi con referencia NTH4L022N120M3S, donde se utilizaron cuatro para el inversor y dos para el MERS. En cuanto al transformador, se seleccionaron dos núcleos en forma de "E" de TDK Electronics de material N27. Como se puede ver en los resultados gráficos, la mayor frecuencia requerida en los pasos 4, 3 y 2 hace que la eficiencia sea más baja que en los demás, a pesar de trabajar con un tanque resonante que se adapta a cada calentamiento.

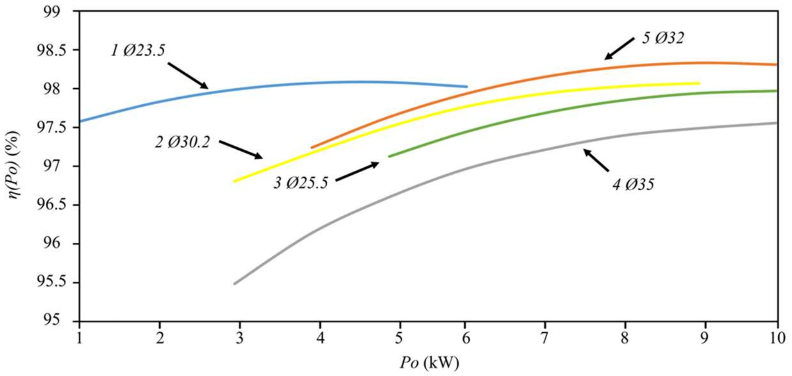

Figura 41. Evolución calculada de la eficiencia del inversor LC con transformador de reactiva y MERS en función de la potencia para cada ciclo de escaneo.

4.3.4 Resultados experimentales

En este apartado se comprueba experimentalmente el funcionamiento del inversor con cada uno de los componentes y del conjunto en completo. Como sucedía en el apartado 4.2.4, el primer paso es comprobar el diseño del trasformador variable, pero debido a que estos resultados no aportan novedad al documento debido a que ambos diseños son similares pese a la disposición del transformador siendo este de activa o reactiva, estos resultados se han omitido, pudiendo ser consultados en [27].

Para verificar el correcto funcionamiento del MERS, se midió la tensión del condensador variable en operación al mismo tiempo que la señal de control de conmutación del condensador. En la Figura 42, se presentan dos capturas de pantalla del osciloscopio que muestran el comportamiento del sistema en dos condiciones diferentes. Como se puede observar en la imagen, la tensión del condensador variable se vuelve cero cuando los MOSFET del MERS están en conducción, lo que limita la tensión que puede aportar el propio condensador.

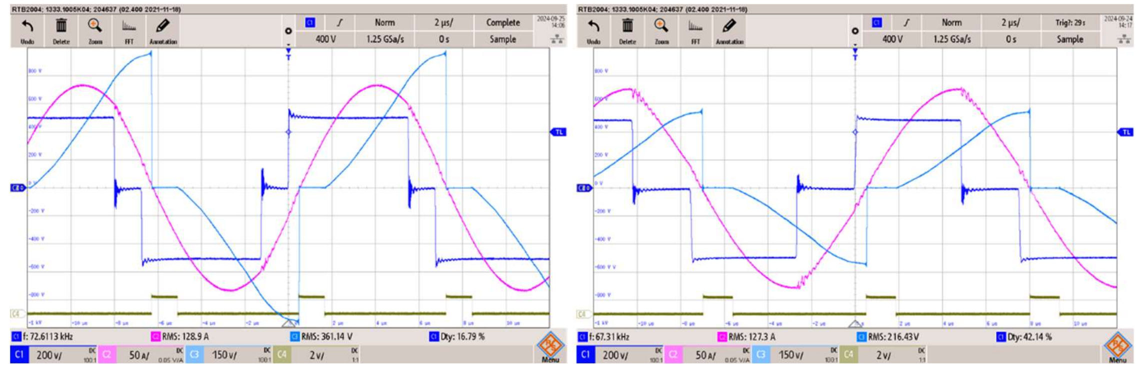

Figura 42. Oscilogramas experimentales del condensador del MERS en dos condiciones diferentes. C1 (azul oscuro) representa la tensión de salida C1 (200 V/div), C2 (magenta) muestra la corriente de salida (50 A/div), C3 (azul claro) muestra la tensión del condensador del MERS (150 V/div) y C4 (marrón) muestra la señal lógica de la puerta del MERS (2 V/div). La base de tiempo es de 2 µs/div.

Para las pruebas experimentales se utilizó un inversor prototipo de 10 kW con la finalidad de probar todo el sistema en su conjunto, el cual integra la FPGA con el control, fuentes de alimentación, controladores de disparo, sensores, MERS y la fuente de corriente controlable del transformador variable. El banco de pruebas utilizado se muestra en la Figura 43, y cada número corresponde a:

1) Inversor de calentamiento por inducción con seis SiC NTH4L022N120M3S.
2) Condensador MERS.
3) Condensador en serie (C_S).
4) Transformador variable.
5) Inductor en serie (L_S).
6) Conjunto de piezas de trabajo.
7) Osciloscopio digital de 300 MHz de ancho de banda (DSO).
8) Sonda de corriente Rogowski.
9) Sonda de tensión diferencial.

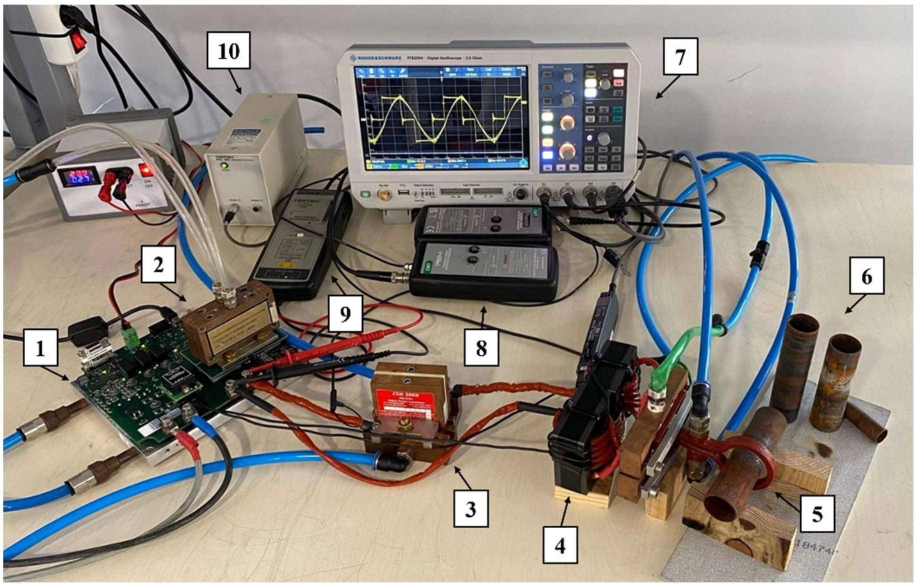

Figura 43. Banco de pruebas del inversor con carga resonante LC, transformador de reactiva y MERS. Las etiquetas numeradas describen los componentes en la parte superior.

La Figura 44 muestra las capturas de pantalla del osciloscopio para las dos mediciones realizadas a distintas potencias en cada ciclo de escaneado. En ellas se puede observar el funcionamiento del convertidor en cada paso y con cada consigna de potencia. Como se puede ver, el sistema se adapta a la frecuencia requerida en cada uno de los ciclos.

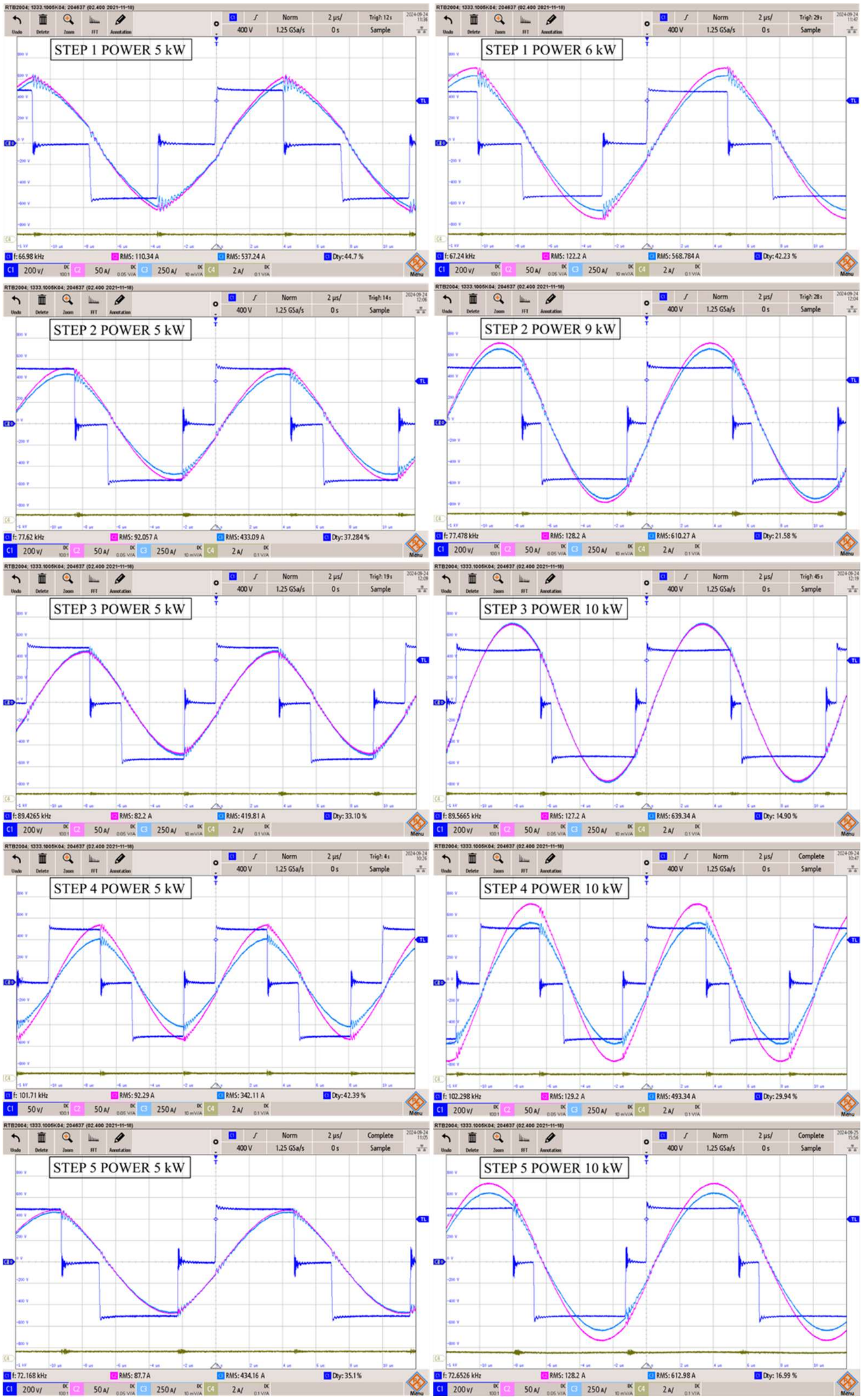

Figura 44. Oscilogramas de pruebas experimentales del inversor LC con transformador de reactiva y diferentes calentamientos. La columna de la izquierda se corresponde la operación a 5 kW, y la derecha a máxima potencia. C1 (azul oscuro) representa la tensión de salida (200 V/div), C2 (magenta) muestra la corriente de salida (50 A/div), C3 (azul claro) muestra la corriente en secundario del transformador (200 A/div) y C4 (marrón) muestra la corriente de bias del transformador (2A/div). La base de tiempo es de 2 µs/div.

En la Tabla 13 se registran los valores de los principales parámetros obtenidos durante las pruebas experimentales del funcionamiento del convertidor. Además, en esta tabla se han añadido los valores teóricos obtenidos a partir de las ecuaciones de diseño, con el fin de verificar su exactitud.

Tabla 13. Comparación de resultados teóricos y medidos a máxima potencia y 5 kW para el resonante LC serie con trasformador de reactiva y MERS.

CICLO DE ESCANEO	**POTENCIA (kW)**	**FRECUENCIA (kHz)**		**DESPLAZAMIENTO DE FASE (°)**		**RELACIÓN DE TRANSFORMACIÓN**		**CAPACIDAD EQUIVALENTE (μF)**	
		Teórico	**Medido**	**Teórico**	**Medido**	**Teórico**	**Medido**	**Teórico**	**Medido**
1	5	67	66,98	79,3	80,46	4,7	4,87	0,66	0,6
	6		67,24	74,4	76,01		4,65		0,65
2	5	77,5	77,62	66,7	67,11	4,77	4,7	0,48	0,47
	9		77,48	38	38,84		4,76		0,47
3	5	89	89,43	60	59,58	4,98	5,11	0,33	0,3
	10		89,57	25,4	26,82		5,03		0,31
4	5	100	101,71	76,6	76,3	3,84	3,71	0,45	0,45
	10		102,3	54	53,89		3,82		0,42
5	5	72	72,17	61,7	63,18	4,88	4,95	0,53	0,5
	10		72,65	28	30,58		4,78		0,52

Finalmente, la eficiencia del convertidor se ha registrado para cada ciclo de calentamiento en todo el rango de potencia. Como se puede observar en la Figura 45, la eficiencia registrada es similar a la calculada teóricamente, situándose en un rango porcentual entre 98,5 % y 95,9 %, dependiendo de la potencia y frecuencia requeridas en cada etapa de calentamiento. Como se analizó previamente, esta eficiencia tiene una alta correlación con la frecuencia de conmutación, ya que las etapas de calentamiento 3 y 4 son las que han registrado la menor eficiencia, debido a que ocurren a frecuencias de 89 kHz y 100 kHz respectivamente.

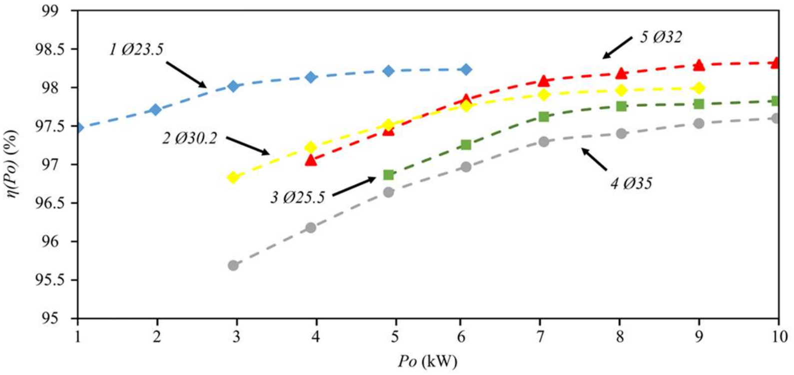

Figura 45. Resultados experimentales de las medidas de la eficiencia del inversor resonante LC con transformador de reactiva y MERS en todo el rango de potencia.

Capítulo 5. Conclusiones y trabajos futuros

5.1 Conclusiones

A partir de los resultados obtenidos de la investigación desarrollada en los tres artículos que componen esta tesis, se destacan importantes avances en el control y diseño de convertidores para aplicaciones de calentamiento por inducción, especialmente en sistemas resonantes de alta frecuencia.

En primer lugar, se evidenció que las técnicas de control basadas en el desplazamiento de fase combinado con inductancias o transformadores variables controlados por corriente permiten operar a frecuencia fija cercana a la frecuencia de resonancia, lo que contribuye a mantener un bajo ángulo de conmutación, reducir la corriente de salida y lograr una alta eficiencia energética durante todo el rango de operación. Estas técnicas destacan por su capacidad de mantener la conmutación suave ZVS incluso frente a cambios bruscos de carga, mejorando así la fiabilidad y el rendimiento del sistema.

En la primera contribución se diseñó un resonante de tres elementos donde el inductor serie se sustituyó por le inductor variable controlado por corriente, permitiendo por tanto operar a frecuencia fija. Las pruebas experimentales realizadas en el prototipo que se compone de un inversor de puente completo con MOSFET de SiC, demostraron que el control propuesto supera a las técnicas tradicionales de desplazamiento de fase a frecuencia fija y de rango estrecho. Se logró una eficiencia superior al 98,5 %, reduciendo las pérdidas por conducción y conmutación, y se demostró que no se pierden las conmutaciones suaves en los cambios de carga.

En la segunda publicación se simplificó el sistema pasando de tres elementos reactivos a dos elementos reactivos. Para lograr esto se implementó un transformador variable controlado por corriente en posición de activa, permitiendo por tanto utilizar un resonante serie LC y añadir aislamiento galvánico en la salida del inversor. Como resultado se obtuvo un comportamiento superior a las dos modulaciones tradicionales en cuanto a eficiencia y a respuesta ante cambios de carga. En algunos casos, se alcanzó una eficiencia superior al 99 % y de nuevo se comprobó que el sistema es capaz de mantener las conmutaciones suaves.

La tercera contribución combina el uso del transformador variable controlado por corriente en posición de reactiva con un condensador variable. Esta combinación innova respecto a la anterior en sentido de que se permite ajustar la potencia, la frecuencia de trabajo y el factor de calidad con un único resonante. Esta flexibilidad resulta fundamental para aplicaciones donde las piezas a tratar presentan geometrías variables, superando las limitaciones de los sistemas que operan con una o dos frecuencias. Las pruebas experimentales corroboraron los cálculos teóricos y mostraron un rango de eficiencia del sistema del 98,5 % al 95,9 % con un rango de frecuencias de 89 a 100 kHz y una potencia de 1 a 10 kW.

En conclusión, las estrategias de control analizadas no solo mejoran la eficiencia global del sistema, sino que también amplían su capacidad para operar bajo diversas condiciones de carga, garantizando la conmutación suave y reduciendo las pérdidas. Estos avances abren nuevas posibilidades para futuras investigaciones en el desarrollo de sistemas de control a frecuencia fija mediante la gestión de elementos reactivos, tanto en tanques resonantes de dos o tres elementos, consolidando así el potencial de estas tecnologías para aplicaciones industriales de calentamiento por inducción.

5.2 Trabajos futuros

La investigación llevada a cabo en este trabajo se ha centrado únicamente en convertidores resonantes para aplicaciones de calentamiento por inducción. Sin embargo, los convertidores resonantes abarcan un gran rango de aplicaciones. En la actualidad, uno de los convertidores más investigados surge de la demanda de sistemas bidireccionales de energía del vehículo eléctrico a red

(V2G) y del vehículo eléctrico a carga (V2L). La topología de este tipo de convertidores es el puente activo dual, debido a que permite la bidireccionalidad regulada de la energía. La Figura 46 muestra el esquemático del DAB resonante.

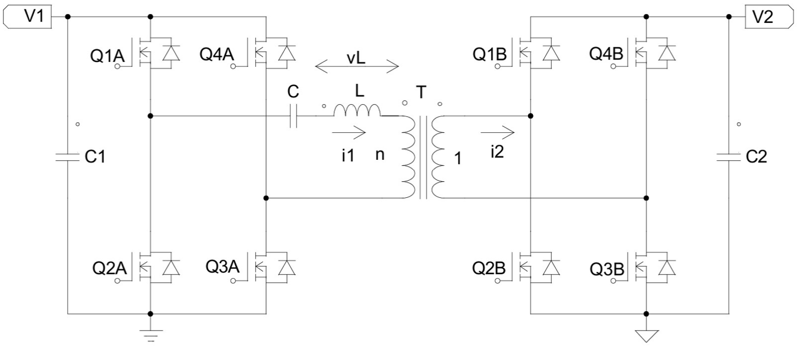

Figura 46. Convertidor DAB resonante LC serie.

Las últimas publicaciones centradas en la mejora de la eficiencia de este convertidor muestran alternativas que pueden no ser resonantes como el estudiado en [57] o resonantes [58]. Ambos trabajos tienen en común que combinan la modulación en frecuencia con otras modulaciones. Debido a esto, una investigación que se encuentra en curso por el autor de la tesis y que deriva de esta misma, consiste en aplicar el inductor variable controlado por corriente en la topología del DAB, en la Figura 47 se muestra el banco de pruebas utilizado para comprobar los resultados preliminares.

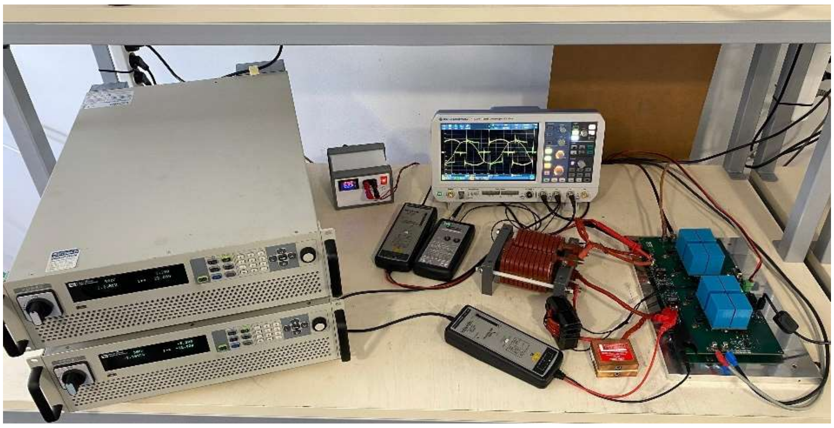

Figura 47. Banco de pruebas del DAB resonante con el inductor variable.

Los resultados experimentales obtenidos de la investigación muestran como el convertidor es capaz de trabajar a frecuencia fija con un amplio rango de potencias gracias a mover la frecuencia de resonancia con el uso del inductor variable controlado por corriente y a la modulación por desplazamiento de fase triple (TPS). Como se puede observar en la Figura 48 el convertidor trabaja minimizando las pérdidas de conmutación. Por una parte, el puente completo mostrado en color magenta no presenta pérdidas por las conmutaciones de los transistores debido a que las conmutaciones a ON son en ZVS y las conmutaciones a OFF son en ZCS, mientras que el puente representado en azul oscuro no tiene pérdidas de conmutación a ON por la conmutación en ZVS.

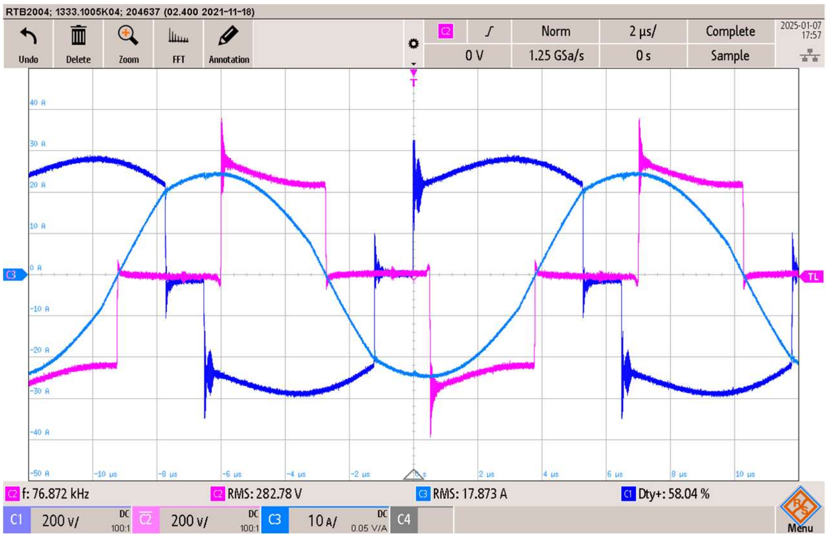

Figura 48. Oscilograma de la prueba experimental del DAB resonante con inductor variable. C1 (azul oscuro) representa la tensión de salida del puente A (200 V/div), C2 (magenta) representa la tensión de salida del puente B (200 V/div) y C3 (azul claro) muestra la corriente por el resonante (10 A/div). La base de tiempo es de 2 µs/div.

Por otro lado, nuevas ramas de investigación acerca del control de los elementos reactivos de los convertidores resonantes se están centrado en el efecto de la dependencia de la tensión continua con la capacidad de los condensadores cerámicos de materiales como el X7F. En [59] los autores aplican este efecto a un convertidor resonante LLC de 90 kHz y 5 W. La aplicación de este efecto en una aplicación para calentamiento por inducción podría ser un sustituto al MERS estudiado en este trabajo de tesis, el hecho de no tener que utilizar transistores MOSFET para limitar la influencia del condensador en el resonante y por tanto mover la frecuencia de resonancia, mejoraría la eficiencia del convertidor.

Referencias

[1]. Mohan, N.; Undeland, T.M.; Robbins, W.; P. *Power Electronics*; John Wiley & Sons, Inc.: Texas 2002. ISBN: 978-0-471-22693-2.

[2]. Dede, E.J.; Esteve, V.; Gonzalez, J.V.; Garcia, J.; Maset, E.; Ramirez, D. A 12 kW/250 kHz series resonant converter for induction heating. Transactions of the South African Institute of Electrical Engineers. Vol. 86, no. 1, pp. 45-48, March 1995.

[3]. Barreto, L.H.S.C; Coelho, E.A.A.; Farias, V.J.; de Oliveira, J. C.; de Freitas, L.C.; Joao Batista Vieira, J. A quasi-resonant quadratic boost converter using a single resonant network. IEEE Transactions on Industrial Electronics, vol. 52, no. 2, pp. 552-557, April 2005.

[4]. Vračar, D.Đ.; A Short Overview of Active-Clamped Resonant DC Link Inverter. 2020 International Symposium on Industrial Electronics and Applications (INDEL), Banja Luka, Bosnia and Herzegovina, 2020, pp. 1-6.

[5]. Lourdes, S.; Luk, P.C.K.; Jinupun, K. Switching strategy for integral cycle converter in a high frequency AC distributed power system. 2009 International Conference on Power Electronics and Drive Systems (PEDS), Taipei, Taiwan, 2009, pp. 1243-1248.

[6]. Esteve, V.; *Influencia de los componentes parásitos en el análisis y diseño de inversores resonantes paralelo para aplicaciones de calentamiento por inducción;* Tesis Doctoral. Universidad de Valencia; Valencia 2004.

[7]. Jordán, J.; *Estudio del Comportamiento de Generadores Serie MOSFET de Alta Potencia y Frecuencia en Condiciones de Cortocircuito;* Tesis Doctoral. Universidad de Valencia; Valencia 2003.

[8]. Esteve, V.; Jordán, J.; Dede, E.J.; Martinez, P.J.; Ferrara, K.J.; **Bellido, J.L.** Comparative analysis and improved design of LLC inverters for induction heating. IET Power Electron. 2023, 16, 1754–1764.

[9]. Esteve, V.; **Bellido, J.L.**; Jordán, J. Optimal Design of a Single-Phase Bidirectional Rectifier. *Energies* 2024, *17*, 1280.

[10]. Esteve, V.; **Bellido, J.L.**; Jordán, J. Efficiency Design of a Single-Phase Bidirectional Rectifier for Home Energy Management Systems. *Electronics* 2025, *14*, 15.

[11]. Esteve, V.; Jordán, J.; Dede, E.J.; **Bellido, J.L.** Enhanced asymmetrical modulation for half-bridge series resonant inverters in induction heating applications. IET Power Electron. 2023, 16, 2482–2491.

[12]. Esteve, V.; Jordan, J.; Sanchis, E.; Dede, E.J.; Maset, E.; Ejea, J.B.; Ferreres, A. Improving the reliability of series resonant inverters for induction heating applications. IEEE Trans. Ind. Electron. 2014, 61, 2564–2572.

[13]. Toshiba, «Power MOSFET Structure and Characteristics» [En línea]. Available: https://toshiba.semicon-storage.com/info/application_note_en_20180726_AKX00061.pdf?did=13413

[14]. Martinez, P.J.; *Estudio de la fiabilidad de los dispositivos HEMT de GaN;* Tesis Doctoral. Universidad de Valencia; Valencia 2021.

[15]. Infineon, «Wide Bandgap Semiconductors (SiC/GaN)» [En línea]. Available: https://www.infineon.com/cms/en/product/technology/wide-bandgap-semiconductors-sic-gan/

[16]. Wolfspeed, «C3M0021120K Data Sheet» [En línea]. Available: https://assets.wolfspeed.com/uploads/2024/01/Wolfspeed_C3M0021120K_data_sheet.pdf

[17]. TDK, «Ferrites and accessories SIFERRIT material N27» [En línea]. Available: https://www.tdk-electronics.tdk.com/download/540184/3a7f957d754f899aec42cd946598c5c4/pdf-n27.pdf

[18]. Medini, D.; Ben-Yaakov, S. A current-controlled variable-inductor for high frequency resonant power circuits. In Proceedings of the 1994 IEEE Applied Power Electronics Conference and Exposition—ASPEC'94, Orlando, FL, USA, 13–17 February 1994.

[19]. **Bellido, J.L.**; Esteve, V.; Jordán, J. Efficiency Optimization in Parallel LLC Resonant Inverters with Current-Controlled Variable-Inductor and Phase Shift for Induction Heating. Electronics 2024, 13, 2593.

[20]. Sun, N.; Chen, D.Y.; Lee, F.C.; Gradzki, P.M.; Knights, M.A. Forward Converter Regulator Using Controlled Transformer. IEEE Trans. Power Electron. 1996, 11, 356–364.

[21]. Suarez, C.; Bernal, D.; Martinez, W. Analysis and Validation of Variable Transformers. In Proceedings of the 2021 IEEE 30th International Symposium on Industrial Electronics (ISIE), Kyoto, Japan, 20–23 June 2021.

[22]. Bernal, D.; Tian, F.; Suarez, C.; Vivert, M.; Martinez, W. Linear Control Compensator for a Variable-Transformer in Wide-Voltage Power Converters. In Proceedings of the 2022 IEEE 31st International Symposium on Industrial Electronics (ISIE), Anchorage, AK, USA, 1–3 June 2022.

[23]. Suarez, C.; Gerardo, D.; Martinez, W.H. Magnetically Controlled Transformer With Variable Turns Ratio and Low Series Inductance: Analysis and Implementation towards Its Application in SMP. IEEE Trans. Power Electron. 2023, 38, 14360–14374.

[24]. Perdigão, M.S.; Alonso, J.M.; Vaquero, D.G.; Saraiva, E.S. Magnetically Controlled Electronic Ballasts with Isolated Output: The Variable Transformer Solution. IEEE Trans. Ind. Electron. 2011, 58, 4117–4129.

[25]. Pajni´ c, M.; Pejovi´ c, P.; Aleksi´ c, O. Design and Analysis of a Novel Coupled Inductor Structure with Variable Coupling Coefficient. IET Power Electron. 2018, 11, 961–967.

[26]. **Bellido, J.L.**; Esteve, V.; Jordán, J. Performance Enhancement in LC Series Resonant Inverters with Current-Controlled Variable-Transformer and Phase Shift for Induction Heating. Electronics 2024, 13, 2911.

[27]. **Bellido, J.L.**; Esteve, V.; Jordán, J. Reactive Elements Control in LC Series Resonant Inverters by Current-Controlled Variable-Transformer and Magnetic Energy Recovery Switch for Induction Heating. Electronics 2024, 13, 4666.

[28]. Zhang, Z. Coupled-Inductors Magnetic in Power Electronics. Ph.D. Thesis, California Institute of Technology, Pasadena, CA, USA, 7 October 1986.

[29]. Rim, C.T.; Mi, C. Coupled Coil Model. In Wireless Power Transfer for Electric Vehicles and Mobile Devices, 1st ed.; John Wiley & Sons, Ltd.: Hoboken, NJ, USA, 2017.

[30]. Isobe, Y.; Miyaji, T.; Kitahara; Fukutani, K.; Shimada, R. Soft-switching inverter for variable frequency induction heating using magnetic energy recovery switch (MERS). In Proceedings of the 13th European Conference on Power Electronics and Applications, Barcelona, Spain, 2009; pp. 1–10.

[31]. Isobe, Y.; Shimada, R. New power supply topologies enabling high performance induction heating by using MERS. In Proceedings of the IECON 2013—39th Annual Conference of the IEEE Industrial Electronics Society, Vienna, Austria, 10–13 November 2013; pp. 5046–5051.

[32]. de Jesus, F.D.; Watanabe, E.H.; de Souza, L.F.W.; Alves, J.E.R. SSR and Power Oscillation Damping Using Gate-Controlled Series Capacitors (GCSC). IEEE Trans. Power Deliv. 2007, 22, 1806–1812.

[33]. de Souza, L.; Watanabe, E.; Alves, J.; Pilotto, L. Thyristor and gate controlled series capacitors: Comparison of components rating. In Proceedings of the 2003 IEEE Power Engineering Society General Meeting (IEEE Cat. No.03CH37491), Toronto, ON, Canada, 13–17 July 2003; Volume 4, pp. 2542–2547.

[34]. Esteve, V.; **Bellido, J.L.**; Jordán, J. State of the Art and Future Trends in Monitoring for Industrial Induction Heating Applications. Electronics 2024, 13, 2591.

[35]. Ahmed, N. High frequency soft switching AC conversion circuit with dual mode PWM/PDM control strategy for high power IH applications. IEEE Trans. Ind. Electron. 2011, 58, 1440–1448.

[36]. Ramalingam, S.R.; Boopathi, C.S.; Ramasamy, S.; Ahsan, M.; Haider, J.; Shahjalal, M. A Single-Coil Multi-Tapped PDM-Based Induction Heating System for Domestic Applications. Electronics 2023, 12, 404.

[37]. Burdío, J.M.; Canales, F.; Barbosa, P.M.; Lee, F.C. A comparison study of fixed-frequency control strategies for ZVS dc/dc series resonant conveters. In Proceedings of the 2001 IEEE 32nd Annual Power Electronics Specialists Conference (IEEE Cat. No.01CH37230), Vancouver, BC, Canada, 17–21 June 2001; pp. 427–432.

[38]. Yang, X.; Sha, D. Automatic Current Limit Strategy for LLC DC-DC Converter for Overload Operation. EEE Trans. Power Electron. 2024, 39, 9917–9928.

[39]. Scirè, D.; Lullo, G.; Vitale, G. Non-Linear Inductor Models Comparison for Switched-Mode Power Supplies Applications. Electronics 2022, 11, 2472.

[40]. Scirè, D.; Lullo, G.; Vitale, G. Design and Modeling of an Interleaving Boost Converter with Quasi-Saturated Inductors for Electric Vehicles. In Proceedings of the 2020 AEIT International Conference of Electrical and Electronic Technologies for Automotive (AEIT AUTOMOTIVE), Turin, Italy, 18–20 November 2020; pp. 1–6.

[41]. Esteve, V.; Jordan, J.; Dede, E.J.; Sanchis-Kilders, E.; Martinez, P.J.; Maset, E.; Gilabert, D. Optimal LLC inverter design with SiC MOSFETs and phase shift control for induction heating applications. IEEE Trans. Ind. Electron. 2022, 69, 11100–11111.

[42]. Wilson, P.R. Modelling and Simulation of Magnetic Components in Electric Circuits. Ph.D. Thesis, Dept. Elect. Comput. Eng., Univ. Southampton, Southampton, UK, November 2001.

[43]. Rudnev, V.; Loveless, D.; Cook, R.; Black, M. Hand Book of Induction Heating; CRC Press: Boca Raton, FL, USA, 2017.

[44]. O'Reilly, J. Multivariable Control for Industrial Applications; Peter Peregrinus Ltd.: London, UK, 1987.

[45]. Boubaker, O.; Zhu, Q.; Mahmoud, M.S. New Trends in Observer-Based Control: A Practical Guide to Process and Engineering Applications; Academic Press: Cambridge, MA, USA, 2019.

[46]. Alonso, J.M.; Perdigão, M.S.; Vaquero, D.G.; Calleja, A.J.; Saraiva, E.S. Analysis, design, and experimentation on constant-frequency DC-DC resonant converters with magnetic control. IEEE Trans. Power Electron. 2012, 27, 1369–1382.

[47]. Grajales, L.; Sabaté, J.A.; Wang, K.R.; Tabisz, W.A.; Lee, F.C. Design of a 10 kW, 500 kHz Phase-Shift Controlled Series-Resonant Inverter for Induction Heating. In Proceedings of the IEEE Industry Applications Society Annual Meeting, Toronto, ON, Canada, 2–8 October 1993; Pp. 843–849.

[48]. Grajales, L.; Lee, F.C. Control System Design and Small-Signal Analysis of a Phase-Shift Controlled Series-Resonant Inverter for Induction Heating. In Proceedings of the IEEE Power Electronics Specialist Conference (PESC), Atlanta, GA, USA, 18–22 June 1995; pp. 450–456.

[49]. Dudrik, J.; Trip, N.-D. Soft-Switching PS-PWM DC–DC Converter for Full-Load Range Applications. IEEE Trans. Ind. Electron. 2010, 57, 2807–2814.

[50]. Yang,X.; Sha, D. Automatic Current Limit Strategy for LLC DC-DC Converter for Overload Operation. IEEE Trans. Power Electron. 2024, 39, 9917–9928.

[51]. Grajales, L.; Lee, F.C. Control System Design and Small-Signal Analysis of a Phase-Shift Controlled Series-Resonant Inverter for Induction Heating. In Proceedings of the IEEE Power Electronics Specialist Conference (PESC), Atlanta, GA, USA, 18–22 June 1995; pp. 450–456.

[52]. Zgraja, J. Dual-Frequency Induction Heating Generator with Adjustable Impedance Matching. IEEE Trans. Ind. Electron. 2019, 66, 8308–8317.

[53]. Frania, K.; Kierepka, K.; Kasprzak, M.; Zimoch, P. Single Three-Phase Inverter for Dual-Frequency Induction Heating. Energies 2024, 17, 2489.

[54]. Esteve, V.; Jordan, J.; Sanchis-Kilders, E.; Dede, E.J.; Maset, E.; Ejea, J.B.; Ferreres, A. Comparative Study of a Single Inverter Bridge for Dual-Frequency Induction Heating Using Si and SiC MOSFETs. IEEE Trans. Ind. Electron. 2015, 62, 1440–1450.

[55]. Lucia, O.; Maussion, P.; Dede, E.J.; Burdio, J.M. Induction heating technology and its applications: Past developments, current technology, and future challenges. IEEE Trans. Ind. Electron. 2014, 61, 2509–2520.

[56]. Esteve, V.; Jordan, J.; Sanchis, E.; Dede, E.J.; Maset, E.; Ejea, J.B.; Ferreres, A. Improving the reliability of series resonant inverters for induction heating applications. IEEE Trans. Ind. Electron. 2014, 61, 2564–2572.

[57]. Esteve, V.; **Bellido, J.L.**; Jordán, J.; Dede, E.J. Improving the Efficiency of an Isolated Bidirectional Dual Active Bridge DC–DC Converter Using Variable Frequency. Electronics 2024, 13, 294.

[58]. M. Yaqoob, K.; Loo, H.; Lai, Y. A Four-Degrees-of-Freedom Modulation Strategy for Dual-Active-Bridge Series-Resonant Converter Designed for Total Loss Minimization. IEEE Transactions on Power Electronics, vol. 34, no. 2, pp. 1065-1081, Feb. 2019.

[59]. Kolberg, I.; Shmilovitz, D.; Ben-Yaakov, S. Ceramic capacitor controlled resonant LLC converters. 2018 IEEE Applied Power Electronics Conference and Exposition (APEC), San Antonio, TX, USA, 2018, pp. 2162-2167

Anexos. Trabajos publicados

Artículo 1:

[19] **Bellido, J.L.**; Esteve, V.; Jordán, J. Efficiency Optimization in Parallel LLC Resonant Inverters with Current-Controlled Variable-Inductor and Phase Shift for Induction Heating. Electronics 2024, 13, 2593. https://doi.org/10.3390/electronics13132593

electronics

MDPI

Article

Efficiency Optimization in Parallel LLC Resonant Inverters with Current-Controlled Variable-Inductor and Phase Shift for Induction Heating

Juan L. Bellido [1,2,*], Vicente Esteve [1] and José Jordán [1]

[1] Department of Electronic Engineering, University of Valencia, Av. University s/n, 46100 Valencia, Spain; vicente.esteve-gomez@uv.es (V.E.); jose.jordan@uv.es (J.J.)
[2] R&D Department, SiCtech Induction, 46980 Paterna, Spain
* Correspondence: juanbe5@alumni.uv.es or jbellido@sictechinduction.com

Abstract: This paper presents a comprehensive analysis of a novel control approach to improve the efficiency of parallel LLC resonant inverters using a combination of a current controlled variable inductor (VI) and phase shift (PS). The proposed control aims to reduce the Root Mean Square (RMS) current, thereby reducing conduction and switching losses, and improving power transfer efficiency, while considering zero-voltage-switching (ZVS) operation, output power variations and load changes. Furthermore, a design methodology for the variable inductor is proposed, and design considerations relevant to this application are discussed. The effectiveness of the proposed approach is evaluated through mathematical modeling and experimental results. The mathematical modeling results show that the proposed approach, utilizing SiC MOSFETs, maintains a maximum efficiency of 98.5% for a 20 kW inverter over a wider range of output power, which is a significant improvement over existing approaches. The experimental results also confirm the effectiveness of the proposed control in improving the efficiency of parallel LLC resonant inverters.

Keywords: LLC inverters induction heating; current-controlled variable inductor; PS power control; silicon carbide (SiC) power MOSFETs

check for updates

Citation: Bellido, J.L.; Esteve, V.; Jordán, J. Efficiency Optimization in Parallel LLC Resonant Inverters with Current-Controlled Variable-Inductor and Phase Shift for Induction Heating. *Electronics* **2024**, *13*, 2593. https://doi.org/10.3390/electronics13132593

Academic Editors: Luis M. Fernández-Ramírez, Ahmed Abu-Siada, Jean-Christophe Crebier, Zhiwei Gao, Kai Fu and Eladio Durán Aranda

Received: 12 May 2024
Revised: 27 June 2024
Accepted: 30 June 2024
Published: 2 July 2024

1. Introduction

Induction heating systems, known as resonance transformation (R.T.), are extensively utilized in various industrial processes such as brazing, hardening, annealing, and other heat-treatment applications, due to their high efficiency, precise control, and rapid heating capability [1]. These systems usually employ resonant inverters, such as series resonant inverters or parallel resonant inverters, to convert DC energy into AC energy [2,3].

The traditional method of controlling the output current or power by varying the switching frequency has several disadvantages, such as a wide noise spectrum, complex filtering, and inefficient use of magnetic components [4–6]. Fixed-frequency or narrow-frequency-range control techniques, such as pulse density modulation (PDM) [7,8], PS [9,10], or the combination of the PS with frequency modulation (FM-PS) control [2,11,12], can address some of these issues. However, they cannot guarantee the soft-switching operation of the resonant converter for large load or output power variations. Therefore, the switching frequency must be increased to achieve ZVS operation, which results in poor performance across the entire power range [4,13]. Even with complex state-plane analysis, the use of a fixed frequency with phase shift in LLC resonant converters requires limitations on the output current in order not to lose smooth switching [14]. Other converter models use saturated or quasi-saturated inductors working in non-linear regions, which results in improved power density, but these techniques do not solve the problem of working with fixed frequencies or extending the range of ZVS operation [15,16]. To overcome these limitations, a new control technique has been proposed which combines a phase shift and variable inductor control (VI-PS).

In this article, the combined use of both techniques in a parallel LLC resonant inverter is thoroughly investigated to achieve enhanced performance. The combined effect of a phase shift and variable inductor control, as the series inductor, across the entire output power range is to reduce the output RMS current, while maintaining the efficiency of the inverter and achieving good performance under load changes, also ensuring ZVS operation. The impact of these control techniques on both conduction and switching losses are analyzed. The experimental results show that the combined use of PS and VI control can provide improved performance compared to traditional narrow or fixed-frequency control techniques.

The paper is organized as follows. Section 2 of the paper discusses the properties of the parallel LLC resonant circuit and provide analysis of the converter operation principle and soft switching commutation. An analysis of a current-control variable inductor and its application to an LLC resonant inverter is provided in Section 3. A design procedure is proposed in Section 4, for an LLC resonant inverter for induction heating, considering the variable series inductor, phase shift angle, and ZVS conditions. In addition, a power loss analysis and the control principles are also provided. In Section 5, the experimental results using an induction heating module are presented and compared with fixed-frequency and narrow-frequency-range phase shift.

2. Parallel LLC Resonant Converter Topology

The parallel LLC resonant circuit, an R.T. circuit consisting of two inductors and a capacitor, along with the equivalent load resistance, forms a series-parallel hybrid topology, as shown Figure 1. The circuit is configured with the heating inductor in parallel with the capacitor to compensate for the reactive energy, while the series inductor is connected in series with them [17].

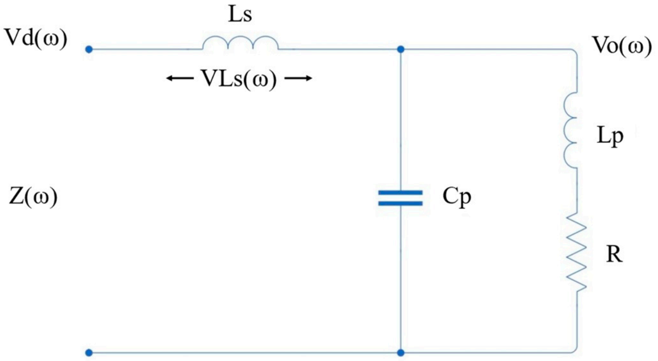

Figure 1. Parallel LLC resonant circuit.

This R.T. configuration allows the parallel LLC circuit to exhibit advantageous characteristics of both series and parallel resonant circuits [18]. When connected to a voltage-fed inverter, it simplifies the input section of the converter as in a series resonant inverter [19–21], where the input inductance in the resonant circuit acts as a current source. Additionally, through the output inductor near parallel resonance, the amplified current functions like a parallel resonant inverter [20,22,23], eliminating the need for current step-up transformers.

As the circuit is composed of three reactive elements, two resonant frequencies exist between them. The parallel resonant angular frequency defined between the parallel inductor and parallel capacitor is expressed as

$$\omega_{op} = \frac{1}{\sqrt{L_p C_p}} \quad (1)$$

while the series resonant angular frequency between the series inductor and the parallel capacitor is

$$\omega_o = \frac{1}{\sqrt{\left(\frac{L_p L_s}{L_p + L_s}\right) C_p}} \tag{2}$$

and their respective quality factors are

$$Q_p = \frac{L_p \omega_{op}}{R} \tag{3}$$

and

$$Q = \frac{L_p \omega_o}{R} \,. \tag{4}$$

The ratio between the inductances is given by

$$\beta = \frac{L_s}{L_p} \,. \tag{5}$$

The expression for the input impedance as a function of the angular frequency is as follows [24]:

$$Z(\omega) = L_p \omega_o (\beta + 1) \frac{\frac{1}{Q}\left(\frac{1}{\beta+1} - \left(\frac{\omega}{\omega_o}\right)^2\right) + j\frac{\omega}{\omega_o}\left(1 - \left(\frac{\omega}{\omega_o}\right)^2\right)}{\left(1 - \left(\frac{\omega}{\omega_{op}}\right)^2\right) + j\frac{\omega}{Q_p \omega_{op}}} \,. \tag{6}$$

By substituting (1) and (2) in (6), the following is obtained:

$$Z(\omega_o) = \frac{L_p \omega_o \beta^2}{Q - j(\beta + 1)} \,. \tag{7}$$

and from this argument, the phase between voltage and current in resonance is determined as

$$\alpha = \arg(Z(\omega_o)) = \arctan\left(\frac{\beta + 1}{Q}\right) . \tag{8}$$

The magnitude and phase of the input impedance of the circuit are shown as a function of angular frequency for a high Q, greater than 6, which is typical for LLC circuits [18,25], in Figure 2. In this figure, the effect of the two resonance frequencies of the circuit can be observed. The parallel resonance frequency is situated at the peak of impedance magnitude, whereas the series resonance frequency is located at the point of minimum impedance. Regarding the phase behavior concerning these points, it is observed that when operating above the series resonance frequency and below the parallel resonance frequency, the phase is positive. However, between these two resonance frequencies, the phase is negative. As the circuit must operate with ZVS, the operating point in the circuit should have a positive phase, and it will be close above the series resonance frequency. This is because the circuit impedance is minimized, thereby optimizing the reactive elements of the LLC resonant circuit when operating with a voltage-fed inverter.

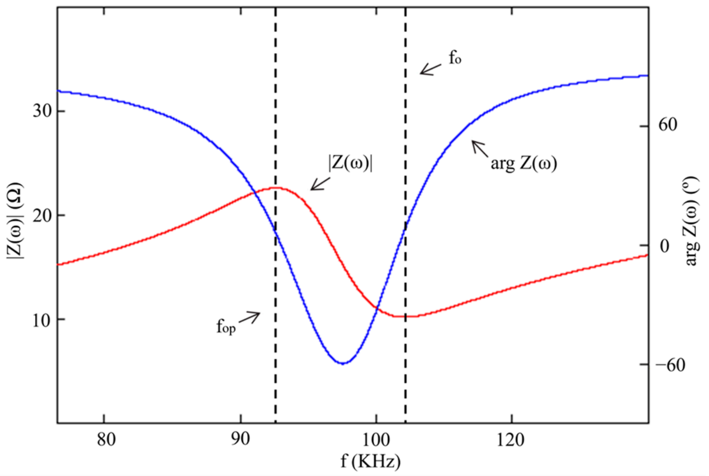

Figure 2. Simulation of magnitude of impedance (red) and phase of impedance (blue) of the parallel LLC resonant circuit.

3. Analysis and Application of Current-Controlled Variable Inductor in Parallel LLC Resonant Circuits

The design of a current-controlled variable inductor has its origins in prior studies [26]. Its operating principle involves saturating the outer part of the inductor core with direct current to vary the effective permeability. As shown in Figure 3, this inductor consists of two overlapped ferrite cores in the shape of an "E". The central branch has an air gap and is wound to form the main inductor (L_{ac}). On the other hand, the two side arms form the saturation control inductor (L_{bias}), which is wound in a series with opposite polarity to decouple L_{ac} from L_{bias}, nullifying the influence of magnetic flux from the L_{ac} winding and preventing induced voltages in L_{bias}.

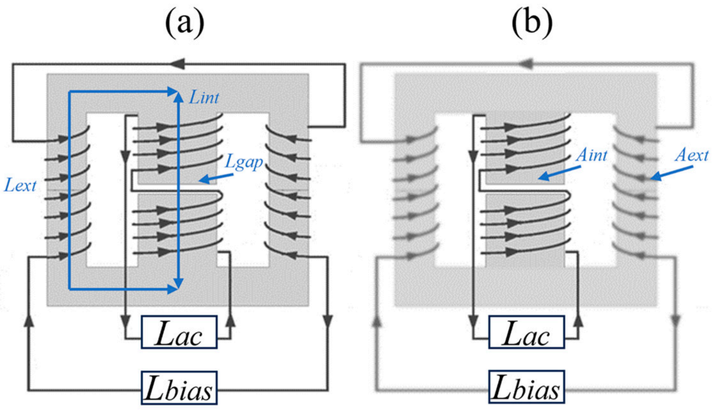

Figure 3. Structure of the current-controlled variable inductor: (**a**) corresponds to zero bias current and (**b**) corresponds to maximum bias current.

For the design of this inductance, using the formula for inductance based on its geometry for an inductor with a ferrite core, the value of the inductance of the central branch is expressed as follows:

$$L_{int} = \frac{\mu_0 \mu_i A_{int} (n_{int})^2}{l_{int}}. \tag{9}$$

where μ_i is the initial permeability of the core, μ_0 is the permeability of air, A_{int} is the effective cross-sectional area of the central branch, n_{int} is the number of turns in the L_{ac} winding, and lint is the length of the central branch.

The value of the inductance due to the air gap is expressed by

$$L_{gap} = \frac{\mu_0 \, A_{int}(n_{\,int})^2}{l_{gap}} \tag{10}$$

where l_{gap} is the length of the air gap.

The leakage inductance represents the magnetic flux that closes through the air and not through the central body of the ferrite,

$$L_{leakage} = \frac{\mu_0 \, 16 A_{int}(n_{\,int})^2}{l_{int}} \tag{11}$$

and the inductance of the two outer branches is given by

$$L_{ext} = \frac{2\mu_0 \widetilde{\mu} \, A_{ext}(n_{\,int})^2}{l_{ext}} \tag{12}$$

where $\widetilde{\mu}$ is the relative permeability without being subjected to DC bias.

Therefore, the following expression is used to calculate the maximum value of L_{ac}:

$$\frac{1}{L_{ac_{max}}} = \left(\frac{1}{L_{ext} + L_{leakage}} + \frac{1}{L_{int}} + \frac{1}{L_{gap}} \right). \tag{13}$$

Because $\widetilde{\mu}$ decreases when exposed to continuous magnetic field intensity (H_{bias}), to which the L_{bias} winding is subjected, the relationship between $L_{ac_{max}}$ and $L_{ac_{min}}$, with the second being the minimum value of L_{ac} for the minimum $\widetilde{\mu}$ due to the maximum H_{bias}, can be obtained using the following expression:

$$\frac{L_{ac_{max}}}{L_{ac_{min}}} = \left(\frac{\frac{2\mu_e \frac{l_{int}}{l_{ext}+l_{int}}}{\widetilde{\mu}+32} + \frac{\mu_e \frac{l_{int}}{l_{ext}+l_{int}}}{\mu_i} + 1}{\frac{2\mu_e \frac{l_{int}}{l_{ext}+l_{int}}}{\mu_i+32} + \frac{\mu_e \frac{l_{int}}{l_{ext}+l_{int}}}{\mu_i} + 1} \right) \tag{14}$$

where μ_{e} is the effective relative permeability of the core with a gap, from the elementary equation of an inductor:

$$L = \frac{\mu_0 \mu_e A_e n^2}{l}. \tag{15}$$

The effect of using this variable inductance in the L_s of the LLC circuit can be observed in Figure 4. If the operating point of the circuit is set near and above the series resonance frequency at the minimum impedance value, it can be observed how both the magnitude and phase of the impedance increase as the value of the series inductance is increased. This effect leads to two substantial advantages.

The first one is that for a fixed frequency, the inverter highest output current and power will occur at the point of minimum series inductance, where both the magnitude and phase of the impedance are minimized. However, when maximum output power is not required, the value of the series inductance can be increased to raise the magnitude of impedance, thereby reducing the output current.

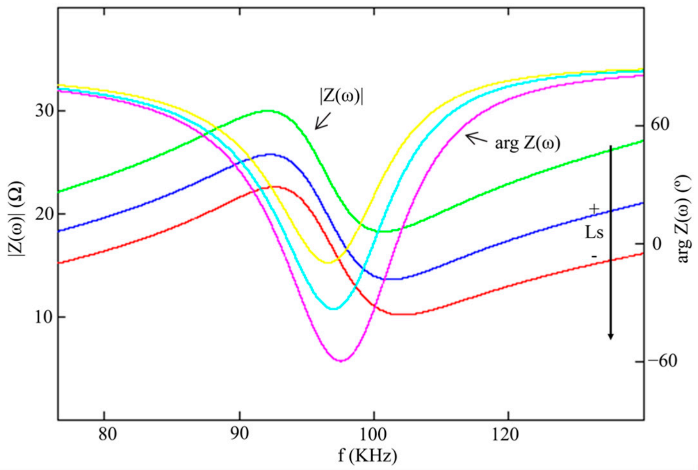

Figure 4. Simulated magnitude of impedance (green, blue, and red) and phase of impedance (yellow, light blue, and magenta) are arranged in descending order of the L_s values of the LLC parallel resonant circuit.

The second advantage is that by varying both magnitude and phase, a better response to load changes is achieved, enabling the maintenance of ZVS even when working very close to the series resonance frequency. Previous studies, when operating with a fixed frequency near the series resonance frequency [4,18,24,27], showed poor inverter performance in response to load changes, leading to the loss of ZVS. In another previous study [28], a good response to load changes was achieved when working near the parallel resonance frequency because the input impedance was higher. However, this resulted in poorer optimization of reactive elements.

Therefore, working with a variable inductance adds a degree of freedom to the circuit, which, when combined with PS, allows for the optimization of the output current of the inverter.

These observations will be demonstrated both theoretically and experimentally later in the article.

Given that a ferrite core will be used for the high frequency LLC series inductance, and considering that induction heating applications operate with high input and output voltages [18], it is necessary to obtain the voltage across the series inductance (V_{L_s}) in order to calculate the magnetic flux density and avoid operating near the saturation point of the L_{ac} core.

From the circuit analysis, the following equation is obtained:

$$V_{L_s}(\omega) = V_d(\omega) - V_o(\omega) \tag{16}$$

here, $V_d(\omega)$ and $V_o(\omega)$ represent the input and output voltages of the LLC circuit, respectively, with $V_d(\omega)$ lying within the range of

$$V_d(\omega) = \begin{cases} V_d, & 0 \leq \omega < \pi \\ -V_d, & \pi \leq \omega < 2\pi. \end{cases} \tag{17}$$

The voltage gain $H_v(\omega)$ is given by

$$H_v(\omega) = \frac{V_o(\omega)}{V_d(\omega)} = \frac{Z(\omega) - jL_s\omega}{Z(\omega)} \tag{18}$$

and the phase difference between the voltages $V_d(\omega)$ and $V_o(\omega)$ is obtained from the argument

$$\phi = \arg(H_v(\omega)). \tag{19}$$

Hence, through the integration of (16) and the subsequent solution of the equation, the expression for the voltage across the series inductor is formulated as follows:

$$V_{L_s}(\omega) = \begin{cases} V_d\left(\frac{\omega}{2} + ncos(\omega - \phi)\right), & 0 \le \omega < \pi \\ -V_d\left(-\frac{\omega}{2} - ncos(\omega - \phi)\right), & \pi \le \omega < 2\pi \end{cases} \tag{20}$$

where n represents the voltage ratio

$$n = \frac{V_p}{V_d} \tag{21}$$

for sufficiently large values of the quality factor Q_p, the value of $V_o(\omega)$ is sinusoidal of the peak output voltage value V_p [24],

$$V_o(\omega) = V_p sin(\omega). \tag{22}$$

Ergo, the maximum value of the series inductor voltage is expressed as

$$V_{L_s} = V_d\left(\frac{\pi}{2} + \frac{V_p}{V_d} cos(\pi - \phi)\right). \tag{23}$$

And the expression of the magnetic flux can be expressed as

$$B_{pk} = \frac{\sqrt{3}V_{L_s}}{8n_{int}A_e f}\ . \tag{24}$$

where

A_e is the effective area (m^2);

f is the applied frequency (Hz).

As mentioned earlier, the operating point where the output power is maximized is when the value of the series inductance is minimized, thus saturating the outer branches of the inductor. At this point, the inductor voltage is at its highest, and therefore, the maximum flux density that the core can withstand is obtained under this assumption.

Considering the relationship $B = \mu H$ and taking into account that the relative permeability of the core will change with exposure to H_{bias} to which the core will be subjected, the relationship between the maximum magnetic flux and the relative permeability for a constant magnetic field (H) is obtained [29].

4. LLC Resonant Inverter Design

4.1. Design Procedure

In the design procedures of the LLC inverter, the inductance value of the heating inductor (L_p) is typically provided from the geometric design parameters [30,31]. And the required power (P_o), frequency, and quality factor is obtained from the heating time, penetration depth into the workpiece, and thermal treatment [32,33]. With these, the capacitance of the capacitor is adjusted to available values, considering its maximum voltage V_p, using

$$C_p = \frac{2Q_p P_o}{\omega {V_p}^2}. \tag{25}$$

With the DC input voltage (V_d) of the inverter, the minimum value of the series inductance is calculated as

$$L_{S_{min}} = L_{ac_{min}} = \frac{2{V_d}^2}{\pi P_o \omega}. \tag{26}$$

After obtaining the series inductor value, the switching frequency (ω_{sw}) is adjusted to operate with a small phase angle by

$$\alpha = \arctan\left(\frac{2Q_p\omega_{sw}}{\omega_o} - \sqrt{4{Q_p}^2}\right) \tag{27}$$

then, the maximum voltage across the capacitor is recalculated using (25) and also the minimum series inductance (26).

The output current is obtained from

$$Irms = \frac{V_d\sqrt{8+(\pi n)^2+2\pi n(2\cos(\gamma))}}{\pi L_s \omega_{sw}} \tag{28}$$

where the voltage phase γ represents the inverter commutation phase relative to the phase of the output voltage [24],

$$\gamma = \pi - arc\sin\left(\frac{1}{n}\right). \tag{29}$$

At this point a ferritic material is selected and the most restrictive value of the flux density is obtained. To do this, the core-loss curves at the operating frequency are compared with the obtained value of B = μH using the maximum permeability variation obtained from the relative permeability variation curves under DC bias.

Applying the effective area relationship for maximum flux density (24) to the winding area yields the expression for the area product as follows:

$$A_p = A_e A_w = \frac{\sqrt{3}V_{L_s} Irms}{8B_{pk} f_{sw} JK} \tag{30}$$

where

A_e is the effective area of the core given by the manufacturer;

J represents current density (A/m^2), and in this case, when working with high-output currents from the inverter and aiming to minimize losses due to current carried in L_{bias}, only L_{ac} is considered for the design since the L_{bias} winding will be negligible;

K is the fill factor, which will be assumed to have a value between 0.5 and 0.9.

Using the obtained value for the area product, a core size is selected to maintain a higher ratio, and the number of turns for L_{ac} is calculated through

$$n_{int} = \frac{\sqrt{3}V_{L_s}}{8A_e f_{sw} B_{pk}}. \tag{31}$$

With the number of turns and the characteristics of the selected core, using the equation (13), $L_{ac_{max}}$ is calculated, and with the previous value of $L_{ac_{min}}$, the relationship between inductances is determined to obtain the necessary $\widetilde{\mu}$ from Equation (14). With this value and the curve on the datasheet regarding the relative permeability subjected to DC bias, the value of H_{bias} is determined to achieve the value of $L_{ac_{min}}$. If the $L_{ac_{min}}$ value is not reached, iteration with a different ferritic material is performed. In the event of obtaining a value within the range, optimization is carried out to reduce the maximum DC current value (I_{bias}) of L_{bias} through the relationship given by

$$I_{bias} 2n_{ext} = H_{bias} 2l_{ext} \tag{32}$$

where

n_{ext} represents the number of turns of an external branch;

l_{ext} is the length of the external branch from center to center of the core (m).

Table 1 presents the initial requirements for an annealing induction heating application [32], and also the results of applying the design procedure discussed earlier, where a ferrite core of N27 material with reference E 70/33/32 from TDK Electronics was ultimately selected.

Table 1. Initial requirements and results of the design.

Magnitude	**Symb.**	**Eq.**	**Value**	**Unit**
Output power	P_o	(36)	20	kW
Quality factor	Q_p	(3)	10	
Switching frequency	f_{sw}	(27)	157	kHz
DC input voltage	V_d	(17)	500	V
Parallel inductor	L_p	(1)	2	µH
Parallel capacitor	C_p	(25)	0.66	µF
Minimun series inductor	$L_{s_{min}}$ $L_{ac_{min}}$	(26)	8	µH
Maximun series inductor	$L_{s_{max}}$ $L_{ac_{max}}$	(13)	14.5	µH

The PS control technique involves shifting the switching phases of the two diagonals of the inverter with a phase angle (φ) ranging from 0 to π. Consequently, this modifies the voltage applied to the LLC resonant circuit, thereby affecting the output current and power of the inverter. Hence, by introducing this factor, the relationship between the input and output voltages of the circuit is now expressed as

$$n(\varphi) = n\ cos\left(\frac{\varphi}{2}\right) \tag{33}$$

and consequently, the phase between the output voltage of the inverter and the output voltage of the resonant circuit is obtained from

$$\gamma(\varphi) = \left| \begin{array}{ll} \pi - arc\sin\left(\frac{1}{n(\varphi)}\right) & \text{if} \quad n(\varphi) > 1 \\ arc\cos\left(\frac{\varphi-\pi}{2n(\varphi)}\right) - \varphi & \text{if} \quad n(\varphi) \leq 1 \end{array} \right. \tag{34}$$

where it has been considered that γ is dependent on φ to maintain soft switching [24] through the following inequality:

$$\gamma(\varphi) \geq \arccos\left(\frac{\varphi - \pi}{2n(\varphi)}\right) - \varphi. \tag{35}$$

For controlling the output power of the inverter, it is considered that by combining the phase shift angle through PS control and the ability to vary the series inductance of the resonant circuit, power can be optimized by adjusting both the voltage applied to the resonant circuit and its impedance.

The equation for output power is expressed as a function of these two variables as follows:

$$P_o(\varphi, L_s) = \frac{{V_d}^2 n(\varphi)(\sin(\gamma(\varphi) + \varphi) + \sin(\gamma(\varphi)))}{L_s \omega_{sw}} \tag{36}$$

and the same operation is performed with the equation for the RMS value of the output current; thus,

$$\frac{I_{RMS}(\varphi, L_s) = \frac{V_d}{\pi L_s \omega_{sw}}}{\sqrt{4\cos(\varphi) + (\pi n(\varphi))^2 + 2\pi n(\varphi)(\cos(\gamma(\varphi) + \varphi) + \cos(\gamma(\varphi))) + 4}.} \tag{37}$$

A system of two equations and two variables is obtained. This system is used to find the optimal operating point for the inverter, ensuring that the output current remains minimized across the entire power range, thus reducing conduction, and switching losses in the transistors.

4.2. Losses Analysis

To verify the advantages of this optimization, the losses of the transistors of the inverter are mathematically analyzed to obtain the efficiency across the entire operating range [19], considering the right commutation to improve the power distribution of the transistors [34,35]. The losses due to the conduction current in each channel of the transistors are given by

$$P_{cd}(\varphi, L_s) = \left(\frac{Irms(\varphi, L_s)}{\sqrt{2}}\right)^2 R_{DS_{on}} \tag{38}$$

where $R_{DS_{on}}$ is the ON-state MOSFET channel resistance.

For switching energy losses, only the turn-OFF switching is considered, as the turn-ON switching will be negligible when operating in ZVS throughout the operating range. To calculate it, the polynomial equation of the turn-OFF switching loss curves from the manufacturer is obtained for the drain voltage equal to V_d and the gate resistance used. It is expressed as follows:

$$E_{off}(\varphi, L_s) = \mathrm{a} I_c(\varphi, L_s)^2 + b I_c(\varphi, L_s) + c \tag{39}$$

where I_c is the switching current, and for the upper transistors, Q1 and Q4, it is derived from the following function:

$$I_{C_{Q1}}(\varphi, L_s) = \frac{V_d}{L_s \omega_{sw}}\left(n(\varphi)\cos(\gamma) + \frac{\pi - \varphi}{2}\right) \tag{40}$$

while the amplitude of the switching current for the lower transistors, Q2 and Q3, is given by

$$I_{C_{Q3}}(\varphi, L_s) = \frac{V_d}{L_s \omega_{sw}}\left(n(\varphi)\cos(\gamma + \varphi) + \frac{\pi - \varphi}{2}\right). \tag{41}$$

Therefore, the power losses for each transistor are obtained from

$$P_{sw}(\varphi, L_s) = E_{off}(\varphi, L_s)\frac{\omega_{sw}}{2\pi}. \tag{42}$$

The losses due to the transistor gate depend on the total gate charge Q_G and the gate-to-source voltage V_G, related through the following expression:

$$P_{gate} = Q_G V_G \frac{\omega_{sw}}{2\pi}. \tag{43}$$

On the other hand, the inductor core losses are due to the magnetic flux density, and the influence of the DC bias is negligible [26,36]; therefore, they can be obtained using the following equation:

$$P_{core}(\varphi, L_s) = P_v V_e \tag{44}$$

where P_v is the core-loss density of the inductor given by the manufacturer for the operating frequency and magnetic flux density, and V_e is its volume.

As a final consideration, for the copper losses P_{wire} of the inductor, it is necessary to know the effective resistance of the winding R_{copper}, taking into account the conductivity, the total length, and the skin effect using

$$P_{wire}(\varphi, L_s) = {I_{RMS}}^2 R_{copper}. \tag{45}$$

To conclude, the total losses are determined by the following equation:

$$\begin{aligned} P_{tot}(\varphi, L_s) = {} & 4P_{cd}(\varphi, L_s) + 2\Big(P_{sw_{Q1}}(\varphi, L_s) + P_{sw_{Q3}}(\varphi, L_s)\Big) + 4P_{gate} \\ & + P_{core}(\varphi, L_s) + P_{wire}(\varphi, L_s) \end{aligned} \tag{46}$$

meanwhile, the efficiency is given by

$$\eta(\varphi, L_s) = \frac{P_o(\varphi, L_s)}{P_o(\varphi, L_s) + P_{tot}(\varphi, L_s)}. \tag{47}$$

For the losses analysis, the SiC MOSFET G320MT12K was used as the transistor for each of the inverter switches. Table 2 presents the characteristics obtained from the datasheet for the efficiency analysis of the inverter.

Table 2. Transistor characteristics.

Magnitude	Symb.	Eq.	Value	Unit
On resistance	$R_{DS_{on}}$	(38)	17	mΩ
Turn-OFF losses	a	(39)	0.0268	μJ/A^2
	b		0.2679	μJ/A
	c		18.929	μJ
Gate charge	Q_G	(43)	180	nC

Considering (36), Figure 5 represents the entire possible operating range, for both the phase shift and series inductance variation, expressed as a function of the inverter output power. In the figure, there is a red dotted curve that results from optimizing the output current of the inverter. Therefore, this is the optimal operating point for control, where the losses in the inverter will be minimized. Following the path of the curve, it can be observed that at high-output powers, the increase in series inductance value is prioritized over increasing the phase shift. This is because reducing the output current is achieved by increasing the input circuit impedance and, when switched with a small phase shift, for the same output current, the switching current is lower. However, when a lower output power is demanded, working with a higher series inductance value, which implies a greater input impedance, this results in applying a lower voltage through a larger phase shift. This enables switching with smaller angles and counteracts the effect of the increased phase between voltage and output current due to the elevated series inductance value.

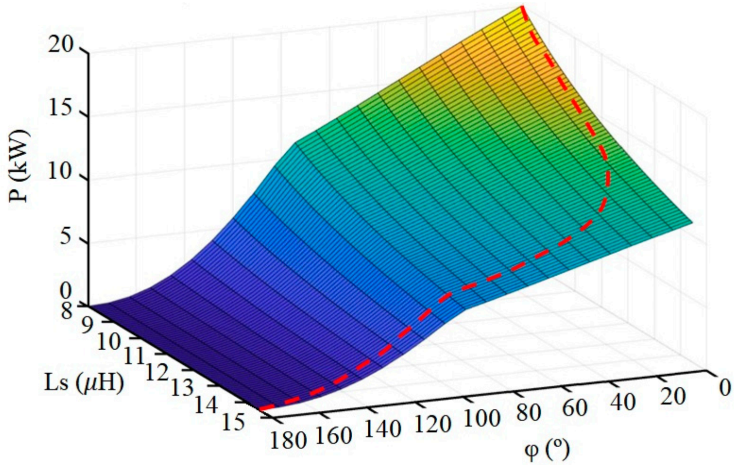

Figure 5. Phase shift and variable inductor as a function of the output power. The red dotted curve corresponds to the optimal control strategy.

To illustrate the difference in efficiency when operating across the entire power range using only PS control, as opposed to including variable inductance VI-PS, the efficiency and output current of both approaches have been compared as a function of power in Figure 6. The starting point for both controls is the same and corresponds to the maximum power value because, in both controls, at that point, the phase shift is minimized, and in the control with the variable inductor, the inductance is set to the minimum value, which is the same value maintained by PS control across its entire power range. As seen in the figure, the improvement in efficiency occurs as the inverter output power decreases because the output RMS current is reduced. This allows for maintaining a performance above 98.5% across the entire operating range and even reaching 99% when the output current is significantly reduced.

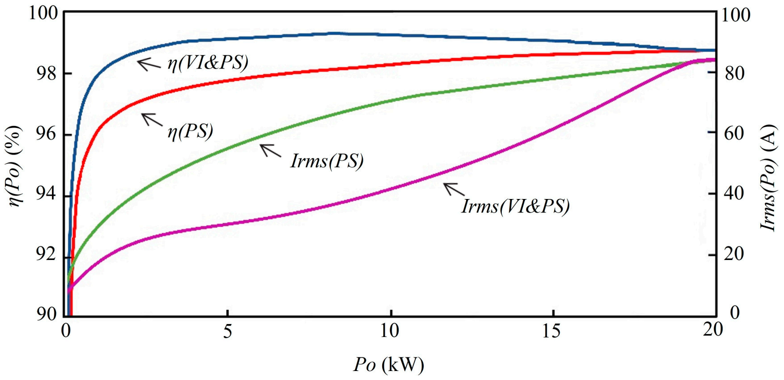

Figure 6. Evolution of the efficiency and output current of the inverter as a function of the output power.

Table 3 shows the breakdown of the losses for the optimization of the VI-PS control compared to the PS control operating at 12 kW.

Table 3. Losses results for 12 kW operation power.

Magnitude	Symb.	Eq.	PS	VI&PS	Unit
Conduction losses	P_{cd}	(38)	45.61	18.478	W
Switching losses	$P_{sw_{Q1}}$	(42)	3.465	7.783	W
Switching losses	$P_{sw_{Q3}}$		3.238	6.075	W
Gate losses	P_{gate}	(43)	0.508	0.508	W
Inductor core losses	P_{core}	(44)	3.57	6.12	W
Inductor wire losses	P_{wire}	(45)	15.499	6.279	W
Total losses	P_{tot}	(46)	216.952	116.065	W

4.3. Control Principles

The simplified VI-PS control scheme is depicted in Figure 7. Due to its multivariable nature, a Multiple Inputs Multiple Outputs (MIMO) system is employed, which is nonlinear and coupled. It is solved using a Proportional Integral Differential (PID) control and a decoupled diagonalization network [37,38]. This configuration enables the manipulation of one variable to affect the other and vice versa, generating a control loop that iterates between them. The system inputs include the input power of the inverter compared with the selected reference, and the phase angle α between the output voltage and current of the inverter, which is fixed at 15°, as defined in Equation (27). Consequently, the output variables are the phase angle φ of the phase shift control (PS) and the direct current (Ibias) of the L_{bias} winding.

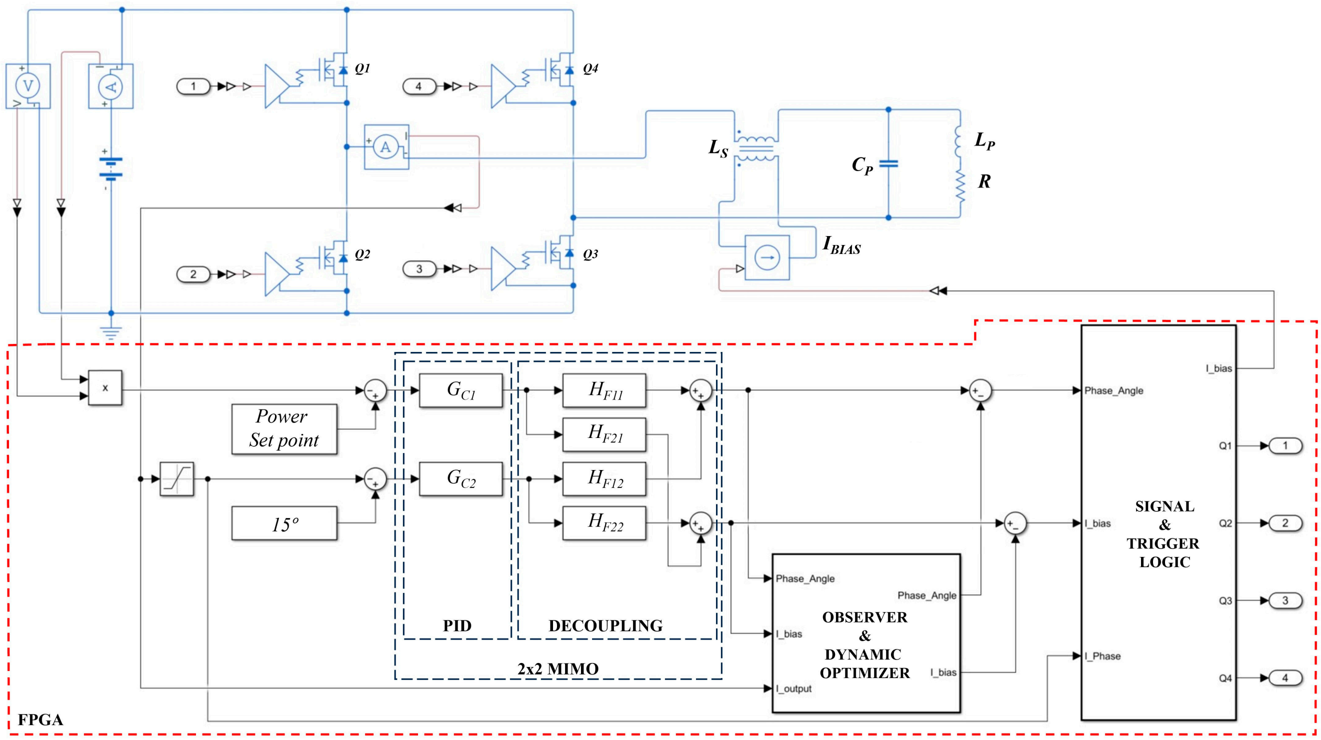

Figure 7. Schematic of the proposed system, detailing the inverter topology, the resonant load LLC with the variable inductor, and the control diagram.

Furthermore, a digital observer with a dynamic optimizer is employed to reduce the RMS value of the inverter output current [39]. In this block, by measuring the inverter output current and comparing it with the values of the phase shift angle and I_{bias}, interventions are made in the outputs to optimize both values. This ensures the inverter operates within the optimal operating range, as represented by the red dashed line in Figure 5. The signal conditioning and triggering logic block, besides generating the triggering signals of the transistors with the corresponding dead times based on the phase shift angle value received from the system, compares the zero-crossings of the current in each cycle to ensure ZVS during switching. If, during the heating process, the angle α shifts significantly, approaching the capacitive region due to changes in the inductance of L_p, modified due to changes in permeability, electrical conductivity of the material, or due to a load jump caused by coupling and decoupling the piece in the inductor, the control system directly decreases the I_{bias} current to increase the value of L_s. This adjustment maintains soft switching, preventing over-voltages or over-currents at the inverter output. Although the variable inductor has been designed to work far from the saturation limits, in case where the inductor becomes saturated, the angle α would be reduced, as seen in Figure 4; this will also be detected in this part of the control, decreasing the bias current to avoid saturation.

5. Experimental Results with Discussions

To conduct the experimental tests discussed in this section, the variable inductance design was first evaluated. The result is shown in Figure 8, which shows the calculated and experimentally measured value of the inductance as a function of the bias current.

As can be seen in Figure 8, there is a dispersion between the calculated value and the experimentally measured value. This deviation is mainly due to the range of dispersion of the initial permeability provided by the manufacturers and its dependence on temperature. Nevertheless, it can be seen that the mathematical model well describes the behavior of the variable detector as a function of the bias current.

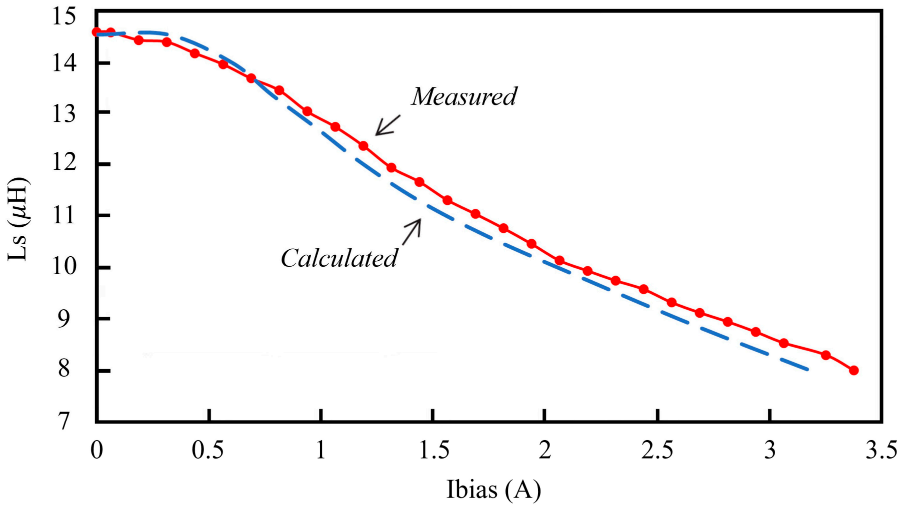

Figure 8. Calculated and measured behavior of the variable inductor due to bias current.

A 20 kW induction heating inverter module was used to test the complete design. This module includes FPGA-based control, sigma–delta modulator sensing stages, isolated power sources, a controllable current source based on the Howland current pump with an OPA548 as a high-current operational amplifier, trigger drivers, transistors, and a water cooler heatsink. The inverter is powered by a 500 VDC supply.

The test bench that was used is shown in Figure 9, and it has been assembled with the design components from Section 4. Each number corresponds to the following:

(1) Induction heating inverter with four SiC G3R20MT12K;
(2) 300 MHz bandwidth DSO;
(3) Differential voltage probe and Rogowski current probe;
(4) Hall effect probe for DC bias current;
(5) Controllable series inductor (L_s);
(6) Parallel capacitor (C_p);
(7) Parallel inductor (L_p);
(8) Water-cooled load.

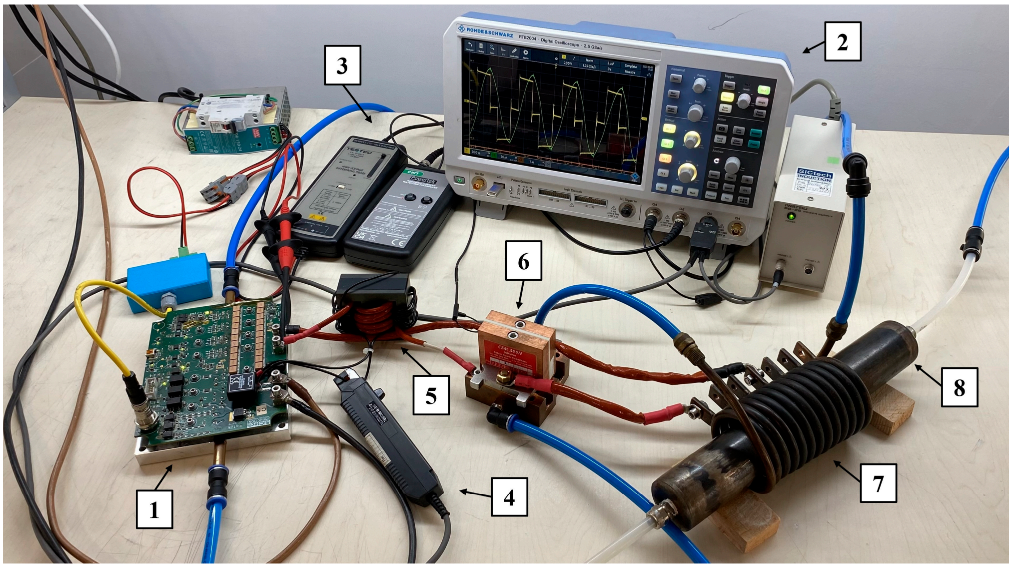

Figure 9. Inverter with LLC resonant load test bench. The numbered labels describe the components on the bottom.

To validate the design, the theoretical values obtained from the equations were compared with the measurements made on the inverter at two power levels. The result is shown in Table 4, where a small dispersion is observed due to the modeling method used and the existence of parasitic elements and losses of other elements are not taken into account in the calculation, such as conductors, connections, temperature dependence components, and the error of the measurement system, voltage, and current sensors.

Table 4. Comparison of theoretical and measured results.

Magnitude	**Symb.**	**12 kW**		**20 kW**		**Unit**
		Theor.	**Meas.**	**Theor.**	**Meas.**	
Phase angle	α	15	15.1	15	14.8	°
Voltage phase	γ	52.4	51.8	39.4	40.7	°
Output current	I_{RMS}	46.6	49.5	83.5	85.1	A
Upper transistors current	$I_{C_{Q1}}$	39.2	40	55.1	55.6	A
Lower transistors current	$I_{C_{Q3}}$	38.6	38.3	54.3	53.7	A

Figure 10 displays oscillograms captured by the DSO for the inverter operating at 60% power with three different control techniques and their response to load changes by rapidly extracting the load from the inductor. The first control strategy is fixed frequency, using the PS control. The second control strategy involves a narrow frequency range, combining frequency modulation with a phase shift (FM-PS). The third strategy, analyzed in this article, is fixed frequency VI-PS control. In all three cases, the LLC resonant circuit remains the same, with the minimum series inductance value. In terms of performance with the same power setpoint, as depicted in the figure, the PS control has been configured at a higher frequency than the resonant design. This adjustment is necessary to operate above the series resonance frequency, ensuring an adequate operating range for the commutation phase α and enabling soft switching [13]. Consequently, for the same power level, the inverter output current is higher with PS control, reaching 64 $\mathrm{A_{RMS}}$, compared to the other control techniques. In the case of the FM-PS control, the output current of 56 $\mathrm{A_{RMS}}$ is slightly higher than that of the VI-PS control. Despite being able to maintain the same phase angle α of 15°, the frequency is higher due to regulation [12,19], and it commutates with a wider phase shift φ, leading to increased switching losses due to the higher current amplitude during OFF switching compared to the VI-PS control. On the other hand, the VI-PS control maintains a closed-phase shift by desaturating the series inductance, allowing for a lower output current of 50 $\mathrm{A_{RMS}}$, and switching with less current due to a narrower φ angle, while maintaining the 15° phase angle α, and a lower frequency closer to the series resonance frequency.

As observed in the load changes behavior, the PS control, despite operating at a higher frequency with increased circuit input impedance and phase angle α, fails to maintain ZVS behavior and control over-current despite widening the phase shift angle. Meanwhile, FM-PS control manages to maintain ZVS behavior but at the cost of a sudden frequency variation of 8 kHz, a complex issue to handle in terms of harmonic filtering. Furthermore, it is observed that the current increases slightly despite the control correction, increasing the angle α width. This effect could be mitigated by allowing the control to increase the frequency even further. Lastly, as shown in the VI-PS control oscillogram, soft switching is preserved, and the over-current caused by the load jump is controlled. This is achieved by rapidly desaturating the external branches of inductor L_s, causing the impedance difference from the load jump to attenuate due to the increased impedance resulting from a higher series inductance in the LLC resonant circuit. It is observed that the change in impedance by increasing L_s is so effective that the control has to decrease the angle to maintain the current level, in contrast to the other two control techniques.

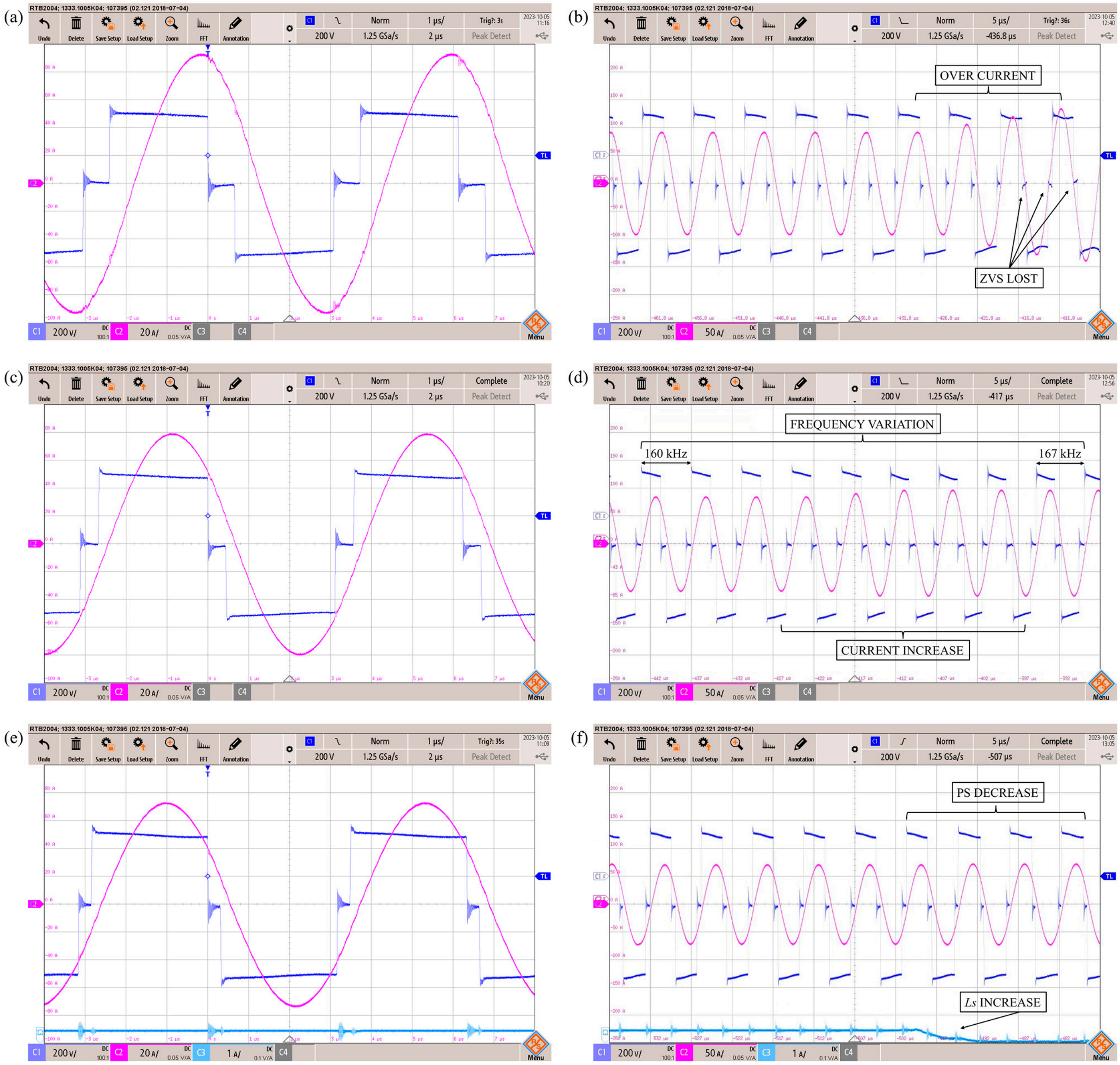

Figure 10. Oscillograms of experimental tests of the LLC inverter with different control strategies: (**a**,**b**) with PS, (**c**,**d**) with FM-PS, and (**e**,**f**) with VI-PS. Figures (**a**,**c**,**e**) correspond to operation at 60% power, and (**b**,**d**,**f**) show the response to a load change at that power level. C1 (dark blue) represents the output voltage (200 V/div), C2 (magenta) shows the output current (20 A/div) in figures (**a**,**c**,**e**) and (50 A/div) in (**b**,**d**,**f**). C3 (light blue) shows the DC bias current (1 A/div) of Ls in (**e**,**f**). The time base is 1 µs/div in (**a**,**c**,**e**) and 5 µs/div in (**b**,**d**,**f**).

Finally, to conclude the comparison between the three control types and validate the design discussed in the article, the inverter efficiency has been measured across the entire power range by the difference of the input power measured directly at the input DC voltage supply and the output power measured by the DSO measurement of the principal value of the instantaneous multiplication of the output voltage and current of the inverter bridge [24], starting from the same frequency and phase shift angle, with the minimum series inductance. As shown in Figure 11, at the starting point, all three controls achieve the same performance. However, as the power decreases, the VI-PS control gradually increases its efficiency, as explained earlier in Section 4. In this figure, in comparison to the theoretical calculation in Figure 6, the measurement for the FM-PS control has been added. Despite maintaining similar performance to the variable inductance control, FM-PS has the disadvantage of losing reactive element optimization. This occurs as the frequency increases with a lower power demand, leading to poorer efficiency and a more complex harmonic filtering. It is crucial to note that in the PS control, in order to handle load jumps or changes in the permeability of the heating inductor, the frequency should be increased, resulting in lower efficiency. As observed in the figure, the measurements closely align with the theoretically calculated values, despite the dispersion in real components and the losses not being accounted for in the theoretical calculation.

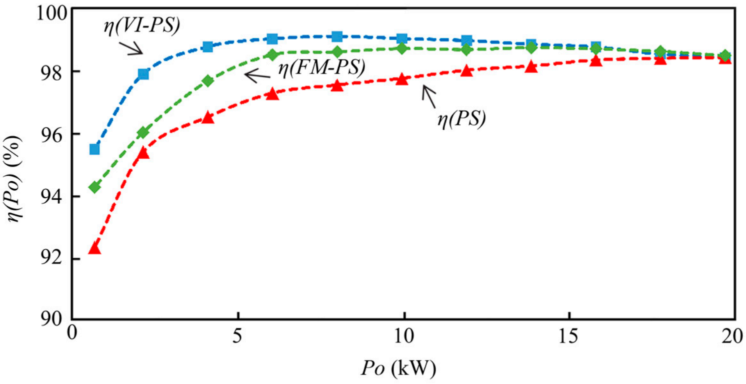

Figure 11. Results of experimental measurements of the inverter efficiency across the entire power range.

6. Conclusions

This article explores the combined effect of variable inductance control with phase shift VI-PS. It analyzes and proposes a design for the variable inductance and the LLC resonant circuit for a high-frequency application in induction heating annealing. The study provides an analysis of the optimal control strategy, reducing the output current, maximizing efficiency across the entire power range, and maintaining ZVS operation even with significant load changes.

The proposed control technique has been implemented in a 20 kW full-bridge inverter using SiC MOSFETs with an LLC resonant load. The experimental results have been validated against theoretical predictions and compared experimentally with two traditional phase shift control techniques: fixed-frequency and narrow-frequency-range control. The comparison was conducted at the same power level, comparing conduction losses in the MOSFET channels and losses due to OFF switching. The behavior for over-currents and soft switching during load jumps was also compared. Both tests were conducted using the same LLC resonant circuit.

Ultimately, it has been demonstrated that at different output power levels, the VI-PS control technique achieves superior efficiencies across the entire operating range compared to traditional control methods. It can maintain efficiency above 98.5% and operate with load jumps while keeping ZVS functionality.

Therefore, this article introduces a novel VI-PS control technique which, by using a variable inductor and a phase shift, achieves higher efficiency over the whole operating range. This is because it allows operation at a fixed frequency close to the series resonance frequency, setting a low-switching angle and reducing the output current value. It also allows operation over a wide range of loads while maintaining ZVS switching. Consequently, this work opens the way for future research on the fixed-frequency control of inverters for induction heating by controlling the reactive elements, whether in two-element, three-element, or multi-element resonant tanks, thus enabling improved efficiency and load range.

Author Contributions: Conceptualization, J.L.B.; Methodology, J.L.B.; Software, J.L.B. and J.J.; Validation, J.L.B. and V.E.; Investigation, J.L.B.; Resources, V.E.; Data curation, V.E. and J.J.; Writing—

original draft, J.L.B.; Supervision, J.L.B. All authors have read and agreed to the published version of the manuscript.

Funding: This research received no external funding.

Data Availability Statement: Data are contained within the article.

Conflicts of Interest: Author Juan L. Bellido was employed by the company SiCtech Induction. The remaining authors declare that the research was conducted in the absence of any commercial or financial relationships that could be construed as a potential conflict of interest.

References

1. Lucia, O.; Maussion, P.; Dede, E.J.; Burdio, J.M. Induction heating technology and its applications: Past developments, current technology, and future challenges. *IEEE Trans. Ind. Electron.* **2014**, *61*, 2509–2520. [CrossRef]
2. Grajales, L.; Sabaté, J.A.; Wang, K.R.; Tabisz, W.A.; Lee, F.C. Design of a 10 kW, 500 kHz phase-shift controlled series-resonant inverter for induction heating. In Proceedings of the Conference Record of the 1993 IEEE Industry Applications Conference Twenty-Eighth IAS Annual Meeting, Toronto, ON, Canada, 2–8 October 1993; pp. 843–849.
3. Kamli, M.; Yamamoto, S.; Abe, M. A 50-150 kHz Half-Bridge inverter for induction heating Application. *IEEE Trans. Ind. Electron.* **1996**, *43*, 163–172. [CrossRef]
4. Burdío, J.M.; Barragán, L.A.; Monterde, F.; Navarro, D.; Acero, J. Asymmetrical voltage-cancellation control for full-bridge series resonant inverters. *IEEE Trans. Power Electron.* **2004**, *19*, 461–469. [CrossRef]
5. Esteve, V.; Bellido, J.L.; Jordán, J. Optimal Design of a Single-Phase Bidirectional Rectifier. *Energies* **2024**, *17*, 1280. [CrossRef]
6. Esteve, V.; Bellido, J.L.; Jordán, J.; Dede, E.J. Improving the Efficiency of an Isolated Bidirectional Dual Active Bridge DC–DC Converter Using Variable Frequency. *Electronics* **2024**, *13*, 294. [CrossRef]
7. Ahmed, N. High frequency soft switching AC conversion circuit with dual mode PWM/PDM control strategy for high power IH applications. *IEEE Trans. Ind. Electron.* **2011**, *58*, 1440–1448. [CrossRef]
8. Ramalingam, S.R.; Boopathi, C.S.; Ramasamy, S.; Ahsan, M.; Haider, J.; Shahjalal, M. A Single-Coil Multi-Tapped PDM-Based Induction Heating System for Domestic Applications. *Electronics* **2023**, *12*, 404. [CrossRef]
9. Grajales, L.; Lee, F.C. Control system design and small-signal analysis of a phase-shift controlled series-resonant inverter for induction heating. In Proceedings of the PESC '95—Power Electronics Specialist Conference, Atlanta, GA, USA, 18–22 June 1995; pp. 450–456.
10. Dudrik, J.; Trip, N.-D. Soft-switching PS-PWM DC–DC converter for full-load range applications. *IEEE Trans. Ind. Electron.* **2010**, *57*, 2807–2814. [CrossRef]
11. Viriya, P.; Thomas, T. Power transfer characteristics of a phase-shift controlled ZVS inverter for the application of induction heating. In Proceedings of the International Power Electronics Conference (IPEC), Tokyo, Japan, 3–7 April 2000; pp. 423–428.
12. Showybul, S.M.; Shakib, I.; Mekhilef, S. A frequency adaptive phase shift modulation control-based LLC series resonant converter for wide input voltage applications. *IEEE Trans. Power Electron.* **2017**, *32*, 8360–8370.
13. Burdío, J.M.; Canales, F.; Barbosa, P.M.; Lee, F.C. A comparison study of fixed-frequency control strategies for ZVS dc/dc series resonant conveters. In Proceedings of the 2001 IEEE 32nd Annual Power Electronics Specialists Conference (IEEE Cat. No.01CH37230), Vancouver, BC, Canada, 17–21 June 2001; pp. 427–432.
14. Yang, X.; Sha, D. Automatic Current Limit Strategy for LLC DC-DC Converter for Overload Operation. *EEE Trans. Power Electron.* **2024**, *39*, 9917–9928. [CrossRef]
15. Scirè, D.; Lullo, G.; Vitale, G. Non-Linear Inductor Models Comparison for Switched-Mode Power Supplies Applications. *Electronics* **2022**, *11*, 2472. [CrossRef]
16. Scirè, D.; Lullo, G.; Vitale, G. Design and Modeling of an Interleaving Boost Converter with Quasi-Saturated Inductors for Electric Vehicles. In Proceedings of the 2020 AEIT International Conference of Electrical and Electronic Technologies for Automotive (AEIT AUTOMOTIVE), Turin, Italy, 18–20 November 2020; pp. 1–6. [CrossRef]
17. Chudjuarjeen, S.; Sangswang, A.; Koompai, C. An improved LLC resonant inverter for induction-heating applications with asymmetrical control. *IEEE Trans. Ind. Electron.* **2011**, *58*, 2915–2925. [CrossRef]
18. Espí, J.M.; Dede, E.J.; García-Gil, R.; Castelló, J. Design of the L-LC resonant inverter for induction heating based on its equivalent SRI. *IEEE Trans. Ind. Electron.* **2007**, *54*, 3178–3187. [CrossRef]
19. Lucía, O.; Burdío, J.M.; Millán, I.; Acero, J.; Barragán, L.A. Efficiency oriented design of ZVS half-bridge series resonant inverter with variable frequency duty cycle control. *IEEE Trans. Power Electron.* **2010**, *25*, 1671–1674. [CrossRef]
20. Dede, E.; Gonzalez, J.; Linares, J.; Jordan, J.; Ramirez, D.; Rueda, P. 25-kW/50-kHz generator for induction heating. *IEEE Trans. Ind. Electron.* **1991**, *38*, 203–209. [CrossRef]
21. Lucía, O.; Burdío, J.M.; Millán, I.; Acero, J.; Puyal, D. Load-adaptive control algorithm of half-bridge series resonant inverter for domestic induction heating. *IEEE Trans. Ind. Electron.* **2009**, *56*, 3106–3116. [CrossRef]
22. Czarkowski, D.; Kazimierczuk, M.K. Phase-controlled series-parallel resonant converter. *IEEE Trans. Power Electron.* **1993**, *8*, 309–319. [CrossRef]

23. Barragán, L.A.; Navarro, D.; Acero, J.; Urriza, I.; Burdío, J.M. FPGA implementation of a switching frequency modulation circuit for emi reduction in resonant inverters for induction heating appliances. *IEEE Trans. Ind. Electron.* **2008**, *55*, 11–20. [CrossRef]
24. Esteve, V.; Jordan, J.; Dede, E.J.; Sanchis-Kilders, E.; Martinez, P.J.; Maset, E.; Gilabert, D. Optimal LLC inverter design with SiC MOSFETs and phase shift control for induction heating applications. *IEEE Trans. Ind. Electron.* **2022**, *69*, 11100–11111. [CrossRef]
25. Sewell, H.I.; Stone, D.A.; Bingham, C.M. Dynamic load impedance matching for induction heater systems. *COMPEL* **2003**, *22*, 30. [CrossRef]
26. Medini, D.; Ben-Yaakov, S. A current-controlled variable-inductor for high frequency resonant power circuits. In Proceedings of the 1994 IEEE Applied Power Electronics Conference and Exposition—ASPEC'94, Orlando, FL, USA, 13–17 February 1994.
27. Ngo-Phi, T.; Nguyen-Quang, N. LLC inverter design procedure for induction heating with quantitative analysis of power transfer. *Vnuhcm J. Eng. Technol.* **2021**, *4*, 738–746.
28. Esteve, V.; Jordán, J.; Dede, E.J.; Martinez, P.J.; Ferrara, K.J.; Bellido, J.L. Comparative analysis and improved design of LLC inverters for induction heating. *IET Power Electron.* **2023**, *16*, 1754–1764. [CrossRef]
29. Wilson, P.R. Modelling and Simulation of Magnetic Components in Electric Circuits. Ph.D. Thesis, Dept. Elect. Comput. Eng., Univ. Southampton, Southampton, UK, November 2001.
30. Wheeler, H.A. Discussion on simple inductance formulas for radio coils. *Proc. Inst. Radio Eng.* **1929**, *17*, 580–582.
31. Wheeler, H.A. Inductance formulas for circular and square coils. *Proc. IEEE* **1982**, *70*, 1449–1450. [CrossRef]
32. Rudnev, V.; Loveless, D.; Cook, R.; Black, M. *Hand Book of Induction Heating*; CRC Press: Boca Raton, FL, USA, 2017.
33. Brown, G.H.; Hoyler, C.N.; Bierwirth, R.A. *Theory and Application of Radio-Frequency Heating*; Van Nostrand: New York, NY, USA, 1947.
34. Esteve, V.; Jordan, J.; Sanchis-Kilders, E.; Dede, E.J.; Maset, E.; Ejea, J.B.; Ferreres, A. Improving the reliability of series resonant inverters for induction heating applications. *IEEE Trans. Ind. Electron.* **2014**, *61*, 2564–2572. [CrossRef]
35. Esteve, V.; Jordán, J.; Dede, E.J.; Bellido, J.L. Enhanced asymmetrical modulation for half-bridge series resonant inverters in induction heating applications. *IET Power Electron.* **2023**, *16*, 2482–2491. [CrossRef]
36. Alonso, J.M.; Perdigão, M.S.; Vaquero, D.G.; Calleja, A.J.; Saraiva, E.S. Analysis, design, and experimentation on constant-frequency DC-DC resonant converters with magnetic control. *IEEE Trans. Power Electron.* **2012**, *27*, 1369–1382. [CrossRef]
37. Rapoport, E.; Pleshivteva, Y. *Optimal Control of Induction Heating Process*; CRC Press: Boca Raton, FL, USA, 2006.
38. O'Reilly, J. *Multivariable Control for Industrial Applications*; Peter Peregrinus Ltd.: London, UK, 1987.
39. Boubaker, O.; Zhu, Q.; Mahmoud, M.S. *New Trends in Observer-Based Control: A Practical Guide to Process and Engineering Applications*; Academic Press: Cambridge, MA, USA, 2019.

Artículo 2:

[26] **Bellido, J.L.**; Esteve, V.; Jordán, J. Performance Enhancement in LC Series Resonant Inverters with Current-Controlled Variable-Transformer and Phase Shift for Induction Heating. Electronics 2024, 13, 2911. https://doi.org/10.3390/electronics13152911

electronics

Article

Performance Enhancement in LC Series Resonant Inverters with Current-Controlled Variable-Transformer and Phase Shift for Induction Heating

Juan L. Bellido [1,2,*], **Vicente Esteve** [1] and **José Jordán** [1]

[1] Department of Electronic Engineering, University of Valencia, Av. University, SN, 46100 Valencia, Spain
[2] R&D Department, SiCtech Induction, 46980 Paterna, Spain
[*] Correspondence: juanbe5@alumni.uv.es

Abstract: This article presents an analysis of a converter based on an LC resonant inverter for induction heating applications. It employs a current-controlled variable transformer (VT) in conjunction with phase shift regulation (PS) to operate at a fixed frequency close to the resonance frequency. The converter maintains a small switching angle, enabling substantial load variations without sacrificing zero voltage switching (ZVS) for the transistors. This innovative method enhances the inverter's performance across the entire operating range. Additionally, a new design of the transformer structure with a variable ratio will be analyzed, enabling mathematical modeling. The obtained results demonstrate a performance exceeding 99%. Both the inverter and variable transformer designs were experimentally validated using a 15 kW, 200 kHz converter for induction heating applications with silicon carbide (SiC) MOSFETs.

Keywords: LC resonant inverters; induction heating; current-controlled variable-transformer; PS power control; silicon carbide (SiC) power MOSFETs

Citation: Bellido, J.L.; Esteve, V.; Jordán, J. Performance Enhancement in LC Series Resonant Inverters with Current-Controlled Variable-Transformer and Phase Shift for Induction Heating. *Electronics* **2024**, *13*, 2911. https://doi.org/10.3390/electronics13152911

Academic Editor: Pedro J. Villegas

Received: 16 June 2024
Revised: 20 July 2024
Accepted: 22 July 2024
Published: 24 July 2024

1. Introduction

Induction heating systems use the principle of electromagnetic induction and Joule's law to cause the workpiece to heat up [1]. They are widely used in both domestic and industrial applications, where they are employed in metal melting, heat treatment, welding, and others. Each application involves different workpieces with different heating requirements, where power and frequency stand as the primary factors influencing the heating process [2,3].

In induction equipment, power regulation can be achieved using either current sources or voltage sources based on the power supply structure. Current sources employ parallel resonant oscillators [4], whereas voltage sources are utilized with series or LLC resonant oscillators [5,6]. Currently, the series resonant inverter has become more prevalent than other topologies. One of the reasons is that it utilizes a compact transformer located at the high-frequency inverter output, providing galvanic isolation and enabling impedance adaptation of the resonant circuit through the transformer ratio [7].

Regarding power modulation, pulse frequency modulation (PFM) is commonly employed, offering a wide operating range at the expense of reduced efficiency due to increased frequency and complex filtering caused by a wide noise spectrum [8]. Furthermore, optimization in magnetic components is lost when the operating frequency is increased from resonance. Other techniques such as pulse density modulation (PDM) or phase-shift modulation (PS) provide improvements in efficiency and filtering as they operate at a fixed frequency close to the resonance frequency [9]. However, they lack a wide operating range, causing the loss of ZVS. More sophisticated control techniques, referred to as narrow-frequency-range methods, combine two of these techniques, such as phase shift modulation with frequency modulation (FM&PS). This combination achieves improved efficiency and performance in response to load changes. However, when a large operating range is required, increasing the frequency is necessary, which degrades optimization [10,11]. The latest publications on maintaining a fixed frequency only focus on LLC-type converters, where in [12], a complex state-plane analysis is used to maintain soft switching, and in [13], a current-controlled variable-inductor is used to enforce the operating range and maintain the ZVS. However, these types of converters have the disadvantage of having to take into account both resonance frequencies when designing the converters, making them complex to control, and they are not suitable for all applications.

To enhance performance, a novel control technique was proposed, combining phase-shift modulation with current control of the transformer ratio (VT&PS). As investigated in this article, the use of a series resonant inverter with an electronically controllable variable transformer ratio allows for the circuit impedance to be adapted dynamically. This enables power control at a fixed frequency through PS modulation while maintaining a fixed low switching angle over a wide operating range, reducing the inverter output current.

This article is divided into the following sections: Section 2 explains the behavior of the series resonant circuit and the influence of the transformer as an impedance adapter. Section 3 analyzes a new model of a controllable variable transformer that can be represented with equations. Section 4 proposes a design procedure for an LC resonant inverter for induction heating with VT&PS, where a mathematical analysis of losses is conducted, and the control principle is discussed. Finally, this will be compared with fixed and variable frequency PS. In Section 5, the design calculations are experimentally verified using a 15 kW induction prototype, comparing it with the two traditional PS control methods.

2. LC Series Resonant Converter Topology

The LC series resonant circuit, as depicted in Figure 1, is composed of a heating inductor (L_s) in series with a capacitor (C_s) to compensate the reactive energy. The equivalent series resistance (R_s) represents the impedance imposed by the piece to be heated. This circuit is connected to the high-frequency inverter through a transformer, providing galvanic isolation and adapting the circuit impedance with the transformer ratio.

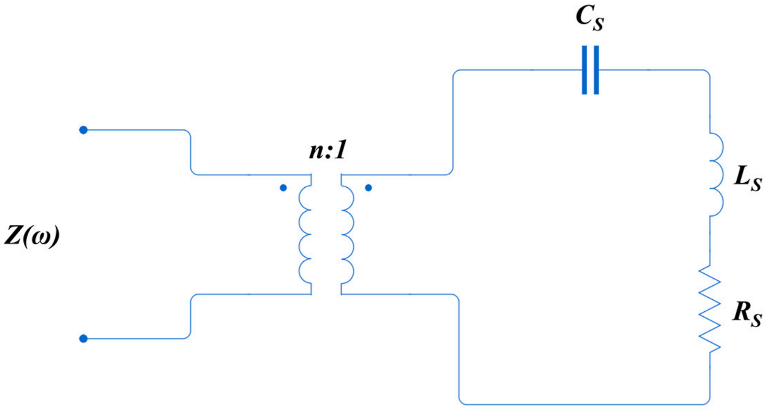

Figure 1. LC series resonant circuit.

The advantages offered by this topology over the parallel LC circuit are the elimination of the input inductance to the inverter, the cost-effectiveness and smaller size of the isolation transformer since it is located at the inverter output rather than in the power supply network, and less complex power regulation [6,9]. The series resonant circuit also presents advantages over LLC, as the design is simpler, using only two reactive elements and simplifying control by eliminating the need to manage two resonance frequencies [6].

The theoretical effect of the transformer as an impedance adapter is expressed as

$$R_p = R_s n^2, \tag{1}$$

where the secondary resistance of the transformer is reflected in the primary (R_p) multiplied by the square of the transformer turns ratio (n). This effect also occurs with the equivalent inductance reflected from the primary (L_p),

$$L_p = L_s n^2, \tag{2}$$

and has the opposite effect on the equivalent capacitance reflected from the primary (C_p)

$$C_p = \frac{C_s}{n^2}. \tag{3}$$

This ensures that changing the transformer turn ratio does not alter the resonance frequency of the circuit,

$$\omega_o = \omega_p = \frac{1}{\sqrt{L_p C_p}} = \frac{1}{\sqrt{L_s n^2 \frac{C_s}{n^2}}} = \frac{1}{\sqrt{L_s C_s}}. \tag{4}$$

and that the quality factor remains unchanged as well

$$Q = Q_p = \frac{L_p \omega_p}{R_p} = \frac{L_s n^2 \omega_o}{R_s n^2} = \frac{L_s \omega_o}{R_s}. \tag{5}$$

However, it has implications regarding the magnitude of impedance, which from the primary side of the transformer, can be expressed as

$$|Z(\omega)| = n^2 \left| R_s + j\omega L_s + \frac{1}{j\omega C_s} \right| = \frac{n^2 R_s}{\cos\alpha}. \tag{6}$$

where α is the argument of the impedance, which represents the phase between voltage and current at resonance, which is given by

$$\alpha = \arg(Z(\omega)) = \arctan\left(\frac{\omega L_p - \frac{1}{\omega C_p}}{n^2 R_p} \right). \tag{7}$$

Therefore, the effect of varying the transformer turns ratio can be observed in Figure 2. The magnitude and phase of the input impedance are plotted against frequency for different turns ratios in an LC series resonant circuit with a Q factor greater than 6, which is typical for induction heating applications [6]. As observed in the figure, for a given frequency, the magnitude of the impedance increases as the transformer ratio increases, exhibiting an opposite trend to the phase. This effect allows for more power to be obtained at the same frequency by increasing the transformer turns ratio. Therefore, this effect can be consistently achieved with the use of a current-controlled variable-transformer. In combination with PS, which varies the effective voltage applied to the resonant circuit, both the power applied to the load and the switching angle can be controlled while maintaining a fixed frequency. This differs from FM&PS control, which achieves a similar behavior in terms of power variation with a fixed switching angle, with the difference being that it needs to modulate the frequency to maintain the phase [10].

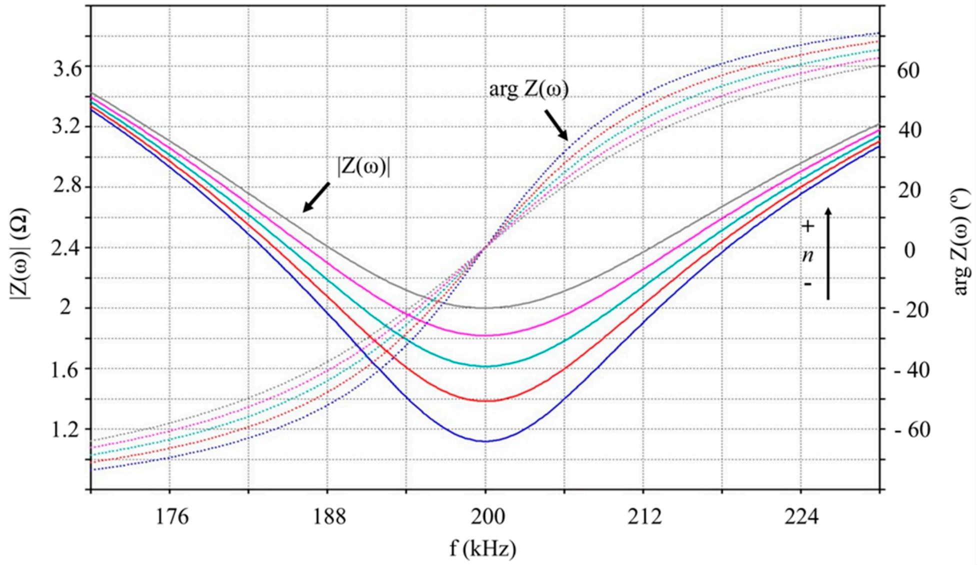

Figure 2. Magnitude of impedance (blue, red, light blue, magenta, and grey continuous curves) and phase of impedance (blue, red, light blue, magenta, and grey dotted curves) are arranged in increasing order of transformer ratio of LC resonant circuit.

3. Analysis of Current-Controlled Variable-Transformer

The analysis of the current-controlled variable-transformer has its origins in previous articles [14,15], and its basic operation is based on the model of the variable inductor already presented in other works [16,17]. Its operational principle is based on distributing the magnetic flux generated by the primary to the secondary by varying the effective permeability of the core using a path that decreases its reluctance when connected to a DC current source [18], thus increasing the influence of the reluctance of the secondary path, which includes an air gap. To achieve this, numerous articles have proposed different magnetic core topologies for various applications. Custom-made non-commercial cores have been constructed, which increase the cost and complicate the design process [19,20]. This issue has been partially addressed by using two "E"-shaped cores [21,22], but even though these are commercial cores, they still require modification due to the position of the air gap. Additionally, they present a complex structure that necessitates an experimental measurement process for transformer design with their relationships.

The structure presented in this article, as shown in Figure 3, addresses these drawbacks by utilizing two commercial "E"-shaped cores with a central air gap, which, symmetrically distributed as described below, allow the inductance model to be easily analyzed. The primary winding is wound between the two outer legs of both cores, which are joined together. The secondary winding is divided between the central legs of the cores, and their windings are connected in parallel. The two lateral arms form the saturation control inductor subjected to DC bias, which is wound in series with opposite polarity to decouple the primary and secondary from DC bias, neutralizing the magnetic flux influence and preventing induced voltages. Therefore, when the core is not subjected to DC bias, the reluctance of the secondary will be lower than that of the core, as it has an air gap, causing the magnetic flux to be closed to a lesser extent by the secondary. However, when the core is subjected to DC bias, the effective permeability of the core decreases by saturating it and thus its reluctance, resulting in the reluctance of the secondary being greater in relation to that of the core, and therefore, magnetic flux is closed through this path.

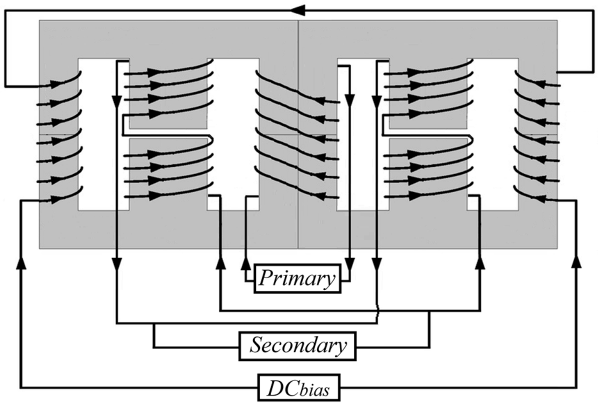

Figure 3. The structure of the current-controlled variable-transformer.

The analysis of the magnetic circuit is based on the relationships that balance the ampere turns and magnetic fluxes of the proposed structure given its symmetry. This allows for the transformer to be analyzed by defining the inductances that compose it [18,23,24]. To maintain symmetry and facilitate design, the inductances reflected from the primary will be analyzed as a single core, and those from the secondary as two in parallel. This leads to the representation of the equivalent inductance circuits shown in Figure 4.

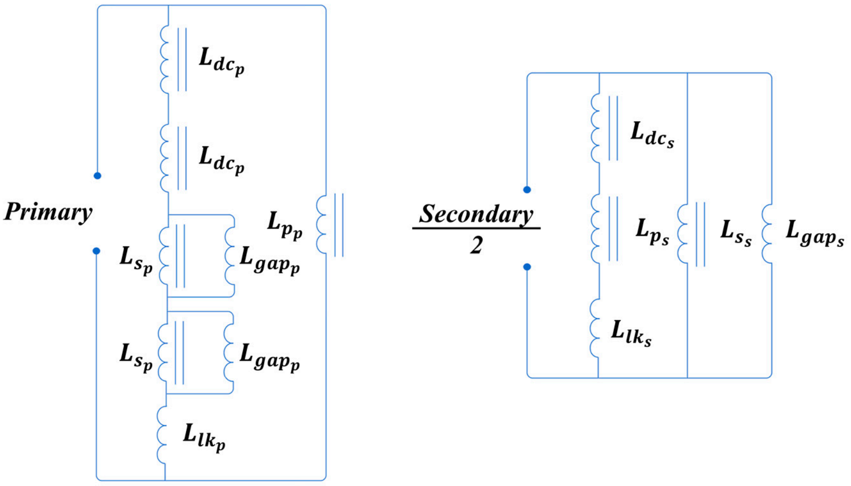

Figure 4. The equivalent inductance circuit of the primary on the left and secondary on the right.

Therefore, the inductance reflected from the primary due to the primary branch and the inductance of the primary branch reflected from the secondary are expressed, respectively, as follows:

$$L_{p_p} = \frac{\mu_0 \mu_i A_p (n_p)^2}{l_{p_p}} \text{ and } L_{p_s} = \frac{\mu_0 \mu_i A_p (n_s)^2}{l_{p_s}}, \tag{8}$$

where μ_0 is the permeability of air, μ_i is the initial permeability of the core, A_p is the effective area of the primary branch, n_p and n_s are the number of turns of the primary and secondary, l_{p_p} is the magnetic path length of the primary arm, and l_{p_s} is the magnetic path length of the primary arm to the secondary.

Regarding the inductances of the secondary branches reflected from the primary and secondary, they are, respectively, expressed as

$$L_{s_p} = \frac{\mu_0 \mu_i A_s (n_p)^2}{l_{s_p}} \text{ and } L_{s_s} = \frac{\mu_0 \mu_i A_s (n_s)^2}{l_{s_s}}, \tag{9}$$

where A_s is the effective area of the secondary branch, l_{s_s} is the magnetic path length of the secondary arm, and l_{s_p} is the magnetic path length of the secondary arm to the primary.

The leakage inductance, which closes through air rather than through the ferrite core, is expressed for both the primary and secondary as

$$L_{lk_p} = \frac{\mu_0 16 A_p (n_p)^2}{l_{p_p}} \text{ and } L_{lk_s} = \frac{\mu_0 16 A_s (n_s)^2}{l_{s_s}}. \tag{10}$$

The inductance due to the saturation branches, both for the primary and secondary, is also expressed as

$$L_{dc_p} = \frac{\mu_0 \widetilde{\mu} A_{dc} (n_p)^2}{l_{dc_p}} \text{ and } L_{dc_s} = \frac{\mu_0 \widetilde{\mu} A_{dc} (n_s)^2}{l_{dc_s}}, \tag{11}$$

where the relative permeability subjected to DC biases is denoted as $\widetilde{\mu}$, A_{dc} is the effective area of the DC bias branch, and l_{dc_p} is the magnetic path length of the same branch.

Finally, the inductances due to the air gap located in the secondary branches are expressed, when viewed from the primary and secondary, as

$$L_{gap_p} = \frac{\mu_0 A_{gap} (n_p)^2}{l_{gap}} \text{ and } L_{dc_s} = \frac{\mu_0 \widetilde{\mu} A_{dc} (n_s)^2}{l_{dc_s}}, \tag{12}$$

where A_{gap} and l_{gap} correspond, respectively, to the effective area and magnetic path length of the air gap.

Therefore, as shown in the equivalent circuit of Figure 4, the maximum primary inductance can be expressed as

$$\frac{1}{L_{p_{max}}} = \left(\frac{1}{L_{p_p}} + \frac{1}{L_{lk_p} + 2L_{dc_p} + \frac{2}{L_{sp} + L_{gap_p}}} \right), \tag{13}$$

while the maximum secondary inductance is given by

$$\frac{1}{2L_{s_{max}}} = \left(\frac{1}{L_{p_s} + L_{dc_s} + L_{lk_s}} + \frac{1}{L_{s_s}} + \frac{1}{L_{gap_s}} \right). \tag{14}$$

Since $\widetilde{\mu}$ decreases when exposed to a continuous magnetic field intensity (H_{bias}), to which the L_{dc} winding is subjected, the ratio between L_{max} and L_{min}, with the latter being the minimum value of inductance due to the minimum $\widetilde{\mu}$ resulting from maximum exposure to H_{bias}, can be obtained using the following expression for the primary as

$$\frac{L_{p_{max}}}{L_{p_{min}}} = \left(\frac{\frac{1}{2\mu_i} + \frac{6 l_{gap}}{2 l_{gap} (74 + 6\mu_i) + 3 l_{ps}}}{\frac{1}{2\mu_i} + \frac{24 (l_{gap} + l_{ps})}{2\mu_e l_{gap} l_{ps} \left(74 + 4\mu_i + \widetilde{\mu}\right) + 1}} \right), \tag{15}$$

and for the secondary as

$$\frac{L_{s_{max}}}{L_{s_{min}}} = \left(\frac{\frac{2\mu_e \frac{l_{ss}}{l_{sp} + l_{ss}}}{\widetilde{\mu} + 32} + \frac{\mu_e \frac{l_{ss}}{l_{sp} + l_{ss}}}{\mu_i} + 1}{\frac{2\mu_e \frac{l_{ss}}{l_{sp} + l_{ss}}}{\mu_i + 32} + \frac{\mu_e \frac{l_{ss}}{l_{sp} + l_{ss}}}{\mu_i} + 1} \right), \tag{16}$$

where μ_e is the effective relative permeability of the core with a gap from the elementary equation of an inductor,

$$L = \frac{\mu_0 \mu_e A_e n^2}{l}. \tag{17}$$

4. VT&PS Resonant Inverter Design

4.1. Design Procedure

In induction heating applications, certain parameters are typically considered, such as the power range, frequency, quality factor, and inductance of the inductor obtained from its geometry. These parameters depend on the thermal treatment, the geometry of the workpiece, and the material [2]. Starting from these parameters with (4), the value of the capacitor is obtained for the frequency at which it is desired to operate [9]. Using the following expression, the switching frequency is adjusted to achieve a small angle (α) between the inverter output voltage and output current.

$$\omega_{sw} = \omega_o \frac{\tan\alpha + \sqrt{\tan^2\alpha + 4Q^2}}{2Q}. \tag{18}$$

The RMS value of the output current is obtained using

$$I_o = \frac{P_o}{\frac{2}{\pi}\sqrt{2}V_d \cos\alpha}, \tag{19}$$

where V_d is the DC input voltage. And the equivalent primary resistance of the transformer is obtained using

$$R_p = \frac{P_o}{(I_o)^2}. \tag{20}$$

The minimum transformer ratio (TR_{mim}) is obtained from (19), (20), (5), and (1) for the maximum power at the switching frequency. On the other hand, the maximum transformer ratio (TR_{max}) is defined by the minimum power and is obtained by recalculating (19), (20), and (1) for this value. In Table 1, the starting values and those obtained from applying the design for the LC series resonant circuit are recorded.

Table 1. The initial requirements and results of the design.

Magnitude	Symb.	Eq.	Value		Unit
Output power range	P_o		15	4	kW
Quality factor	Q		10		
Frequency	f_o		200		kHz
DC input voltage	V_d		500		V
Inductor	L_s		1		µH
Capacitor	C_s	(4)	0.63		µF
Switching angle	α		15		°
Switching frequency	f_{sw}	(18)	203		kHz
RMS output current	I_o	(19)	32	8.5	A
Primary resistance	R_p	(20)	14.7	55.1	Ω
Transformer ratio	TR	(1)	10.7	20	

For magnetic core design and selection, the first step is to apply the effective area ratio for the maximum flux density (B_{max}) to the area of the winding, resulting in the following expression of the area product:

$$A_p = A_e A_w = \frac{V_d I_o}{2F_{sw} B_{max} J K}, \tag{21}$$

where

A_e is the specific area of the core (m^2).

A_w is the core winding area (m^2).

J represents the current density (A/m^2).

K is the fill factor, which will be assumed to have a value between 0.5 and 0.9.

With the obtained value, a core with dimensions larger than those calculated is selected, and the loss curves in the core at the operating frequency are compared with the value obtained from $B = \mu H$ using the maximum variation of permeability obtained from the curves of relative permeability variation under DC bias, ensuring that the obtained value is less restrictive than that used for the calculation of the area product. Then, the minimum number of turns that the primary of the transformer should have is calculated using the following expression:

$$n_p = \frac{V_d}{4F_{sw} B_{max} A_e}. \tag{22}$$

With the number of turns of the primary being obtained through expressions (13) and (15) the value of the minimum inductance of the transformer's primary is obtained, i.e., when it is subjected to maximum DC bias [25]. This corresponds to the value of the minimum primary inductance in an open circuit $L_{p_{min_{oc}}}$, and it is assumed that 20% of this value will be the minimum primary inductance in short circuit $L_{p_{min_{cc}}}$, resulting in the primary coupling coefficient (K_p) having a typical value of 0.8,

$$K_p = 1 - \frac{L_{p_{min_{cc}}}}{L_{p_{min_{oc}}}}. \tag{23}$$

Therefore, the mutual inductance (L_M) is obtained from

$$L_M = \frac{L_{p_{min_{oc}}} K_p}{1 - K_p}. \tag{24}$$

And the maximum secondary inductance reflected from the primary of the transformer is expressed as

$$L_{sec_{max}} = \frac{\left(L_M / K_p\right)^2}{2L_{p_{min}}}. \tag{25}$$

Regarding the secondary inductance when the primary is short-circuited, it is obtained for the value of the desired maximum transformation ratio:

$$L_{s_{min_{cc}}} = \frac{L_{sec_{max}}}{{TR_{max}}^2}. \tag{26}$$

To obtain the value of the minimum secondary inductance, which corresponds to the open-circuit test value, it is again considered that the secondary coupling factor (K_s) will be the typical value of 0.8, allowing it to be obtained with the following expression:

$$L_{s_{min_{oc}}} = \frac{L_{s_{min_{cc}}}}{1 - K_s}. \tag{27}$$

With the value of $L_{s_{min_{oc}}}$, (14) and (16) are used to determine the number of turns that will yield that inductance value.

To obtain the value of the minimum transformation ratio, it is considered that the coupling coefficients of the primary and secondary are minimum. This is because when the core is not exposed to DC bias, the flux closes to a greater extent through the outer branches of the core. Therefore, the communication coupling coefficient (K) approaches 0.05. These approximations will be experimentally verified later to validate the design.

$$K = \sqrt{K_p K_s}. \tag{28}$$

Therefore, the minimum transformation ratio is obtained using the maximum primary and secondary inductances obtained from (13), (15) and (14), and (16), respectively, as follows:

$$TR_{min} = \frac{1}{K}\sqrt{L_{s_{max}} \Big/ L_{p_{max}}}. \tag{29}$$

If the minimum obtained ratio is less than or equal to the desired one, the design can be considered acceptable. The final step involves using the value of $\widetilde{\mu}$ employed in Equations (15) and (16) to determine the necessary H_{bias} to reach the minimum inductance values. For this purpose, the curve on the datasheet regarding the relative permeability subjected to DC bias is consulted, optimizing the balance between the bias current (I_{bias}) and the number of turns of the saturation winding (n_{dc}) given by the following expression:

$$I_{bias} 2n_{dc} = H_{bias} 2l_{dc}, \tag{30}$$

where

H_{bias} is the continuous magnetic field intensity.

l_{dc} is the length of the dc control branch from the center to the center of the core (m).

In combination with the transformer ratio control, phase shift control (PS) will be utilized. The phase shift angle factor (φ), ranging from 0 to 180°, varies the output voltage of the inverter applied to the resonant circuit using the following expression:

$$V_{ab}(\varphi) = \frac{2\sqrt{2}}{\pi} V_d cos\frac{\varphi}{2}. \tag{31}$$

Therefore, the output current of the inverter as a function of the phase shift angle and the transformer ratio is given by

$$I_o(\varphi, TR) = \frac{2\sqrt{2}}{\pi R_s TR^2} V_d \cos\frac{\varphi}{2} \cos\left(\alpha + \frac{\varphi}{2}\right). \tag{32}$$

And the output power as a function of these two variables is expressed as

$$P_o(\varphi, TR) = \left(\frac{2\sqrt{2}V_d}{\pi}\right)^2 \frac{1}{R_s TR^2} \cos^2\frac{\varphi}{2} \cos^2\left(\alpha + \frac{\varphi}{2}\right) \tag{33}$$

In Figure 5, the entire operating range allowed in the output power of Equation (33) with the combination of the transformer ratio variation and the phase shift is depicted for the design carried out. As observed in the figure, a dashed red line corresponding to the point of maximum efficiency operation for the entire output power range was plotted. This was obtained by optimizing Equation (32) while maintaining a switching angle (α) of 15 degrees.

In Figure 6, the simplified diagram of the VT&PS control scheme is depicted. The control system inputs are the power and the angle between the voltage and output current, and due to the two control variables, a Multiple Inputs Multiple Outputs (MIMO) system is used, which is nonlinear and coupled, acting with Proportional Integral Differential (PID) control and a decoupled diagonalization network [26,27]. The outputs of this system will therefore be the bias current and the phase angle. To optimize the system and operate at the point of maximum efficiency, represented in Figure 5 by the red dashed line, Equation (32) is used to reduce the effective value of the inverter output current with a digital observer with a dynamic optimizer [28]. Finally, in logical signal conditioning and in the triggering block, the transistor gate signals with dead times are generated, ensuring that the system operates in ZVS. In the event of a load jump due to rapid load extraction or a change in the permeability of the workpiece causing a change in the inductor value, the system acts quickly by changing the transformer ratio, achieving coupling or decoupling between the load and the inverter. This principle also prevents the transformer from saturating due to primary voltage, despite having designed the transformer to avoid operating near saturation by the primary. This could happen if there is an overvoltage of V_d.

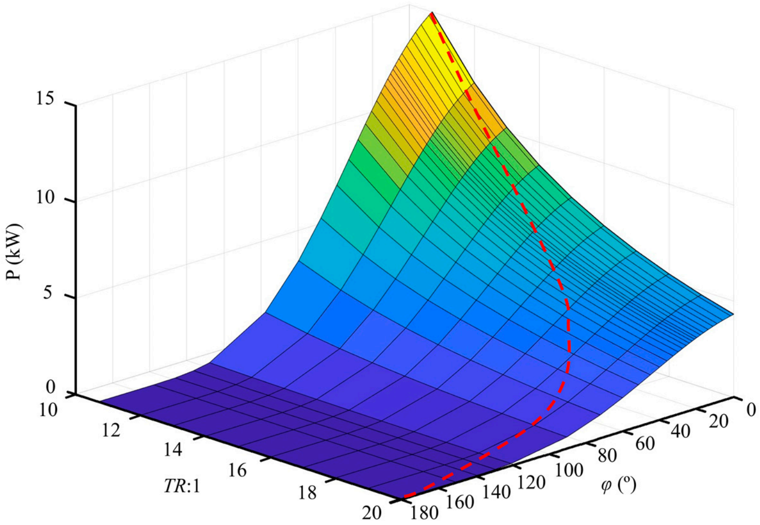

Figure 5. The phase shift and variable transformer as functions of the calculated output power. The red dotted curve corresponds to the optimal control strategy.

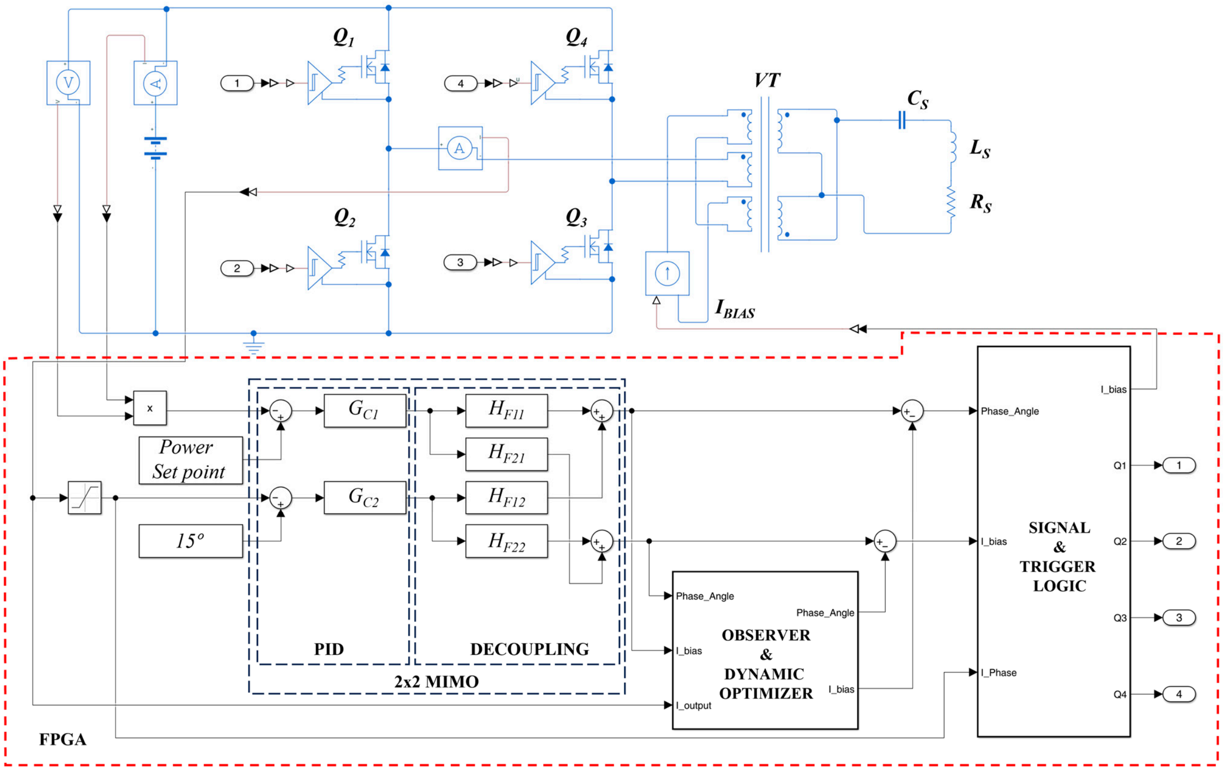

Figure 6. A schematic of the proposed system, detailing the inverter topology, the resonant load LLC with the variable inductor, and the control diagram.

4.2. Losses Analysis

The losses of the inverter and the transformer are mathematically analyzed to verify the improvements introduced by this design over the entire operating range. For this purpose, the optimal phase shift [5,29] switching sequence combined with the variable transformer is utilized.

As for the losses due to the current conducted through the channel of the MOSFETs used in the inverter, they are given by the following expression:

$$P_{cd}(\varphi, TR) = \left(\frac{I_o(\varphi, TR)}{\sqrt{2}}\right)^2 R_{DS_{on}} \tag{34}$$

where $R_{DS_{on}}$ is the ON state MOSFET resistance channel.

For the switching losses, only the OFF losses of the MOSFETs have been considered, as the inverter operates in ZVS throughout the operating range, making the ON switching losses negligible. The energy is obtained from the polynomial equation of the manufacturer's OFF state switching loss curves for the drain voltage equal to V_d and the gate resistance used, resulting in

$$E_{off}(\varphi, TR) = aI_c(\varphi, TR)^2 + bI_c(\varphi, TR) + c \tag{35}$$

where I_c corresponds to the switching current of each transistor and is expressed by the following equation:

$$I_c(\varphi, TR) = \frac{2\sqrt{2}}{\pi R_s TR^2} V_d \cos\frac{\varphi}{2} \cos\left(\alpha + \frac{\varphi}{2}\right) \sin(\alpha). \tag{36}$$

Therefore, the power losses for each transistor are obtained from

$$P_{sw}(\varphi, TR) = E_{off}(\varphi, TR)\frac{\omega_{sw}}{2\pi}. \tag{37}$$

The losses due to the transistor gate depend on the total gate charge Q_G and the gate-to-source voltage V_G, related through the following expression:

$$P_{gate} = Q_G V_G \frac{\omega_{sw}}{2\pi}. \tag{38}$$

Regarding the losses of the transformer, we must consider the losses in the core due to the magnetic flux density, with the influence of DC bias being negligible [18,30]. Therefore, they can be obtained using the following equation:

$$P_{TC} = P_{DT} V_T \tag{39}$$

where P_{DT} is the core loss density of the transformer given by the manufacturer for the operating frequency and magnetic flux density, and V_T is its volume.

For the copper losses P_{TW} of the transformer, it is necessary to determine the effective resistance of the primary winding R_p and the secondary winding R_s, taking into account the conductivity, the total length, and the skin effect. The losses are obtained through

$$P_{TW} = I_o(\varphi, TR)^2 (R_p + R_s). \tag{40}$$

Finally, the total losses are obtained from

$$P_{tot}(\varphi, TR) = 4P_{cd}(\varphi, TR) + 4P_{sw}(\varphi, TR) + 4P_{gate} + P_{TC} + P_{TW}. \tag{41}$$

Meanwhile, the efficiency is given by

$$\eta(\varphi, TR) = \frac{P_o(\varphi, TR)}{P_o(\varphi, TR) + P_{tot}(\varphi, TR)}. \tag{42}$$

4.3. Comparison With Fixed and Variable Frequency

Compared to the fixed frequency design, it is necessary to increase the switching frequency to achieve a larger angle between the output voltage and current [7]; for a Q of 10, an angle of 35° is estimated. Therefore, using Equation (18), the switching frequency for that angle is obtained.

On the other hand, in the FM&PS regulation, the frequency is varied such that the value of α is approximately equal to $\varphi/2$, thus maintaining a constant angle [29]. Therefore, Equation (18) can be rewritten as

$$\omega_{sw} = \omega_o \frac{\tan\frac{\varphi}{2} + \sqrt{\tan^2\frac{\varphi}{2} + 4Q^2}}{2Q}. \tag{43}$$

The equivalent resistance in the secondary side will increase with respect to frequency according to Equation (6), resulting in Equations (32) and (33) being rewritten as

$$I_o(\varphi, \omega_{sw}) = \frac{2\sqrt{2}Q}{\pi L_s \omega_{sw} n^2} V_d \cos\frac{\varphi}{2} \cos\left(\alpha + \frac{\varphi}{2}\right). \tag{44}$$

for the current and for the power as

$$P_o(\varphi, \omega_{sw}) = \left(\frac{2\sqrt{2}V_d}{\pi}\right)^2 \frac{Q}{L_s \omega_{sw} n^2} \cos^2\frac{\varphi}{2} \cos^2\left(\alpha + \frac{\varphi}{2}\right). \tag{45}$$

Table 2 summarizes the differences in design due to the different types of controls, while Table 3 reflects the differences in losses involved in each of the designs operating at 10 kW. The advantages of using SiC MOSFETs in high-frequency induction applications have already been analyzed in previous work [31]. Therefore, for the loss analysis, the C3M0120100K was used as the transistor for each of the inverter switches, as it not only met the specifications for operation in the safe area but also offered the best performance when calculating the losses. The specifications of this transistor can be found in Table 4. For the two ferrite cores of the transformer, the material selected was N27 with shape reference E 70/33/32 from TDK Electronics.

Table 2. The differences in the operating characteristics of the controls.

Magnitude	Symb.	PS		FM&PS		VT&PS		Unit
Switching frequency	f_{sw}	243		203	278	203		kHz
Switching angle	α	35	15	15		15		°
RMS output current	I_o	38	19	32	9.7	32	8.5	A
Transformer ratio	$TR_{max/min}$	10.7		10.7		10.7	20	

Table 3. Losses for 10 kW operation power.

Magnitude	Symb.	PS	FM&PS	VT&PS	Unit
Conduction losses	P_{cd}	30.92	19.78	16.72	W
Switching losses	P_{sw}	3.83	4.26	3.75	W
Gate losses	P_{gate}	0.115	0.128	0.112	W
Core losses	P_{TC}	10.2	11.22	10.2	W
Wire losses	P_{TW}	9.8	9.28	10.03	W
Total losses	P_{tot}	159.47	117.16	102.57	W

Table 4. Transistor characteristics.

Magnitude	Symb.	Equation	Value	Unit
On resistance	$R_{DS_{on}}$	(34)	120	mΩ
Turn OFF losses	a	(35)	0.0213	μJ/A^2
	b		0.436	μJ/A
	c		18.991	μJ
Gate charge	Q_G	(38)	22	nC

To observe the improvement in efficiency resulting from this new control compared to conventional ones, the variations in efficiency and output current with respect to the operating power are plotted in Figure 7. As observed when comparing the VT&PS and FM&PS controls, the starting point at maximum power is similar, but the VT&PS control increases efficiency as the current decreases because the transformer increases its ratio, adapting the load to the optimal operating point. The FM&PS control exhibits a similar behavior, but increasing the frequency as the power decreases does not reduce losses as effectively. On the other hand, the PS control maintains a lower efficiency from the beginning because the output current is higher due to having to operate with a larger switching angle.

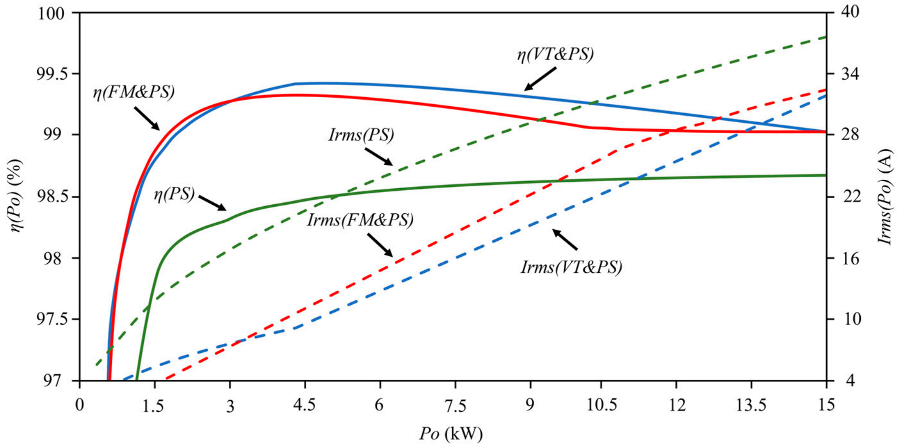

Figure 7. The calculated evolutions of the efficiency and output current of the inverter as functions of the output power for the three control strategies.

5. Experimental Results

To obtain the experimental results of the system, first, the design of the variable transformer was evaluated. Table 5 compares the theoretical values used for the transformer design with the measured values from the short-circuit and open-circuit tests for the primary and secondary of the transformer. These measurements were made to check the assumptions of the coupling factors both in the primary and secondary for the saturated and unsaturated transformers. On the other hand, Table 6 checks the transformer ratios for different levels of DC bias and how this influences the primary and the secondary inductance. As can be seen in both tables, there are deviations in the values due to component dispersions and possible measurement errors.

Table 5. Theoretical and measured values of transformer inductances.

Control Current	**Theoretical Inductance (µH)**				**Measured Inductance (µH)**			
	Open Circuit		**Short Circuit**		**Open Circuit**		**Short Circuit**	
$I_{dc}\ (A)$	$L_{p_{oc}}$	$L_{s_{oc}}$	$L_{p_{cc}}$	$L_{s_{cc}}$	$L_{p_{oc}}$	$L_{s_{oc}}$	$L_{p_{cc}}$	$L_{s_{cc}}$
0	1198	85.5	1018	84.2	1222	90.5	1100	89.6
1	244.4	38.18	48.9	7.64	254	40.5	54.1	7.99

Table 6. Theoretical and measured values of transformer ratios.

Control Current	**Theoretical**			**Measured**		
$I_{dc}(A)$	L_p(µH)	L_s(µH)	**TR**	L_p(µH)	L_s(µH)	**TR**
0	1198	85.5	5.6	1222	90.51	7.02
0.25	820.9	65.2	9.5	767.2	60.854	10.7
0.5	425.6	44.9	13.2	435.5	41.281	12.9
0.75	296.52	39.5	16.3	300.2	42.613	16.1
1	244.4	38.18	20	254.16	40.49	20.8

To carry out the measurements that verify the accuracy of the entire design, a 15 kW inverter module was used, which integrates the FPGA to implement the control, sensors, drivers, transistors, and a controllable current source based on the Howland current pump with an OPA548 as a high-current operational amplifier. The inverter is cooled by a water cooler, and the power supply comes from a controllable source. Table 7 shows the main part numbers of the components used in the inverter.

Table 7. The main components of the inverter.

Component	**Manufacturer**	**Reference**
Transistor	Wolfspeed, Durham, NC, USA, EE. UU.	C3M0120100K
Gate driver	Infineon, Neubiberg, Germany	1ED3120MC12H
Output current sensor	Allegro, Manchester UK	ACS37003KMCATR-085B5
DC current sensor	Infineon, Neubiberg, Germany	TLE4971
Hight current op-amp	Texas Instruments, Dallas, TX, USA, EE.UU.	OPA548
FPGA	AMD, Santa Clara, CA, USA, EE. UU.	Zynq 7000

The test bench used is shown in Figure 8, and each number corresponds to the following:

(1) Induction heating inverter with four SiC C3M0120100K;
(2) DSO with 300 MHz bandwidth;
(3) Differential voltage probe and Rogowski current probe;

(4) Hall effect probe;
(5) Variable transformer;
(6) Capacitor (C_s);
(7) Inductor (L_s);
(8) Workpiece.

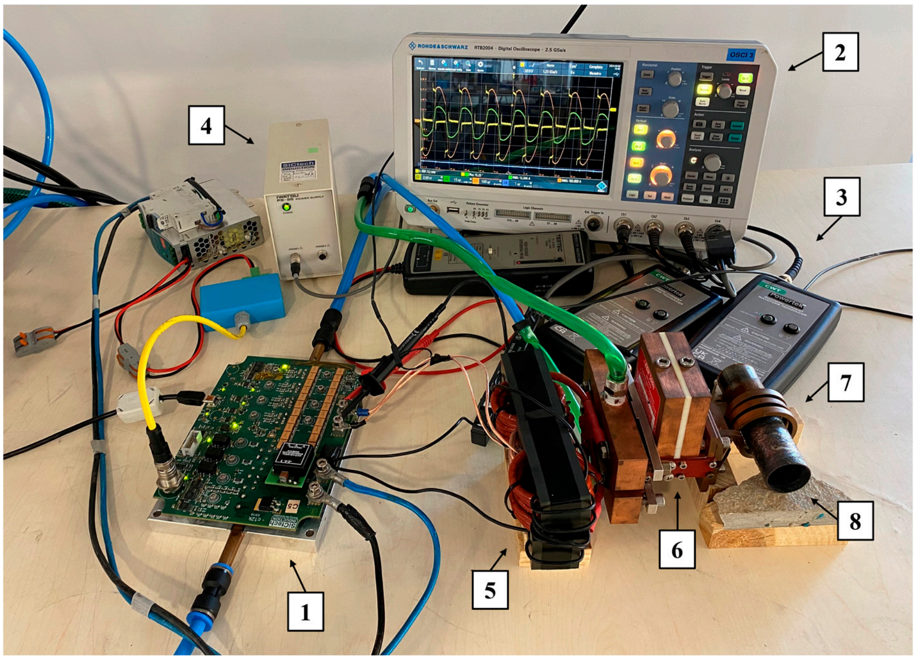

Figure 8. The inverter, variable transformer, and LC resonant load test bench. The numbered labels describe the components on the bottom.

In Table 8, the measured values of the main quantities involved in the design are compared with the theoretical values at two power levels. As can be seen, there is no considerable variation; however, there are deviations due to the parasitic elements of the system that were not considered in the design.

Table 8. Comparison of theoretical and measured results.

Magnitude	**Symb.**	**10 kW**		**15 kW**		**Unit**
		Theor.	**Meas.**	**Theor.**	**Meas.**	
Phase angle	α	15	15.04	15	14.9	°
Transformer ratio	TR	12.5	12.51	10.7	10.82	
Output current	I_{RMS}	22.7	22.85	31.9	32.25	A

Figure 9 shows the oscillograms captured by the DSO for the inverter operating at 10 kW of power with three different control techniques and their responses to changes in the load by quickly removing the workpiece from the inductor. For all three control methods, the results obtained from the designs in Table 2 were used. As observed in the left column, the fixed-frequency PS control requires operation at a higher frequency, resulting in a 33° switching angle at that power level. On the other hand, the other two controls, having two variables, can maintain a 15° angle. In the case of FM&PS, this is due to the increased frequency to 229.8 kHz, and in the case of VT&PS, it is due to impedance adaptation of the load by increasing the transformer ratio to 12.5. Additionally, this load adaptation allows for a lower output current from the inverter compared to the other two controls, which is 22.85 A RMS. Furthermore, it is observed that with a more adapted load due to the higher ratio, the width of the phase shift angle is smaller, reducing losses from OFF switching of the transistors as they have to switch off at a lower current level.

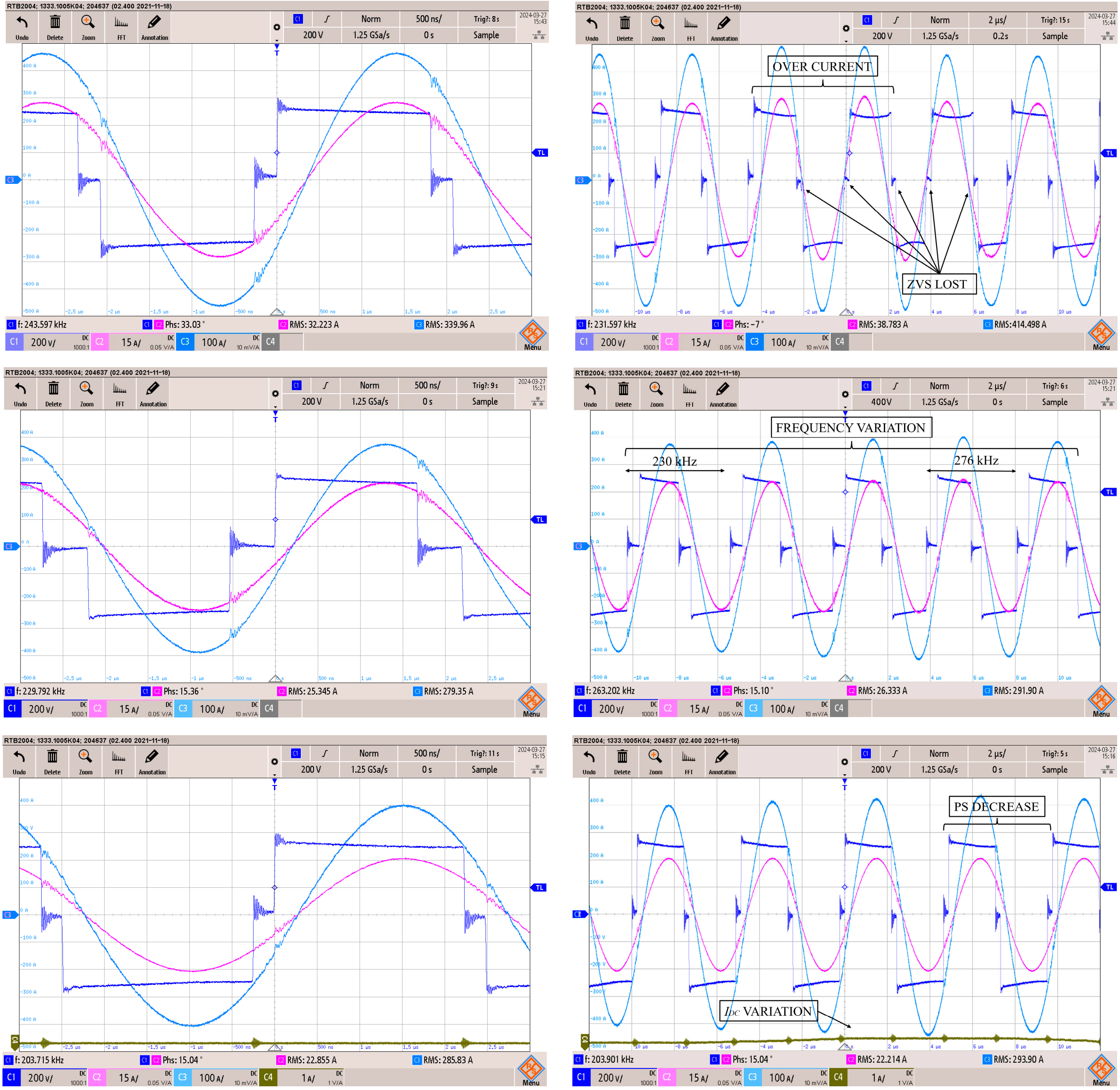

Figure 9. Oscillograms of experimental tests for the LC inverter with different control strategies: PS in the first row, FM&PS in the second row, and VT&PS in the third row. The left column represents operation at 10 kW, and the right column shows the response to a load change at that power level. C1 (dark blue) represents the output voltage (200 V/div), C2 (magenta) shows the output current (15 A/div), C3 (light blue) shows the output current at the secondary of the transformer (100 A/div), and C4 (bround) displays the DC bias current (1 A/div) of the variable transformer in the third row. The time base is 500 ns/div in the left column and 2 µs/div in the right column.

On the other hand, in response to load changes, the PS control, lacking direct regulation with the phase between the output voltage and current, loses ZVS in five commutations, and an overcurrent in the inverter is observed. Both consequences lead to increased losses in the inverter. In the case of FM&PS control, the angle is maintained, but at the expense of changing the frequency from 230 to 267 kHz, which complicates filtering and reduces the optimization of the reactive elements of the resonant circuit. Lastly, VT&PS control is able to maintain the angle by adapting the circuit impedance with an increase in the transformer ratio from 12.5 to 14.3, allowing for a fixed frequency with ZVS.

Finally, to conclude the comparison among the three types of control and validate the design discussed in the article, the inverter efficiency was measured across the entire power range by calculating the difference between the input power measured directly at the DC voltage supply and the output power measured by instantaneously multiplying the voltage and output current of the inverter bridge using the DSO [31]. Starting from maximum power, as shown in Figure 10, both FM&PS and VT&PS controls achieve the same efficiency because the transformer ratio and frequency are identical. On the other hand, the PS control begins with lower efficiency due to its higher phase shift angle between the voltage and current and the higher frequency. However, as the power decreases, VT&PS control gradually increases its efficiency due to impedance matching by increasing the transformer ratio, unlike FM&PS control, which achieves lower efficiency due to increased output current and frequency. This demonstrates a superior performance of over 99% across the entire operating range, which is higher with VT&PS control compared to FM&PS. As observed in the figure, the measurements closely align with the theoretically calculated values despite the dispersion in real components and the losses not accounted for in the theoretical calculation.

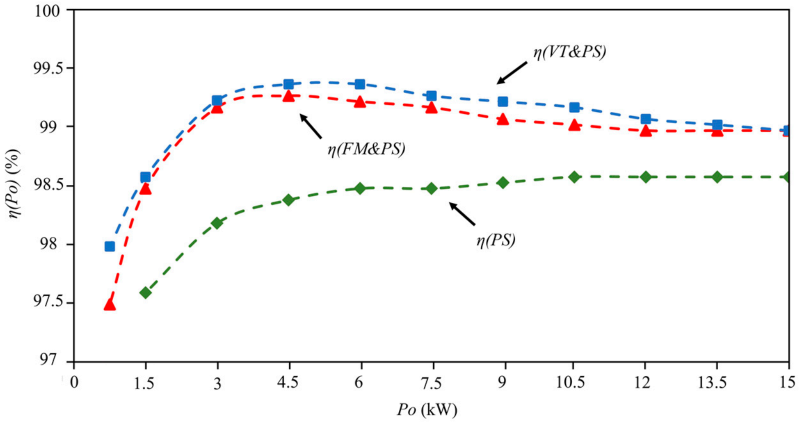

Figure 10. The results of the experimental measurements of the inverter efficiency across the entire power range.

6. Conclusions

This work introduces a novel control technique (VT&PS) which, through the use of a current controlled variable transformer and phase shift, allows for fixed frequency operation close to the resonant frequency in a series LC resonant. This allows for higher efficiency over the entire operating range, a low switching angle, and operation over a wide range of loads while maintaining ZVS.

A new variable transformer design, integrated with a series LC resonant design for induction heating applications, is analyzed and mathematically modeled. The optimal operating point at which the inverter output current is reduced and the implementation of the inverter control scheme are proposed.

The design is corroborated by measuring the values of the transformer inductances and using it together with a 15 kW induction heating inverter with SiC Mosfets and the proposed control. The efficiency and load change behaviors are measured for the proposed control and the two conventional alternatives.

This demonstrates that the inverter is capable of operating at a fixed frequency, close to the resonant frequency, with a fixed angle that reduces the output current, achieving an efficiency of over 99%, and that it is able to operate in the face of the load changes effects common in induction heating applications.

Author Contributions: Conceptualization, J.L.B.; methodology, J.L.B.; software, J.L.B. and J.J; validation, V.E. and J.J.; formal analysis, V.E.; investigation, J.L.B.; resources, V.E.; data curation, J.J.; writing—original draft preparation, J.L.B.; writing—review and editing, J.L.B. All authors have read and agreed to the published version of the manuscript.

Funding: This research received no external funding.

Data Availability Statement: Data are contained within the article.

Conflicts of Interest: Author Juan L. Bellido was employed by the company SiCtech Induction. The remaining authors declare that the research was conducted in the absence of any commercial or financial relationships that could be construed as a potential conflict of interest.

References

1. Lucia, O.; Maussion, P.; Dede, E.J.; Burdio, J.M. Induction Heating Technology and Its Applications: Past Developments, Current Technology, and Future Challenges. *IEEE Trans. Ind. Electron.* **2014**, *61*, 2509–2520. [CrossRef]
2. Rudnev, V.; Loveless, D.; Cook, R.; Black, M. *Hand Book of Induction Heating*; CRC Press: Boca Raton, FL, USA, 2017.
3. Esteve, V.; Bellido, J.L.; Jordán, J. State of the Art and Future Trends in Monitoring for Industrial Induction Heating Applications. *Electronics* **2024**, *13*, 2591. [CrossRef]
4. Rasheed, F.A.; Abdulbaqi, I.M. Analysis of a Current-Fed Parallel Resonant Inverter for Induction Heating Applications. In Proceedings of the IEEE 2021 1st Babylon International Conference on Information Technology and Science (BICITS), Babil, Iraq, 28–29 April 2021.
5. Esteve, V.; Jordán, J.; Dede, E.J.; Bellido, J.L. Enhanced Asymmetrical Modulation for Half-Bridge Series Resonant Inverters in Induction Heating Applications. *IET Power Electron.* **2023**, *16*, 2482–2491. [CrossRef]
6. Esteve, V.; Jordán, J.; Dede, E.J.; Martinez, P.J.; Ferrara, K.J.; Bellido, J.L. Comparative Analysis and Improved Design of LLC Inverters for Induction Heating. *IET Power Electron.* **2023**, *16*, 1754–1764. [CrossRef]
7. Grajales, L.; Sabaté, J.A.; Wang, K.R.; Tabisz, W.A.; Lee, F.C. Design of a 10 kW, 500 kHz Phase-Shift Controlled Series-Resonant Inverter for Induction Heating. In Proceedings of the IEEE Industry Applications Society Annual Meeting, Toronto, ON, Canada, 2–8 October 1993; pp. 843–849.
8. Acero, J.; Burdio, J.M.; Barragan, L.A.; Navarro, D.; Llorente, S. EMI Improvements Using the Switching Frequency Modulation in a Resonant Inverter for Domestic Induction Heating Appliances. In Proceedings of the IEEE 35th Annual Power Electronics Specialists Conference, Aachen, Germany, 20–25 June 2004.
9. Grajales, L.; Lee, F.C. Control System Design and Small-Signal Analysis of a Phase-Shift Controlled Series-Resonant Inverter for Induction Heating. In Proceedings of the IEEE Power Electronics Specialist Conference (PESC), Atlanta, GA, USA, 18–22 June 1995; pp. 450–456.
10. Ahmed, N. High Frequency Soft Switching AC Conversion Circuit with Dual Mode PWM/PDM Control Strategy for High Power IH Applications. *IEEE Trans. Ind. Electron.* **2011**, *58*, 1440–1448. [CrossRef]
11. Dudrik, J.; Trip, N.-D. Soft-Switching PS-PWM DC–DC Converter for Full-Load Range Applications. *IEEE Trans. Ind. Electron.* **2010**, *57*, 2807–2814. [CrossRef]
12. Yang, X.; Sha, D. Automatic Current Limit Strategy for LLC DC-DC Converter for Overload Operation. *IEEE Trans. Power Electron.* **2024**, *39*, 9917–9928. [CrossRef]
13. Bellido, J.L.; Esteve, V.; Jordán, J. Efficiency Optimization in Parallel LLC Resonant Inverters with Current-Controlled Variable-Inductor and Phase Shift for Induction Heating. *Electronics* **2024**, *13*, 2593. [CrossRef]
14. Sun, N.; Chen, D.Y.; Lee, F.C.; Gradzki, P.M.; Knights, M.A. Forward Converter Regulator Using Controlled Transformer. *IEEE Trans. Power Electron.* **1996**, *11*, 356–364.
15. Suarez, C.; Bernal, D.; Martinez, W. Analysis and Validation of Variable Transformers. In Proceedings of the 2021 IEEE 30th International Symposium on Industrial Electronics (ISIE), Kyoto, Japan, 20–23 June 2021.
16. Scire, D.; Lullo, G.; Vitale, G. EMI Filter Re-Design in a SMPS with Inductor in Saturation. In Proceedings of the 2021 IEEE 15th International Conference on Compatibility, Power Electronics and Power Engineering (CPE-POWERENG), Florence, Italy, 14–16 July 2021; pp. 1–7.
17. Scirè, D.; Lullo, G.; Vitale, G. Non-Linear Inductor Models Comparison for Switched-Mode Power Supplies Applications. *Electronics* **2022**, *11*, 2472. [CrossRef]
18. Medini, D.; Ben-Yaakov, S. A Current-Controlled Variable-Inductor for High Frequency Resonant Power Circuits. In Proceedings of the IEEE Applied Power Electronics Conference Exposition (ASPEC), Orlando, FL, USA, 13–17 February 1994; Volume 1.
19. Bernal, D.; Tian, F.; Suarez, C.; Vivert, M.; Martinez, W. Linear Control Compensator for a Variable-Transformer in Wide-Voltage Power Converters. In Proceedings of the 2022 IEEE 31st International Symposium on Industrial Electronics (ISIE), Anchorage, AK, USA, 1–3 June 2022.

20. Suarez, C.; Gerardo, D.; Martinez, W.H. Magnetically Controlled Transformer With Variable Turns Ratio and Low Series-Inductance: Analysis and Implementation towards Its Application in SMP. *IEEE Trans. Power Electron.* **2023**, *38*, 14360–14374.
21. Perdigão, M.S.; Alonso, J.M.; Vaquero, D.G.; Saraiva, E.S. Magnetically Controlled Electronic Ballasts with Isolated Output: The Variable Transformer Solution. *IEEE Trans. Ind. Electron.* **2011**, *58*, 4117–4129. [CrossRef]
22. Pajnić, M.; Pejović, P.; Aleksić, O. Design and Analysis of a Novel Coupled Inductor Structure with Variable Coupling Coefficient. *IET Power Electron.* **2018**, *11*, 961–967. [CrossRef]
23. Zhang, Z. Coupled-Inductors Magnetic in Power Electronics. Ph.D. Thesis, California Institute of Technology, Pasadena, CA, USA, 7 October 1986.
24. Rim, C.T.; Mi, C. Coupled Coil Model. In *Wireless Power Transfer for Electric Vehicles and Mobile Devices*, 1st ed.; John Wiley & Sons, Ltd.: Hoboken, NJ, USA, 2017.
25. Wilson, P.R. Modelling and Simulation of Magnetic Components in Electric Circuits. Ph.D. Thesis, Department of Electronics and Computer Science, University of Southampton, Southampton, UK, November 2001.
26. Rapoport, E.; Pleshivtseva, Y. *Optimal Control of Induction Heating Process*; CRC Press: Boca Raton, FL, USA, 2006.
27. O'Reilly, J. *Multivariable Control for Industrial Applications*; Peter Peregrinus Ltd.: London, UK, 1987.
28. Boubaker, O.; Zhu, Q.; Mahmoud, M.S. *New Trends in Observer-Based Control: A Practical Guide to Process and Engineering Applications*; Academic Press: Cambridge, MA, USA, 2019.
29. Esteve, V.; Jordan, J.; Sanchis, E.; Dede, E.J.; Maset, E.; Ejea, J.B.; Ferreres, A. Improving the reliability of series resonant inverters for induction heating applications. *IEEE Trans. Ind. Electron.* **2014**, *61*, 2564–2572. [CrossRef]
30. Alonso, J.M.; Perdigão, M.S.; Vaquero, D.G.; Calleja, A.J.; Saraiva, E.S. Analysis, Design, and Experimentation on Constant-Frequency DC-DC Resonant Converters with Magnetic Control. *IEEE Trans. Power Electron.* **2012**, *27*, 1369–1382. [CrossRef]
31. Esteve, V.; Jordan, J.; Dede, E.J.; Sanchis-Kilders, E.; Martinez, P.J.; Maset, E.; Gilabert, D. Optimal LLC inverter design with SiC MOSFETs and phase shift control for induction heating applications. *IEEE Trans. Ind. Electron.* **2022**, *69*, 11100–11111. [CrossRef]

Artículo 3:

[27] **Bellido, J.L.**; Esteve, V.; Jordán, J. Reactive Elements Control in LC Series Resonant Inverters by Current-Controlled Variable-Transformer and Magnetic Energy Recovery Switch for Induction Heating. Electronics 2024, 13, 4666.
https://doi.org/10.3390/electronics13234666

electronics

Article

Reactive Elements Control in LC Series Resonant Inverters by Current-Controlled Variable-Transformer and Magnetic Energy Recovery Switch for Induction Heating

Juan L. Bellido [1,2,*], Vicente Esteve [1] and José Jordán [1]

[1] Department of Electronic Engineering, University of Valencia, Av. University s/n, 46100 Valencia, Spain
[2] R&D Department, SiCtech Induction, 46980 Paterna, Spain
* Correspondence: juanbe5@alumni.uv.es or jbellido@sictechinduction.com

Abstract: This work consists of the analysis and design of a LC series resonant inverter with reactive element control for induction heating hardening applications. This novel method uses a current-controlled variable transformer (VT) to control the reflected inductance of the inductor in the resonant, and a magnetic energy recovery switch (MERS) to vary the influence of the capacitor as a reactive power compensation element. This converter topology allows quality factor (Q) or operating frequency (f_{sw}) to be adjusted, making it possible to harden workpieces of different geometries and materials with a single converter. In the article, the design of both elements will be studied and tested. Experimental results were carried out with a 10 kW induction heating inverter prototype, with a frequency range of 60 kHz to 100 kHz and a quality factor of 6 to 10, measuring efficiencies above 95%.

Keywords: LC resonant inverters; induction heating; current-controlled variable-transformer; magnetic energy recovery switch; PS power control; silicon carbide (SiC) power MOSFETs

check for updates

Citation: Bellido, J.L.; Esteve, V.; Jordán, J. Reactive Elements Control in LC Series Resonant Inverters by Current-Controlled Variable-Transformer and Magnetic Energy Recovery Switch for Induction Heating. *Electronics* **2024**, *13*, 4666. https://doi.org/10.3390/electronics13234666

Academic Editors: Luis M. Fernández-Ramírez, Fabio Corti, Ahmed Abu-Siada, Jean-Christophe Crebier, Zhiwei Gao, Kai Fu and Eladio Durán Aranda

Received: 4 October 2024
Revised: 18 November 2024
Accepted: 21 November 2024
Published: 26 November 2024

1. Introduction

The influence of induction heating at industrial level has increased due to the transition towards less polluting systems that do not rely on non-renewable energies such as gas, which was one of the main energy sources for heat treatment of metal pieces. Within induction heating applications, scan hardening is one of the most challenging, as this surface heat treatment of workpieces has to harden only the surface part without affecting the internal part of the workpiece, in order to increase the abrasion and fatigue resistance without affecting the hardness and flexibility of the internal part of the workpiece [1]. Surface hardening consists of subjecting the workpiece to be heated to a magnetic field generated by a coil called heating inductor, powered by a high current and high-frequency power supply. Foucault or Eddy currents induced inside the workpiece cause heat due to Joule and hysteresis losses. The depth of the heated zone depends on the frequency of the current due to the skin effect as well as the heat conduction and magnetic property.

The advent of the electric vehicle has led to the development of new hardening scanning systems due to the appearance of parts with complex geometries that must withstand the torque of electric motors, such as cogwheel, gears and splined hubs, with the added difficulty that they are combined into a single shaft shaped part that must be hardened at different frequencies, see Figure 1. The most basic heating systems base their operation on adjusting the resonant tank by changing transformer taps or by making combinations of series and parallel capacitors to reach the optimum operating point. The problem is that these manual changes cannot be made during the heating process, so they are only optimal if the working load does not physically change or modify its electrical resistive properties during heating, which is not true in a real induction heating process. Until now, the sequential use of dual frequencies has been considered [2], a medium frequency (MF) to heat the quasi-cylindrical zone close to the surface of the workpiece and a high frequency (HF) to heat the surfaces closer to the inductor, such as the tip and flanges of the teeth. But this process requires two resonant tanks with two different inductors and two power supplies, which means having four reactive elements set at two working frequencies, as well as needing a fast mechanical transfer system of the workpiece between the two inductors (Figure 2a).

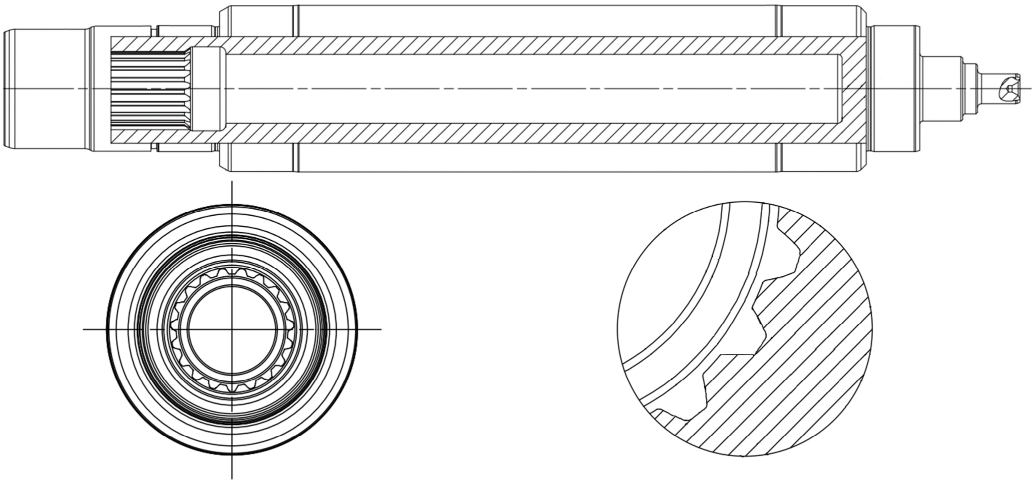

Figure 1. Drive Spline Shaft scheme for Electric Vehicle.

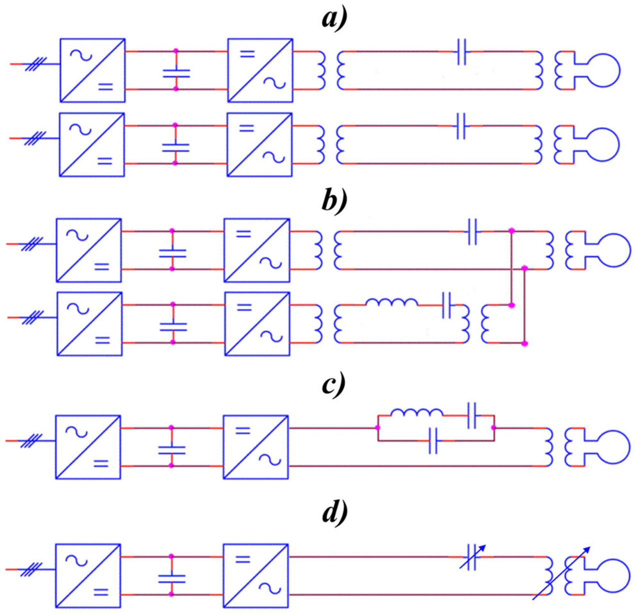

Figure 2. Multiple frequency converter topologies. (**a**) Dual frequency independent, (**b**) Dual frequency with single inductor, (**c**) Dual frequency with single converter and (**d**) Variable frequency with reactive element control.

As an alternative to this topology, several authors have proposed different combinations of resonant tanks and power supplies, in [3] they propose a common inductor for both resonant tanks, but it is still necessary to have four reactive elements and two power supplies (Figure 2b). Another improvement was introduced in [4], where using the same inductor and a sinusoidal pulse width modulation (SPWM), one of the power supplies can be dispensed with, at the cost of having to keep the four reactive elements and losing the zero-voltage soft switching (ZVS) (Figure 2c). These proposals are currently used in the industry, but they have drawbacks such as being limited by design to only two hardening frequencies, which does not make them valid for parts with variable geometries like the one in Figure 1. Furthermore, all of them use variable frequency modulation (FM) [5,6] or combinations of variable frequency with phase shift (FM-PS) [7,8]. As demonstrated, the heat generated by the induced currents in the workpiece is concentrated in a surface layer of thickness δ, which is the penetration depth and is defined by

$$\delta = \sqrt{\frac{\rho}{\pi \mu f}}\,, \tag{1}$$

where μ is the magnetic permeability ρ is the electrical resistivity of the part and f is the applied frequency, which means that if during heating the frequency varies due to modulation, the depth of penetration varies, which can invalidate the workpiece. Figure 3 shows the penetration depth of 1040 carbon steel as a function of frequency. To address this problem, several authors have focused their studies on fixed frequency induction systems. In [9] the output power of the inverter is regulated only by the phase shift (PS), with the drawback that the system loses ZVS soft switching if the applied power decreases or load changes are performed. In [10] a narrow frequency range is used, which combines PS with small frequency variations, thus improving the efficiency of the inverter and further optimising the resonant tank. In [11], a topology of three reactive elements LLC is used, with the series inductance being a current-controlled variable inductor, which together with the PS allows the output power to be regulated without varying the frequency, increasing the efficiency of the converter over the entire operating range and maintaining the switching in ZVS even with load changes. However, this topology has the disadvantage of having to use three reactive elements for a single frequency. Finally, in [12] another solution is proposed to keep the frequency fixed and improve efficiency by using a current-controlled variable transformer, which allows the impedance of the load to be adapted at any moment. However, despite the availability of solutions to regulate the power at a fixed frequency, these solutions only allow the part to be heated at one frequency, which does not make them suitable for hardening complex geometries or parts with different materials.

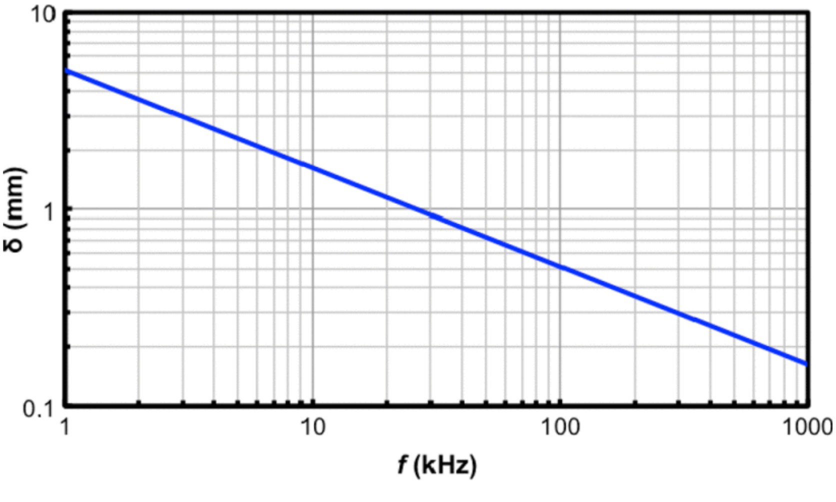

Figure 3. Penetration depth in carbon steel 1040 in front of frequency.

In contrast of the topologies presented previously, Figure 2a–c, in this article the control of the reactive elements of the resonant tank is proposed, for which a current controlled variable transformer (VT) is used to vary the ratio of the transformer to be coupled to the heating inductor, in order to control the reflected inductance of the inductor in the resonant tank and a magnetic energy recovery switch (MERS) to vary the influence of the capacitor as a reactive energy compensation element, Figure 2d. As studied below, the combination of these elements together with the PS regulation to vary the output power of the inverter, allows switching to the optimum frequency required by the hardening for the depth of penetration taking into account the position of the workpiece and the inductor in the scanning process.

The article is structured as follows. Section 2 analyses the series resonant LC circuit where the influence of the reactive elements in the induction system is analysed. In Section 3, the current controlled variable transformer is analysed and designed, while in Section 4, the MERS is analysed. In Section 5, the resonant tank and the inverter are designed for the specifications of an application, the working principle of the control system is discussed and the theoretical efficiency of the inverter is calculated. In Section 6, experimental tests are performed to validate the design and, finally, conclusions are presented in Section 7.

2. LC Series Resonant Converter Topology

The series LC circuit, common to all the topologies considered previously, is shown in Figure 4. It consists of a heating inductor (L_s) in series with a capacitor (C_P) that compensates the reactive power of the circuit. As can be seen, a transformer is also used to adapt the inductor to the resonant tank by amplifying the inductance. Together with them, a series resistor (R_s) is represented, which represents the value of the equivalent resistance of the piece to be heated.

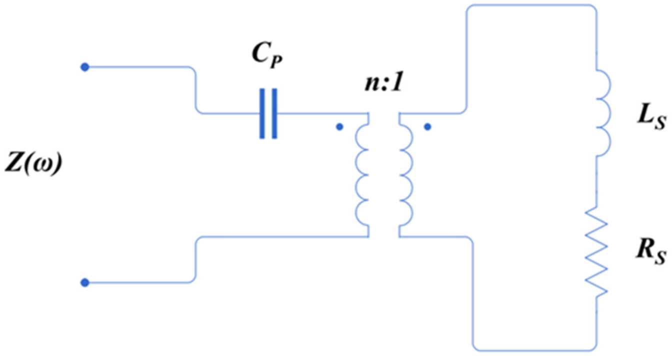

Figure 4. LC series resonant circuit.

The behaviour of the transformer consists in adapting the inductance to the desired capacitor and operating frequency, so that the inductance reflected in the primary of the transformer is expressed as

$$L_p = L_s n^2, \tag{2}$$

where the secondary series inductance (L_s) of the transformer is reflected in the primary multiplied by the square of the transformer turns ratio (n). This effect also occurs with the equivalent resistance reflected from the primary (R_p),

$$R_p = R_s n^2. \tag{3}$$

As can be seen from the following equation, the resonant frequency is affected by the transformation ratio,

$$\omega_o = \omega_p = \frac{1}{\sqrt{L_p C_p}} = \frac{1}{\sqrt{n^2 L_s C_p}}, \tag{4}$$

and also affects the quality factor of the resonant tank for a fix active power

$$Q = \frac{L_p \omega_o {I_o}^2}{P_o} = \frac{n^2 L_s \omega_o {I_o}^2}{P_o}. \tag{5}$$

The quality factor is a decisive parameter in induction heating, it measures the amount of reactive power in the inductor in relation to the active power that can be applied. The choice of the quality factor is determined by aspects such as the material of the workpiece to be heated, the geometry, the type of heat treatment and the coupling between the workpiece and the inductor [13]. In induction heating systems, the inductor has physical dimensions that cannot be varied during heating. Therefore, in the case of parts with irregular dimensions or different material combinations, it is important to choose a quality factor value that allows the part to be correctly coupled throughout the heating process to deliver the desired power. This parameter is important because as is known the reflected impedance of the work piece in the inductor varies during heating, either because of the variable geometry of the part, because it is composed of different materials, because of temperature-dependent changes in the permeability, penetration depth and electrical resistance of the piece, or because of the quality factor of the circuit.

Figure 5a, shows how the shape of the quality factor of a series LC resonant varies as a function of frequency, where the two reactive elements are kept constant. The curve shows at its peak the value of Q that defines its shape. As can be seen, the maximum power deliver occurs at the resonant frequency. On the other hand, Figure 5b shows the effect of varying only the primary reflected inductance of the heating inductor by varying the transformation ratio. Due to the relationship between inductance and frequency in the quality factor, the quality factor increases with increasing inductance. It has to be taken into account that the equivalent series resistor $\left(R_p\right)$ is set to a value that does not exceed the maximum active power of the equipment, in order to achieve this, it is considered that the resistance of the workpiece to be heated is not fixed, as it varies during the heating process to maintain a constant $\left(R_p\right)$. The opposite case is represented in Figure 5c, where the increase in capacitor capacitance causes the resonant frequency to decrease, without being compensated by an increase in inductance, which causes the quality factor to decrease. Therefore, as shown in Figure 5d, the effect of being able to control the two reactive elements of the system ensures that the quality factor is maintained over an entire frequency range, or decreased or increased by varying only one of the two elements and the working frequency.

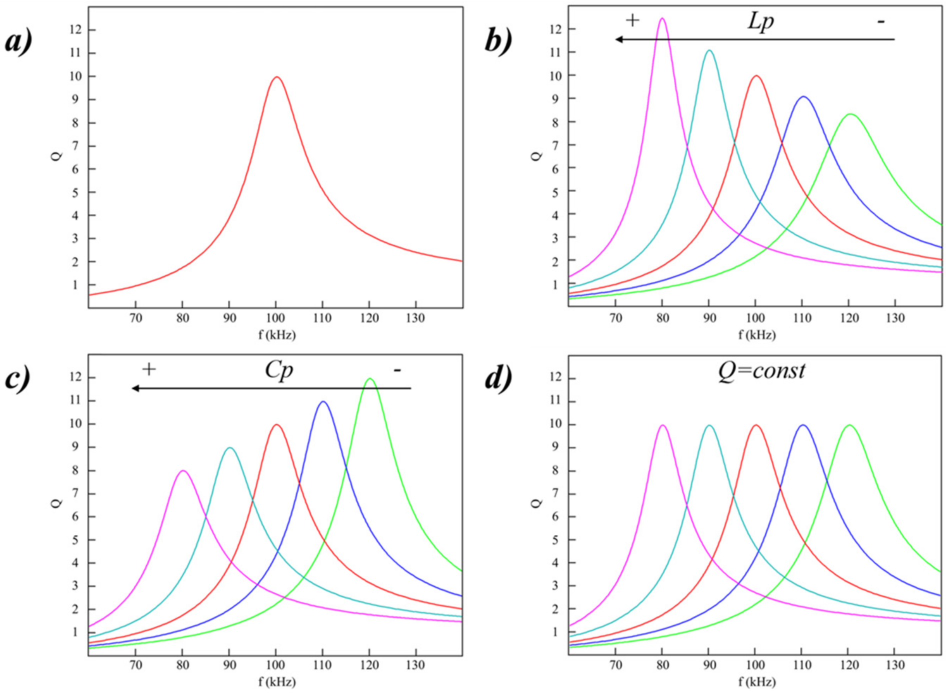

Figure 5. Quality factor behavior for a constant R_p. (**a**) Two elements resonant, (**b**) Resonant with variable transformer, (**c**) Resonant with variable capacitor and (**d**) Resonant with control of the two reactive elements. The peak of the curve corresponds to the quality factor value of the curve.

3. Analysis and Design of Current-Controlled Variable Transformer

The analysis of the current controlled variable transformer has its origin in previous articles [14,15]. Its principle of operation is based on distributing the magnetic flux generated by the primary to the secondary by varying the effective permeability of the core through a path that decreases its reluctance when connected to a direct current source [16], thus increasing the influence of the reluctance of the secondary path, which includes an air gap. In transformer design, core geometry, windings and air gap position have been discussed in numerous articles [17,18]. But for simplicity of design by using a commercial core and because it can be easily modelled mathematically, the one proposed in [12] is used for this work, with the difference that now this transformer will not be used to match the impedance of the resonant, but to match the influence of the inductor inductance in the resonant tank.

The structure used is shown in Figure 6 and uses two «E» shaped commercial cores with a central air gap distributed over the two cores. The primary winding is wound between the two outer legs of both cores, which are linked together. The secondary winding is split between the centre legs of the cores, and their windings are connected in parallel. The two side arms form the saturation control inductor under DC bias, which is wound in series with opposite polarity to decouple the primary and secondary from DC bias, neutralising the influence of magnetic flux and avoiding induced voltages. Therefore, when the core is not subjected to DC bias, the reluctance of the secondary will be lower than that of the primary, as it has an air gap, which causes the magnetic flux to be closed to a lesser extent by the secondary. However, when the core is DC biased, the effective permeability of the core decreases by saturating it and, therefore, its reluctance, so the reluctance of the secondary is higher in relation to that of the core and, therefore, the magnetic flux is closed by this path.

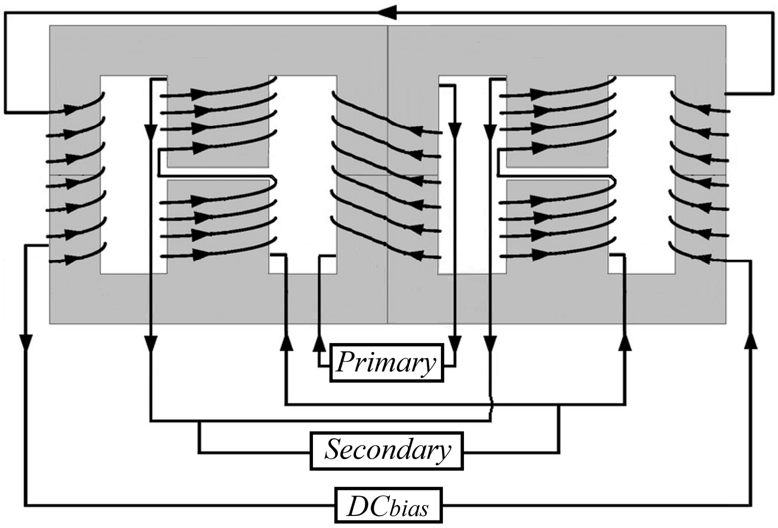

Figure 6. Structure of the Current-Controlled Variable-Transformer.

The mathematical modelling of the transformer is based on the magnetic circuit due to the relationships that balance the ampere-turns and magnetic fluxes. As shown in Figure 7, to maintain symmetry, the primary is analysed as a single core and the secondary as two in parallel.

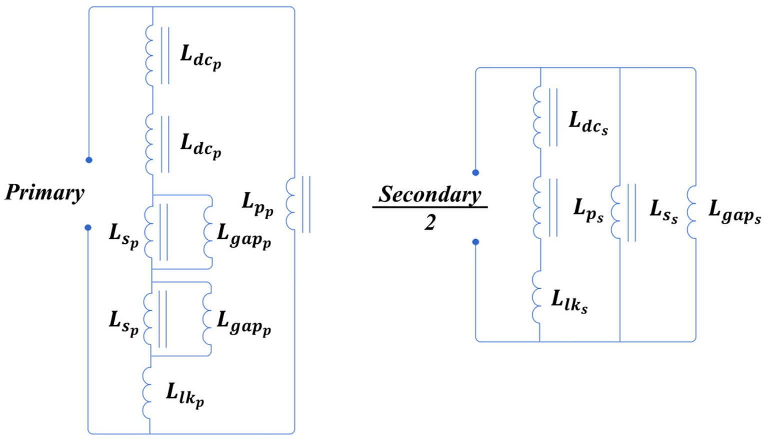

Figure 7. Equivalent inductance circuit of primary at the left and secondary at the right.

As for the primary inductance, it is reflected in primary and secondary by the following expressions,

$$L_{p_p} = \frac{\mu_0 \mu_i A_p (n_p)^2}{l_{p_p}} \text{ and } L_{p_s} = \frac{\mu_0 \mu_i A_p (n_s)^2}{l_{p_s}}, \tag{6}$$

where μ_0 is the air permeability, the initial permeability of the core is μ_i, the effective area of the primary branch corresponds to A_p, n_p and n_s are the number of turns of the primary and secondary and the magnetic path length is l_{p_p} y l_{p_s} for primary to primary and primary arm to the secondary.

The expressions of the inductances of the secondary branches reflected from the primary and the secondary are as follows

$$L_{s_p} = \frac{\mu_0 \mu_i A_s (n_p)^2}{l_{s_p}} \text{ and } L_{s_s} = \frac{\mu_0 \mu_i A_s (n_s)^2}{l_{s_s}}, \tag{7}$$

where the effective area of the secondary branch is A_s, the magnetic path length of the secondary arm corresponds to l_{s_s}, and the magnetic path length from the secondary to the primary arm belongs to l_{s_p}.

The expression of the leakage inductance is also obtained, this inductance belongs to the inductance that closes through the air instead of through the ferrite core and has been obtained experimentally from [16]

$$L_{lk_p} = \frac{\mu_0 16 A_p (n_p)^2}{l_{p_p}} \text{ and } L_{lk_s} = \frac{\mu_0 16 A_s (n_s)^2}{l_{s_s}}. \tag{8}$$

As for the inductance of the saturation control branches it is expressed for primary and secondary as

$$L_{dc_p} = \frac{\mu_0 \widetilde{\mu} A_{dc} (n_p)^2}{l_{dc_p}} \text{ and } L_{dc_s} = \frac{\mu_0 \widetilde{\mu} A_{dc} (n_s)^2}{l_{dc_s}}, \tag{9}$$

where $\widetilde{\mu}$ is the relative permeability under DC bias, the effective area of the saturation control branch is A_{dc} and magnetic path length is l_{dc_p}.

Finally, for both the primary and secondary branches, the inductances due to the air gap located in the secondary branches are expressed as follows

$$L_{gap_p} = \frac{\mu_0 A_{gap} (n_p)^2}{l_{gap}} \text{ and } L_{dc_s} = \frac{\mu_0 \widetilde{\mu} A_{dc} (n_s)^2}{l_{dc_s}}, \tag{10}$$

where A_{gap} is the effective area and l_{gap} correspond to the and magnetic path length of the air gap.

The distribution of the magnetic path lengths is shown in Figure 8.

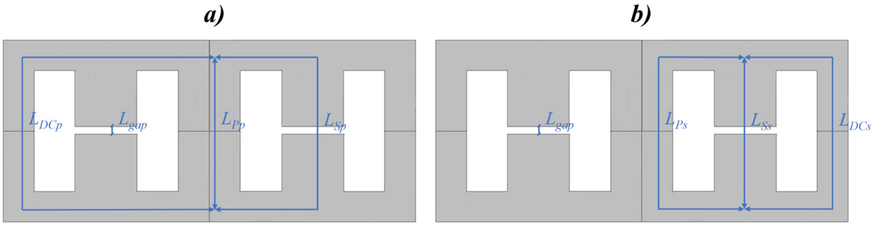

Figure 8. Magnetic path lengths distribution. (**a**) primary side and (**b**) secondary side.

The maximum primary inductance obtained from the equivalent circuit in Figure 4, can be expressed as

$$\frac{1}{L_{p_{max}}} = \left(\frac{1}{L_{p_p}} + \frac{1}{L_{lk_p} + 2L_{dc_p} + \frac{2}{L_{sp} + L_{gap_p}}} \right), \tag{11}$$

while the maximum secondary inductance is given by

$$\frac{1}{2L_{s_{max}}} = \left(\frac{1}{L_{p_s} + L_{dc_s} + L_{lk_s}} + \frac{1}{L_{s_s}} + \frac{1}{L_{gap_s}} \right). \tag{12}$$

To obtain the ratio between the maximum inductance, with the core unsaturated, and the minimum L_{min}, with the core saturated, it must be considered that it is due to the minimum $\widetilde{\mu}$ resulting from the maximum exposure to H_{bias}, because $\widetilde{\mu}$ decreases when exposed to a continuous magnetic field strength. Therefore, the expression for primary is obtained as

$$\frac{L_{p_{max}}}{L_{p_{min}}} = \left(\frac{\frac{1}{2\mu_i} + \frac{6l_{gap}}{2l_{gap}(74+6\mu_i)+3l_{p_s}}}{\frac{1}{2\mu_i} + \frac{24(l_{gap}+l_{p_s})}{2\mu_e l_{gap} l_{p_s}\left(74+4\mu_i+\widetilde{\mu}\right)+1}} \right), \tag{13}$$

and for the secondary as

$$\frac{L_{s_{max}}}{L_{s_{min}}} = \left(\frac{\frac{2\mu_e \frac{l_{s_s}}{l_{s_p}+l_{s_s}}}{\widetilde{\mu}+32} + \frac{\mu_e \frac{l_{s_s}}{l_{s_p}+l_{s_s}}}{\mu_i} + 1}{\frac{2\mu_e \frac{l_{s_s}}{l_{s_p}+l_{s_s}}}{\mu_i+32} + \frac{\mu_e \frac{l_{s_s}}{l_{s_p}+l_{s_s}}}{\mu_i} + 1} \right), \tag{14}$$

where μ_e is obtained from the elementary equation of an inductor and corresponds to the effective relative permeability of the core with a gap,

$$L = \frac{\mu_0 \mu_e A_e n^2}{l}. \tag{15}$$

4. Analysis of Magnetic Energy Recovery Switch

The electronic control of the capacitor of a resonant tank has already been studied in previous works. In [19], a MERS was used in a parallel LC converter to vary the working frequency of the resonant, but using a parallel topology presented the problem of having to use a controlled rectifier with a series inductance to act as a current source for the parallel capacitor. To implement a MERS, four insulated gate bipolar transistors (IGBTs) are used, limiting the maximum frequency to 30 kHz, which is not high enough for small penetration depths. On the other hand, increasing the duty cycle of the capacitor increases its influence on the resonant, decreasing the frequency, which implies a loss of the quality factor, i.e., the ability to deliver power to the part to be heated. In [20] the topology is simplified using a series LC converter, but in this case four IGBTs are used to form the full bridge and another four for the MERS, and the frequency is still limited to 30 kHz and also the quality factor is lost as the frequency decreases. The controllable capacitor topology has also been published in other papers as Gate-Controlled Series Capacitors (GCSC) [21,22], where it is applied to the subsynchronous resonance phenomenon of a steam turbine-generator, but the application frequencies are low, allowing the use of thyristors to control the capacitor. Therefore, and because the desired frequencies for hardening applications are usually in the range of 50 kHz to 100 kHz [1], this work presents a new MERS design that uses only two SiC Metal-Oxide Semiconductor Field-Effect Transistors (MOSFETs) to control the influence of the capacitor. The proposed topology can be seen in Figure 9.

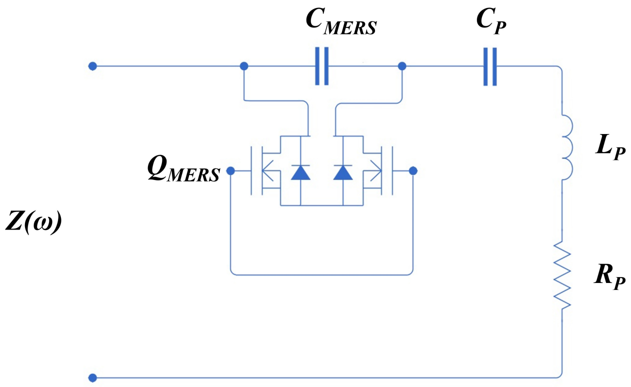

Figure 9. LC series resonant MERS topology.

The operating principle consists of short-circuiting the capacitor during a certain phase to reduce the reactive energy compensation of the capacitor, so that during that instant the voltage provided by the MERS capacitor to the inductor will be zero, due to the fact that no current is flowing through it. To avoid stretches in which the compensated energy is zero, the topology has another capacitor in series (C_s) that maintains the minimum value as current is continuously flowing through it. This effect allows the power applied to the load to be varied without varying the input frequency of the series resonant tank or decrease the resonance frequency of the LC tank by varying the effective capacity of the capacitor.

The conduction angle of the capacitor (γ) is between 0 and π radians, and the reactance of the MERS capacitor can be expressed by the following equation,

$$X_{MERS}(\gamma) = \frac{V_{eff(\gamma)}}{I_{eff(\gamma)}} = X_C\sqrt{\frac{4\pi - 4\gamma + 3\sin(2\gamma) - 2\gamma\cos(2\gamma) + 2\pi\cos(2\gamma)}{2\pi - 2\gamma + \sin(2\gamma)}}, \tag{16}$$

where the effective current of the capacitor is defined as

$$I_{eff(\gamma)} = \frac{I}{\sqrt{\pi}}\sqrt{\int_{\gamma}^{\pi} \sin(\phi)^2 d\phi}, \tag{17}$$

and the effective voltage as

$$V_{eff(\gamma)} = \frac{IX}{\sqrt{\pi}}\sqrt{\int_{\gamma}^{\pi} (-\cos(\phi) + \cos(\gamma))^2 d\phi}. \tag{18}$$

where (X_C) is the reactance of the capacitor used to form the MERS, (I) is the peak current of the capacitor and (ϕ) is the angle between 0 and 2π radians.

Figure 10 shows the typical waveforms of the circuit when it is excited with a square voltage wave and the MERS intervenes to reduce the influence of the capacitor. As can be seen during the MERS conduction period, the voltage of this capacitor cancels out, thus observing a change in the trend of the output current, which is only influenced by the series capacitor.

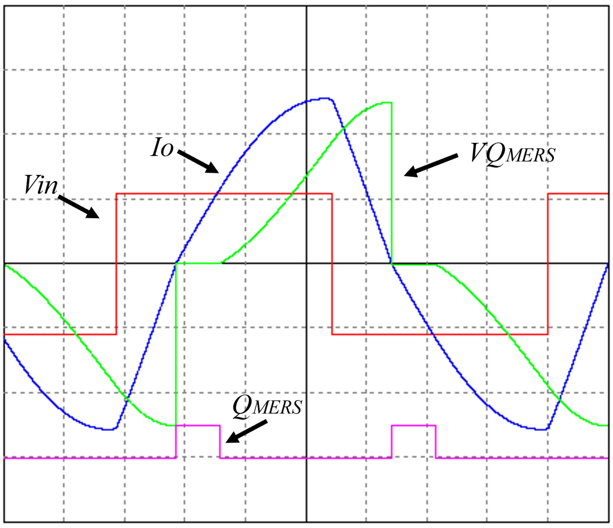

Figure 10. Example of waveforms of the influence of MERS on the serial LC resonant. Blue represents the output current, red shows the input voltage, green shows the capacitor voltage and magenta displays the MERS gate signal.

To avoid losses in MERS, the turn ON of the MOSFETs conduction is synchronised with the zero crossing of the series resonant current, thus making the ON conduction of the transistor without current, which allows ON losses to be neglected. In Figure 11, this effect can be seen in the behaviour of the MERS. As can be seen in the figure, the conduction of the MERS MOSFETS occurs when the current goes through zero. It can also be seen how the current through the capacitor compensation circuit corresponds to the output current, which is the current flowing through the resonant tank.

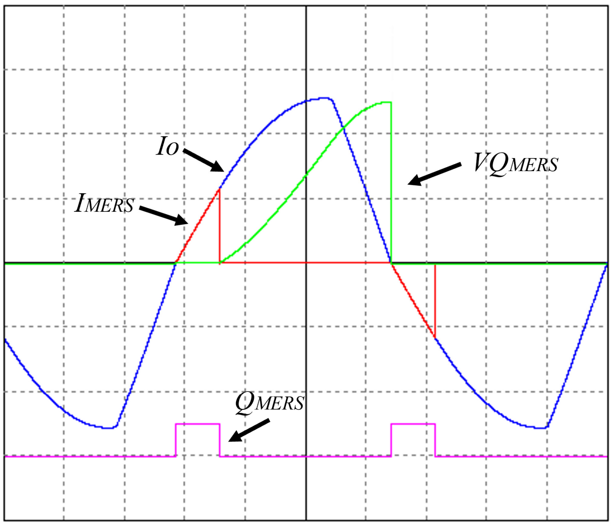

Figure 11. Example of waveforms of MERS operation in the LC series resonant. Blue represents the output current, red shows the MERS current, green shows the MERS voltage on one transistor and magenta displays the MERS gate signal.

5. Reactive Elements Control Inverter Design, Control and Efficiency

5.1. Design Procedure

In practical hardening applications, single coil inductors closely coupled to the workpiece are used. As stated above, the purpose of this design is to use a single heating station with a single inductor, therefore, the inductor geometry, which will be set by a diameter larger than the largest diameter of the part to be heated, will provide the inductance value of the inductor [23]. The diameter of the workpiece will also set the quality factor, as this must increase as the workpiece is decoupled from the inductor to continue applying the desired power to the workpiece [1]. Another characteristic set by the part to be heated is the depth of penetration, which is used to determine the frequency at which the inverter should switch. Table 1 shows the example parameters for the scan hardening of a variable geometry workpiece made of 1040 carbon steel, using a one turn inductor with a diameter of 40 mm.

Table 1. Initial Requirements.

Scan Step	Workpiece Diameter (mm)	Penetration Depth (mm)	Frequency (kHz)	Quality Factor	Maximum Power (kW)
1	23.5	0.7	67	10	6
2	30.2	0.6	77.5	8	9
3	25.5	0.55	89	9	10
4	35	0.5	100	6	10
5	32	0.65	72	7	10

From the initial requirements, the design parameters of the individual heating stages can be obtained. For this purpose, the resonance frequency of the LC tank is obtained by the following equation

$$\omega_o = \frac{2Q\omega_{sw}}{tan\alpha + \sqrt{\tan^2\alpha + 4Q^2}}, \tag{19}$$

where ω_{sw}, is the switching frequency expressed in angular form and α is the phase angle between the output voltage and current of the inverter.

With the power requirement and quality factor, the current that must flow through the inductor can be obtained using the following expression

$$I_L = \sqrt{\frac{P_o Q}{\omega_{sw} L}}, \tag{20}$$

as well as the output current of the inverter,

$$I_o = \frac{P_o}{\frac{2}{\pi}\sqrt{2}V_d \cos\alpha}, \tag{21}$$

where the DC input voltage of the inverter corresponds to V_d. Obtaining from these two the transformer ratio required for each of the heating cycles

$$n = \frac{I_L}{I_o}, \tag{22}$$

and therefore the primary inductance of the transformer is expressed as

$$L' = n^2 L. \tag{23}$$

Therefore, the capacitance value of the combination between the series capacitor C_s and the MERS capacitor C_{MERS}, is expressed as

$$C_{Eq} = \frac{\left(\frac{1}{\omega_o}\right)^2}{L'} . \tag{24}$$

By means of the value of the voltage to be distributed between the two capacitors,

$$V_{C_{Eq}} = \frac{I_o}{\omega_{sw} C_{Eq}} , \tag{25}$$

the value of the two capacitors composing the resonant is selected, so that the equivalent value of the MERS can be obtained by the following expression

$$C_{MERS} = \frac{1}{\frac{1}{C_{Eq}} - \frac{1}{C_s}} . \tag{26}$$

In Table 2, the values resulting from the design can be found, where the capacitance of both capacitors is 0.66 μF.

Table 2. Results of the Design.

Scan Step	Workpiece Diameter (mm)	Inductor Current (Arms)	Transformer Ratio	Equivalent Capacitor (μF)	MERS Capacitance (μF)
1	23.5	567	4.7	0.65	3.58
2	30.2	608	4.77	0.48	1.73
3	25.5	634	4.98	0.33	0.66
4	35	488	3.84	0.45	1.4
5	32	622	4.88	0.53	2.73

Regarding the design of the variable transformer, the selection of the core with the number of turns of the windings is the most important part, as the inductance ratio must be respected. Therefore, the product area, which is defined by the effective area A_e and the winding area A_w, is applied by the following expression

$$A_p = A_e A_w = \frac{V_{C_{Eq}} I_o}{2 f_{sw} B_{max} J K} , \tag{27}$$

where:

B_{max} corresponds to the maximum flux density (T).
J corresponds to the maximum current density (A/m^2).
K is a constant defined between 0.5 and 0.9, indicating the capacity of the winding.

The next step consists of iterating to obtain a less restrictive value than the one used in the area product. To do this, a core of larger dimensions than those calculated in the previous step is chosen, and using the core loss curves at the lowest operating frequency, it is sought that the value obtained for the flux density (B = μH) is less than the maximum, the permeability being that of maximum variation obtained from the curves of variation of the relative permeability under DC bias polarization. Therefore, with the characteristics of the core, the minimum number of turns in the primary is obtained with the following equation:

$$n_p = \frac{V_{C_{Eq}}}{4 f_{sw} B_{max} A_e} . \tag{28}$$

Using Equations (11) and (13), the value of the minimum primary inductance is obtained using the above number of turns. This inductance will correspond to the maximum DC bias inductance [24], which is the minimum open circuit primary inductance $L_{p_{min_{oc}}}$, where 20% can be assumed to be the typical value of the minimum short circuit inductance $L_{p_{min_{cc}}}$ resulting in a minimum primary coupling coefficient (K_p) of 0.8.

$$K_p = 1 - \frac{L_{p_{min_{cc}}}}{L_{p_{min_{oc}}}} \; . \tag{29}$$

Then, the mutual inductance (L_M) is obtained from the following expression

$$L_M = \frac{L_{p_{min_{oc}}} K_p}{1 - K_p} \; . \tag{30}$$

Maximum secondary inductance, reflected from the primary of the transformer, is expressed as

$$L_{sec_{max}} = \frac{\left(L_M / K_p\right)^2}{2L_{p_{min}}} \; . \tag{31}$$

Maximum transformer ratio is obtained from the inductance of the secondary when the primary is short-circuited.

$$L_{s_{min_{cc}}} = \frac{L_{sec_{max}}}{{TR_{max}}^2} \; . \tag{32}$$

The open circuit test value corresponds to the value of the minimum secondary inductance. To obtain it, it is considered that 0.8 is the typical secondary coupling factor (K_s), which allows us to obtain its value with the following expression

$$L_{s_{min_{oc}}} = \frac{L_{s_{min_{cc}}}}{1 - K_s} \; . \tag{33}$$

Therefore using (12) and (14) the number of turns can be obtained.

The value of the minimum transformation ratio is obtained from the minimum primary and secondary coupling coefficients. Because when the core is not exposed to DC bias, the magnetic flux is mostly closed through the outer branches of the core. Resulting in a coupling coefficient (K) of 0.05. This will be experimentally confirmed later when the design is validated.

$$K = \sqrt{K_p K_s}. \tag{34}$$

Given the ratio of the maximum primary and secondary inductances obtained from (11), (13) and (12), (14) gives the minimum transformer ratio

$$TR_{min} = \frac{1}{K} \sqrt{L_{s_{max}} / L_{p_{max}}}. \tag{35}$$

The design will be successful if the minimum ratio obtained is less than or equal to the desired ratio, leading to the last procedure. This consists of reaching the minimum inductance values by means of the value of $\widetilde{\mu}$ used in Equations (13) and (14) in order to determine the necessary H_{bias}.

For this purpose, using the following expression it can be optimize the relationship between the bias current (I_{bias}) and the number of turns of the saturation winding (n_{dc})

$$I_{bias} 2 n_{dc} = H_{bias} 2 l_{dc} \; , \tag{36}$$

where:

H_{bias} is the continuous magnetic field intensity.
l_{dc} is the length of the dc control branch from center to center of the core (m).

To regulate the converter power once the resonant is matched with the variable transformer and MERS, phase shift (PS) control is used. This phase shift varies the voltage applied to the resonant between 0 and 180° and is expressed as (φ). The following expression defines the fundamental harmonic rms output voltage of the inverter

$$V_o(\varphi) = \frac{2\sqrt{2}}{\pi} V_d cos\frac{\varphi}{2}. \tag{37}$$

And, therefore, the output current of the inverter can be expressed as a function of the phase shift, the transformation ratio and the equivalent capacity due to the MERS in-fluence by the following equation

$$I_o(\varphi, TR, C_{Eq}) = \frac{2V_d Q\sqrt{2C_{Eq}L}}{\pi \mathrm{TR}L}\cos\frac{\varphi}{2}\cos(\alpha). \tag{38}$$

In the same way that the output power of the converter is expressed by means of

$$P_o(\varphi, TR, C_{Eq}) = \frac{8{V_d}^2 Q}{\pi^2 TR}\sqrt{\frac{C_{Eq}}{L}}\cos^2\frac{\varphi}{2}\cos^2(\alpha). \tag{39}$$

5.2. Control Operation Principle

The control of the reactive elements has to act on the MERS capacitor to vary the effective capacitance of the resonant, on the variable transformer ratio to increase or decrease the reflected inductance of the inductor in the primary, and on the phase angle to vary the voltage applied to the load. And these act on the control setpoints, i.e., the inverter power and switching frequency, which are set by the part to be heated at each point in the scanning process.

Figure 12 shows the simplified scheme of the proposed control. In the first stage, each input acts independently with its setpoint by means of a proportional integral and differential (PID) control where the first control loop has as input the inverter input power, with which the error is obtained by comparing it with the setpoint. The PID control obtains the phase shift percentage which in the final block will result in the transistors gate signals at the switching frequency. Its behaviour is expressed by the Equation (40). The second control loop is the converter output current, which is compared to the optimum current, Equation (39). This is because the inductor current can vary by the transformer ratio or by the inverter output current, being more optimal to obtain the current by the transformer ratio than by the inverter output, taking into account that the resonance frequency will vary with the transformer ratio. The last block will be responsible for controlling the bias current injected into the transformer. The third control loop is the optimal switching angle, i.e., the angle between the inverter output voltage and the output current, which is expressed by the following equation

$$\omega_{sw} = \omega_o \frac{\tan\frac{\varphi}{2} + \sqrt{\tan^2\frac{\varphi}{2} + 4Q^2}}{2Q}, \tag{40}$$

where the switching frequency must be varied so that the angle α is approximately equal to $\varphi/2$, thus maintaining a constant optimum angle [25]. As shown in the equation and considering the fixed switching frequency as the heating parameter, the system must vary by the MERS the resonant frequency to obtain the optimal value, Equations (4) and (27). Therefore, this loop regulates the MERS duty cycle, adapting to the switching frequency and the zero crossing of the current in the last block.

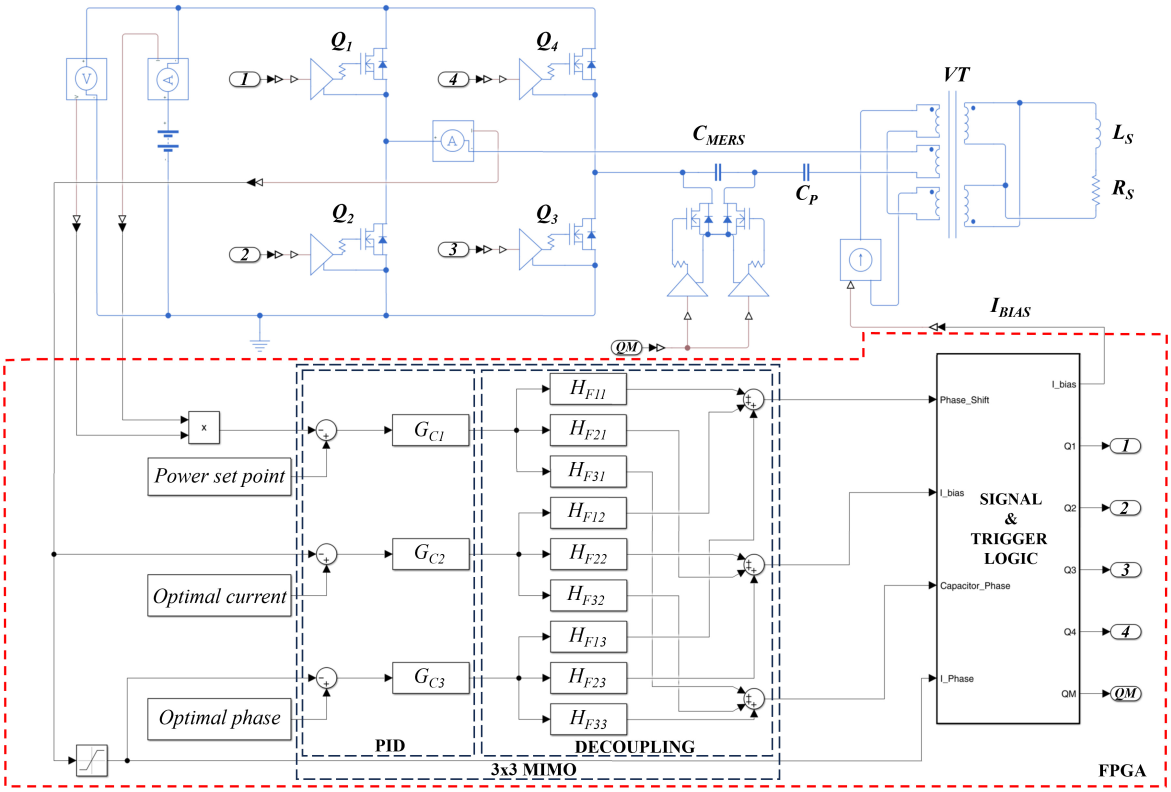

Figure 12. Schematic of the proposed system, detailing the inverter topology, the resonant load LC with the variable inductor, MERS and the control diagram.

As has been observed, the system equations are all related to each other and, therefore, being a 3x3 system, with multiple inputs and multiple outputs (MIMO), a coupled non-linear system is used, where each regulation is decoupled with the diagonalisation network [26,27].

5.3. Losses Analysis

This section analyzes the theoretical losses of the inverter, the MERS and the variable transformer.

As for the inverter losses, the losses due to the current conducted through the channel of the MOSFETs are given by the following expression

$$P_{cd}(\varphi, TR, C_{Eq}) = \left(\frac{I_o(\varphi, TR, C_{Eq})}{\sqrt{2}}\right)^2 R_{DS_{on}}, \tag{41}$$

where $R_{DS_{on}}$ is the ON state MOSFET resistance channel.

The switching losses are due to the OFF losses of the MOSFETs, due to the ZVS operation of the converter, since it switches above the resonance frequency, which makes the ON switching losses negligible. For its analysis the energy is obtained from the polynomial equation of the manufacturer's OFF state switching loss curves for the drain to source voltage equal to V_d and the gate resistance used, resulting in

$$E_{off}(\varphi, TR, C_{Eq}) = aI_c(\varphi, TR, C_{Eq})^2 + bI_c(\varphi, TR, C_{Eq}) + c, \tag{42}$$

where I_c corresponds to the switching current of each transistor and is expressed by the following equation,

$$I_c(\varphi, TR, C_{Eq}) = \frac{2V_dQ\sqrt{2C_{Eq}L}}{\pi \mathrm{TRL}} \cos\frac{\varphi}{2}\cos(\alpha)\sin(\alpha). \tag{43}$$

Therefore, the power losses for each transistor are obtained from

$$P_{sw}(\varphi, TR, C_{Eq}) = E_{off}(\varphi, TR)\frac{\omega_{sw}}{2\pi}\ . \tag{44}$$

In the same way that the conduction losses of the MOSFETs used in MERS are calculated using the following equation

$$P_{MERS_{cd}}(\varphi, TR, C_{Eq}) = \left(I_o(\varphi, TR, C_{Eq})\sin(\gamma)\right)^2 R_{DS_{on}}. \tag{45}$$

As well as only the OFF switching power losses of the transistor is considered

$$E_{MERS_{off}}(\varphi, TR, C_{Eq}) = aI_{MERS_c}(\varphi, TR, C_{Eq})^2 + bI_{MERS_c}(\varphi, TR, C_{Eq}) + c, \tag{46}$$

where the amplitude of the switching current is given by the following expression

$$I_{MERS_c}(\varphi, TR, C_{Eq}) = \frac{2V_d Q\sqrt{2C_{Eq}L}}{\pi \mathrm{TR}L}\cos\frac{\varphi}{2}\cos(\alpha)\sin(\gamma). \tag{47}$$

This results in the following expression for the switching losses

$$P_{MERS_{sw}}(\varphi, TR, C_{Eq}) = E_{off}(\varphi, TR)\frac{\omega_{sw}}{2\pi}. \tag{48}$$

As for the transformer losses, the core losses due to magnetic flux density must be considered, as the influence of DC polarization being negligible [16,28]. Therefore, they can be obtained by means of the following equation

$$P_{TC} = P_{DT}V_T, \tag{49}$$

where P_{DT} is the transformer core loss density given by the manufacturer for the operating frequency and magnetic flux density, and V_T is its volume.

For the P_{TW} copper losses of the transformer, it is necessary to determine the effective resistance of the primary winding R_p and of the secondary winding R_s, taking into account the conductivity, the total length and the skin effect. The losses are obtained by

$$P_{TW} = I_o(\varphi, TR, C_{Eq})^2(R_p + R_s). \tag{50}$$

Finally, the total losses are obtained from

$$\begin{aligned} P_{tot}(\varphi, TR, C_{Eq}) \quad &= 4P_{cd}(\varphi, TR, C_{Eq}) + 4P_{sw}(\varphi, TR, C_{Eq}) \\ &+2P_{MERS_{cd}}(\varphi, TR, C_{Eq}) + 2P_{MERS_{sw}}(\varphi, TR, C_{Eq}) + P_{TC} + P_{TW}, \end{aligned} \tag{51}$$

meanwhile, the efficiency is given by

$$\eta(\varphi, TR) = \frac{P_o(\varphi, TR, C_{Eq})}{P_o(\varphi, TR, C_{Eq}) + P_{tot}(\varphi, TR, C_{Eq})}\ . \tag{52}$$

Figure 13 shows the efficiency evolution in front of output power for the power ranges of each heating scan step. The components selected for the final design were SiC MOSETs from Onsemi Scottsdale AZ with reference NTH4L022N120M3S where four were used for the inverter and two for the MERS. As for the transformer, two E-shaped cores from TDK Electronics Munich Germany with N27 material and 70/33/32 geometry were selected. As can be seen in the plotted results, the higher frequency required in steps 4, 3 and 2 makes the efficiency lower than in the rest, despite working with a resonant tank that adapts to each heating.

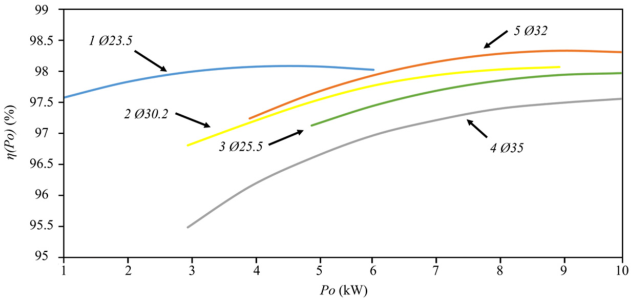

Figure 13. Calculated evolution of the efficiency of the inverter as a function of the output power for each scan step.

6. Experimental Results

For this section, the variable transformer and MERS designs were first verified and then used in the inverter prototype to verify the correct operation of the complete system.

In order to evaluate the design of the transformer, first step was to compare the theoretical values of the maximum and minimum inductance of the primary and secondary inductances with the experimental measurements, in order to check the veracity of the design and verify that the previous assumptions were correct. Table 3 shows these results for the maximum and minimum bias current. Despite observing a small dispersion in the values, the design is correct, since this dispersion is due to the parasitic elements not considered in the design and to the accuracy of the measurement.

Table 3. Theoretical and measured values of transformer inductances.

Control Current	**Theoretical Inductance (µH)**				**Measured Inductance (µH)**			
	Open Circuit		**Short Circuit**		**Open Circuit**		**Short Circuit**	
$I_{dc}\ (A)$	$L_{p_{oc}}$	$L_{s_{oc}}$	$L_{p_{cc}}$	$L_{s_{cc}}$	$L_{p_{oc}}$	$L_{s_{oc}}$	$L_{p_{cc}}$	$L_{s_{cc}}$
0	1103.1	79.37	1.22	0.793	1124.9	82.7	1.14	0.816
1	227.3	34.89	0.544	0.236	232.4	29.53	0.489	0.256

As for the measurements of the entire saturation range of the transformer designed, Table 4, the ratios and variations of its inductances were measured, resulting in a small dispersion that will not affect the operation of the converter and that is due to the same reasons as in the previous results.

Table 4. Theoretical and measured values of transformer ratios.

Control Current	**Theoretical**			**Measured**		
I_{dc} **(A)**	L_p **(µH)**	L_s **(µH)**	**TR**	L_p **(µH)**	L_s **(µH)**	**TR**
0	1103.1	79.37	2	1124.9	82.7	1.82
0.25	478.06	60.45	3	472.89	58.16	3.1
0.5	333.12	42.79	4	327.93	41.68	4.34
0.75	258.32	35.43	5.5	275.5	35.01	5.36
1	227.3	34.89	7	232.4	29.53	6.58

To check the correct operation of the MERS, the voltage of the variable capacitor in operation was measured at the same time as the switching control signal of the capacitor. In Figure 14 below, two oscilloscope screenshots have been taken to show the behavior of the system at two different conditions. As can be seen in the image, the variable capacitor voltage becomes zero when the MERS MOSFETS are in conduction, and it can also be seen that this signal coincides with the zero crossings of the inverter output current.

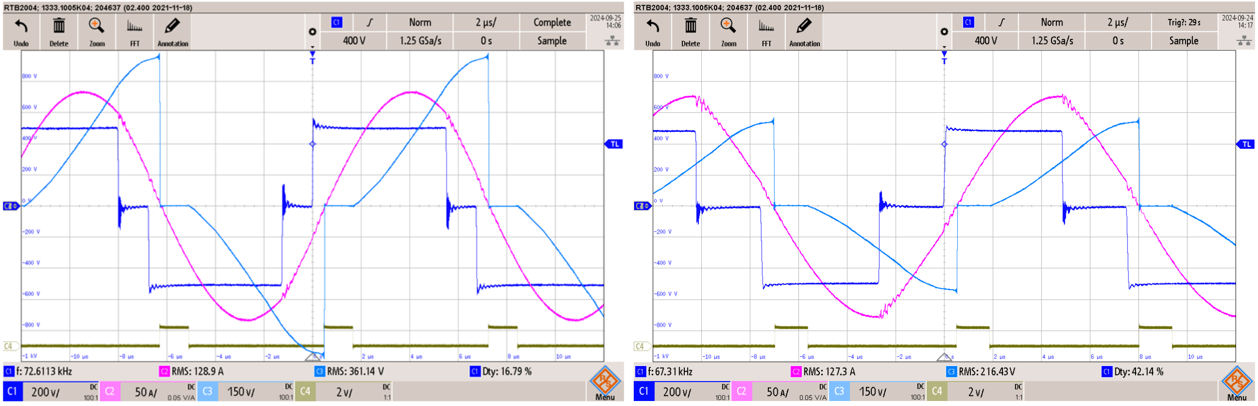

Figure 14. Oscillograms of experimental tests for MERS capacitor at two different conditions. C1 (dark blue) represents the output voltage (200 V/div), C2 (magenta) shows the output current (50 A/div), C3 (light blue) shows the voltage of the MERS capacitor (150 A/div) and C4 (bround) displays the MERS gate logic signal (2 V/div). The time base is 2 us/div.

A 10 kW prototype inverter was used to test the whole system as a whole, which integrates the FPGA with the control, power supplies, firing controllers, sensors, MERS and the controllable current source of the variable transformer. The test bench used is shown in Figure 15, and each number corresponds to:

(1) Induction heating inverter with six SiC NTH4L022N120M3S.
(2) MERS capacitor.
(3) Series capacitor (C_p).
(4) Variable transformer.
(5) Series inductor (L_s).
(6) Set of workpieces.
(7) 300 MHz bandwidth DSO.
(8) Rogowski current probe.
(9) Differential voltage probe.
(10) Hall effect probe.

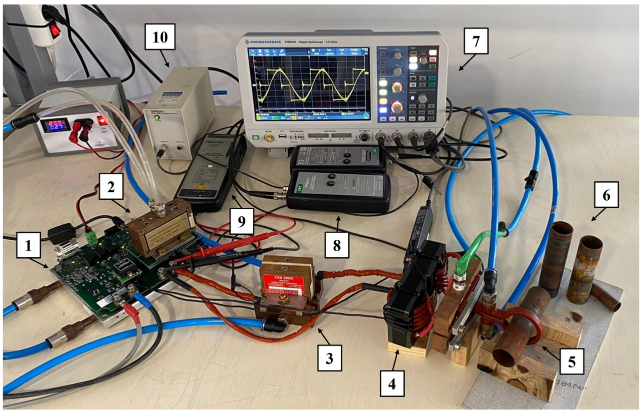

Figure 15. Inverter, MERS capacitor, variable transformer, and LC resonant load test bench. The numbered labels describe the components on the bottom.

In Table 5, the values of the main parameters obtained during the experimental tests of the converter operation have been recorded. In this table, the theoretical values of the design equations have also been added, in order to verify their veracity. Additionally, Figure 16 shows the screenshot of the oscilloscope for each of the measurements. In them it can be seen the converter operation for each step and setpoint of power. How it is observed, the system adapts to the frequency required in each of the steps.

Table 5. Comparison of theoretical and measured results at maximum power and 5 kW.

Scan Step	Power (kW)	Frequency (kHz)		Phase Shift (°)		Transformer Ratio		Equivalent Capacitor (μF)	
		Theor.	Meas.	Theor.	Meas.	Theor.	Meas.	Theor.	Meas.
1	5	67	66.98	79.3	80.46	4.7	4.87	0.66	0.6
	6		67.24	74.4	76.01		4.65		0.65
2	5	77.5	77.62	66.7	67.11	4.77	4.7	0.48	0.47
	9		77.48	38	38.84		4.76		0.47
3	5	89	89.43	60	59.58	4.98	5.11	0.33	0.3
	10		89.57	25.4	26.82		5.03		0.31
4	5	100	101.71	76.6	76.3	3.84	3.71	0.45	0.45
	10		102.3	54	53.89		3.82		0.42
5	5	72	72.17	61.7	63.18	4.88	4.95	0.53	0.5
	10		72.65	28	30.58		4.78		0.52

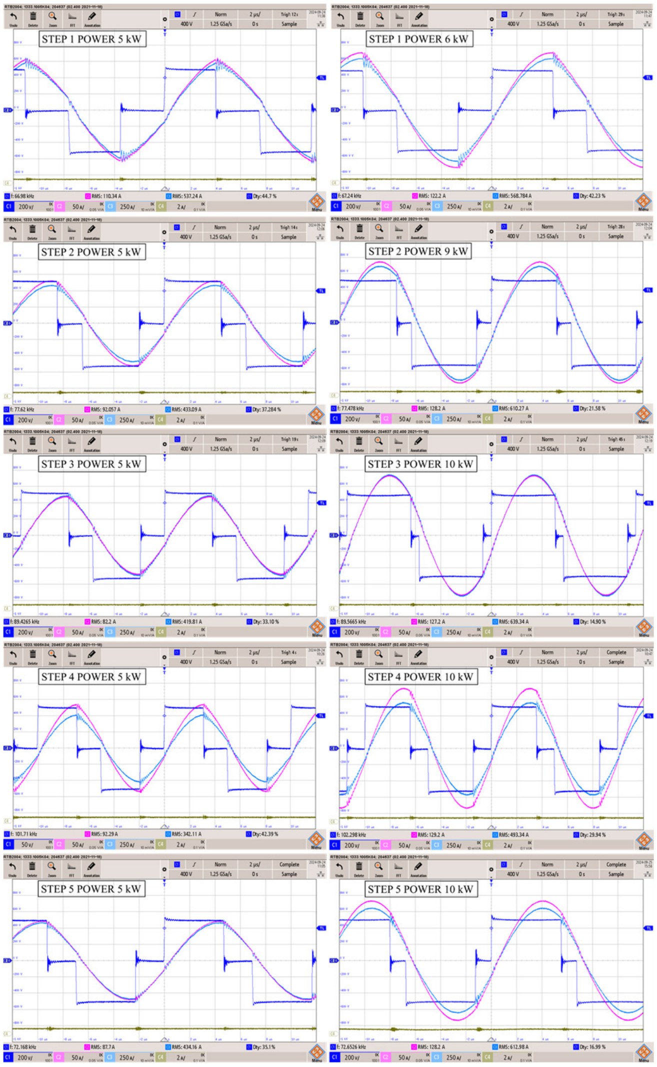

Figure 16. Oscillograms of experimental tests for the LC resonant inverter with rective elements control for different heating steps and power. The left column represents operation at 5 kW, and the right column shows the operation at maximun power. C1 (dark blue) represents the output voltage (200 V/div), C2 (magenta) shows the output current (50 A/div), C3 (light blue) shows the output current at the secondary of the transformer (250 A/div) and C4 (bround) displays the DC bias current (2 A/div) of the variable transformer. The time base is 2 us/div.

Finally, the efficiency of the converter has been recorded for each heating step over the entire power range of each step. As can be seen in Figure 17, the recorded efficiency is similar to the theoretically calculated one, being this one between a percentage range of 98.5% and 95.9%, depending on the desired power and the required frequency in each heating step. As previously obtained, this efficiency has a high correlation with the switching frequency, since heating steps 3 and 4 are the ones that have registered the lowest efficiency, because they occur at frequencies of 89 kHz and 100 kHz respectively.

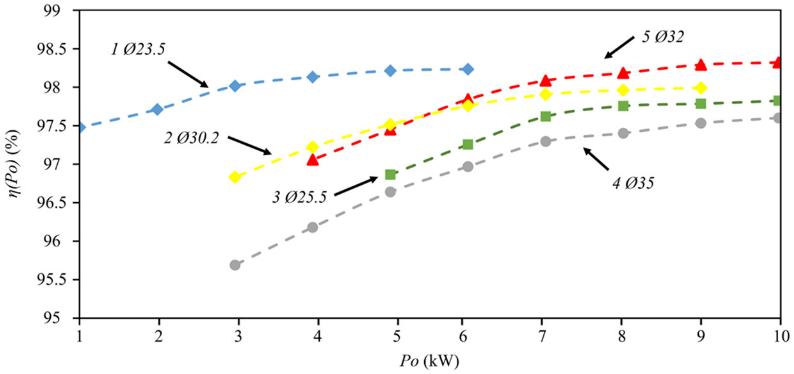

Figure 17. Results of the experimental measurements of the inverter efficiency in the power ranges of each step.

7. Conclusions

This paper presents a novel control method for series inverters in induction heating applications that require hardening of pieces with variable geometries, where the use of one or two frequencies is not sufficient to meet the requirements of the application. This system makes it possible to vary the working frequency maintaining the quality factor and allows the power and the working frequency to be varied independently. For this purpose, a current-controlled variable transformer has been used to adapt the inductor inductance to the resonant tank, a variable capacitor called MERS that varies the reactive power compensation to the inductor and the phase shift control to regulate the converter output power at fixed frequency. In the article, each of the stages has been analyzed and designed and mathematical expressions have been obtained to design and calculate the efficiency of the converter. All this has been experimentally tested with a prototype that has reached 10 kW with a maximum frequency of 100 kHz and a quality factor of 10. The measured efficiency of the system remained in the range of 98.5% and 95.9%.

Author Contributions: Conceptualization, J.L.B.; Methodology, J.L.B.; Software, J.L.B. and J.J.; Validation, J.L.B. and V.E.; Investigation, J.L.B.; Resources, V.E.; Data curation, V.E. and J.J.; Writing—original draft, J.L.B.; Supervision, J.L.B.; Project administration, V.E.; Funding acquisition, J.J. All authors have read and agreed to the published version of the manuscript.

Funding: This research received no external funding.

Data Availability Statement: Data are contained within the article.

Conflicts of Interest: Author Juan L. Bellido was employed by the company SiCtech Induction. The remaining authors declare that the research was conducted in the absence of any commercial or financial relationships that could be construed as a potential conflict of interest.

References

1. Esteve, V.; Bellido, J.L.; Jordán, J. State of the Art and Future Trends in Monitoring for Industrial Induction Heating Applications. *Electronics* **2024**, *13*, 2591. [CrossRef]
2. Zgraja, J. Dual-Frequency Induction Heating Generator with Adjustable Impedance Matching. *IEEE Trans. Ind. Electron.* **2019**, *66*, 8308–8317. [CrossRef]
3. Frania, K.; Kierepka, K.; Kasprzak, M.; Zimoch, P. Single Three-Phase Inverter for Dual-Frequency Induction Heating. *Energies* **2024**, *17*, 2489. [CrossRef]

4. Esteve, V.; Jordan, J.; Sanchis-Kilders, E.; Dede, E.J.; Maset, E.; Ejea, J.B.; Ferreres, A. Comparative Study of a Single Inverter Bridge for Dual-Frequency Induction Heating Using Si and SiC MOSFETs. *IEEE Trans. Ind. Electron.* **2015**, *62*, 1440–1450. [CrossRef]
5. JAcero, J.M.; Burdio, L.A.; Barragan, L.; Navarro, D.; Llorente, S. EMI improvements using the switching frequency modulation in a resonant inverter for domestic induction heating appliances. In Proceedings of the IEEE 35th Annual Power Electronics Specialists Conference, Aachen, Germany, 20–25 June 2004.
6. Esteve, V.; Bellido, J.L.; Jordán, J.; Dede, E.J. Improving the Efficiency of an Isolated Bidirectional Dual Active Bridge DC–DC Converter Using Variable Frequency. *Electronics* **2024**, *13*, 294. [CrossRef]
7. Grajales, L.; Lee, F.C. Control system design and small-signal analysis of a phase-shift controlled series-resonant inverter for induction heating. In Proceedings of the PESC '95—Power Electronics Specialist Conference, Atlanta, GA, USA, 18–22 June 1995; pp. 450–456.
8. Esteve, V.; Jordán, J.; Dede, E.J.; Martinez, P.J.; Ferrara, K.J.; Bellido, J.L. Comparative analysis and improved design of LLC inverters for induction heating. *IET Power Electron.* **2023**, *16*, 1754–1764. [CrossRef]
9. Grajales, L.; Sabaté, J.A.; Wang, K.R.; Tabisz, W.A.; Lee, F.C. Design of a 10 kW, 500 kHz phase-shift controlled series-resonant inverter for induction heating. In Proceedings of the Conference Record of the 1993 IEEE Industry Applications Conference Twenty-Eighth IAS Annual Meeting, Toronto, ON, Canada, 2–8 October 1993; pp. 843–849.
10. Dudrik, J.; Trip, N.-D. Soft-switching PS-PWM DC–DC converter for full-load range applications. *IEEE Trans. Ind. Electron.* **2010**, *57*, 2807–2814. [CrossRef]
11. Bellido, J.L.; Esteve, V.; Jordán, J. Efficiency Optimization in Parallel LLC Resonant Inverters with Current-Controlled Variable-Inductor and Phase Shift for Induction Heating. *Electronics* **2024**, *13*, 2593. [CrossRef]
12. Bellido, J.L.; Esteve, V.; Jordán, J. Performance Enhancement in LC Series Resonant Inverters with Current-Controlled Variable-Transformer and Phase Shift for Induction Heating. *Electronics* **2024**, *13*, 2911. [CrossRef]
13. Lucia, O.; Maussion, P.; Dede, E.J.; Burdio, J.M. Induction heating technology and its applications: Past developments, current technology, and future challenges. *IEEE Trans. Ind. Electron.* **2014**, *61*, 2509–2520. [CrossRef]
14. Sun, N.; Chen, D.Y.; Lee, F.C.; Gradzki, P.M.; Knights, M.A. Forward Converter Regulator Using Controlled Transformer. *IEEE Trans. Power Electron.* **1996**, *11*, 356–364.
15. Suarez, C.; Bernal, D.; Martinez, W. Analysis and Validation of Variable Transformers. In Proceedings of the 2021 IEEE 30th International Symposium on Industrial Electronics (ISIE), Kyoto, Japan, 20–23 June 2021.
16. Medini, D.; Ben-Yaakov, S. A Current-Controlled Variable-Inductor for High Frequency Resonant Power Circuits. In Proceedings of the IEEE Applied Power Electronics Conference Exposition (ASPEC), Orlando, FL, USA, 13–17 February 1994; Volume 1.
17. Suarez, C.; Gerardo, D.; Martinez, W.H. Magnetically Controlled Transformer with Variable Turns Ratio and Low Series-inductance: Analysis and Implementation towards Its Application in SMP. *IEEE Trans. Power Electron.* **2023**, *38*, 14360–14374.
18. Pajnić, M.; Pejović, P.; Aleksić, O. Design and Analysis of a Novel Coupled Inductor Structure with Variable Coupling Coefficient. *IET Power Electron.* **2018**, *11*, 961–967. [CrossRef]
19. TIsobe, Y.; Miyaji, T.; Kitahara; Fukutani, K.; Shimada, R. Soft-switching inverter for variable frequency induction heating using magnetic energy recovery switch (MERS). In Proceedings of the 13th European Conference on Power Electronics and Applications, Barcelona, Spain, 2009; pp. 1–10.
20. Isobe, T.; Shimada, R. New power supply topologies enabling high performance induction heating by using MERS. In Proceedings of the IECON 2013—39th Annual Conference of the IEEE Industrial Electronics Society, Vienna, Austria, 10–13 November 2013; pp. 5046–5051. [CrossRef]
21. de Jesus, F.D.; Watanabe, E.H.; de Souza, L.F.W.; Alves, J.E.R. SSR and Power Oscillation Damping Using Gate-Controlled Series Capacitors (GCSC). *IEEE Trans. Power Deliv.* **2007**, *22*, 1806–1812. [CrossRef]
22. de Souza, L.; Watanabe, E.; Alves, J.; Pilotto, L. Thyristor and gate controlled series capacitors: Comparison of components rating. In Proceedings of the 2003 IEEE Power Engineering Society General Meeting (IEEE Cat. No.03CH37491), Toronto, ON, Canada, 13–17 July 2003; Volume 4, pp. 2542–2547. [CrossRef]
23. Wheeler, H.A. Inductance formulas for circular and square coils. *Proc. IEEE* **1982**, *70*, 1449–1450. [CrossRef]
24. Wilson, P.R. Modelling and Simulation of Magnetic Components in Electric Circuits. Ph.D. Thesis, Department of Electronics and Computer Science, University of Southampton, Southampton, UK, November 2001.
25. Esteve, V.; Jordan, J.; Sanchis, E.; Dede, E.J.; Maset, E.; Ejea, J.B.; Ferreres, A. Improving the reliability of series resonant inverters for induction heating applications. *IEEE Trans. Ind. Electron.* **2014**, *61*, 2564–2572. [CrossRef]
26. O'Reilly, J. *Multivariable Control for Industrial Applications*; Peter Peregrinus Ltd.: London, UK, 1987.
27. Rapoport, E.; Pleshivtseva, Y. *Optimal Control of Induction Heating Process*; CRC Press: Boca Raton, FL, USA, 2006.
28. Alonso, J.M.; Perdigão, M.S.; Vaquero, D.G.; Calleja, A.J.; Saraiva, E.S. Analysis, Design, and Experimentation on Constant Frequency DC-DC Resonant Converters with Magnetic Control. *IEEE Trans. Power Electron.* **2012**, *27*, 1369–1382. [CrossRef]

Anexos. Otras publicaciones relativas a la tesis

Publicación 1:

[57] Esteve, V.; **Bellido, J.L.**; Jordán, J.; Dede, E.J. Improving the Efficiency of an Isolated Bidirectional Dual Active Bridge DC–DC Converter Using Variable Frequency. Electronics 2024, 13, 294. https://doi.org/10.3390/electronics13020294

electronics

MDPI

Article

Improving the Efficiency of an Isolated Bidirectional Dual Active Bridge DC–DC Converter Using Variable Frequency

Vicente Esteve [1,*], Juan L. Bellido [1,2], José Jordán [1] and Enrique J. Dede [1,2]

[1] Department of Electronic Engineering, University of Valencia, Av. University s/n, 46100 Burjassot, Spain; jbellido@sictechinduction.com (J.L.B.); jose.jordan@uv.es (J.J.); enrique.dede@uv.es (E.J.D.)
[2] R&D Department, SiCtech Induction, 46980 Paterna, Spain
* Correspondence: vesteveg@uv.es

Abstract: This article presents a control method for an isolated bidirectional dual active bridge DC–DC converter (IBDC) where single phase shift (SPS) and variable frequency (VF) modulations are combined simultaneously with the purpose of improving the efficiency of the converter applied to the bidirectional charging of electric vehicles batteries. A complete power characterization of the dual active bridge (DAB) converter is carried out. The combined control achieves lossless turn-on and turn-off on the primary bridge for a wide range of output powers. A comparative study of power losses between the traditional SPS control and the combined method proposed here was also carried out. A prototype with an output power of 10 kW was built based on Silicon Carbide (SiC) Metal Oxide Semiconductor Field-Effect Transistors (MOSFET), with which a peak efficiency close to 99% was obtained, thus verifying the viability of the method.

Keywords: power conversion; bidirectional DC–DC converter; battery energy storage; dual active bridge; single phase shift; variable frequency modulation

check for updates

Citation: Esteve, V.; Bellido, J.L.; Jordán, J.; Dede, E.J. Improving the Efficiency of an Isolated Bidirectional Dual Active Bridge DC–DC Converter Using Variable Frequency. *Electronics* **2024**, *13*, 294. https://doi.org/10.3390/electronics13020294

Academic Editors: Tripathi Ravi Nath, Manoj Badoni, Vijay Kumar Singh and Shun-Chung Wang

Received: 11 December 2023
Revised: 1 January 2024
Accepted: 4 January 2024
Published: 9 January 2024

1. Introduction

A successful energy transition requires new strategies and careful planning to integrate all new technologies and devices for the production and storage of electrical energy. This is what some authors call “smart electrification” [1]. In this regard, electric vehicles (EVs) play a relevant role. When electric vehicles are parked and plugged-in, they can supply power to the grid or the owner’s home to meet demand peaks in what are known as vehicle-to-grid (V2G) or vehicle-to-home (V2H) strategies. Additionally, the energy stored in their batteries can help to regulate both the voltage and frequency on the grid. To achieve these capabilities, it is necessary that the converters that connect the grid with the EVs allow the bidirectional flow of energy [2].

Figure 1 shows a diagram that describes the mentioned solution for the case of a single-phase 230 V AC mains supply. The SPBR (single phase bidirectional rectifier) block is connected to the power grid through an inductance. The BDC (bidirectional DC–DC converter) block connects the EV battery to the DC link capacitor. The electronic control of the complete converter allows us to regulate the amplitude and direction of the current I_2 for the given values of the SPBR output voltage V_1 and nominal battery voltage V_2. In a conventional battery charging process, the current I_2 flows from the network to the battery. When the battery energy is used to supply power to the grid, the direction of I_2 is the opposite [3]. It is also possible to integrate renewable energy systems and bidirectional EV chargers to facilitate smart electrification and reduce net operating costs by providing grid support and using the EV battery as a power reserve [4].

The typical topology for the SPBR block consists of a conventional transistorized single-phase full bridge boost rectifier with a pulse width modulation controlled by the input current and output voltage operating at a unity power factor and with power reversal capability [5,6]. For three-phase mains, the preferred solution adopted is based on full bridges of three transistor legs [7,8].

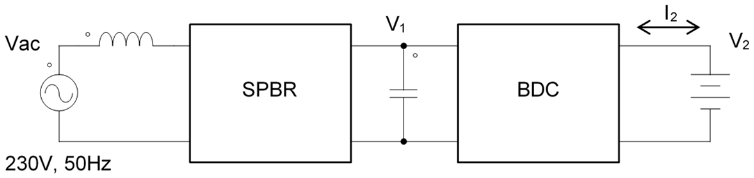

Figure 1. Block diagram of a V2G(H) converter.

The most immediate solution for the BDC consists of a simple bidirectional DC/DC converter [9], but for safety reasons, this converter must have galvanic isolation; these are the isolated bidirectional DC–DC converters (IBDC). The most accepted solution is a converter that uses two full bridges of transistors (dual active bridges—DABs) [10] or two half-bridges (dual active half-fridges—DAHBs) [11] connected so that the output of one is the input of the other. For large power levels, this topology can be optimized by using multiphase DABs [12]. One way to improve efficiency and electromagnetic interference (EMI) emission is the use of resonant DABs [13] or by means of broadband devices such as silicon carbide (SiC) [14] and gallium nitride (GaN) [15].

In DABs, the control and direction of the flow of the transferred power is carried out by shifting the operation of each of the bridges through different control techniques: single phase shift SPS [16], extended phase shift EPS [17], dual phase shift DPS [18] and triple phase shift TPS [19]. All of them are modifications of the SPS method to improve the transmission power capacity and the efficiency of the converter maintaining the zero voltage switch (ZVS) condition and minimizing the circulating current.

To achieve further improvements, hybrid control techniques are used where the DAB is controlled by phase shifting and variable frequency modulations, in sequential or independent mode, to extend the operating range of the converter while maintaining ZVS conditions [20,21] or introducing a circulating current suppression control (CCSC) that affects the DAB power transfer [22]. Ref. [23] proposes the use of a variable frequency control strategy plus an additional control loop to find the point of maximum efficiency for medium frequency (25 kHz). Other authors use variable frequency in a series resonant dual active bridge (SR-DAB) [24] or combining it with triple phase shift (VF-TPS) [25]. In order to further develop the study of these hybrid control techniques, this paper describes a variable frequency non-resonant isolated bidirectional DAB DC–DC converter (VF-IBDC) based on SiC MOSFET transistors operating at high frequency that combines SPS and VF modulations simultaneously so that the switching processes are carried out at zero voltage and also at zero current switching (ZCS) conditions in a wide operating range. In this way, high efficiency peaks, close to 99%, can be obtained with moderate EMI.

The paper is structured as follows: Section 2 focuses on the configuration of the proposed IBDC converter. In Section 3, an analysis of the conventional SPS-IBDC converter is conducted, followed by the analysis and design considerations for the proposed modulation in Section 4. Section 5 presents the comparative analysis of power losses and efficiency of the converters. In Section 6, the proposed VF-IBDC control method is introduced. The validation of results using experimental data is presented in Section 7. Finally, the conclusions are drawn.

2. IBDC Configuration

Figure 2 shows the simplified schematic of the DAB-IBDC converter which consists of two full bridges with active switches in the primary and the secondary sides, connected via the high-frequency transformer T that provides the required galvanic isolation and voltage matching between two voltage levels V_1 and V_2. The inductor L, which also includes the leakage inductance of the transformer, serves as the instantaneous energy storage device. The duty ratio of the switching signal is 50%, but there is a phase shift

ϕ between primary and secondary bridges that defines the amplitude and direction of the power flow. C1 is the DC link capacitor connected to the output voltage V_1 of the SPBR and C2 is the output capacitor of the DAB-IBDC. In this point of voltage V_2, the EV battery is connected. In charge mode, the power flows from C1 to C2. When the battery supplies power to the grid (discharge mode), the power flows in the opposite direction. All transistors are SiC MOSFET.

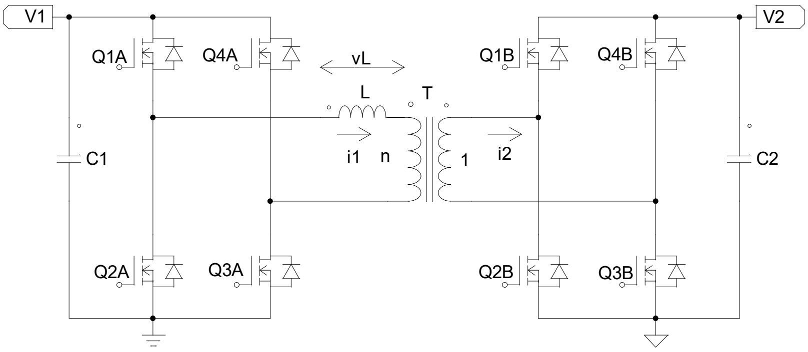

Figure 2. DAB-IBDC configuration.

The design has been made for a fast bidirectional charging application of lithium-ion EV batteries using a typical conventional charging process [26]. Table 1 shows several values that serve as specifications for the converter design. When the converter delivers maximum power in the first phase of the charging process, the output current must be regulated independently of the existing battery voltage.

Table 1. DAB-IBDC specifications.

Specification	Symbol	Value	Unit
Maximum Power	P_{max}	10	kW
Initial Switching Frequency	f	100	kHz
Regulated DC Input Voltage	V_1	385	V
Minimum DC Output Voltage	$V_{2\,min}$	285	V
Maximum DC Output Voltage	$V_{2\,max}$	400	V
Maximum Output Current	I_2	25	A

3. Analysis of the SPS-IBDC

Figure 3 shows the main simplified waveforms of the SPS-IBDC in charge mode (top) and discharge mode (bottom). The black waveforms are the switching signals of transistor Q1A and Q3A in the primary bridge, and Q1B and Q3B in the secondary bridge. The switching signals of Q2A and Q4A, and Q2B and Q4B are delayed by 180°. All of these signals are shown as square signals (with duty cycle D = 0.5) because dead time was not considered to simplify the graph. The blue waveforms represent the voltage across the inductance L, the red waveforms show the output current of the primary bridge, and the green waveforms are the input current of the secondary bridge. Note that the sign of ϕ determines the mode of operation so that if ϕ is positive, the converter acts in charge mode, and if ϕ is negative, it acts in discharge mode.

To extract properties and be able to design the circuit, it is necessary to carry out a complete analysis to obtain the equations that describe the behavior of its voltages and currents. The aim is to obtain a single set of equations that can describe the circuit in charging or discharging operating mode at the same time. The observation of the similarities and differences of the voltage waveforms in the inductance allows us to define two new parameters, δ and $V_2{}^*$, given by

$$\delta = \left| \begin{array}{lll} \varphi & \text{if} & \varphi \geq 0 \\ \varphi + \pi & \text{if} & \varphi < 0 \end{array} \right. \tag{1}$$

$$V_2^* = \left| \begin{array}{rll} V_2 & \text{if} & \varphi \geq 0 \\ -V_2 & \text{if} & \varphi < 0. \end{array} \right. \tag{2}$$

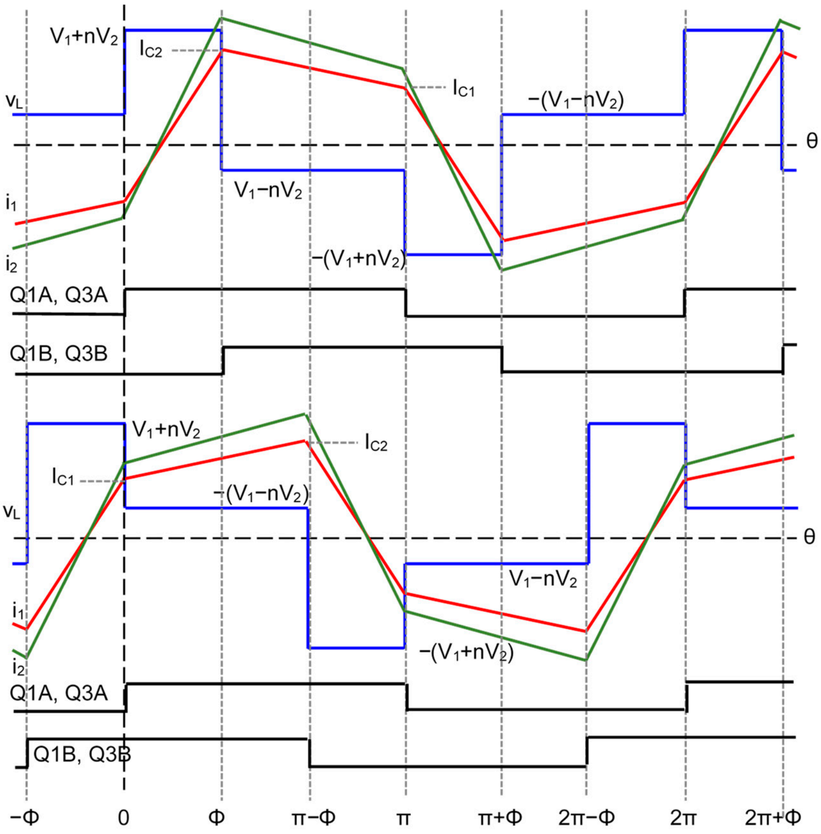

Figure 3. Simplified voltage and current waveforms of SPS-IBDC.

After this, the voltage $v_L(\theta)$ of the inductance and the output current of the primary bridge $i_1(\theta)$ for any operating cycle can be determined by means of next piecewise equations:

$$v_L(\theta) = \left| \begin{array}{lll} V_1 + nV_2^* & \text{if} & 0 \leq \theta < \delta \\ V_1 - nV_2^* & \text{if} & \delta \leq \theta < \pi \\ -(V_1 + nV_2^*) & \text{if} & \pi \leq \theta < \pi + \delta \\ -(V_1 - nV_2^*) & \text{if} & \pi + \delta \leq \theta < 2\pi \end{array} \right. \tag{3}$$

$$i_1(\theta) = \left| \begin{array}{lll} \frac{V_1+nV_2^*}{L\omega}\theta + \frac{nV_2^*(\pi-2\delta)-\pi V_1}{2L\omega} & \text{if} & 0 \leq \theta < \delta \\ \frac{V_1-nV_2^*}{L\omega}\theta + \frac{nV_2^*(\pi+2\delta)-\pi V_1}{2L\omega} & \text{if} & \delta \leq \theta < \pi \\ -\frac{V_1+nV_2^*}{L\omega}\theta + \frac{nV_2^*(\pi+2\delta)+3\pi V_1}{2L\omega} & \text{if} & \pi \leq \theta < \pi + \delta \\ -\frac{V_1-nV_2^*}{L\omega}\theta + \frac{nV_2^*(-3\pi-2\delta)+3\pi V_1}{2L\omega} & \text{if} & \pi + \delta \leq \theta < 2\pi \end{array} \right. \tag{4}$$

with $\omega = 2\pi f$ where f is the switching frequency. Integrating the square of (3) and (4), it is possible to calculate the corresponding root mean square (rms) values:

$$V_{1rms} = \frac{1}{\pi}\sqrt{\delta(nV_1 + V_2)^2 + (\pi - \delta)(V_2 - nV_1)^2} \tag{5}$$

$$I_{1rms} = \frac{\pi}{2\sqrt{3}L\omega}\sqrt{V_1{}^2 + 2nV_1V_2\left(-4\frac{\delta^3}{\pi^3} + 6\frac{\delta^2}{\pi^2} - 1\right) + n^2V_2{}^2} \tag{6}$$

and the values of the switching currents can be obtained:

$$I_{C1} = \frac{\pi V_1 - nV_2(\pi - 2\delta)}{2L\omega} \tag{7}$$

$$I_{C2} = \frac{n\pi V_2 - V_1(\pi - 2\delta)}{2L\omega}. \tag{8}$$

The value of the active power transferred between the primary and the secondary bridges can be obtained by calculating the average value of the instantaneous product of the voltage and the current in the transformer given by:

$$P = \frac{nV_1V_2\delta(\delta - \pi)}{\pi L\omega}. \tag{9}$$

When the phase shift ϕ is 90°, the maximum value of the power is transferred, which is

$$P_{\max} = \frac{n\pi\, V_1V_2}{4L\omega}. \tag{10}$$

Figure 4 shows the evolution of the transferred power in units normalized to the maximum power value given in (10) as a function of the phase ϕ for the minimum and maximum values of the voltage V_2 of the battery. The power transferred during the charging or discharging process at maximum output current (positive or negative) should remain between the two curves.

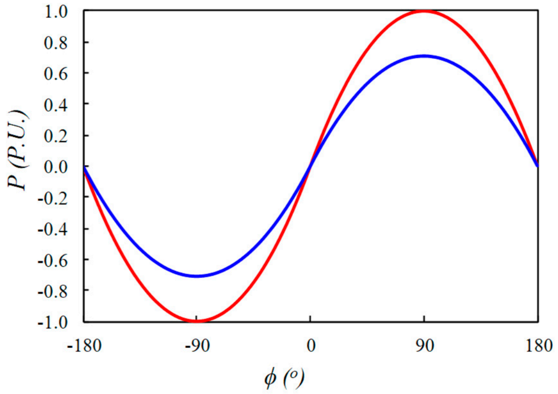

Figure 4. Transferred power of the SPS-IBDC versus phase shift. The red line corresponds to V_2 = 400 V, and the blue line corresponds to V_2 = 285 V.

From (10), the equation that allows the design of the inductance L can be obtained,

$$L = \frac{nV_1V_2}{8P_{\max}f}. \tag{11}$$

To improve the efficiency and reduce the EMI of the converter, it is necessary that the switching of the transistors be carried out in ZVS mode. This is only possible when (4) is positive, which determines a minimum value for the phase given by

$$\delta_{\min} = \frac{\pi\,(nV_2 - V_1)}{2nV_2}; \tag{12}$$

therefore, the range where ZVS is possible is

$$\delta_{\min} < |\varphi| \le \pi/2. \tag{13}$$

Substituting (12) into (9), we got

$$P_{\min} = \frac{V_1(n^2{V_2}^2 - {V_1}^2)}{8nLV_2 f} \tag{14}$$

then, the power range in ZVS mode is determined by

$$P_{\min} < |P| \leq P_{\max}. \tag{15}$$

4. Analysis of the VF-IBDC

In the previous section, conditions were found to keep the primary (or secondary) bridge working in ZVS mode, and it is only possible to obtain ZCS switching for the δ_{min} phase where the waveforms become those shown in Figure 5.

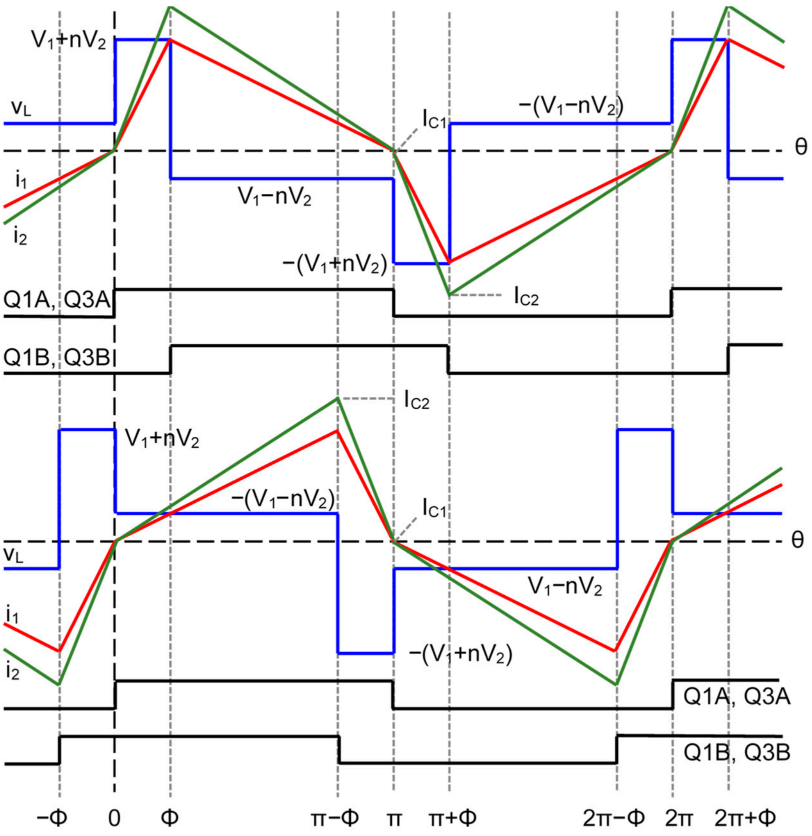

Figure 5. Simplified voltage and current waveforms of VF-IBDC.

The signals in Figure 5 are the same as those in Figure 3, also showing the waveforms in charge mode (top) and discharge mode (bottom). Note that both turn-on and turn-off switching are carried out near the zero crossing of the current. This is an ideal situation where switching losses are minimal. To extend this condition with other power values, we should modify the switching frequency while maintaining the ZVS-ZCS condition with the appropriate adjustment of the phase so that δ meets (12). Therefore, the power is determined by (14) varying the phase shift and the switching frequency simultaneously. This is the concept of hybrid control that we present in the first section of this paper.

To carry out the converter design, the allowed frequency variation range must initially be set. Extending the frequency to very high values would increase the switching losses of the semiconductors and cause excessive conductor losses due to the skin effect, while frequencies that are too low would raise the flux density of the transformer and inductor core, increasing its losses or even causing magnetic saturation. In the present design, the allowed range goes from 100 kHz to 400 kHz for the highest possible range of transferred power.

If the output current I_2 is maintained at its maximum value for any value of battery voltage between V_{2min} and V_{2max}, the following design equation can be obtained to determine the value of the ratio transformer n:

$$n = \frac{V_1}{V_{2\max} V_{2\min}} \sqrt{\frac{k V_{2\max}{}^2 - V_{2\min}{}^2}{k-1}} \tag{16}$$

where $k = f_1/f_2$. Since (14) shows that power is inversely proportional to frequency, values for f_1 and f_2 are chosen in the lower part of the determined range. Given f_1 = 100 kHz and f_2 = 200 kHz, n = 1.65 is obtained.

Now, (11) is not valid and the value of L is obtained by isolating it from (14),

$$L = \frac{V_1 (n^2 V_{2\max}{}^2 - V_1{}^2)}{8 n P_{\max} V_{2\max} f}. \tag{17}$$

Taking into account the values in Table 1 and the value of n in (16), a value of L = 10.48 µH is obtained.

Figure 6 shows the evolution of the absolute value of transferred power in normalized units in function of the switching frequency for the minimum and maximum values of the voltage V_2 of the battery. The power transferred at maximum output current in ZVS and ZCS condition should remain between the two curves.

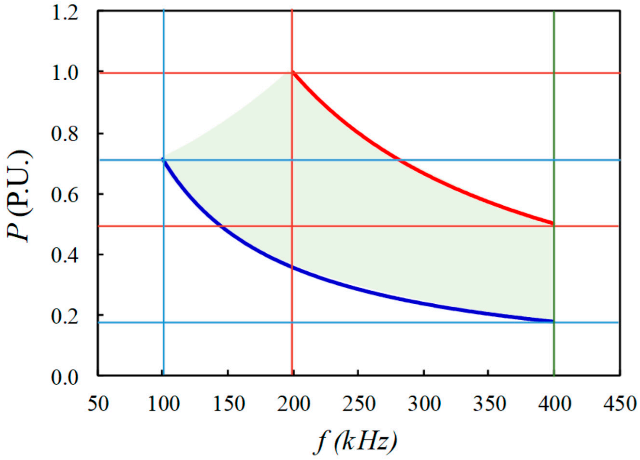

Figure 6. Transferred power of the VF-IBDF converter versus switching frequency. The red line corresponds to V_2 = 400 V, and the blue line corresponds to V_2 = 285 V.

5. Comparative Analysis of Power Losses and Efficiency

A power loss analysis of the SPS-IBDC and VF-IBDC has been carried out considering the contribution of conduction and switching losses of the transistors, and the power losses of the core and the windings of the inductor and the transformer. In this study, residual losses in other non-active components (capacitors, cables, etc.) have not been considered. The analysis of P_{sw} focuses solely on the turn-off losses of the inverter bridge transistors as the turn-on switching losses are negligible due to the ZVS condition [27].

In the practical implementation of the converter, the primary and secondary bridge switches have been configured differently. The primary bridge is made up of four switches with a single transistor; however, as the secondary bridge has more losses, each of its switches has two transistors in parallel. The transistor chosen is the SiC MOSFET C3M0016120K of V_{DS} = 1200 V and R_{Dson} = 16 mΩ.

The losses in the diodes have been neglected since the conduction of the reverse current is also carried out through the transistor channel except during dead times. Thus, conduction losses for each transistor can be calculated only using (18).

$$P_{CD1} = \left(\frac{I_{1rms}}{\sqrt{2}}\right)^2 R_{DSon} \tag{18}$$

$$P_{CD2} = \left(\frac{nI_{1rms}}{2\sqrt{2}}\right)^2 R_{DSon} \tag{19}$$

where P_{CD1} represents the conduction power losses of the primary bridge and P_{CD2} represents the conduction power losses of secondary bridge.

The switching power losses of each transistor of the primary and secondary bridges can be calculated using the graphs of the turn-off switching energy E_{off} provided by the manufacturer using the following polynomial function.

$$E_{off1} = a\ {I_{C1}}^2 + b\ I_{C1} + c \tag{20}$$

$$E_{off2} = a\left(\frac{nI_{C2}}{2}\right)^2 + b\ \frac{nI_{C2}}{2} + c \tag{21}$$

where a, b and c take the following values:

$$a = 0.048\ \mu\text{JA}^{-1/2}$$

$$b = 1.064\ \mu\text{JA}^{-1}$$

$$c = 10\ \mu\text{J}$$

The switching turn-off losses of each transistor can be calculated with

$$P_{SW1} = E_{off1}f \tag{22}$$

$$P_{SW2} = E_{off2}f. \tag{23}$$

On the other hand, the core losses of the inductor can be obtained using next equation:

$$P_{II} = P_{DI}V_{II} \tag{24}$$

where P_{DI} is the core loss density of the inductor given by the manufacturer for the operating frequency and magnetic flux density, and V_{II} is its volume. The inductor core is composed of two pieces of KOOL MU 6527 U core from Magnetics.

Analogously, the losses of the transformer core can be obtained by

$$P_{TI} = P_{DT}V_{TI} \tag{25}$$

where P_{DT} is the core loss density of the transformer, and V_{TI} is its volume. The transformer core is made with two pieces of the uncoated ferrite core U 126/91/20 from Magnetics. In both cases, the designs have been made with a flux density that guarantees non-saturation of the magnetic material. Specifically, the maximum flux density in the inductor core is 190 mT, and it is 100 mT in the transformer core.

In order to calculate the copper losses P_{IC} of the inductor, it is necessary to know the effective resistance of the winding R_I taking into account the conductivity, the total length and the skin effect using

$$P_{IC} = {I_{Irms}}^2 R_I. \tag{26}$$

For the two windings of the transformer, the power loss P_{TC} is given by

$$P_{TC} = {I_{Irms}}^2\left(R_{T1} + n^2R_{T2}\right) \tag{27}$$

where R_{T1} and R_{T2} are the effective resistance of the primary and secondary transformer windings, respectively.

Therefore, the total power loss of the converter is

$$P_{tot} = 4(P_{CD1} + P_{SW1}) + 8(P_{CD2} + P_{SW2}) + P_{II} + P_{TI} + P_{IC} + P_{TC} \tag{28}$$

and the efficiency of the inverter can be calculated using

$$\eta = \frac{P_o}{P_o + P_{tot}} \tag{29}$$

Table 2 shows the calculated results of the power loss analysis for the VF-IBDC converter specified in Table 1 operating at maximum output current.

Table 2. Power loss analysis of VF-IBDC.

Magnitude	**Symbol**	**V_2 = 400 V**	**V_2 = 285 V**	**Unit**
Primary bridge transistor conduction losses	P_{CD1}	7.2	3.6	W
Second. Bridge transistor conduction losses	P_{CD2}	4.9	2.5	W
Primary bridge transistor switching losses	P_{SW1}	2.0	1.0	W
Second. Bridge transistor switching losses	P_{SW2}	28.7	8.7	W
Total primary bridge losses	$4(P_{CD1} + P_{SW1})$	36.8	18.6	W
Total secondary bridge losses	$8(P_{CD2} + P_{SW2})$	269.1	89.6	W
Total inductor core losses	$P_{II} + P_{IC}$	18.6	2.6	W
Total transformer losses	$P_{TI} + P_{TC}$	74.6	10.4	W
Efficiency	η	96.2	98.3	%

Figure 7 shows the evolution of the power losses and the efficiency of the VF-IBDC converter for different values of the output power expressed in normalized units referring to the value of the maximum output power. When the battery has its minimum voltage value (285 V), the loss and efficiency curves are shown in blue, while for the maximum voltage value (400 V), the curves are red. As the maximum charging current is the same in both cases (25 A), the maximum power obtained is reduced from 10,000 W to 7125 W when the battery voltage goes from 400 V to 285 V.

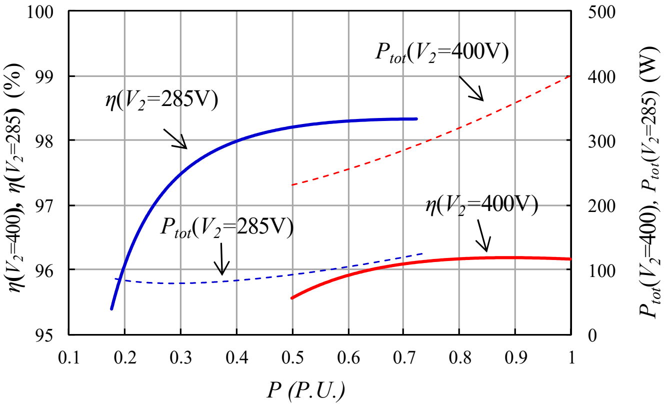

Figure 7. VF-IBDC's total power losses (dashed line) and efficiency (solid line) in front of output power for V_2 = 400 V (red) and V_2 = 285 V (blue).

Table 3 shows the calculated results of the power loss analysis for the SPS-IBDC working in the same conditions maintaining the transformer configurations and changing the value of L = 15.88 μH in order to obtain the maximum power determined in (11).

Table 3. Power loss analysis of SPS-IBDC.

Magnitude	Symbol	V_2 = 400 V	V_2 = 285 V	Unit
Primary bridge transistor conduction losses	P_{CD1}	9.7	6.2	W
Second. bridge transistor conduction losses	P_{CD2}	6.6	4.2	W
Primary bridge transistor switching losses	P_{SW1}	17.4	17.4	W
Secondary bridge transistor switching losses	P_{SW2}	29.0	17.6	W
Total primary bridge losses	$4(P_{CD1} + P_{SW1})$	108.5	94.2	W
Total secondary bridge losses	$8(P_{CD2} + P_{SW2})$	284.9	174.2	W
Total inductor losses	$P_{II} + P_{IC}$	18.9	9.6	W
Total transformer losses	$P_{TI} + P_{TC}$	75.8	38.5	W
Efficiency	η	95.4	95.8	%

To complete the comparative loss analysis, Figure 8 shows the power losses and efficiency of the SPS-IBDC converter versus output power.

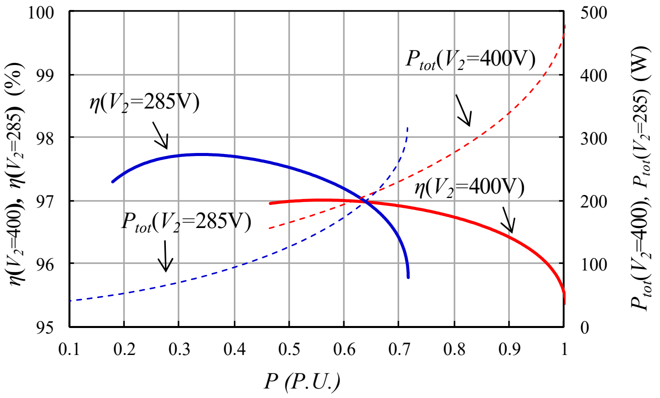

Figure 8. SPS-IBDC total power losses (dashed line) and efficiency (solid line) in front of output power for V_2 = 400 V (red) and V_2 = 285 V (blue).

Comparing Tables 2 and 3, it is observed that the VF-IBDC presents an efficiency improvement of 6 percentage points at minimum battery voltage and maximum charging current. Looking at Figures 7 and 8, a general improvement in efficiency is also observed at high output power values.

6. VF-IBDC Control Schema

The control circuit designed to implement the VF-IBDC is an adaptive variable frequency and phase shift system that must be able to perform ZVS and quasi-ZCS in the primary bridge under wide operating conditions. Figure 9 shows the block diagram of the proposed control circuit.

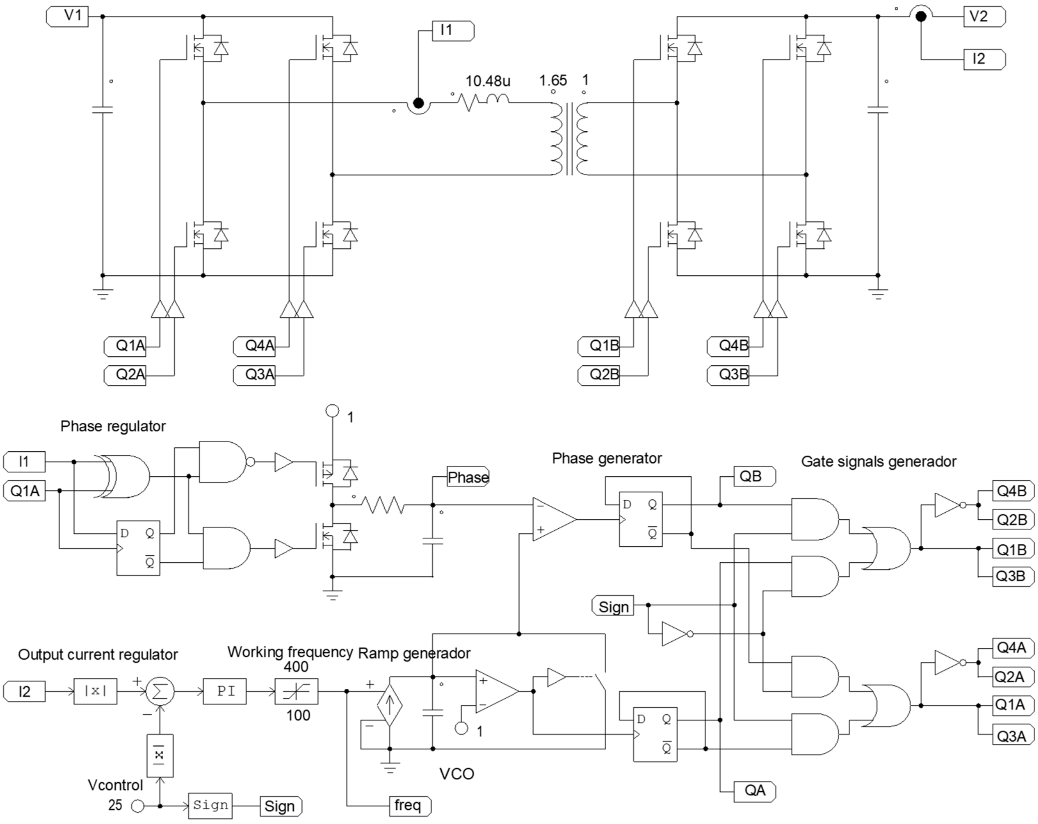

Figure 9. Block diagram of the proposed control circuit.

The main variable to control is the battery charging current I2, taking into account that its sign is defined as positive when the converter is in charge mode and negative when it acts in discharge mode. Since the phase detector and the VCO act like a phase-locked loop, the signal Q1A will be in phase with the primary bridge output current I1 to guarantee the ZVS-ZCS primary bridge operation. The output current I2 is regulated with the PI controller, keeping its absolute value equal to the reference value Vcontrol, obtaining the values of switching frequency that enters the VCO. The sign block detects the sign of the current reference and controls the gate signals generator to manage the power transfer direction of the converter. Other secondary loops not shown in this diagram would limit the values of V1, I1 and V2 during the power transfer process.

7. Experimental Results

This section shows the experimental results obtained by testing a 10 kW VF-IBDC converter operating according to the specifications shown in Table 1. The values of the components of the circuit are those obtained in previous sections. For the experimental verification, a test bed was constructed, consisting of the following elements:

A. A primary bridge with four C3M0016120K SiC MOSFETs mounted on a water cooling heatsink.
B. A secondary bridge with eight C3M0016120K SiC MOSFETs mounted on a water cooling heatsink.
C. An inductor L of 10.5 µH (including transformer leakage inductance).
D. A transformer T with n = 10:6.
E. An integrated digital electronic control on an FPGA-based system.

A and B are fully functional full bridge modules that include sensors, transistor trigger circuits and a power supply with galvanic isolation and high common-mode transient immunity (CMTI). V1 and V2 have been realized through IT6012C-800-50 bidirectional laboratory power supplies. Figure 10 shows a picture of the test bed used to obtain the following experimental results.

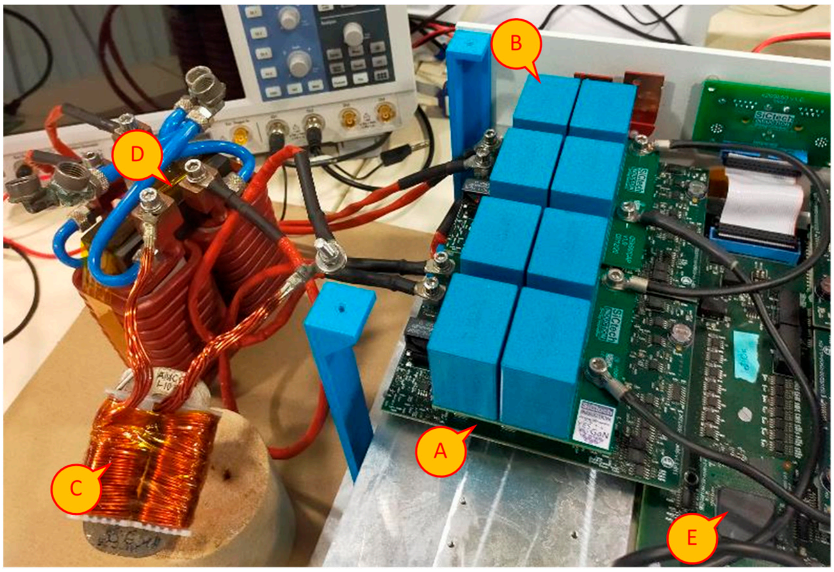

Figure 10. Test bed.

Figure 11 displays waveforms captured by a digital oscilloscope for the VF-IBDC converter operating at full power in charge mode with 385 V at the input. In Figure 11a, the output voltage is 400 V, and in Figure 11b, the output voltage is 285 V. In order to keep ZVS and quasi-ZCS conditions, the frequency changes from 197 kHz (V_2 = 400 V) to 98 kHz (V_2 = 285 V). The control circuit regulates the output current of 25 A constant in both cases.

(**a**) (**b**)

Figure 11. Experimental waveforms of the VF-IBDC in charge mode with V_1 = 385 V and V_2 = 400 V (**a**) when P = 10 kW and (**b**) when P = 7125 W. C1 (dark blue) is the inductor voltage (500 V/div), C2 (magenta) is the primary bridge output current (20 A/div), and C3 (light blue) is the secondary bridge input current (20 A/div). Time base is 0.5 µs/div.

Figure 12 shows oscillograms in discharge mode when the power goes from V_2 = 400 V in Figure 12a or V_2 = 285 V in Figure 12b with V_1 = 385 V. Now, the regulated current I_2 is −25 A. The change of frequency in discharge mode is quite similar to that in charge mode.

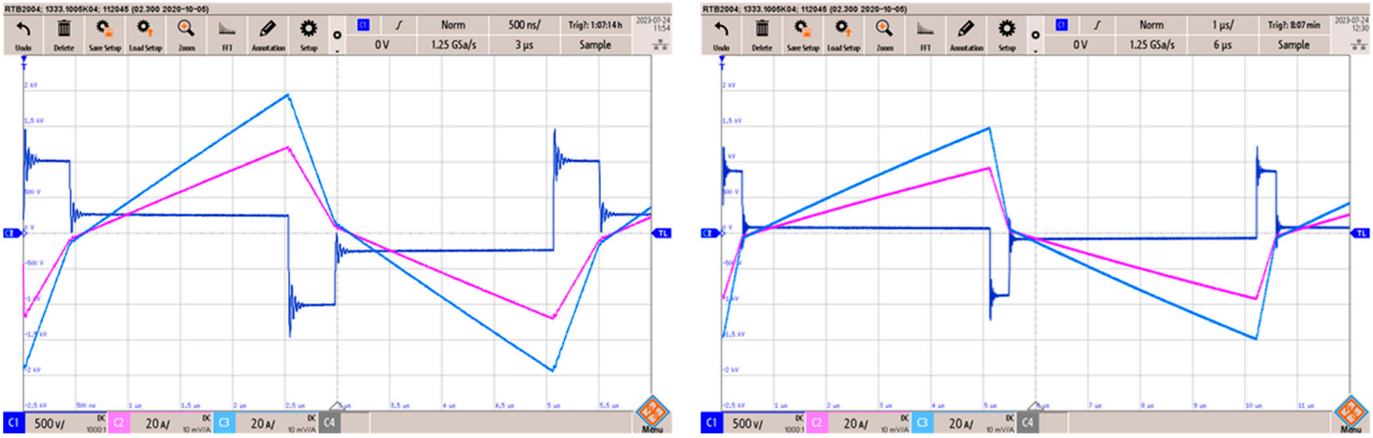

(**a**) (**b**)

Figure 12. Experimental waveforms of the VF-IBDC in discharge mode with V_1 = 385 V and V_2 = 400 V (**a**) when P = 10 kW and (**b**) when P = 7125 W. C1 (dark blue) is the inductor voltage (500 V/div), C2 (magenta) is the primary bridge output current (20 A/div) and C3 (light blue) is the secondary bridge input current (20 A/div). Time base is 0.5 μs/div.

Finally, Figure 13 shows the experimental measurements of the efficiency in charge mode regulating the output current until 25 A with V_1 = 385 V when V_2 is 400 V (red lines) and 285 V (blue lines). The results obtained in discharge mode were very similar. Note that there are some differences between the experimental and calculated results that may be due to the modeling method used, the existence of losses of other elements not taken into account in the calculation (capacitors, conductors, parasitic components, voltage and current sensors, etc.) and also the measurement process.

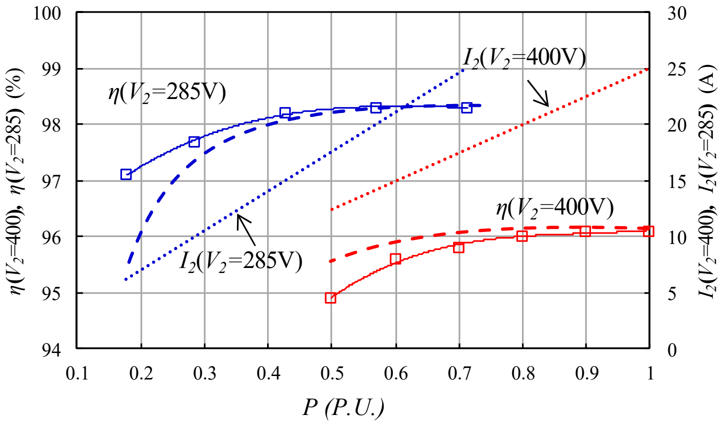

Figure 13. Calculated and experimental efficiency of VF-IBDC converter in function of normalized output power. Solid lines and marking symbols represent the experimental measurements. Dashed lines represent theoretical predictions. Dotted lines represent the evolution of the current I_2 during the tests.

8. Discussion and Conclusions

This paper has carried out a complete study of the VF-IBDC converter that explores the combined effect of a variable frequency and a phase shift to control an isolated bidirectional dual active bridge DC–DC converter so that its primary bridge operates under ZVS and quasi-ZCS conditions over a wide operating range.

After an in-depth analysis of the operation of the SPS-IBDC, a complete design procedure has been presented that allows for the design of a VF-IBDC converter for a specific application of bidirectional charging of electric vehicle batteries.

To verify the viability of the design, a comparative analysis of power losses was developed that determined that the VF-IBDC converter is an enhanced solution that allows us to improve efficiency by up to 6 percentage points compared to the standard SPS method.

A fully functional control circuit has also been presented, easily implementable on the PSIM simulator, which allows us to check the correct operation of the converter and which was the basis of the control finally implemented on an FPGA-based system.

The feasibility of this design has been verified with the construction and testing of a 10 kW converter using SiC MOSFET transistors where an efficiency greater than 98% was achieved.

Author Contributions: Conceptualization and methodology, V.E.; software, J.L.B.; validation, J.J.; formal analysis, V.E.; resources, E.J.D.; data curation, J.L.B.; writing, editing and visualization, V.E. and J.L.B.; supervision, V.E.; project administration and funding acquisition, E.J.D. All authors have read and agreed to the published version of the manuscript.

Funding: This work has been carried out in the framework of the European Project "YESvGaN". The project has received funding from the Electronic Component Systems for European Leadership Joint Undertaking (ECSEL JU), under grant agreement No. 101007229. This Joint Undertaking receives support from the European Union's Horizon 2020 Research and Innovation Programme, and Germany, France, Belgium, Austria, Sweden, Spain, and Italy.

Data Availability Statement: The data presented in this study are available on request from the corresponding author. The data are not publicly available due to privacy restrictions.

Conflicts of Interest: Authors Juan L. Bellido and Enrique J. Dede were employed by the company SiCtech Induction. The remaining authors declare that the research was conducted in the absence of any commercial or financial relationships that could be construed as a potential conflict of interest.

References

1. IRENA. *Smart Electrification with Renewables: Driving the Transformation of Energy Services*; International Renewable Energy Agency: Abu Dhabi, Saudi Arabia, 2022.
2. Zhou, K.; Fang, H.; Liu, Y. Driving–Charging Integrated Controller for Electric Vehicles. *IEEE Access* **2022**, *10*, 66545–66563. [CrossRef]
3. Monteiro, V.; Pinto, J.G.; Afonso, J.L. Operation Modes for the Electric Vehicle in Smart Grids and Smart Homes: Present and Proposed Modes. *IEEE Trans. Veh. Technol.* **2016**, *65*, 1007–1020. [CrossRef]
4. Bassa de los Mozos, A.; Chandra Mouli, G.R.; Bauer, P. Evaluation of topologies for a solar powered bidirectional electric vehicle charger. *IET Power Electron.* **2019**, *12*, 3675–3687. [CrossRef]
5. Kim, H.-S.; Ryu, M.-H.; Baek, J.-W.; Jung, J.-H. High-Efficiency Isolated Bidirectional AC–DC Converter for a DC Distribution System. *IEEE Trans. Power Electron.* **2012**, *28*, 1642–1654. [CrossRef]
6. Singh, B.; Singh, B.N.; Chandra, A.; Al-Haddad, K.; Pandey, A.; Kothari, D.P. A review of single -phase improved power quality AC-DC converters. *IEEE Trans. Ind. Electron.* **2003**, *50*, 962–981. [CrossRef]
7. Kolar, J.W.; Friedli, T. The essence of three-phase PFC rectifier systems—Part I. *IEEE Trans. Power Electron.* **2013**, *28*, 176–198. [CrossRef]
8. Schrittwieser, L.; Kolar, J.W.; Soeiro, T.B. Novel SWISS Rectifier Modulation Scheme Preventing Input Current Distortions at Sector Boundaries. *IEEE Trans. Power Electron.* **2017**, *32*, 5771–5785. [CrossRef]
9. Jahnes, M.; Zhou, L.; Eull, M.; Wang, W.; Preindl, M. Design of a 22-kW Transformerless EV Charger with V2G Capabilities and Peak 99.5% Efficiency. *IEEE Trans. Ind. Electron.* **2023**, *70*, 5862–5871. [CrossRef]
10. Inoue, S.; Akagi, H. A bidirectional dc-dc converter for an energy storage system with galvanic isolation. *IEEE Trans. Power Electron.* **2007**, *22*, 2299–2306. [CrossRef]
11. Inoue, S.; Ishigaki, M.; Takahashi, A.; Sugiyama, T. Design of an Isolated Bidirectional DC–DC Converter with Built-in Filters for High Power Density. *IEEE Trans. Power Electron.* **2021**, *36*, 739–750. [CrossRef]
12. De Doncker, R.W.; Divan, D.M.; Kheraluwala, M.H. A three-phase soft-switched high-power-density DC/DC converter for high-power applications. *IEEE Trans. Ind. Appl.* **1991**, *27*, 63–73. [CrossRef]
13. Mi, C.; Wang, C.; Gargies, S. Operation, design and control of dual H-bridge-based isolated bidirectional dc-dc converter. *IET Power Electron.* **2008**, *1*, 507–517. [CrossRef]
14. Lee, B.-K.; Kim, J.-P.; Kim, S.-G.; Lee, J.-Y. An Isolated/Bidirectional PWM Resonant Converter for V2G(H) EV On-Board Charger. *IEEE Trans. Veh. Technol.* **2017**, *66*, 7741–7750. [CrossRef]
15. Biela, J.; Schweizer, M.; Waffler, S.; Kolar, W. SiC versus Si Evaluation of potentials for performance improvement of inverter and dc-dc converter systems by SiC power semiconductors. *IEEE Trans. Ind. Electron.* **2011**, *58*, 2872–2882. [CrossRef]

16. Zhang, Z.; Huang, J.; Xiao, Y. GaN-Based 1-MHz Partial Parallel Dual Active Bridge Converter with Integrated Magnetics. *IEEE Trans. Ind. Electron.* **2021**, *68*, 6729–6738. [CrossRef]
17. Zhao, B.; Yu, Q.; Sun, W. Extended-phase-shift control of isolated bidirectional dc-dc converter for power distribution in microgrid. *IEEE Trans. Power Electron.* **2012**, *27*, 4667–4680. [CrossRef]
18. Zhao, B.; Song, Q.; Liu, W. Power characterization of isolated bidirectional dual-active-bridge dc-dc converter with dual-phase-shift control. *IEEE Trans. Power Electron.* **2012**, *27*, 4172–4176. [CrossRef]
19. Krismer, F.; Kolar, J.W. Efficiency-optimized high-current dual active bridge converter for automotive applications. *IEEE Trans. Ind. Electron.* **2012**, *59*, 2745–2760. [CrossRef]
20. Chan, H.L.; Cheng, K.W.E.; Sutanto, D. ZCS-ZVS bidirectional phase-shifted dc-dc converter with extended load range. *IEE Proc. Electr. Power Appl.* **2003**, *150*, 269–277. [CrossRef]
21. Hiltunen, J.; Väisänen, V.; Juntunen, R.; Silventoinen, P. Variable-Frequency Phase Shift Modulation of a Dual Active Bridge Converter. *IEEE Trans. Power Electron.* **2015**, *30*, 7138–7148. [CrossRef]
22. Aguilar, R.; Tarisciotti, L.; Pereda, J. Circulating Current Suppression in DAB Assisted Low-Voltage Variable Frequency MMC. *IEEE Trans. Ind. Appl.* **2022**, *58*, 6322–6331. [CrossRef]
23. Erni, I.R.; Vidal-Idiarte, E.; Calvente, J.; Guasch-Pesquer, L. Small Signal Modelling for Variable Frequency Control with Maximum Efficiency Point Tracking of DAB Converter. *IEEE Access* **2021**, *9*, 85289–85299. [CrossRef]
24. Chen, T.; Yu, R.; Huang, A.Q. A Bidirectional Isolated Dual-Phase-Shift Variable-Frequency Series Resonant Dual-Active-Bridge GaN AC–DC Converter. *IEEE Trans. Ind. Electron.* **2023**, *70*, 3315–3325. [CrossRef]
25. Tang, Y.; Hu, W.; Cao, D.; Hou, N.; Li, Z.; Li, Y.W.; Chen, Z.; Blaabjerg, F. Deep Reinforcement Learning Aided Variable-Frequency Triple-Phase-Shift Control for Dual-Active-Bridge Converter. *IEEE Trans. Ind. Electron.* **2023**, *70*, 10506–10515. [CrossRef]
26. Meng, J.; Ricco, M.; Luo, G.; Swierczynski, M.; Stroe, D.-I.; Stroe, A.-I.; Teodorescu, R. An Overview and Comparison of Online Implementable SOC Estimation Methods for Lithium-Ion Battery. *IEEE Trans. Ind. Appl.* **2018**, *54*, 1583–1591. [CrossRef]
27. Esteve, V.; Jordán, J.; Dede, E.J.; Martinez, P.J.; Ferrara, K.J.; Bellido, J.L. Comparative analysis and improved design of LLC inverters for induction heating. *IET Power Electron.* **2023**, *16*, 1754–1764. [CrossRef]

Publicación 2:

[9] Esteve, V.; **Bellido, J.L.**; Jordán, J. Optimal Design of a Single-Phase Bidirectional Rectifier. Energies 2024, 17, 1280. https://doi.org/10.3390/en17061280

energies

Article

Optimal Design of a Single-Phase Bidirectional Rectifier

Vicente Esteve [1,*], Juan L. Bellido [1,2] and José Jordán [1]

[1] Department of Electronic Engineering, University of Valencia, 46100 Valencia, Spain; jbellido@sictechinduction.com (J.L.B.); jose.jordan@uv.es (J.J.)
[2] R&D Department, SiCtech Induction, 46980 Paterna, Spain
* Correspondence: vesteveg@uv.es

Abstract: This article outlines the comprehensive design and control approach for a single-phase bidirectional rectifier (SPBR) used in bidirectional charging of electric vehicle batteries. The operational parameters of the inverter are determined through a thorough analysis of all switching sequences to accurately assess power losses, considering the type of switching device chosen in each case, enabling proper component sizing, and understanding converter efficiency. An exclusive electronic control circuit is examined, governing two converter operation modes: boost rectifier with power factor correction (PFC) and sine pulse inverter width modulation (SPWM) with a minimum number of adjustments made automatically. One problem that arises when addressing the design of an SPBR is determining the operating frequency. To address this issue, this study offers to conduct a comparative analysis of losses using various power devices and magnetic circuits to determine the optimal operating frequency for achieving maximum energy efficiency. To validate the design's feasibility, a prototype with 10 kW output power was constructed, achieving a peak efficiency of approximately 97.5% in both directions, unity power factor (PF), and total harmonic distortion (THD) of less than 7% during full power operation.

Keywords: index terms; power conversion; bidirectional converters; boost rectifier with power factor correction; SPWM inverters; efficiency

check for updates

Citation: Esteve, V.; Bellido, J.L.; Jordán, J. Optimal Design of a Single-Phase Bidirectional Rectifier. *Energies* **2024**, *17*, 1280. https://doi.org/10.3390/en17061280

Academic Editor: Mihaela Popescu

Received: 7 February 2024
Revised: 26 February 2024
Accepted: 5 March 2024
Published: 7 March 2024

1. Introduction

A successful transition to sustainable energy requires innovative strategies and meticulous planning to effectively integrate emerging technologies and devices for electricity production and storage. This concept is often referred to as "smart electrification" by various authors [1]. Electric vehicles (EVs) are playing a significant role in this transition. When EVs are parked and connected to charging stations, they can contribute power to the grid or the owner's home during peak demand periods, a concept known as vehicle-to-grid (V2G) or vehicle-to-home (V2H) strategies. Moreover, the energy stored in EV batteries can be utilized to stabilize voltage and frequency fluctuations on the grid. To enable these functionalities, converters linking the grid to EVs must facilitate bidirectional energy flow [2].

Figure 1 depicts a diagram illustrating the described solution for a single-phase 230 V AC mains supply scenario [3]. The SPBR (single-phase bidirectional rectifier) block connects to the power grid via an inductance. The BDC (bidirectional DC-DC converter) block links the EV battery to the DC-link capacitor. Through the electronic control of the complete converter, the amplitude and direction of current I_2 can be regulated for the specified values of SPBR output voltage V_1 and nominal battery voltage V_2. In a conventional battery charging process, current I_2 moves from the network to the battery. Conversely, when the battery's energy is utilized to supply power to the grid, the direction of I_2 is reversed [4]. Furthermore, integrating renewable energy systems and bidirectional EV chargers facilitates smart electrification and reduces network operating costs by providing grid support and leveraging the EV battery as a power reserve [5].

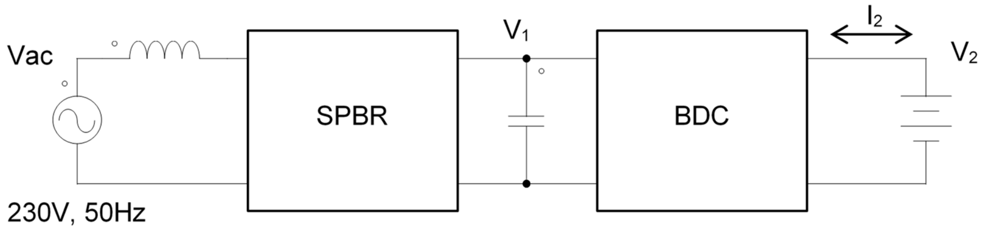

Figure 1. Block diagram of a V2G(H) converter.

The most immediate solution for the BDC involves a basic bidirectional DC-DC converter [6]. However, for safety purposes, this converter must incorporate galvanic isolation. These converters are known as isolated bidirectional DC-DC converters (IBDC). A widely accepted solution involves using a converter that utilizes either two full bridges of transistors dual active bridges DAB (dual active bridges DAB) [7] or two half-bridges (dual active half-bridges DAHB) [8] connected in a configuration where the output of one serves as the input of the other. For high power levels, this topology can be further optimized by employing multiphase DAB [9].

The typical topology for the SPBR block comprises a conventional transistorized single-phase full-bridge boost rectifier with pulse-width modulation controlled by the input current and the output voltage, operating at unity power factor and possessing power reversal capability [10,11]. In the case of three-phase mains, the preferred solution adopted is based on full bridges with three transistor legs [12,13].

Until now, several pulse width modulation (PWM) strategies have been utilized in a single-phase AC-DC converter such a bipolar (BPWM), unipolar (UPWM) [14,15], hybrid modulation (HPWM) [16], and hysteresis current control (HCC) [17]. In order to reduce power losses and electromagnetic interferences (EMI), soft switching modulation [18] and resonant rectifiers [19] have been presented that can include galvanic isolation [20].

In recent years, significant research efforts have been directed towards enhancing the efficiency of these converters, especially concerning bidirectional power flow. While many existing studies have proposed solutions for bidirectional power conversion, a research gap persists regarding the criteria for selecting the optimal operating frequency to enhance efficiency and ensure bidirectional power flow in single-phase systems.

Another important objective of this paper is to explore the possibility of optimizing the efficiency of the converter. Several design parameters play a role in enhancing efficiency, including the selection of power devices, operating frequency, and the design of magnetic components [21–23].

This paper introduces a comprehensive design and control methodology for a single-phase bidirectional rectifier (SPBR) applied to the bidirectional charging of electric vehicle batteries. A thorough analysis of all switching sequences has been conducted to define the operating conditions of the converter accurately. This analysis enables the precise determination of all power losses, facilitating proper component sizing and understanding of converter efficiency. Additionally, a fully operational control circuit, easily implementable on the PSIM simulator, has been presented. This circuit allows the verification of the correct operation of the converter and serves as the foundation for the control system that is ultimately implemented on an FPGA-based system. Furthermore, a comparative analysis of losses is performed using various power devices and magnetic circuits to ascertain the optimal operating frequency for achieving the maximum energy efficiency.

In summary, this paper aims to fill a research gap by presenting a novel approach for the design and control of SPBRs, offering an improved method for determining the optimal operating frequency of SPBR converters for bidirectional power conversion applications in modern single-phase power systems.

The paper is structured as follows: Section 2 focuses on the configuration of the SPBR converter. In Section 3, an analysis of the SPBR converter is conducted, followed by analysis of power loss and efficiency of the converter in Section 4. In Section 5, the proposed SPBR control method is introduced. Section 6 presents the comparative analysis that permits to determinate de optimal operating frequency. The validation of results using experimental data is presented in Section 7. Finally, the conclusions are drawn.

2. SPBR Configuration

Figure 2 shows the simplified configuration of the SPBR. The converter consists of a full bridge with four switches connected to the single-phase grid via inductors, which are used to filter the grid current. In order to provide bidirectional current flow, transistors can conduct positive and negative currents. Electrolytic capacitor is used for voltage filtering at the DC side of the inverter.

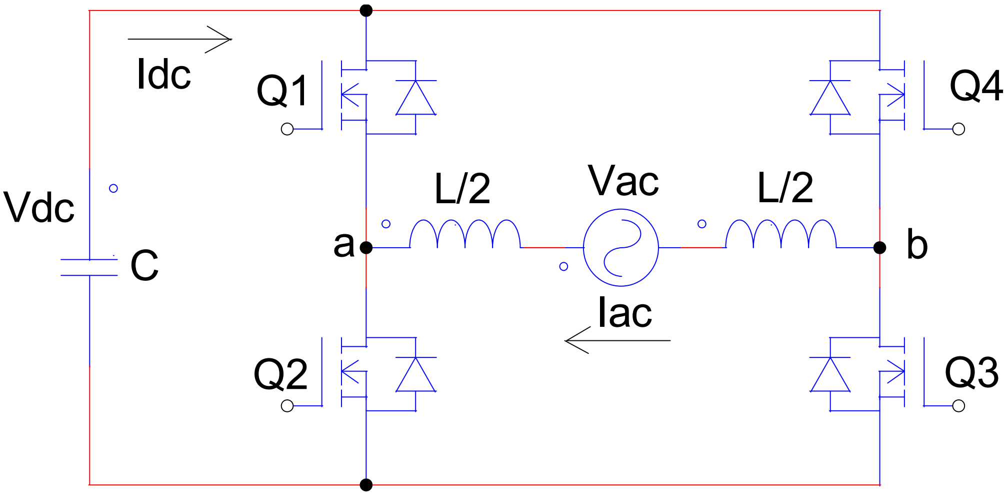

Figure 2. SPBR configuration.

Since the converter is bidirectional, it has two modes of operation. When power flows from the DC side to the AC side, the converter acts as a voltage source inverter (VSI); however, when power is drawn from the mains, the converter acts as a PFC active boost rectifier. By the means of the SPWM technique, switching signals are obtained by comparing a sinusoidal voltage with a triangle wave, obtaining on the AC side of the converter a PF near the unit with low THD. Using a UPWM control technique, the effective switching frequency is doubled and that results in a smaller ripple in the DC side current and a significantly lower harmonic content on the AC side compared to the BPWM [14].

The design has been made for a fast bidirectional charging application of lithium-ion EV batteries using a typical conventional charging process [24]. Table 1 shows several values that serve as specifications for the converter design.

Table 1. SPBR specifications.

Specification	Symbol	Value	Unit
Maximum Power	P	10	kW
Mains Voltage	V_{AC}	230	V
Mains Frequency	f	50	Hz
Regulated DC Voltage	V_{DC}	385	V
Power Factor	PF	1	
Total Harmonic Distortion	THD	7	%
Mains Current Ripple	ΔI_{AC}	5	A
DC Voltage Ripple	ΔV_{DC}	5	V
Efficiency	η	97.5	%

For this application, the standardized values of the European single-phase electrical network have been chosen. The choice of the DC voltage value has been selected as a typical value that allows for proper regulation without penalizing efficiency. The network quality values, ripples, and efficiency are typical objective values for the application. The operating frequency of the converter has not been specified since it will be determined as a result of the comparative study conducted in Section 6.

3. Analysis of the SPBR

The main design equations of the converter, valid for both inverter and rectifier operations, have been presented in well-known technical manuals and application notes [15,25]. The conduction cycle of the SPWM modulation varies proportionally with the amplitude of the mains voltage and its maximum value is calculated as follows:

$$D_{\max} = \frac{\eta V_{AC}\sqrt{2}}{V_{DC}}. \tag{1}$$

The total line inductance filter was obtained with the following equation:

$$L = \frac{(1 - D_{\max})V_{AC}}{2\sqrt{2} f_S \Delta I_{AC}} \tag{2}$$

and the capacitance of the *DC* side filter is calculated as follows:

$$C = \frac{\eta P}{4\pi f V_{DC} \Delta V_{DC}}. \tag{3}$$

The *AC* and *DC* currents are obtained with the following equations:

$$I_{ACrms} = \frac{P}{\eta \; PF \; V_{AC}}, \tag{4}$$

$$I_{DC} = \frac{\eta P}{V_{DC}}. \tag{5}$$

Figure 3 shows the switching sequence of a complete period of the SPBR operating in rectifier mode. This figure is organized in four two columns for positive (left) and negative (right) mains voltage cycle. The top of each column shows the waveforms of the four gate trigger signals V_{G1}, V_{G2}, V_{G3}, and V_{G4} of the transistors and the current I_{AC} in the inductor. The switching sequence steps are identified by numbers, and the corresponding inverter schematics for each step are presented below. The current-carrying devices are drawn with solid lines, and the voltage-blocking devices are drawn with dotted lines. The direction of the current and the polarity of the voltage obtained at the end of each step have been expressed using arrows and ±signs. The capacitors $C_1 \ldots C_4$ represent the output capacitance of the transistors. To simplify the diagrams, only one inductor has been drawn.

In the rectifier mode, current normally flows from the AC side to the DC side through the transistors in reverse mode while they are active. This occurs in time intervals ①, ④, ⑦, and ⑩. When the high-side and low-side MOSFETs of a vertical arm of the bridge are turned-on simultaneously, a short circuit occurs between the V_{DC} and its ground, generating a very large current spike. A period of dead time is provided for turning-off both MOSFETs to prevent such current spikes from occurring, while the inductor current continues to flow. During the dead time, this inductor current flows to the body diode on the opposite side of MOSFET until the corresponding parallel transistor is activated. This occurs in the intervals ②, ⑥, ⑧, and ⑫. For a correct visualization of the different driving states, the dead times are shown to be exaggerated with respect to the cycle period.

The first line of numbers in the waveform header marks the switching transitions. Time intervals ⑤ and ⑪ are relatively soft transitions controlled by the inductor current, while ③ and ⑨ are hard switching where the reverse recovery current of the diode occurs. In time intervals ④ and ⑩, the inductance is charged, and only the DC capacitor feeds the load. In the rest of time intervals, the current flows directly from the mains to the load.

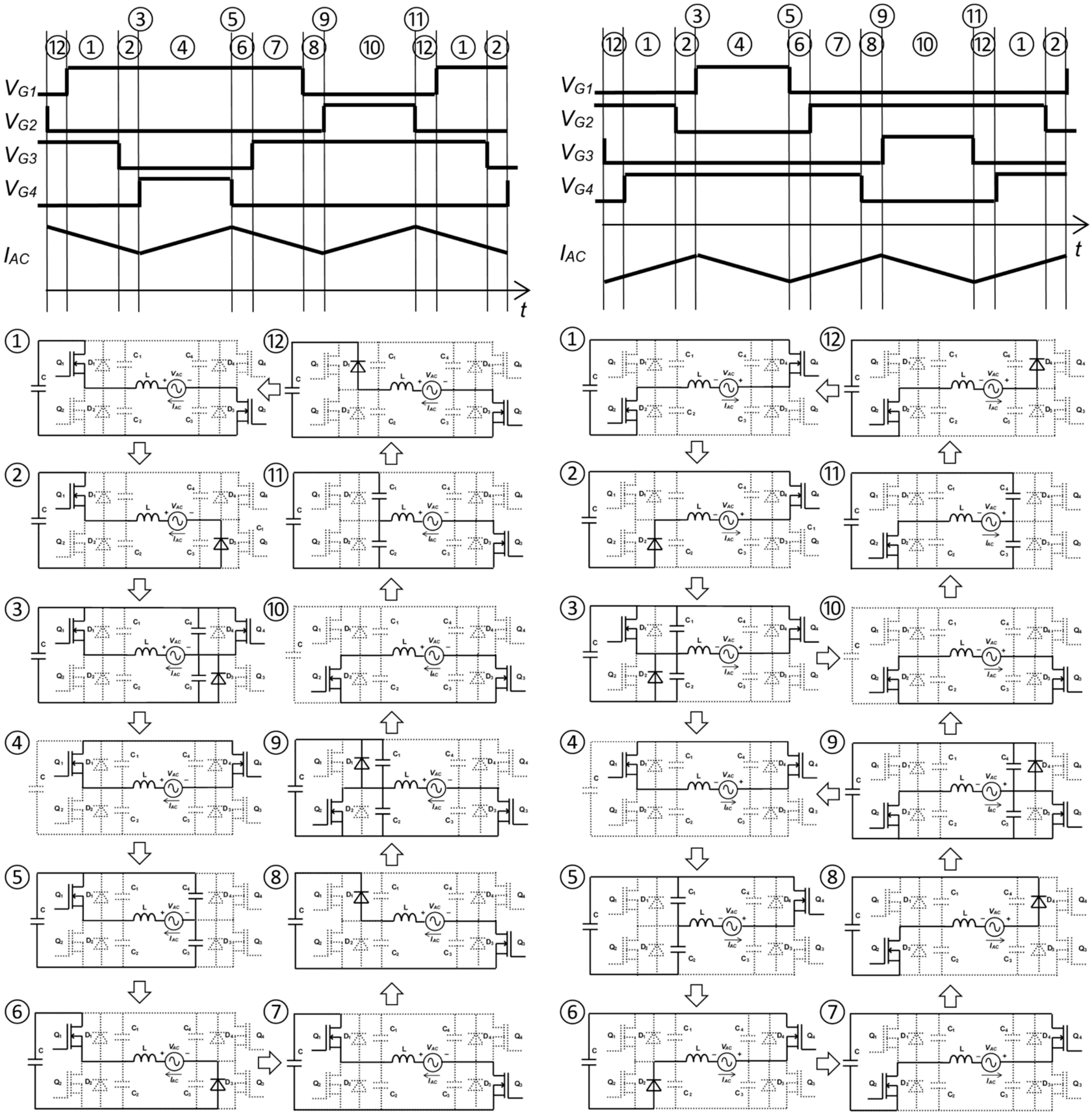

Figure 3. Switching sequence in rectifier mode.

Figure 4 shows the switching sequence of a complete period of the SPBR operating in inverter mode. Now, the conduction of the transistors is direct in time intervals ①, ④, ⑦, and ⑩, allowing the flow of the current from the DC side to the mains. Direct diode conduction occurs in the dead times ③, ⑤, ⑨, and ⑪ and the recovery process occurs in ⑥ and ⑫.

Notably, in both operation modes, when employing IGBT transistors, the reverse current from the switching device must pass through the free-wheeling diode. Consequently, the sequence will be simplified by removing the intervals during which the transistor channel is utilized for reverse currents. Also, the frequency of the inductor current is twice the switching frequency.

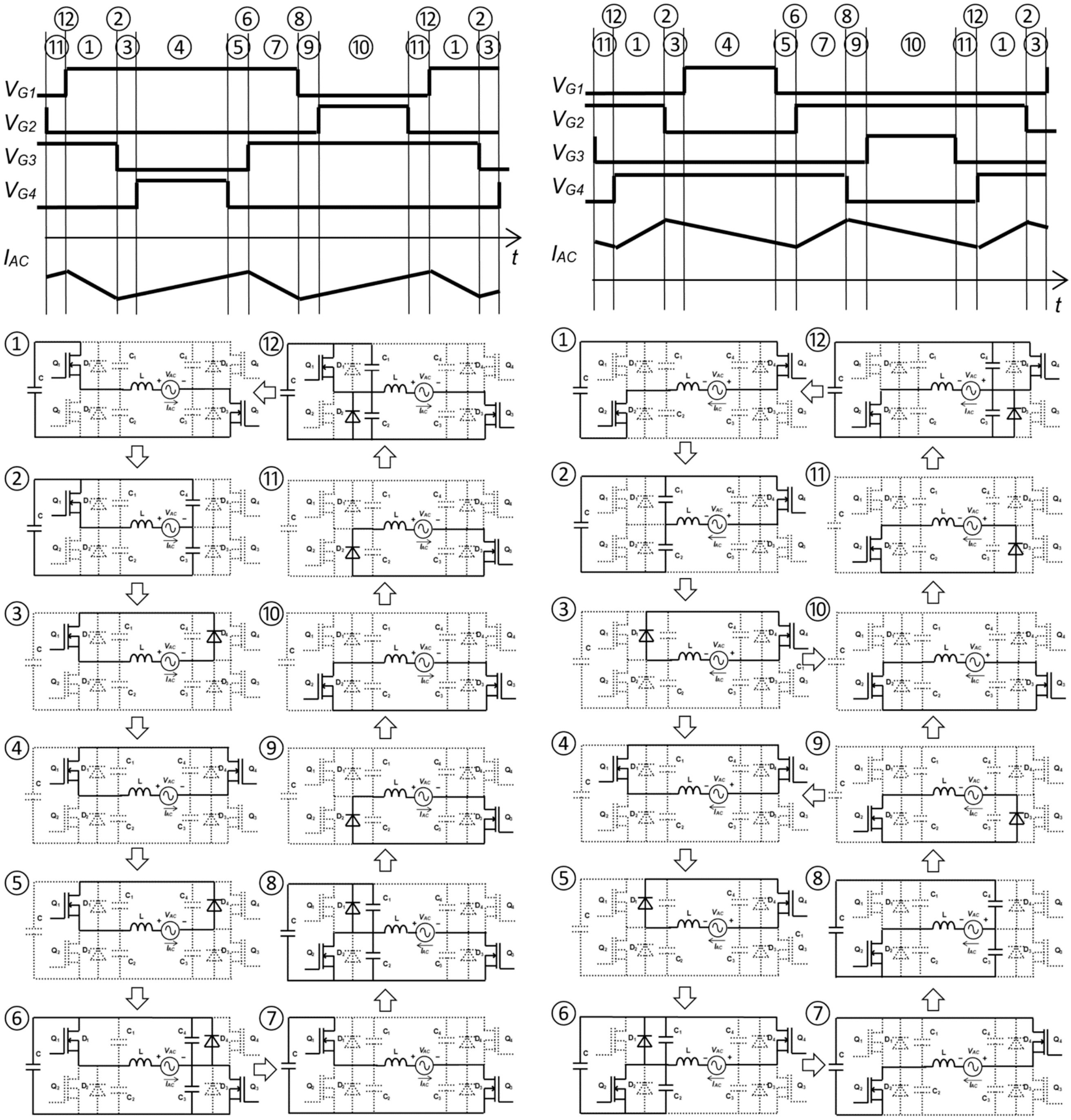

Figure 4. Switching sequence in inverter mode.

4. Power Loss Analysis

A power loss analysis of the SPBR has been carried out considering all the contribution of conduction and switching losses of the transistors including losses from inductances and capacitors. Other losses have not been considered in this study.

In order to calculate the conduction power loss of the transistors P_{QC}, two different cases must be considered. For SiC MOSFET and GaN transistors, it is calculated with the following equation:

$$P_{QC} = I_{Qrms}{}^{2} R_{DSon} \tag{6}$$

where I_{Qrms} is the root means square (rms) value of the current through the transistor that is calculated with the following equation:

$$I_{Qrms} = \sqrt{\frac{{I_{ACrms}}^2}{2} + \frac{{\Delta I_{AC}}^2}{6}}. \tag{7}$$

However, for IGBTs, the conduction loss analysis must take into account that the positive current flows through the transistor, while the negative current flows through the diode according to the next equation:

$$P_{QC} = I^2_{Trms} r_T + I_{Tavg} V_{CE(sat)} + I^2_{Drms} r_D + I_{Davg} V_F \tag{8}$$

where I_{Trms} and I_{Tavg} are the rms and average values of the transistor direct current, and I_{Drms} and I_{Davg} are the rms and average values of the free-wheeling diode. The loss model of the transistor and diodes is given by the parameters $V_{CE(sat)}$, r_T, V_F, and r_D that can be extracted from the manufacturer's data.

The switching power loss of the transistor must consider both turn-on and turn-off switching losses using the next equation:

$$P_{QS} = (E_{OFF} + E_{ON}) f \tag{9}$$

where E_{ON} and E_{OFF} are, respectively, the accumulated switching ON and OFF energies in a mains cycle. E_{OFF} is calculated using the graphs provided by the manufacturer using the following polynomial function [26].

$$E_{OFF} = \sum_{i=0}^{f_S/2f} a(I_S(i) + \Delta I_{AC})^2 + b(I_S(i) + \Delta I_{AC}) + c \tag{10}$$

where a, b, and c take values given by manufactures, and $I_S(i)$ is the transistor current in the different turn-off transitions:

$$I_S(i) = \sqrt{2} I_{AC} \sin\left(2\pi \frac{f}{f_S} i\right). \tag{11}$$

Analogously, the accumulated switching energy in turn-on can be calculate with the following equation:

$$E_{ON} = \sum_{i=0}^{f_S/2f} d(I_S(i) - \Delta I_{AC})^2 + e(I_S(i) - \Delta I_{AC}) + g \tag{12}$$

Finally, the total power loss of each converter transistor is given by the following equation:

$$P_Q = P_{QC} + P_{QS}. \tag{13}$$

Although several losses are generated in the capacitor, including series resistance, leakage, and dielectric loss, these losses are simplified by considering the equivalent series resistance ERS and calculating the total capacitor loss with the following equation:

$$P_{CR} = {I_{Crms}}^2 ESR \tag{14}$$

where I_{Crms} is the rms value of the capacitor currents given by the following equation:

$$I_{Crms} = \frac{P}{\eta} \sqrt{\frac{8\sqrt{2}}{3\pi V_{AC} V_{DC}} - \frac{1}{{V_{DC}}^2}}. \tag{15}$$

Since the inductor conduction loss is generated by the DC resistance (DCR) of the winding that forms the inductor, the corresponding power loss is calculated as follows:

$$P_{LR} = \left({I_{ACrms}}^2 + 2{\Delta I_{AC}}^2\right) DCR. \tag{16}$$

The calculation of the core loss is too complex, but it can be approximated using the equation of Steinmetz:

$$P_{LC} = K(2f_S)^{\alpha} \Delta B^{\beta} V_e \tag{17}$$

where the specific parameters K, α, and β, and the magnetic material effective volume V are given by the provider of the magnetic core. ΔB can be rewritten in terms of inductance by considering Faraday's equation and its effect on inductor current. Assuming a small variation in L, the inductor current change given in the next equation can be used.

$$\Delta B = \frac{L\,\Delta I_{AC}}{N\,A_e} \tag{18}$$

where A_e is the magnetic material effective area.

Therefore, the total power loss of the converter operating in any mode is given by the following equation:

$$P_{TOT} = 8P_Q + P_{CR} + 2(P_{LR} + P_{LC}). \tag{19}$$

where two transistors are in parallel for each bridge switch.

Consequently, the efficiency is given by the following equation:

$$\eta = 1 - \frac{P_{TOT}}{P}. \tag{20}$$

Once the power losses are known, the thermal design of the transistors can be carried out. Considering the thermal design data in Table 3, the maximum temperature of the transistor junction can be determined using the following equation:

$$T_J = T_A + P_Q(R_{thJC} + R_{thCH}) + 8P_Q R_{thHA}. \tag{21}$$

5. Converter Control

The simplified control scheme of the proposed SPBR is depicted in Figure 5, consisting of a unipolar modulation technique. UPWM typically requires two sinusoidal modulating waves, *Vsin* and its inverter, which have the same magnitude and frequency but are 180 degrees out of phase. These two modulating waves are compared in the block "SPWM Modulator" with a common triangular carrier wave, operating at the switching frequency fs, and generating two gating signals, V_{G1} and V_{G4}, for the upper two switches Q_1 and Q_4 and its complementary signals V_{G2} and V_{G3} for the other two lower switches Q_2 and Q_3. It is important to note that the upper two devices do not switch simultaneously, distinguishing them from BPWM where all four devices switch at the same time. The inverter output voltage V_{ab} (Figure 2) switches between either zero and $+V_{DC}$ during the positive half cycle or zero and $-V_{DC}$ during the negative half cycle of the fundamental frequency; hence, this scheme is called unipolar modulation.

Vsin is generated by the block "Phase Regulator" that modifies the phase of a voltage reference obtained from the network voltage so that the phase between the current and the voltage in the AC side of the converter is zero. This phase is measured by the block "Phase Detector". The amplitude of this reference is modified by the block "Amplitude Regulator" where the output of the DC voltage regulator is selected if the converter operates in the rectifier mode, or the output of the DC current regulator is selected if it operates in the inverter mode.

The unipolar switched inverter offers reduced switching losses and generates less EMI. From an efficiency standpoint, it appears that the unipolar switched inverter has an advantage. This scheme effectively doubles the switching frequency as far as the output harmonics are concerned, compared to the bipolar-switching scheme that reduces the amplitude of the high-frequency current ripple.

As the SPBR acts as a boost converter when operating in the rectified mode, the control system itself cannot limit the capacitor charging current until its voltage reaches the peak value of the grid voltage; therefore, a "Soft Start" auxiliary current control circuit must be used.

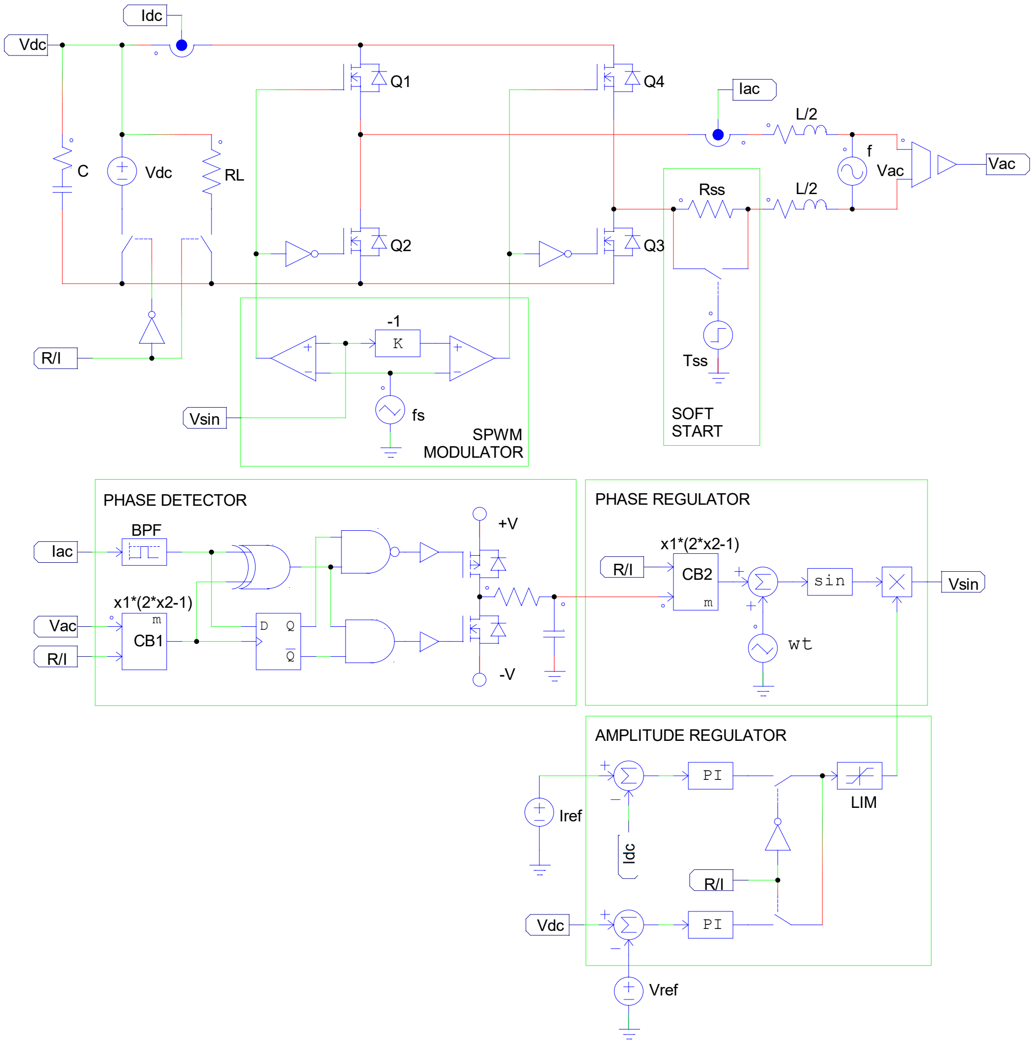

Figure 5. Schematic of the SPBR control.

Given that the circuit must be bidirectional, the converter control should be able to operate in both rectifier and inverter modes with minimal changes, preferably automatically. For this purpose, the signal R/I automatically configures the control for use in the rectifier (R/I = H) or the inverter (R/I = L) mode by changing the polarity of the reference signal in the “Phase Detector” and the “Phase Regulator” and swapping the current and voltage feedback on the DC side for the “Amplitude Regulation” circuit block. Notably, to simplify this control circuit, the generation of dead times has not been considered.

6. Comparative Analysis

In this Section, an analysis of converter losses will be conducted, taking into account the choice of three different switch device technologies. The optimal design depends primarily on the choice of operating frequency, which determines the losses of the power stage and the inductors. In the practical implementation of the converter, the complete bridge is formed by four switches with two transistors of 650 V in parallel to each other. Table 2 shows the main characteristics of the chosen devices for this comparative study.

Table 2. Devices of the power stage.

Symbol	Parameter	Value	Unit
	Si IGBT FGH75T65SHDTL4		
$V_{CE(sat)}$	Collector to emitter sat. voltage	1.2	V
r_T	Transistor forward resistance	6	mΩ
V_F	Diode forward voltage	0.9	V
r_D	Diode forward resistance	17	mΩ
$R_{thJC\ trans.}$	Thermal resist. junction-case	0.33	K/W
$R_{thJC\ diode}$	Thermal resist. junction-case	0.65	K/W
R_{thCH}	Thermal resist. case-heatsink	0.3	K/W
	SiC MOSFET C3M0060065K		
$R_{DS(on)}$	Drain-source on-state resistance	60	mΩ
a	E_{OFF} first coefficient	10	nJ/A^2
b	E_{OFF} second coefficient	−190	nJ/A
c	E_{OFF} constant term	6.75	μJ
d	E_{ON} first coefficient	40	nJ/A^2
e	E_{ON} second coefficient	1.8	μJ/A
g	E_{ON} constant term	39	μJ
R_{thJC}	Thermal resist. junction-case	0.99	K/W
R_{thCH}	Thermal resist. case-heatsink	0.3	K/W
	GaN Transistor GS66508T		
$R_{DS(on)}$	Drain-source on-state resistance	50	mΩ
a	E_{OFF} first coefficient	0	nJ/A^2
b	E_{OFF} second coefficient	233	nJ/A
c	E_{OFF} constant term	0	μJ
d	E_{ON} first coefficient	17.6	nJ/A^2
e	E_{ON} second coefficient	1.59	μJ/A
g	E_{ON} constant term	24.1	μJ
R_{thJC}	Thermal resist. junction-case	0.5	K/W
R_{thCH}	Thermal resist. case-heatsink	0.5	K/W
C	**DC Capacitor**	8.5	mF
ESR	Capacitor equivalent series res.	30	mΩ
I_{Crms}	Capacitor current (rms)	26.8	A
P_{RC}	Total capacitor loss	22.1	W
	Heatsink LAM 6 100		
R_{thJA}	Thermal resist. heatsink-ambient	0.2	K/W
T_A	Ambient temperature	40	°C

With all these data, total semiconductors power losses can be calculated using (13).

The design of the inductor also depends on the operating frequency. Its value is determined by (2), and the choice of the number of turns and the magnetic material also depends on the frequency. The construction of the magnetic core will be performed by stacking the several pieces of the KOOL MU 0077192A7 toroidal core. The winding of the inductor will be made with AWG 7 copper cable. A maximum winding factor of 45%

has been chosen, which determines that the maximum number of turns of the inductor is 21. To design the number of core pieces to be stacked, we must set the maximum magnetic flux density to approximately half of its maximum value of 1T that is given by the following equation:

$$B = \frac{L \cdot I_{ACrms}}{\sqrt{2}N \cdot NC \cdot A_e} + \Delta B \tag{22}$$

where L is total inductance calculated in (2), and A_e is the effective magnetic area of each toroidal piece that composed del core. N and NC are the winding turn numbers and the number of stacked cores of each individual inductance. N is calculated with the following equation:

$$N = \sqrt{\frac{L}{2NC \cdot A_L}} \tag{23}$$

where A_L is the effective inductance per square turn of each toroidal core piece. Table 3 shows the main data that allow the designing of the magnetic components.

Table 3. Inductor design parameters (each core piece).

Symbol	Parameter	Value	Unit
I_{ACrms}	Inductor current (rms)	44.6	A
A_e	Core cross effective section	229	mm^2
K	Parameter for core loss density	1.055	
α	Parameter for core loss density	1.988	
β	Parameter for core loss density	33.1	
V_e	Core effective volume	28,600	mm^3
A_L	Effective inductance per square turn	85	nH/T^2

Figure 6 shows the results of the magnetic design in front of bridge-operating frequency. Notably, these curves exhibit discontinuous behavior since both the number of turns and the magnetic flux density are limited. This results in the need to stack an additional toroidal piece in the core when these limits are reached, leading to N and B values that do not correspond to monotonic functions.

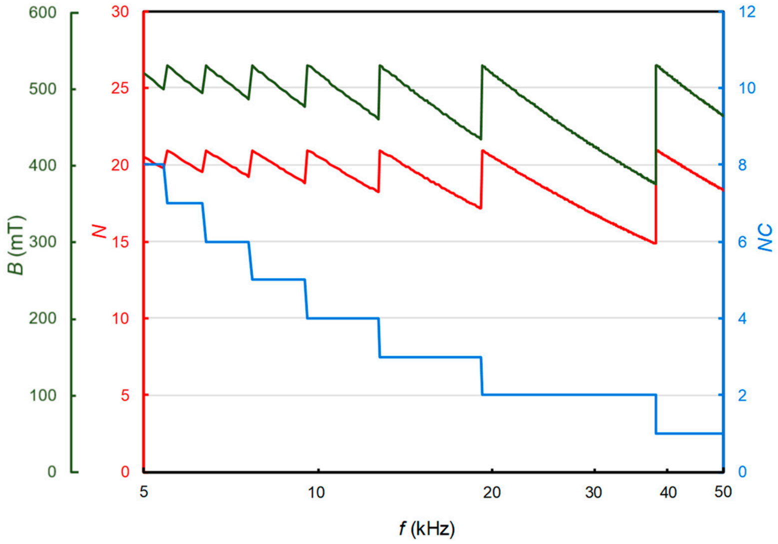

Figure 6. Inductor turns N (red), magnetic flux density B (green), and number of staked cores NC (blue) in front of bridge-operating frequency.

Once the core of each inductance is defined, its power loss can be calculated using (17), introducing the total core volume $NC \cdot V_e$.

To calculate the power losses of the winding, (16) will be used considering that the resistance of AWG 7 wire is 1.63 mΩ per meter, and the total length of the winding is determined by the number of turns and the final geometry of the core.

Taking into account Equations (19) and (20), it is possible to construct the graph of Figure 7 that shows the results obtained for the total power losses and the efficiency of the converter for the three types of devices used as a function of the bridge-operating frequency.

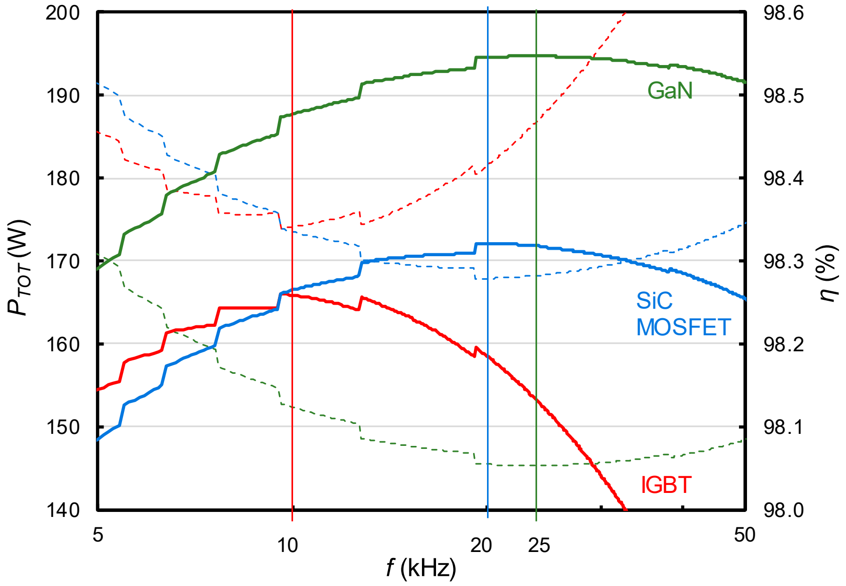

Figure 7. Total power losses (dashed lines) and efficiency (solid lines) of the converter using Si IGBT (red), SiC MOSFET (blue), and GaN transistors (green) in front of bridge-operating frequency.

This graph allows us to find the optimal operating frequency where the maximum efficiency is achieved for each case. It is observed that, with IGBT, the optimal frequency is approximately 10 kHz, with SiC MOSFET, it is 20 kHz, and with GaN transistors, it is 25 kHz. The highest efficiency would be achieved using GaN transistors, with which an efficiency of 98.54% would be achieved. For both SiC MOSFET and GaN converters, the inductors are constructed with a stack of two pieces, while for the IGBT converter, each inductor has four pieces, resulting in the doubling of the volume and mass. Table 4 shows a summary of the results obtained in this study.

Table 4. Summary of the results.

Symbol	Parameter	Value	Unit
Si IGBT FGH75T65SHDTL4			
Optimal f	Operating optimal frequency	10	kHz
L	Inductor value	2 × 144	μH
P_{QC} *trans.*	Transistor cond. losses (each)	3.3	W
P_{QC} *diode.*	Diode cond. losses (each)	10.1	W
P_{QS}	Switching losses (each)	2.1	W
P_{Q} *total.*	Bridge total losses	124	W
P_{LR}	Inductor L/2 conduction loss	13.1	W
P_{LC}	Inductor L/2 core loss	0.8	W
P_{TOT}	Total converter losses	174	W
T_{J}	Junction temperature	91	°C

Table 4. *Cont.*

Symbol	Parameter	Value	Unit
	SiC MOSFET C3M0060065K		
Optimal f	Operating optimal frequency	20	kHz
L	Inductor value	2 × 72	μH
P_{QC}.	Conduction losses (each)	15	W
P_{QS}	Switching losses (each)	1.0	W
P_Q *total.*	Bridge total losses	128	W
P_{LR}	Inductor L/2 conduction loss	8	W
P_{LC}	Inductor L/2 core loss	1.1	W
P_{TOT}	Total converter losses	168	W
T_J	Junction temperature	100	°C
	GaN Transistor GS66508T		
Optimal f	Operating optimal frequency	25	kHz
L	Inductor value	2 × 57	μH
P_{QC}.	Conduction losses (each)	12.5	W
P_{QS}	Switching losses (each)	0.8	W
P_Q *total.*	Bridge total losses	106	W
P_{LR}	Inductor L/2 conduction loss	7.2	W
P_{LC}	Inductor L/2 core loss	1.3	W
P_{TOT}	Total converter losses	145	W
T_J	Junction temperature	87	°C

7. Experimental Results

This Section shows the experimental results obtained by testing a 10 kW SPBR converter operating according to the specifications shown in Table 1. The values of the components of the circuit are those obtained in the previous Sections. For the experimental verification, a test bed was constructed, consisting of the following elements:

A. A full bridge with eight C3M0060065K SiC MOSFETs with a FPGA-based control mounted on a heatsink.
B. An AC side inductor composed of two pieces of 72 μH.
C. A DC capacitor made of 22 pieces of 390 μF in parallel.
D. Regenerative Bidirectional Programmable DC Power Supply.
E. Mains (230 V, 50 Hz).
F. Digital Storage Oscilloscope (DSO) and probes.
G. Power Analyzer.

The DC side is connected to the IT6012C-800-50 bidirectional laboratory power supply that acts like an electronic load in the rectifier mode or like a voltage supply in the inverter mode. The AC side is connected to the mains. Figure 8 shows a picture of the test bed used to obtain the following experimental results.

Figure 9 shows the experimental measurements of the efficiency in the inverter mode and the rectifier mode regulating power up to 10 kW. The results obtained in both operation modes were very similar. Notably, there are some differences between the experimental and calculated results that may be due to the modeling method used and the existence of losses of other elements not taken into account in the calculation (conductors, connections, parasitic components, voltage and current sensors, etc.) and also due to the measurement process.

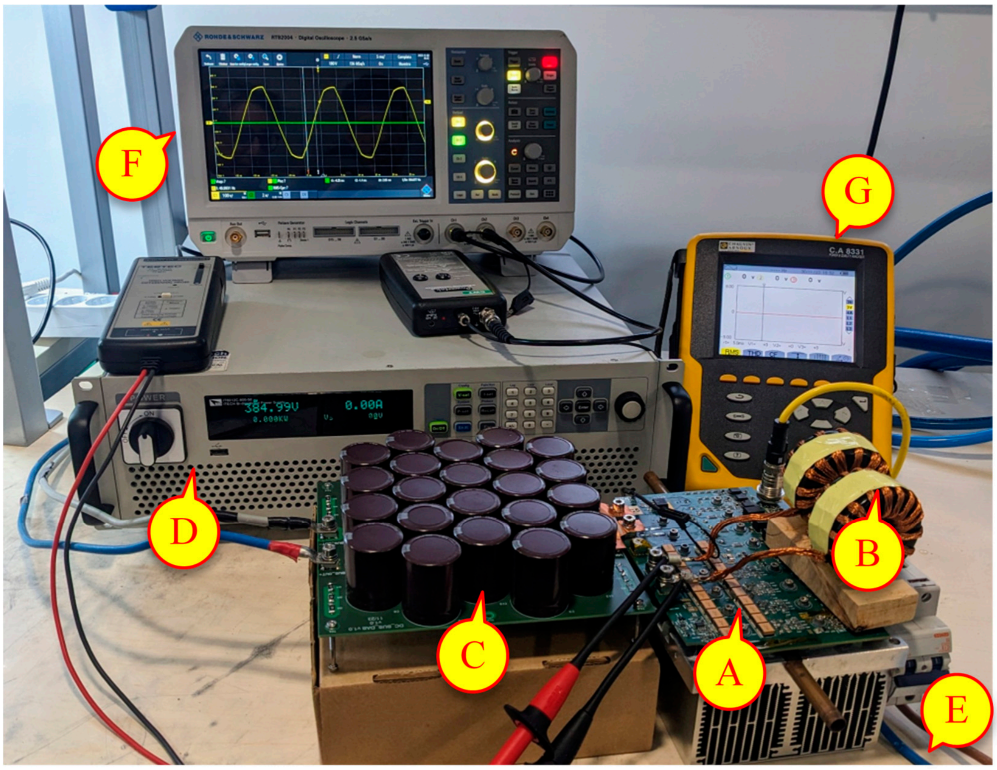

Figure 8. SPBR test bed.

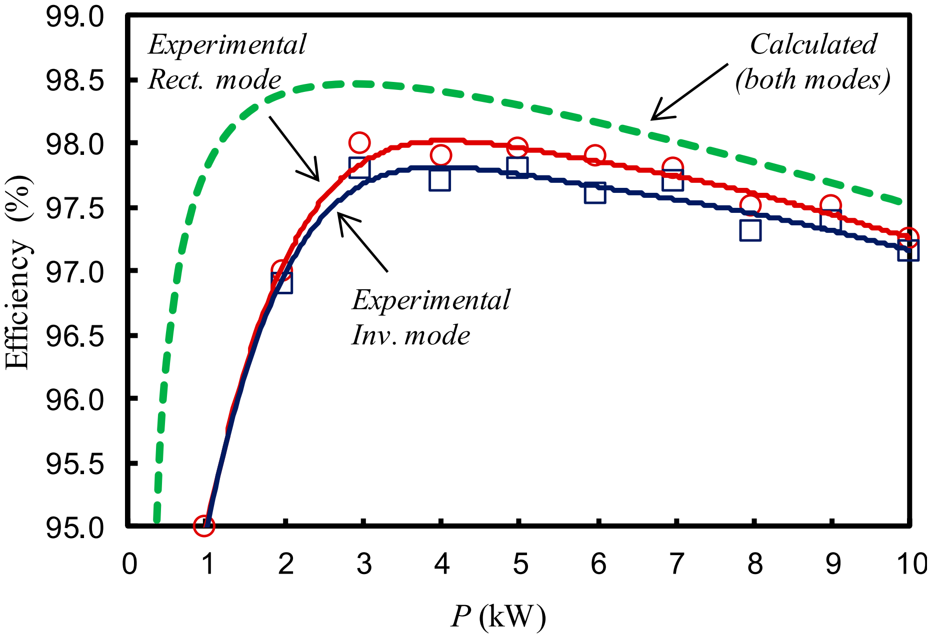

Figure 9. Calculated and experimental efficiency of SPBR converter functioning on the AC active power in the rectifier mode and the DC power in the inverter mode. Solid lines and marking symbols represent the experimental measurements. Dashed lines represent calculated predictions.

Finally, Figure 10 display waveforms captured by digital oscilloscope for the SPBR converter operating in the rectifier and inverter modes at full power with 385 V on the DC side and 230 V_{rms} on the AC side. The switching frequency is 20 kHz. The measured power factor was 1.0, and the THD was less than 7%.

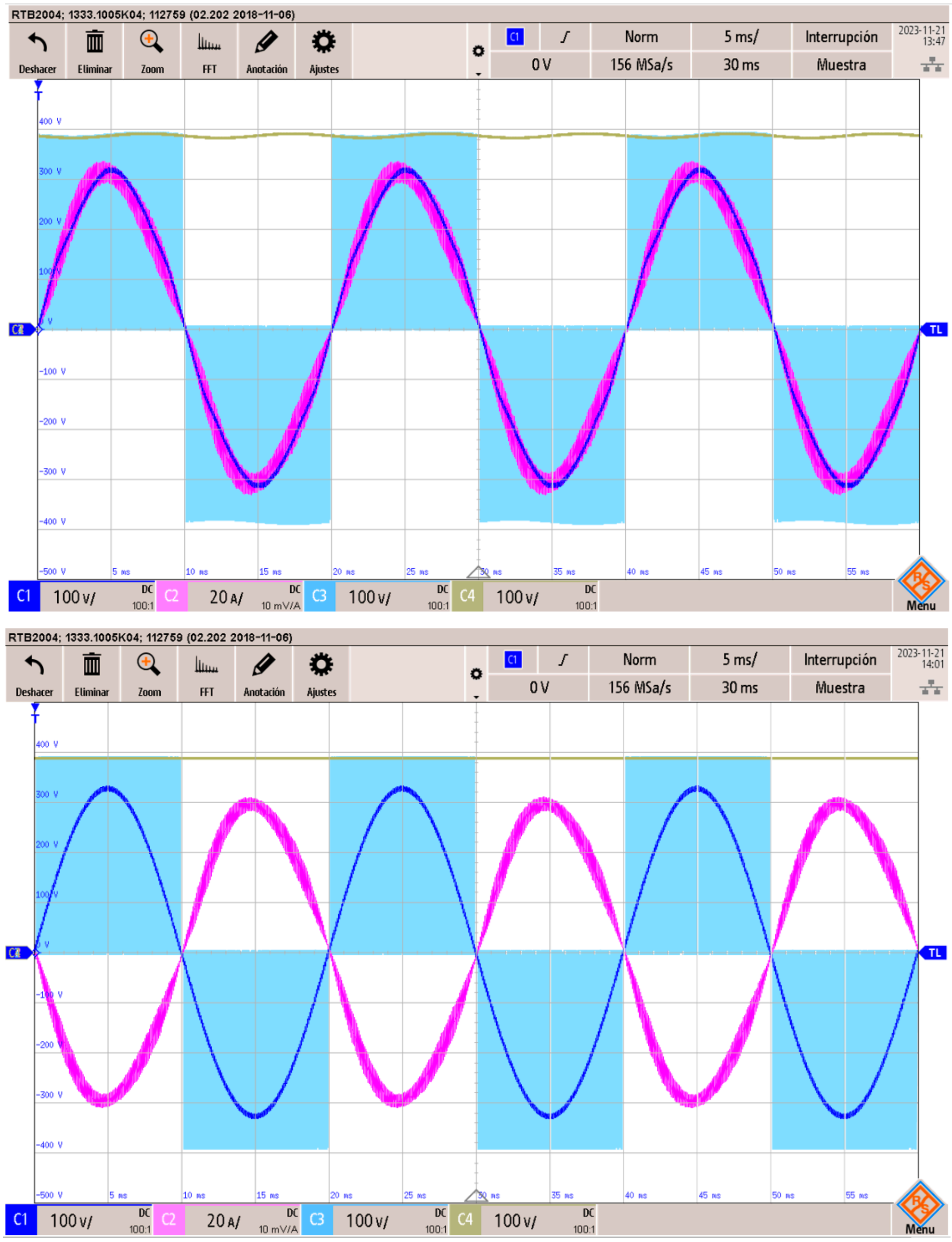

Figure 10. Experimental waveforms of the SPBR in the rectifier mode (**top**) and the inverter mode (**bottom**). C_1 (dark blue) is the mains voltage V_{AC} (100 V/div), C_2 (magenta) is the mains current I_{AC} (20 A/div), C_3 (light blue) is the bridge voltage V_{ab} (100 V/div), and C_4 (brown) is the *DC* voltage V_{DC} (100 V/div). Time base is 5 ms/div.

A fully functional control circuit designed for unipolar operation mode was also presented that can be easily implemented in the PSIM simulator. It has made it possible to verify the correct operation of the converter and was the basis of the control finally implemented in a system based on FPGA.

The feasibility of this design has been verified with the construction and testing of a 10 kW converter using SiC MOSFET transistors, where an efficiency greater than 97% was achieved.

8. Conclusions

The power stage and control circuit of a single-phase bidirectional rectifier (SPBR) used for the bidirectional charging of electric vehicle batteries was fully designed in this study.

The working conditions of the converter have been determined by a thorough examination of its switching sequence in the rectifier and inverter operation modes.

To verify the viability of the design, a complete analysis of power losses was developed, making possible the accurate designing of parts and estimating the converter's efficiency since all power losses have been correctly calculated. All these data determined that the SPBR converter is an effective solution.

By conducting a comprehensive loss study using different types of semiconductor devices, a method has been developed that allows the selection of the optimal operating frequency, thereby maximizing converter efficiency.

The results of this study are directly applicable to the design of bidirectional input converters in electric vehicle charging applications connected to single-phase electrical grids. The bidirectional characteristic of this converter allows its use in smart grids or systems where the energy stored in electric vehicle batteries can be utilized to stabilize voltage and frequency fluctuations in the grid.

Conducting further research is planned to extend the obtained results to other SPBR converter topologies and with the selection of different magnetic components for the design of the inductance in the AC side of the converter.

Author Contributions: Methodology, V.E.; Software, J.L.B.; Validation, J.L.B. and J.J.; Investigation, J.J.; Writing—original draft, V.E.; Writing—review & editing, V.E. and J.L.B.; Supervision, V.E. All authors have read and agreed to the published version of the manuscript.

Funding: This research received no external funding.

Data Availability Statement: Data are contained within the article.

Conflicts of Interest: Author Juan L. Bellido was employed by the company SiCtech Induction. The remaining authors declare that the research was conducted in the absence of any commercial or financial relationships that could be construed as a potential conflict of interest.

Abbreviations

Acronyms

AWG	American Wire Gauge
BDC	Bidirectional DC-DC Converter
BPWM	Bipolar Pulse Width Modulation
DAB	Dual Active Bridges
DAHB	Dual Active Half-Bridges
DCR	DC Resistance
DSO	Digital Storage Oscilloscope
EMI	Electromagnetic Interference
ESR	Equivalent Series Resistance
EV	Electric Vehicle
FPGA	Field-Programmable Gate Array
GaN	Gallium Nitride
HCC	Hysteresis Current Control
HPWM	Hybrid Modulation Pulse Width Modulation
IBDC	Isolated Bidirectional DC-DC Converters
IGBT	Isolated Gate Bipolar Transistor
MOSFET	Metal-Oxide-Semiconductor Field-Effect Transistor
PF	Power Factor
PFC	Power Factor Correction
PWM	Pulse Width Modulation
Si	Silicon
SiC	Silicon Carbide
SPBR	Single-Phase Bidirectional Rectifier
SPWM	Sine Pulse Inverter Width Modulation
THD	Total Harmonic Distortion

UPWM	Unipolar Pulse Width Modulation
V2G	Vehicle-to-Grid
V2H	Vehicle-to-Home
VSI	Voltage Source Inverter

References

1. IRENA. *Smart Electrification with Renewables: Driving the Transformation of Energy Services*; International Renewable Energy Agency: Abu Dhabi, United Arab Emirates, 2022.
2. Zhou, K.; Fang, H.; Liu, Y. Driving–Charging Integrated Controller for Electric Vehicles. *IEEE Access* **2022**, *10*, 66545–66563. [CrossRef]
3. Esteve, V.; Bellido, J.L.; Jordán, J.; Dede, E.J. Improving the Efficiency of an Isolated Bidirectional Dual Active Bridge DC–DC Converter Using Variable Frequency. *Electronics* **2024**, *13*, 294. [CrossRef]
4. Monteiro, V.; Pinto, J.G.; Afonso, J.L. Operation Modes for the Electric Vehicle in Smart Grids and Smart Homes: Present and Proposed Modes. *IEEE Trans. Veh. Technol.* **2016**, *65*, 1007–1020. [CrossRef]
5. de los Mozos, A.B.; Mouli, G.R.C.; Bauer, P. Evaluation of topologies for a solar powered bidirectional electric vehicle charger. *IET Power Electron.* **2019**, *12*, 3675–3687. [CrossRef]
6. Jahnes, M.; Zhou, L.; Eull, M.; Wang, W.; Preindl, M. Design of a 22-kW Transformerless EV Charger with V2G Capabilities and Peak 99.5% Efficiency. *IEEE Trans. Ind. Electron.* **2023**, *70*, 5862–5871. [CrossRef]
7. Inoue, S.; Akagi, H. A bidirectional dc–dc converter for an energy storage system with galvanic isolation. *IEEE Trans. Power Electron.* **2007**, *22*, 2299–2306. [CrossRef]
8. Inoue, S.; Ishigaki, M.; Takahashi, A.; Sugiyama, T. Design of an Isolated Bidirectional DC–DC Converter with Built-in Filters for High Power Density. *IEEE Trans. Power Electron.* **2021**, *36*, 739–750. [CrossRef]
9. De Doncker, R.W.; Divan, D.M.; Kheraluwala, M.H. A three-phase soft-switched high-power-density DC/DC converter for high-power applications. *IEEE Trans. Ind. Appl.* **1991**, *27*, 63–73. [CrossRef]
10. Kim, H.-S.; Ryu, M.-H.; Baek, J.-W.; Jung, J.-H. High-Efficiency Isolated Bidirectional AC–DC Converter for a DC Distribution System. *IEEE Trans. Power Electron.* **2013**, *28*, 1642–1654. [CrossRef]
11. Singh, B.; Singh, B.N.; Chandra, A.; Al-Haddad, K.; Pandey, A.; Kothari, D.P. A review of single-phase improved power quality AC-DC converters. *IEEE Trans. Ind. Electron.* **2003**, *50*, 962–981. [CrossRef]
12. Kolar, J.W.; Friedli, T. The essence of three-phase PFC rectifier systems—Part I. *IEEE Trans. Power Electron.* **2013**, *28*, 176–198. [CrossRef]
13. Schrittwieser, L.; Kolar, J.W.; Soeiro, T.B. Novel SWISS Rectifier Modulation Scheme Preventing Input Current Distortions at Sector Boundaries. *IEEE Trans. Power Electron.* **2017**, *32*, 5771–5785. [CrossRef]
14. Salmon, J.; Wang, L.; Noor, N.; Krieger, A.W. A carrier-based unipolar PWM current controller that minimizes the PWM-cycle average current error using internal feedback of the PWM signals. *IEEE Trans. Power Electron.* **2007**, *22*, 1708–1718. [CrossRef]
15. Mohan, N.; Undeland, T.; Robbins, W. *Power Electronics Converters, Applications, and Design*; Wiley: New Delhi, India, 2003.
16. Li, R.T.H.; Chung, H.S.-H.; Lau, W.-H.; Zhou, B. Use of hybrid PWM and passive resonant snubber for a grid-connected CSI. *IEEE Trans. Power Electron.* **2010**, *25*, 298–309. [CrossRef]
17. Shukla, A.; Ghosh, A.; Joshi, A. Hysteresis modulation of multilevel inverters. *IEEE Trans. Power Electron.* **2011**, *26*, 1396–1409. [CrossRef]
18. Liao, Y.-H. A Novel Reduced Switching Loss Bidirectional AC/DC Converter PWM Strategy with Feedforward Control for Grid-Tied Microgrid Systems. *IEEE Trans. Power Electron.* **2014**, *29*, 1500–1513. [CrossRef]
19. Su, M.; Wu, S.; Dan, H.; Xu, J.; Sun, Y.; Wang, H.; Liu, Y.; Xiong, W.; Liang, X. A Natural Bidirectional Isolated Single-Phase AC/DC Converter with Wide Output Voltage Range for Aging Test Application in Electric Vehicle. *IEEE J. Emerg. Sel. Top. Power Electron.* **2021**, *9*, 3489–3500. [CrossRef]
20. Du, Y.; Bhat, A.K.S. Analysis and Design of a High-Frequency Isolated Dual-Tank LCL Resonant AC–DC Converter. *IEEE Trans. Ind. Appl.* **2016**, *52*, 1566–1576.
21. Wyss, J.; Biela, J. Optimal Design of Bidirectional PFC Rectifiers and Inverters Considering 2L and 3L Topologies with Si, SiC, and GaN Switches. *IEEJ J. Ind. Appl.* **2019**, *8*, 975–983. [CrossRef]
22. Biela, J.; Kolar, J.W.; Deboy, G. Optimal design of a compact 99.3% efficient single-phase PFC rectifier. In Proceedings of the 2010 Twenty-Fifth Annual IEEE Applied Power Electronics Conference and Exposition (APEC), Palm Springs, CA, USA, 21–25 February 2010; pp. 1397–1404.
23. Georgakas, K.; Safacas, A. Switching frequency determination of a bidirectional AC–DC converter to improve both power factor and efficiency. *Electr. Power Syst. Res.* **2011**, *81*, 1572–1582. [CrossRef]
24. Meng, J.; Ricco, M.; Luo, G.; Swierczynski, M.; Stroe, D.-I.; Stroe, A.-I.; Teodorescu, R. An Overview and Comparison of Online Implementable SOC Estimation Methods for Lithium-Ion Battery. *IEEE Trans. Ind. Appl.* **2018**, *54*, 1583–1591. [CrossRef]

25. Abdel-Rahman, S.; Fontana, N. *CoolSiC Totem-Pole PFC Design Guide and Power Loss Modelling*; Infineon Technologies AG: Neubiberg, Germany, 2023.
26. Esteve, V.; Jordán, J.; Dede, E.J.; Martinez, P.J.; Ferrara, K.J.; Bellido, J.L. Comparative analysis and improved design of LLC inverters for induction heating. *IET Power Electron.* **2023**, *16*, 1754–1764. [CrossRef]

Publicación 3:

[34] Esteve, V.; **Bellido, J.L.**; Jordán, J. State of the Art and Future Trends in Monitoring for Industrial Induction Heating Applications. Electronics 2024, 13, 2591. https://doi.org/10.3390/electronics13132591

electronics

MDPI

Article

State of the Art and Future Trends in Monitoring for Industrial Induction Heating Applications

Vicente Esteve [1,*], Juan L. Bellido [1,2] and José Jordán [1]

[1] Department of Electronic Engineering, University of Valencia, 46100 Valencia, Spain; jbellido@sictechinduction.com (J.L.B.); jose.jordan@uv.es (J.J.)
[2] R&D Department, SiCtech Induction, 46980 Paterna, Spain
* Correspondence: vesteveg@uv.es

Abstract: Induction surface hardening (ISH) processes are widely used in the heat treatment of numerous industrial components, especially in the automotive industry. Since this industry operates under very demanding quality standards, it is crucial for these heat treatment processes to meet rigorous specifications to ensure the safety and reliability of the produced components. This implies the precise and repeatable control of certain parameters throughout the manufacturing process of each of the parts treated, through precise and reliable instrumentation in electromagnetically harsh environments. The main objective of this work is to define the monitoring process for an industrial IHS application, determining the control needs and the methods of measurement, recording, and verification of the parameters that ensure the quality of the process. This paper describes the monitoring process of induction surface hardening, emphasizing the use of sensors and modern measurement and control systems. A comprehensive monitoring system supported by a programmable logic controller (PLC) and mixed acquisition and instrumentation systems (analog and digital) implemented with a high-performance Field Programmable Gate Array (FPGA) will be presented.

Keywords: index terms; monitoring; sensors; instrumentation; induction heating; industrial application; energy conversion

check for updates

Citation: Esteve, V.; Bellido, J.L.; Jordán, J. State of the Art and Future Trends in Monitoring for Industrial Induction Heating Applications. *Electronics* **2024**, *13*, 2591. https://doi.org/10.3390/electronics13132591

Academic Editor: Pedro J. Villegas

Received: 7 June 2024
Revised: 27 June 2024
Accepted: 30 June 2024
Published: 1 July 2024

1. Introduction

Induction heating is a heat treatment method widely employed in various industrial applications [1]. In this process, the workpiece, which is the part to be heated, is positioned within a magnetic field generated by a coil known as the heating inductor. An induction heating converter supplies this coil with a high-amplitude and high-frequency current [2]. The heat is generated in the workpiece through Foucault or eddy currents induced on its surface, resulting in Joule and hysteresis losses. The depth of the heated zone, referred to as the penetration depth δ, is contingent upon the frequency of the current, primarily due to the skin effect, as well as the heat conduction properties. Higher operating frequencies result in a shallow skin depth, whereas lower frequencies lead to a greater penetration depth [3].

The load of induction heating converters comprises the heating inductor and its equivalent loss resistance, which can be connected in series or parallel depending on the model. To compensate for the reactive energy of the load, a capacitor is added, creating a resonant load. The capacitor may be connected in series, as seen in series resonant inverters (SRI) [4–6], or in parallel, as observed in parallel resonant inverters (PRI) [7–9]. Both types of inverters are utilized in applications such as forging, welding, melting, hardening, and various other metal heat treatment processes.

ISH is a specific type of induction heating treatment in which a metal part is heated using induction and subsequently quenched. During the quenching process, the metal undergoes a martensitic transformation, resulting in the increased hardness of the part.

Induction hardening is particularly useful for selectively hardening specific areas of a part or assembly without impacting the overall properties of the part. This method allows for precise control over the hardening process, making it a preferred choice in various industrial applications where localized strengthening is required. Many mechanical parts, such as shafts, gears, and springs, are subjected to induction surface hardening.

The design of an induction heating system for induction surface hardening must take into account the specific requirements, including the characteristics of the part to be heated, the desired penetration depth, and the geometry of the inductor. These factors play a crucial role in determining the optimal parameters for the power converter design, ensuring effective and efficient heat treatment processes. By carefully considering these factors, engineers can tailor the induction heating system to meet the precise needs of the application, resulting in consistent and reliable surface hardening outcomes.

The integral control of an induction surface hardening process is more complex compared to most other industrial thermal processes. The primary variable to control precisely is the energy delivered to the workpiece reliably and repeatedly, ensuring it reaches a specific location within the workpiece to meet heat treatment specifications. The challenge in this application is that time intervals are measured in seconds and fractions of seconds, and power densities can reach hundreds of kilowatts per square centimeter. In some cases, this raises the workpiece surface temperature with gradients up to 2200 K/s or more, with a typical temperature accuracy better than 2%. These rapid temperature variations occur in high-speed sweep heating operations, such as sweep speeds of 10 cm/s with a coil length of 2.5 cm, or with small parts in static heating operations (single shot), where heating times can be 0.5 s or less [2,10].

Precise control of the cooling fluid will also be critical to cool the workpiece at the required rate and achieve the desired metallurgical structure. Furthermore, this process control must be implemented in a noisy electromagnetic environment, usually in conjunction with functions to control complex and fast machines and with a separate system to monitor the process and the workpiece to ensure product quality. All this makes the control of the induction hardening process one of the most complex industrial heat treatment applications.

Therefore, process monitoring is a necessary quality requirement. If data are recorded and stored for each cycle, they become a powerful tool for diagnosing variations in the process or for reviewing the cause when parts are found out of specification after the induction surface hardening process.

A review of the existing literature reveals a lack of comprehensive works covering all aspects related to monitoring in industrial ISH applications. This underscores the novelty of this article, which specifies the main parameters that define the application and details how they are monitored and controlled. The paper is structured as follows: Section 2 focuses on the different control process modes and the analysis of monitoring parameters. In addition, various modern methods of metallographic testing for verification is conducted. Section 3 develops the study of the verification and recording methods and presents the validation of results using an experimental setup. Finally, in Section 4, the conclusions are drawn.

2. Methods and Materials

Surface induction hardening systems typically employ either scanning or static heating methods, often incorporating rotating components within the inductor. During the process, the entire area is heated uniformly for a predetermined duration.

Scanner systems are widely used for induction heating. Scanners allow the piece to be thermally treated progressively in the direction of the axis of the workpiece. The piece remains rotating supported on two points while the induction coil or the piece moves at a controlled speed. Scanners are very versatile and can be used for both vertical and horizontal applications. Typical scanners are controlled by computer numerical control (CNC), which allows for precise positioning, speed, power, rotation, and quenching control.

Piece loading and rotation systems can vary from simple manually operated mechanisms to fully robotic ones.

Machines that enable static heating do not provide movement of the workpiece, only rotation. The workpiece is placed inside or in proximity to an induction coil and it is heated and cooled in place. Obviously, this is the least versatile system and requires a specially designed inductor that fits perfectly to the desired heating profile on the workpiece, but it can be very cost-effective for the right application [11].

Figure 1 shows two images that illustrate the main features of the scanning (left) and static (right) heating methods.

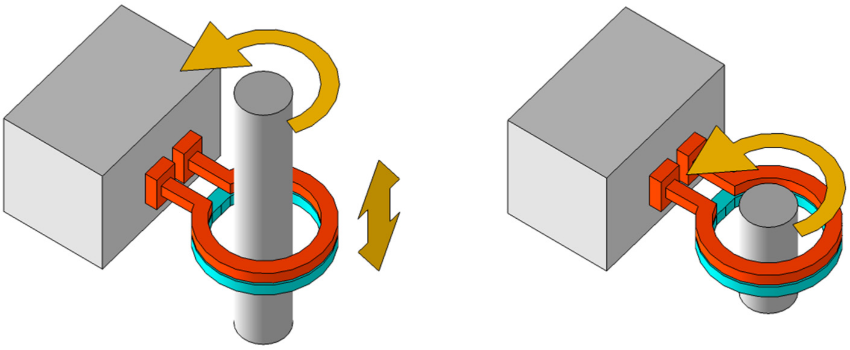

Figure 1. Scanning (**left**) (with vertical movement) and static (**right**) (only rotation) heating methods.

The control modes for the heat treatment of discrete parts are typically in open-loop mode (without a feedback loop), configuring the position of the part and inductor, the converter power, and the heating and quenching time. Open-loop control then fundamentally depends on the power converter, which can be controlled in closed-loop mode (feedback to a set point) to ensure that the requested power level is the power level supplied [2,10]. Some of the main control design elements in ISH are safety, process control and machine operation, productivity, repeatability, and ease of configuration and operation. Methods of controlling the various variables that govern the surface hardening process are discussed in the following section.

Figure 2 shows the diagram of an induction surface hardening installation where the basic elements that compose it can be found. The system is basically composed of the heating subsystem, the quenching subsystem, the parts manipulator subsystem, and the control subsystem.

The heating subsystem is constituted by the induction converter, which is connected to the electrical power supply and generates and regulates the power applied to the workpiece through the heating inductor. After induction heating, the workpiece is rapidly cooled by the quenching system, which includes valves and flow control elements, as well as pressure control devices and a heat exchanger to maintain a constant temperature of the cooling fluid. The installation included a system of specific manipulators that positioned the parts in the inductors with high precision. This subsystem also performs the rotational movements of the workpiece and the displacements of the inductor and the quench. The control subsystem is based on a PLC equipped with all the necessary sensors and actuators to monitor and control the system parameters.

Process monitoring is widespread in various applications, especially in the automotive industry. Ideally, the control system should obtain information that is as accurate as possible. For example, feedback on the voltage and current of the heating coil terminals should be made as close as possible and with good accuracy and noise immunity. In this way, monitoring during induction heating eliminates variables from the power circuit, such as loose bolts and components prone to deterioration such as capacitors and transformers. All elements of the control design are critical, from focusing on the ladder logic necessary to properly, reliably, and safely control the process to wiring the machine with proper grounding and separation of power conductors from control conductors, low-level signal wiring from higher signal levels, and the isolation of servo controls from all other signals. Although the requirements of the monitoring system vary with the application, below is a list of parameters that are typically controlled.

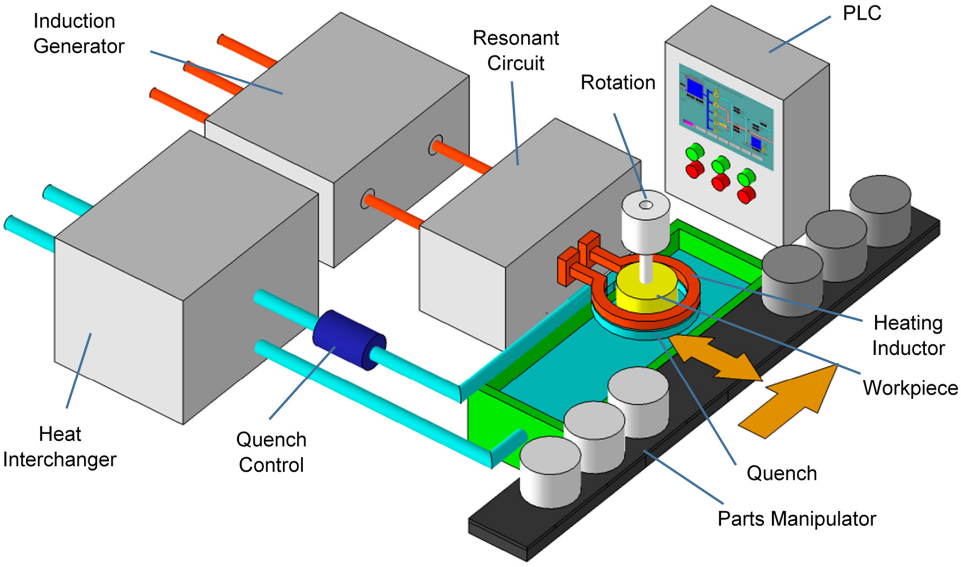

Figure 2. Diagram of an induction surface hardening installation.

2.1. Heating Position

The parts and the inductor itself must be accurately positioned. Sensors may be needed to ensure that these elements are correctly located. However, it is also possible to use novel methods based on measuring the characteristic parameters of the resonant circuit [12,13]. An incorrect position of the inductor or the workpiece leads to significant changes in the fundamental parameters of the resonant circuit, which are the resonance frequency and its equivalent resistance. By measuring these parameters before the hardening process, these positions can be verified, and it is also possible to detect deformations of the inductor or even changes in the dimensions or material of the workpiece. In order to find a method to measure these parameters of the resonant circuit, we must first conduct a preliminary study of the power converter.

Figure 3 shows the typical system configuration of a series converter for induction heating. The output power stage consists of a single-phase voltage-source full bridge inverter using four IGBT modules. The output of the inverter is connected to a series resonant circuit, composed by C_L, L_L, and R_L, through the matching transformer T_1. C_d is the dc-link capacitor and C_s is an AC coupling capacitor. The DC power supply for the inverter is a three-phase diode bridge rectifier connected to the 400 V, 50 Hz power line through the inductance L_d. An example of a typical design for medium-power applications would be characterized by a working frequency of 50 kHz and an output power of 100 kW. The values of the main components of the power converter for this example are shown at the bottom of Figure 3.

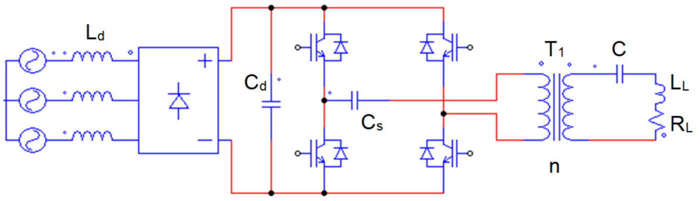

$L_d = 100\mu H$; $C_d = C_s = 100\mu F$; $n = 7{:}1$; $C = 6.7\ \mu F$; $L_L = 1.5\ \mu H$; $R_L = 47 m\Omega$

Figure 3. Typical configuration of the induction power converter.

Since the frequency selectivity of a resonant circuit is large for induction heating application, if the frequency f of the square wave voltage at the output of the inverter is very close to the resonant frequency f_o, only its first harmonic must be considerate for power calculations. Under these conditions, the following equation is obtained [14].

$$\frac{4V_d}{n^2\pi}\sin\omega_o t = L_L\frac{di_o}{dt} + \frac{1}{C}\int i_o dt + R_L i_o \tag{1}$$

where V_d is the DC voltage, i_o is the current of the resonant circuit, $\omega_o = 2\pi f_o = 1/\sqrt{L_L C}$, and n is the transformer turn ratio of T1. Assuming that the quality factor of the series resonant circuit $Q = L_L\omega_o/R_L >> 1$, the output current of the inverter i_o is given by

$$i_o = \frac{4V_d}{n^2\pi R_L}\left(1 - e^{-\frac{R_L}{2L_L}t}\right)\sin\omega_o t \tag{2}$$

Considering that the converter generates a short power pulse of a few switching cycles with a duration of T_{on}, the envelope of the resonant current i_E exhibits the first-order response shown by the black solid shape in Figure 4 that is given by

$$i_E = \begin{cases} I_{\max}(1 - e^{-t/\tau}) & (0 \le t \le T_{on}) \\ i_E(T_{on})e^{-(t-T_{on})/\tau} & (T_{on} \le t) \end{cases} \tag{3}$$

where I_{max} is the maximum current in the case of a large value of T_{on}, and the time constant is

$$\tau = \frac{2L_L}{R_L} = \frac{2Q}{\omega_o} \tag{4}$$

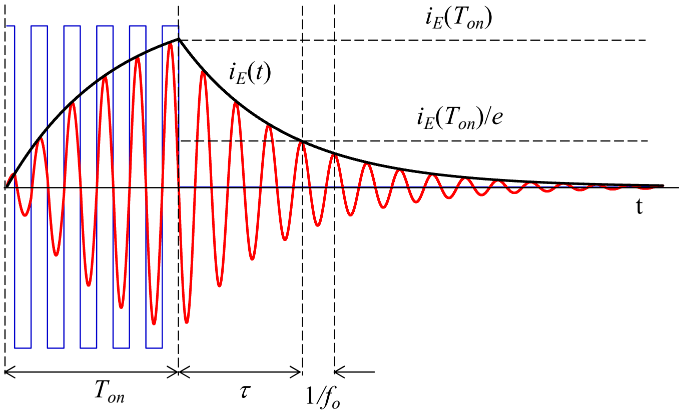

Figure 4. Induction converter waveforms for short power pulse. The blue trace is the converter output voltage and the red trace is the resonant current i_o. The black trace is the envelope of the resonant current.

Setting $t = T_{on} + \tau$ in the second equation of (3) results in $i_E(T_{on} + \tau) = i_E(T_{on})/e$, which allows us to measure the value of the time constants of the envelope τ. Also, it is possible to measure the period of the free oscillation of the resonant current whose inverse value is the resonant frequency f_o. With this measurement made by the FPGA's fast acquisition platform of the converter electronic control, it is possible to determine the characteristic values of the resonant load.

This procedure can be performed each time just before the heating process without altering the process, since the time required is a few milliseconds and the energy utilized is completely negligible.

2.2. Heating Time

The heating time is generally controlled accurately using electronic timers provided by programmable controllers, but care must still be taken with very short heating times due to the inaccuracy of controller cycle times. Modern controllers have highly precise and repetitive timers, so time variation is usually not a problem. It is crucial to transfer the electronic signal defining the heating time as directly as possible to the power converter to prevent uncontrolled delays caused by intermediate devices.

2.3. Power Level

The power level of the induction heating generator must be monitored and controlled using accurate measuring systems from the acquisition of the voltage $v(t)$ and the current $i(t)$ in the heating inductor. The instantaneous power is defined by

$$P(t) \;=\; v(t)i(t) \tag{5}$$

The average power or active power is the mean value of the instantaneous power:

$$P \;=\; \frac{1}{T}\int_{0}^{T} v(t)i(t)dt \tag{6}$$

The apparent power is the product of the root mean square (RMS) values of voltage and current:

$$S \;=\; V_{RMS}I_{RMS} \tag{7}$$

and the reactive power, which does not have a dissipative character (energy storage), is

$$Q \;=\; \sqrt{S^2 - P^2} \tag{8}$$

To conduct the power measurement, electronic wattmeters are typically used which are analog/digital circuits that correspond to what is indicated in the block diagram of Figure 5.

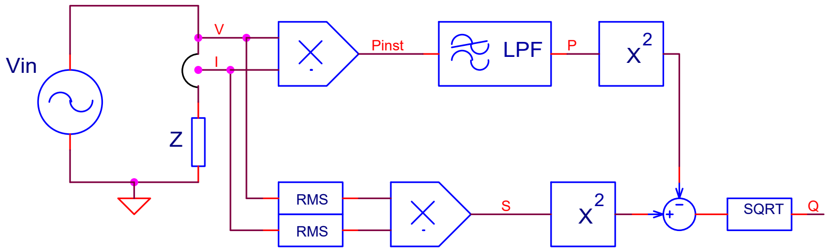

Figure 5. Electronic wattmeter block diagram.

The accuracy of these instruments is very high but other factors may affect the actual power level reaching the workpiece, such as noise affecting the generator regulation accuracy or overheating of components conducting and distributing generator output power, such as contactors, transformers, electrical connections, and other elements.

In certain applications such as dual frequency induction hardening where the total power delivered to the workpiece is the combination of two powers with different frequencies. The circuit in Figure 5 must be duplicated and connected to the power circuits through selective frequency filters, making it possible to split the total power into two components with different frequency.

2.4. Energy

The energy must be monitored. The energy applied to the inductor–workpiece assembly during the process must be measured. The energy is measured in kilowatt-seconds and is widely used to monitor the heating process quality. The electrical energy is given by the following expression:

$$E = \int_{t_1}^{t_2} P(t)d(t) \tag{9}$$

where t_1 and t_2 correspond, respectively, to the initial and final instants of the measurement. Therefore, once this measurement interval is defined, the measuring equipment must integrate the power. If it is constant during the measurement period, the energy will simply be the product of the power and the time interval. The electronic systems are circuits that correspond to what is indicated in the following block diagram.

The voltage-controlled oscillator (VCO) circuit obtains a square or rectangular signal whose frequency is proportional to the instantaneous power. The counter implicitly performs the integration (accumulation) of the power, which is subsequently displayed. The 1/N divider block allows the specification of the selected units and the scaling factors incorporated into the measurement for visualization.

Equivalent to what was indicated in the previous section, in dual frequency applications the circuit in Figure 6 should be duplicated to calculate the energy that corresponds to each frequency.

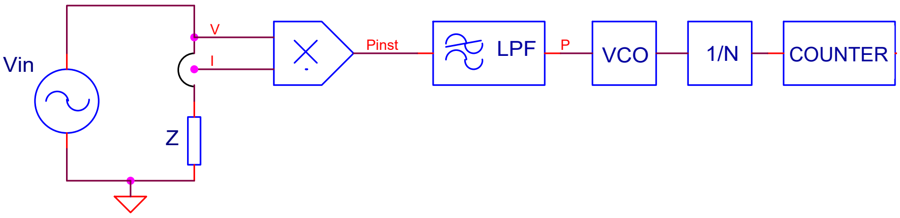

Figure 6. Block diagram of an electronic energy measurement system.

2.5. Temperature Monitoring

Thermocouples or infrared cameras are used to measure and monitor the temperature of the workpiece during heating to ensure it reaches the desired level for the intended heat treatment process. For applications like bright annealing with a consistently clean surface, it can work quite well. However, for most heat treatment applications, there may be visualization or emissivity issues, and the preferred pyrometer may need multiple control ranges. An optical pyrometer can be used as an over-temperature control trip with a limited range, for example, 10% of the desired final temperature. This is generally a reliable approach. Another more accurate method is to measure the surface temperature fields during induction heating using a high-speed infrared camera system. Image analysis tools have been implemented to automatically extract the temporal evolution of isotherms [15].

To increase the accuracy of temperature measurement, modern infrared thermometers consist of a double laser sight. The two laser beams follow the infrared optical path to mark the position of the measuring field at any distance. At the focus point, both lasers intersect, which greatly promotes exact alignment and reduces measurement errors. Figure 7 shows an ISH application where temperature measurement is performed with a dual laser sight infrared thermometer located at some distance from the workpiece.

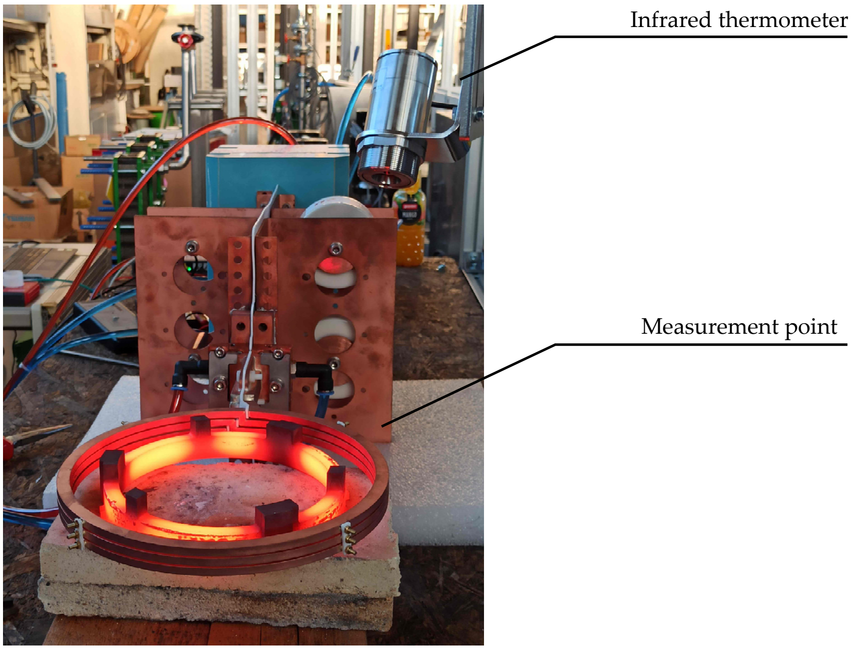

Figure 7. Temperature monitoring using a dual laser sight infrared thermometer (Optris, Berlin, Germany).

2.6. Rotation Speed

Many applications have fixed rotation speeds, and speed is not critical. However, in high-power and short-time heating cycles, it may be important to verify that the rotation speed is correct. The majority of speed sensors detect the motion of ferromagnetic structures, such as gearwheels or shafts, based on the variation in magnetic flux. When the sensor passes over a tooth or gap, the impact on the magnetic field changes accordingly. These changes in the magnetic field can be converted into electrical variables and subsequently conditioned. In other words, the variation in the magnetic field reflects the electrical output signal of the sensor. The measuring principles are based on Hall-effect sensors or inductive sensors. From these data, a PLC calculates and displays the rotation speed.

2.7. Quench Position

The quench position is typically controlled by the cooling fixture, which is usually installed on the inductor or internally machined within the inductor itself. Therefore, the position of the shower is determined by the heating position.

2.8. Quench Delay

Quench delay is an important part of the process. It is the time from the end of heating to the start of quench and sometimes needs to be designed taking into account the quench valve operation time.

2.9. Quench Time

This time must be controlled and monitored during static heating cycles. Scanning cycles may have cooling initiated at the beginning of heating or controlled at a later time. Usually, the accuracy in monitoring this time is not critical.

The delay and duration of the quench are programmed and monitored with the timers included in the PLC.

2.10. Quench Flow and Pressure

Quench flow and pressure must be controlled and monitored. Manually adjusted valves are typically used to produce a fixed flow. They can also be controlled by the programmable controller using electro-hydraulic servo actuators if the process requires variation in flow and pressure during the process. Typically, cooling flow and pressure are monitored to ensure they are above a certain minimum value.

2.11. Quench Temperature

This temperature must be controlled and monitored. The workpiece quench rate and thus the related metallographic processes are highly dependent on the quench liquid temperature that is typically controlled using a feedback analog system that controls a solenoid valve on the cold water side of the heat exchanger, maintaining the cooling liquid temperature as constant.

IHS facilities have modern pressure, flow, and temperature measurement systems such as those shown in Figure 8.

Figure 8. Pressure, flow, and temperature sensors.

2.12. Quench Liquid Composition

The concentration of dissolved quench agents must be controlled, generally by manual checking with a refractometer at regular intervals. Digital refractometers increase results reliability in comparison with analog refractometers, eliminating operator dependency and assisting with error detection.

2.13. Metallurgical Analysis

In any case, the best way to determine if a process is functioning correctly is through a metallurgical analysis. The laboratory typically assesses the quality-related material properties of ferrous materials. Here, several measuring techniques are available, allowing for the microstructure to be directly analyzed, for example, by x-ray diffraction and optical or electron microscopy. Traditionally, destructive testing methods are used to measure the mechanical properties, such as hardness and tensile strength, of metallic materials. However, modern industrial production is highly automated, necessitating automated quality inspection. The quality characteristics of raw materials, semi-finished, and final products should be assessed not only in material laboratories but also concurrently with or integrated into production processes. This objective can only be achieved by the application of appropriate nondestructive testing (NDT) methods.

The available systems for NDT quality inspections utilize optical, thermal, mechanical, electromagnetic, or acoustic methods. Today, the most popular are the backscattering and 3MA methods.

2.13.1. Backscattering Method

Ultrasonic waves traveling through polycrystalline materials, such as steel, are scattered at interfaces within the material where there are changes in density and/or elastic properties. Typically, ultrasonic waves scatter in all directions, including back towards the ultrasonic transducer that generated the initial pulse. The amount of backscattered ultrasound received by the transducer depends on the ratio of the size of the scattering geometry to the wavelength of the ultrasound, as well as the degree of material property difference at the interface, which is referred to as acoustic impedance change [16].

In regions where the ultrasonic wavelength is large compared to the size of the scattering geometry, higher ultrasound frequencies (or shorter wavelengths) lead to an increased intensity of ultrasonic backscattering. Additionally, the intensity of backscattering rises with the average effective size of the scattering geometry, such as the grain size of the polycrystalline steel. By using an appropriate frequency of around 20 MHz, the microstructural change between the hardened case (typically fine-grained martensite) and the core material with a coarse-grained microstructure results in a distinct increase in backscattering intensity. This phenomenon is observed when the ultrasonic pulse encounters the interface, and standard time-of-flight evaluation determines the depth position of the interface, corresponding to the surface hardening depth (SHD). The thickness of the hardened zone can be calculated by measuring the time it takes for the sound pulse to travel from the surface of the part to the location where scattering occurs, using the known sound velocity of the material.

2.13.2. 3MA Method

The name 3MA stands for Micromagnetic Multiparameter Microstructure and Stress Analysis. It is a systematic and technical combination of four micromagnetic methods: Barkhausen noise (BN), harmonic analysis of the tangential magnetic field strength (HA), multi-frequency eddy current analysis (EC), and incremental permeability (IP) [17].

This micromagnetic method is highly versatile, as evidenced by its wide range of applications, including the quantitative determination of hardness, hardening depth, residual stress, and other material parameters. Today, specialized 3MA systems are available for both manual and automated testing of various materials, semi-finished goods, and final products made of steel, cast iron, or other ferromagnetic materials.

Both methods are valuable for verifying the quality of ISH. Specifically, they allow for the determination of penetration depth and hardness, while also enabling the detection of surface crack failures [18].

3. Results Analysis and Discussion

Some of the verification and recording methods have been briefly discussed. These and others are further explained in this section [19].

3.1. Profiling

Profiling techniques have been successfully implemented in various industrial heat treatment applications, as well as in the manufacturing and maintenance of electronic products and circuit boards, clearly demonstrating their contribution to improving process quality [20]. Profiling is the most accurate method for measuring processes when rapid changes are anticipated and need to be tracked. This allows for the detection of variations in high or low amplitudes, as well as early and late starts. Profiles compare the actual value with both a high and low limit simultaneously during the process to reject the treated part if any of the limits are exceeded and can be saved for later viewing and exported for analysis in spreadsheet software. Limit modifications can be adjusted for better control and then imported back into the system.

It is crucial to determine which parameters are the most suitable for being controlled through profiling. Figure 9 shows an example of power and energy recording during a 3 s heating process. Although the limits have been applied equally for both parameters, it is evident that power profiling provides more information than energy profiling. This capability enables the detection of specific anomalies that may not directly impact the measurement of the final energy but could indicate potential faults affecting the quality of the heat treatment. Table 1 shows the data acquired for the preparation of the profile.

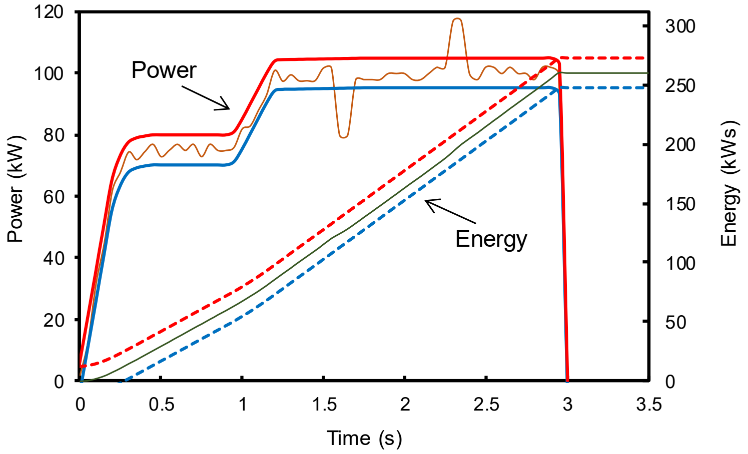

Figure 9. Profiling of power and energy is depicted in the figure. The orange trace represents the power, while the green trace represents the energy. The red and blue lines (solid and dashed) indicate the maximum and minimum allowed values, respectively.

Table 1. Results obtained for an experimental ISH process of 3 s of heating time.

Time (s)	Power (kW)	Energy (kW·s)
0.0	0.0	0.0
0.5	75.0	29.5
1.0	80.0	67.3
1.5	99.8	115.6
2.0	100.0	165.6
2.5	100.0	215.6
3.0	0.0	260.5

3.2. System Faults

Faults are typically monitored using a programmable logic controller (PLC) or other controller type. Historically, faults in the PLC are monitoring high and low limits during the process. If the level of the monitored signal should not vary during the cycle, for example, the cooling temperature, this is an acceptable means of monitoring. Monitoring software can track the number of occurrences and be exported for analysis as needed.

3.3. Statistical Process Control (SPC)

Using collected numerical data, SPC monitors processes to ensure compliance with a quality standard. Statistical process control is a good measure of process stability. SPC does not provide immediate feedback for a good or bad part but it is valuable for verifying that the process is not varying over a longer sample.

The proposed procedures have been implemented through a high-speed measurement and recording system designed for monitoring the power delivered by an induction heating converter in an IHS application. This system has been built and tested. The data collected are transmitted to a programmable logic controller (PLC), which serves as the human–

machine interface (HMI) of the installation. The PLC displays the temporal evolution of the power alongside various other operating parameters of the converter. Figure 10 shows an image of the HMI of the system where power profiling is performed.

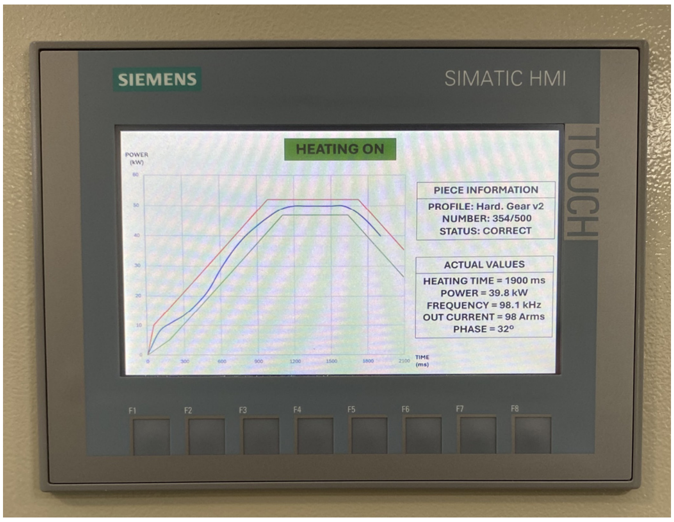

PIECE INFORMATION
PROFILE: Hard. Gear v2
NUMBER: 354/500
STATUS: CORRECT

ACTUAL VALUES
HEATING TIME = 1900 ms
POWER = 39.8 kW
FREQUENCY = 98.1 kHz
OUT CURRENT = 98 Arms
PHASE = 32°

Figure 10. Experimental profiling of power.

The induction heating converter incorporates a System-on-Chip (SoC) from the Zynq 7000 family (XILINX, San Jose, CA, USA), which integrates a microcontroller consisting of a single-core ARM Cortex-A9 responsible for communications between the PLC and the 28 nm Artix 7 FPGA.

The system operates by sampling information from sensors with the FPGA during each switching cycle of the inverter, followed by filtering to mitigate noise from the dv/dt of the MOSFETs switching. Analog sensors measure the direct current bus voltage and current, allowing the instantaneous power applied to the heating workpiece to be derived from their product. This power value is compared to a setpoint for power using a Proportional Integral Derivative (PID) controller to regulate the power setpoint. The control system output is the number of counts equivalent to the switching period of the transistors. The FPGA generates transistor gate signals considering the switching time along with dead time during switching transitions.

Both the filtered sensor and the power value are sent from the FPGA to the microcontroller via the AMBA bus, which enables internal connectivity between these two devices. Similarly, the microcontroller sends the power setpoint value and commands to initiate and stop the heating process to the FPGA.

To communicate between the inverter and the user, a S7 CPU (Siemens AG, Berlin, Germany) is employed, along with a CM 1241 communication module enabling UART communication via an RS485 connection between the PLC and the microcontroller. This setup allows the user to observe heating profiles derived from the applied instantaneous power and adjust power setpoints based on the specific heating requirements of the workpiece.

Figure 11 shows a sequence of experimental images that describes the surface induction hardening process.

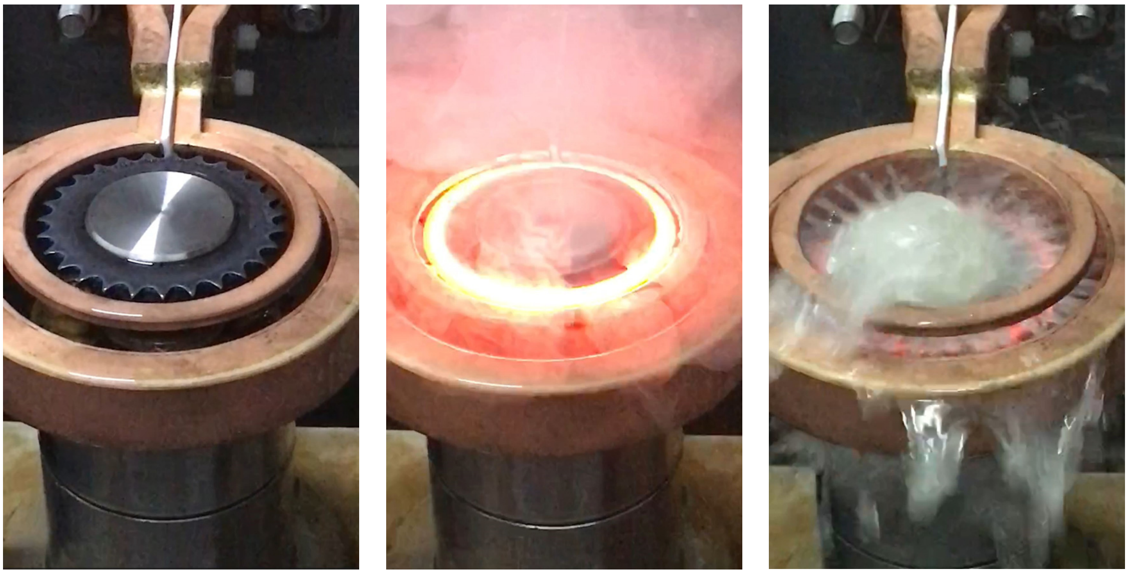

(**a**) (**b**) (**c**)

Figure 11. Experimental ISH process: (**a**) inductor and workpiece placement, (**b**) rotating and heating, and (**c**) quenching.

4. Conclusions

This article has outlined the process of monitoring surface hardening through induction, conducting a detailed examination of the fundamental parameters that determine the quality of the heat treatment. It differs from other previous studies because it is presented as a comprehensive work covering all aspects related to monitoring in industrial ISH applications, emphasizing the study of sensors and modern measurement and control systems. Additionally, a quality control system based on profiling essential system parameters has been introduced. Nondestructive testing techniques for controlling metallographic parameters that can be performed online during heat treatment have also been discussed.

In addition, an experimental comprehensive monitoring system supported by a programmable logic controller (PLC) and mixed acquisition and instrumentation systems (analog and digital) implemented with a high-performance Field Programmable Gate Array (FPGA) has been presented. More research is planned to expand the results obtained and apply them in a real industrial application.

Author Contributions: Methodology, V.E.; Software, J.L.B.; validation, J.L.B. and J.J.; investigation, J.J.; writing—original draft, V.E.; writing—review and editing, V.E. and J.L.B.; supervision, V.E. All authors have read and agreed to the published version of the manuscript.

Funding: This research received no external funding.

Data Availability Statement: Data are contained within the article.

Conflicts of Interest: Author Juan L. Bellido was employed by the company SiCtech Induction. The remaining authors declare that the research was conducted in the absence of any commercial or financial relationships that could be construed as a potential conflict of interest.

References

1. Lucia, O.; Maussion, P.; Dede, E.J.; Burdio, J.M. Induction heating technology and its applications: Past developments, current technology, and future challenges. *IEEE Trans. Ind. Electron.* **2014**, *61*, 2509–2520. [CrossRef]
2. Rudnev, V.; Loveless, D.; Cook, R.; Black, M. *Hand Book of Induction Heating*; CRC Press: Boca Raton, FL, USA, 2017.
3. Brown, G.H.; Hoyler, C.N.; Bierwirth, R.A. *Theory and Application of Radio-Frequency Heating*; Van Nostrand: New York, NY, USA, 1947.
4. Park, N.-J.; Lee, D.-Y.; Hyun, D.-S. A power-control scheme with constant switching frequency in class-d inverter for induction-heating jar application. *IEEE Trans. Ind. Electron.* **2007**, *54*, 1252–1260. [CrossRef]

5. Faucher, S.; Forest, F.; Gaspard, J.-Y.; Huselstein, J.-J.; Joubert, C.; Montloup, D. Frequency-synchronized resonant converters for the supply of multiwinding coils in induction cooking appliances. *IEEE Trans. Ind. Electron.* **2007**, *54*, 441–452.
6. Lucía, O.; Burdío, J.M.; Millán, I.; Acero, J.; Barragán, L.A. Efficiency oriented design of ZVS half-bridge series resonant inverter with variable frequency duty cycle control. *IEEE Trans. Power Electron.* **2010**, *25*, 1671–1674. [CrossRef]
7. Dede, E.; Gonzalez, J.; Linares, J.; Jordan, J.; Ramirez, D.; Rueda, P. 25-kW/50-kHz generator for induction heating. *IEEE Trans. Ind. Electron.* **1991**, *38*, 203–209. [CrossRef]
8. Shenkman, A.; Axelrod, B.; Chudnovsky, V. Assuring continuous input current using a smoothing reactor in a thyristor frequency converter for induction metal melting and heating applications. *IEEE Trans. Ind. Electron.* **2001**, *48*, 1290–1292. [CrossRef]
9. Zhao, K.B.; Sen, P.C.; Premchandran, G. A thyristor inverter for medium-frequency induction heating. *IEEE Trans. Ind. Electron.* **1984**, *IE-31*, 34–36. [CrossRef]
10. Davies, J.; Simpson, P. *Induction Heating Handbook*; McGraw-Hill: New York, NY, USA, 1979.
11. Russell, C. Technologies advancing scan and single-shot induction hardening capabilities. *Int. J. Microstruct. Mater. Prop. (IJMMP)* **2018**, *13*, 113–126. [CrossRef]
12. Sarnago, H.; Lucía, O.; Burdio, J.M. A Versatile Resonant Tank Identification Methodology for Induction Heating Systems. *IEEE Trans. Power Electron.* **2018**, *33*, 1897–1901. [CrossRef]
13. Lucia, O.; Navarro, D.; Guillén, P.; Sarnago, H.; Lucia, S. Deep Learning-Based Magnetic Coupling Detection for Advanced Induction Heating Appliances. *IEEE Access* **2019**, *7*, 181668–181677. [CrossRef]
14. Esteve, V.; Sanchis-Kilders, E.; Jordán, J.; Dede, E.J.; Cases, C.; Maset, E.; Ejea, J.B.; Ferreres, A. Improving the Efficiency of IGBT Series-Resonant Inverters Using Pulse Density Modulation. *IEEE Trans. Ind. Electron.* **2011**, *58*, 979–987. [CrossRef]
15. Larregain, B.; Vanderesse, N.; Bridier, F.; Bocher, P.; Arkinson, P. Method for accurate surface temperature measurements during fast induction heating. *J. Mater. Eng. Perform.* **2013**, *22*, 1907–1913. [CrossRef]
16. Baqeri, R.; Honarvar, F.; Mehdizad, R. Case depth profile measurement of hardened components using ultrasonic backscattering method. In Proceedings of the 18th World Conference on Nondestructive Testing, Durban, South Africa, 16–20 April 2012.
17. Kennamer, T.; Collins, D. Process Monitoring to Reduce/Eliminate Destructive Testing in Induction Heat Treating. In Proceedings of the 22th Heat Treating Society Conference, Indianapolis, IN, USA, 15–17 September 2003; pp. 112–114.
18. Wolter, B.; Gabi, Y.; Conrad, C. Nondestructive Testing with 3MA—An Overview of Principles and Applications. *Appl. Sci.* **2019**, *9*, 1068. [CrossRef]
19. Oswald-Tranta, B. Induction Thermography for Surface Crack Detection and Depth Determination. *Appl. Sci.* **2018**, *8*, 257. [CrossRef]
20. Hsieh, S.-J. Thermal profiling techniques for electronics inspection. *Thermosense XXIX* **2007**, *6541*, 120–128.

Publicación 4:

[10] Esteve, V.; **Bellido, J.L.**; Jordán, J. Efficiency Design of a Single-Phase Bidirectional Rectifier for Home Energy Management Systems. Electronics 2025, 14, 15. https://doi.org/10.3390/electronics14010015

electronics

MDPI

Article

Efficiency Design of a Single-Phase Bidirectional Rectifier for Home Energy Management Systems

Vicente Esteve *, Juan L. Bellido and José Jordán

Department of Electronic Engineering, University of Valencia, 46100 Valencia, Spain;
jbellido@sictechinduction.com (J.L.B.); jose.jordan@uv.es (J.J.)
* Correspondence: vesteveg@uv.es

Abstract: This paper examines the current state of Home Energy Management Systems (HEMSs), highlighting the key role of the single-phase bidirectional rectifier (SPBR). It provides a detailed design process for the converter used in HEMSs, with a particular focus on the bidirectional charge and discharge of high-voltage batteries. The converter's operating conditions were determined through a comprehensive evaluation of its components, which were designed and assessed to enable accurate power loss calculations. This approach ensures proper component sizing and a clear understanding of the converter's efficiency. A specialized electronic control circuit manages two operating modes of the converter: a boost rectifier with power factor correction (PFC) and a sinusoidal pulse width modulation (SPWM) inverter. To validate the design, a 7.4 kW prototype was developed using silicon carbide (SiC) metal oxide semiconductor field effect transistors (MOSFETs). The prototype achieved a peak efficiency of nearly 98% in both modes, with a unity power factor (PF) and total harmonic distortion (THD) below 7% at full power.

Keywords: home energy management system; power conversion; bidirectional converters; boost rectifier with power factor correction; energy efficiency

Academic Editor: Costas Psychalinos

Received: 19 November 2024
Revised: 18 December 2024
Accepted: 23 December 2024
Published: 24 December 2024

Citation: Esteve, V.; Bellido, J.L.; Jordán, J. Efficiency Design of a Single-Phase Bidirectional Rectifier for Home Energy Management Systems. *Electronics* **2025**, *14*, 15. https://doi.org/10.3390/electronics14010015

1. Introduction

A key challenge that technology faces today is finding ways to balance the increasing demand for energy with the need to fulfill sustainability requirements in order to mitigate the environmental impact of energy generation. Since electricity is a limited resource, managing its consumption in both homes and businesses is essential, not only for ecological reasons, but also to enable power companies to meet demand efficiently [1]. In this context, home energy management systems (HEMSs) are essential for improving the efficient use of electrical energy. The information collected about energy consumption, combined with the tariff plans provided by suppliers, allows for reduced electricity bills and flexible accommodation of renewable energy sources (RESs) [2]. An efficient and economical HEMS must take into account not only modern appliances, but also energy storage systems (ESSs) and plug-in electric vehicles (PEVs), among others, to reduce costs and mitigate peak demand on the low-voltage grid (LVG). This facilitates the management of the random charging and discharging of electric vehicles (EVs), photovoltaic (PV) energy generation, and the internal consumption of the home, achieving a minimal energy draw from the grid. Additionally, excess energy produced or stored can be fed back into the grid when deemed necessary.

The future potential of HEMSs is very promising. In this context, it is worth mentioning that some studies predict a growth of HEMSs in the European market of 12.5% annually until 2029 [3]. This growth is driven by several factors, including the increasing emphasis on real-time energy conservation, the convenience offered by cloud computing and data analytics, and enhanced device interconnectivity [4].

The implementation of an HEMS relies on the proper connection and control of converters to ensure a continuous flow of energy between the various components of the system. There are two clearly differentiated strategies for establishing this connection: DC coupling and AC coupling.

Figure 1a shows an HEMS where the converters are coupled through a DC bus, which serves as a temporary energy storage element accessible by all converters. The system manages the energy from the battery of the PEV via a bidirectional DC–DC converter (BDC), allowing the battery to either charge or discharge from the DC bus. Similarly, a bidirectional DC–DC converter could be applied to an energy storage battery, which would form the ESS of the HEMS. The RES, constituted by photovoltaic panels or any other renewable energy generator, is connected to the DC bus through a unidirectional converter, which controls the energy output through maximum power point tracking (MPPT) [5].

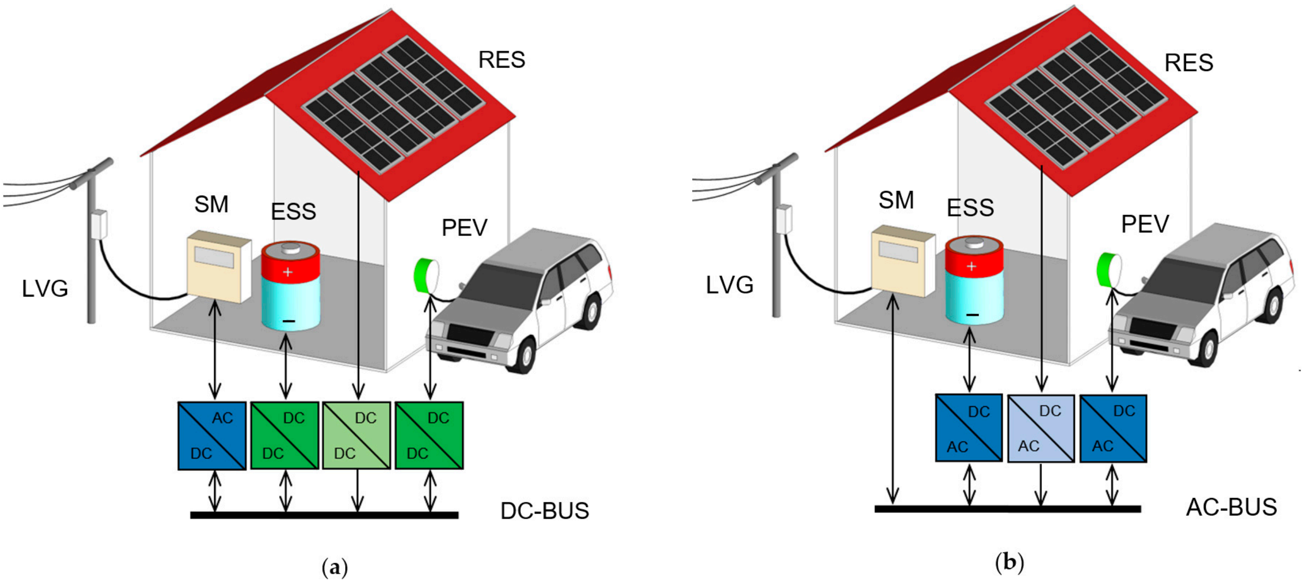

(**a**) (**b**)

Figure 1. Diagram of an HEMS with DC coupling (**a**) and AC coupling (**b**).

Finally, the DC bus is connected to the LVG via a bidirectional AC–DC converter. In typical European households, the LVG consists of a 230 V, 50 Hz single-phase grid, with a maximum power capacity of 7.4 kW (32 A) [6]. In this power range, the DC–DC converters usually adopt the dual active bridge (DAB) topology [7], which employs a medium frequency (20 kHz–150 kHz) with zero voltage switching (ZVS) operation to minimize electromagnetic interference (EMI) and maximize energy efficiency by reducing switching losses in the converter's semiconductor devices [8].

For this application, the AC–DC converter is a single-phase bidirectional rectifier (SPBR) that connects to the LVG to either receive or supply energy to the grid. The smart meter (SM) is responsible for measuring the parameters that characterize the home's connection to the LVG. Galvanic isolation within the system is typically located in all DC–DC converters to ensure that different devices inside the home can operate with maximum safety. In this case, the bidirectional AC–DC converter can be designed without galvanic isolation, utilizing the LVG and DC-bus reference.

Figure 1b illustrates the AC coupling of the system's converters. Now, all of the converters are connected on the AC side of the house, which is linked to the LVG through the SM. All of the converters used are bidirectional AC–DC, except for the converter connected to the RES, which operates unidirectionally. Unlike the DC coupling, in this case, the galvanic isolation is provided by the AC–DC converters, typically using two-stage AC–DC and DC–DC converters [9,10].

Figure 2 illustrates a simplified schematic of a bidirectional DC–DC converter employing a dual active bridge (DAB) topology. This design features two full bridges with active switches on both the primary and secondary sides, interconnected through a high-frequency transformer, T, which ensures galvanic isolation and facilitates voltage matching between two voltage levels, V_1 and V_2. The inductor, L, incorporating the transformer's leakage inductance, acts as the instantaneous energy storage component. The switching signal has a duty ratio of 50%, with a phase shift ϕ between the primary and secondary bridges that determines both the magnitude and direction of power flow. The capacitor C1 serves as the DC link capacitor for the output voltage V_1 of the SPBR, while C2 functions as the output capacitor for the DAB. If a battery is connected at the voltage point V_2, in charge mode, power flows from C1 to C2, transferring energy to the battery. In discharge mode, when the battery supplies power back to the grid, the power flow reverses direction.

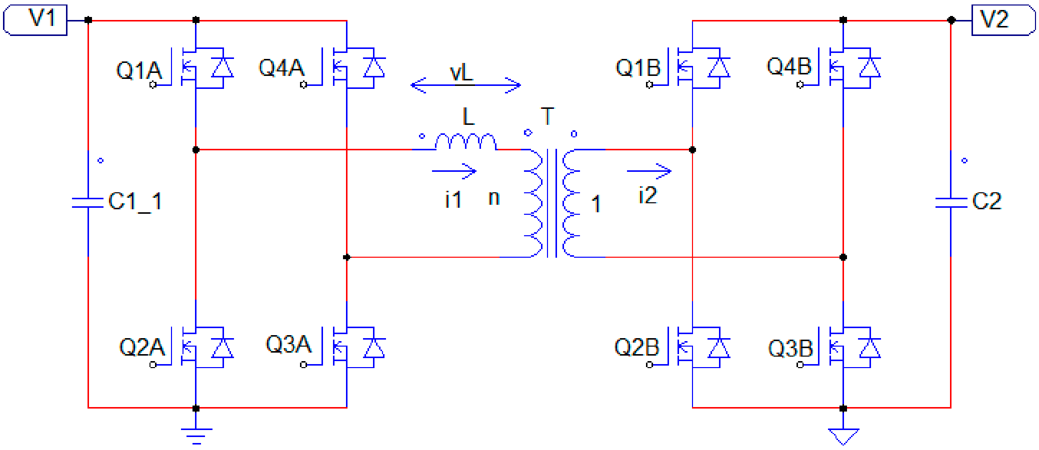

Figure 2. DC–DC converter with DAB configuration.

Several works exist now in the literature that analyze and compare the performance of the AC-coupling and DC-coupling solutions [11–13]. According to these authors, although the number of complete converters used in the HEMS with AC coupling is lower than in the case of DC coupling, their complexity and relatively high loss values often recommend DC coupling. In any case, it is observed that the use of bidirectional AC–DC converters is present in both topologies, which indicates that we should initially conduct a more detailed study of single-phase bidirectional rectifiers.

The typical topology for the SPBR is a transistorized single-phase full-bridge boost rectifier, controlled by pulse width modulation (PWM) to regulate the input current and output voltage so that it can operate at a unity input power factor and capable of power reversal [14,15]. Various PWM strategies have been employed in single-phase AC–DC converters, including bipolar PWM (BPWM), unipolar PWM (UPWM) [16,17], hybrid modulation (HPWM) [18], and hysteresis current control (HCC) [19]. To reduce power losses and minimize electromagnetic interference (EMI), soft-switching modulation [20] and resonant rectifiers [21] have been proposed, which may include galvanic isolation [22].

This article presents a comprehensive design and loss analysis methodology for a single-phase bidirectional rectifier, intended for bidirectional AC–DC converters in HEMS applications. This analysis enabled precise power loss calculations, leading to accurate component sizing and an efficient determination of the converter's performance. The control system was thoroughly verified to ensure the proper operation of the converter and to serve as the basis for the control implementation based on an FPGA circuit.

In summary, this paper addresses a research gap by introducing a novel approach to the design of single-phase bidirectional rectifiers. It utilizes an advanced approach for determining the optimal operating frequency of SPBR converters, specifically designed for bidirectional power conversion in actual single-phase power systems. Additionally, a comprehensive loss analysis is conducted.

The remainder of this paper is structured as follows: Section 2 discusses and analyses the structure and working process of the proposed converter. This section also shows the design principles of the proposed circuit and performs a complete loss analysis. The results obtained through calculations and experimental measurements are further given in Section 3. Finally, conclusions are drawn in Section 4.

2. Methods and Materials

2.1. Configuration of the SPBR

Figure 3 shows the simplified configuration of the SPBR, which is based on a full bridge with four SiC MOSFET switches that enable its bidirectional operation. The connection to the single-phase grid is made through inductors that filter the grid current. The bidirectional function is made possible because the transistors can conduct both positive and negative currents. An EMI filter is installed on the AC side to suppress conducted interference emissions. A capacitor bank is used for voltage filtering on the DC side of the inverter.

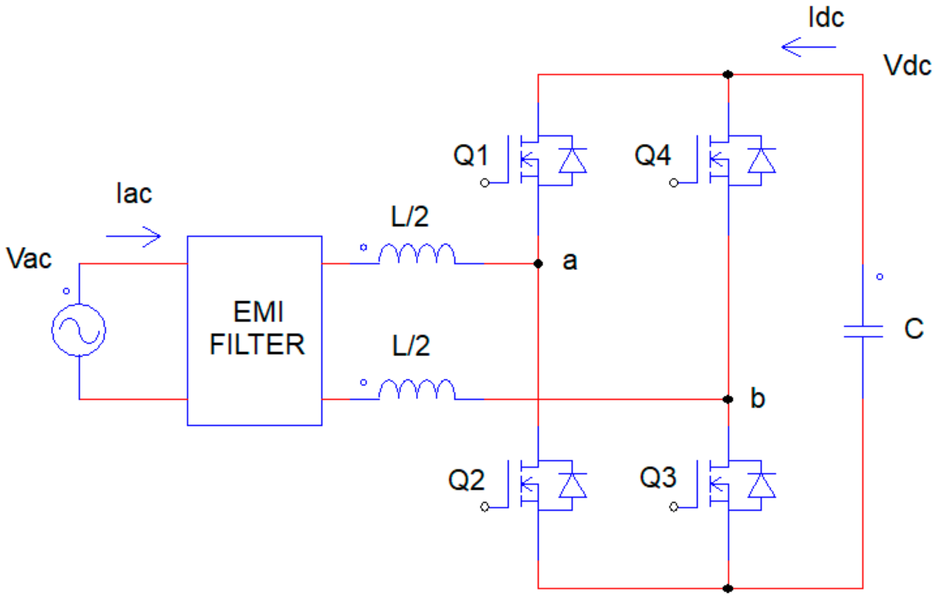

Figure 3. SPBR configuration.

The converter is bidirectional, allowing it to operate in two distinct modes. When power flows from the DC side to the AC side, it functions as a voltage source inverter (VSI). In this mode, the sign of *Iac* is positive, while the sign of *Idc* is negative. In contrast, when power is drawn from the mains, it acts as an active boost rectifier for power factor correction (PFC). In this mode, the sign of *Iac* is negative, while the sign of *Idc* is positive. The sinusoidal pulse width modulation (SPWM) technique generates the switching signals by comparing a sinusoidal voltage with a triangular waveform, resulting in a power factor close to unity and a low total harmonic distortion (THD) on the AC side. By employing the UPWM control technique, the effective switching frequency is doubled, which reduces ripple in the DC-side current and significantly lowers harmonic distortion on the AC side compared to BPWM [16].

The SPBR is designed for use as a bidirectional AC–DC converter for an HEMS application with DC coupling [23]. The main specifications for the converter design are shown in Table 1.

Table 1. SPBR specifications.

Specification	Symbol	Value	Unit
Maximum Power	P	7.4	kW
Mains Voltage	V_{AC}	230	V
Mains Frequency	f	50	Hz
Regulated DC Voltage	V_{DC}	400	V
Power Factor	PF	1	
Total Harmonic Distortion	THD	7	%
Mains Current Ripple	ΔI_{AC}	5	A
DC Voltage Ripple	ΔV_{DC}	5	V
Efficiency	η	98	%
Switching Frequency	f_S	20	kHz

Improving efficiency depends on several design parameters, such as the selection of power devices, the choice of the operating frequency, and the design of magnetic components. For this type of converter, the switching frequency is one of the most difficult magnitudes to specify. Recent studies allow for finding the optimal frequency that maximizes efficiency and minimizes the size and mass of the converter's components [24].

2.2. Initial Analysis of the SPBR

The primary design equations for the converter, applicable to both inverter and rectifier modes, are available in well-known technical articles and books, as well as application notes from component manufacturers [16,25]. The duty cycle of sinusoidal pulse-width modulation (SPWM) adjusts proportionally to the amplitude of the grid voltage, with its peak value being

$$D_{\max} = \frac{\eta V_{AC}\sqrt{2}}{V_{DC}} \tag{1}$$

The value of the input filter inductance is determined using

$$L = \frac{(1 - D_{\max})V_{AC}}{2\sqrt{2} f_S \Delta I_{AC}} \tag{2}$$

The capacitance of the DC side is

$$C = \frac{\eta P}{4\pi f V_{DC} \Delta V_{DC}} \tag{3}$$

The current in the AC side is obtained with

$$I_{ACrms} = \frac{P}{\eta\ PF\ V_{AC}} \tag{4}$$

and the current in the DC side is

$$I_{DC} = \frac{\eta P}{V_{DC}} \tag{5}$$

A complete detailed harmonic analysis of the SPBR will allow for more results to be contributed to this analysis [26].

2.3. Design of the AC Inductor

The inductor design is influenced by the operating frequency [25]. According to Equation (2), its value is calculated to be L = 164 µH, which can be split into two inductors of L/2 = 82 µH each, connected in series with the two active conductors of the LVG. The design of the number of turns and the selections of the magnetic material depends on the frequency. For this converter, the preferred magnetic core will be constructed by stacking several pieces of the KOOL MU 0077192A7 toroidal core. The inductor will be wound using AWG 7 copper wire. A maximum winding factor of 45% has been chosen, limiting the inductor to a maximum of 22 turns. The selection of the maximum magnetic flux density is influenced by the maximum acceptable losses in the coil, which ultimately determine the core temperature rise. In this design, it is acceptable to set the maximum magnetic flux density to approximately half of its maximum value of 1 T, as calculated by the following equation:

$$B = \frac{L \cdot I_{ACrms}}{\sqrt{2}N \cdot NC \cdot A_e} + \Delta B \tag{6}$$

where L is total inductance obtained with Equation (2), and A_e is the effective magnetic area of each toroidal piece of core. From Equation (6), it is possible to determine the number of core pieces NC to be stacked. The winding turns N is calculated with

$$N = \sqrt{\frac{L}{2NC \cdot A_L}} \tag{7}$$

Here, A_L represents the effective inductance per square turn of each toroidal core. Table 2 provides key data essential for designing the magnetic components.

Table 2. Parameters of the magnetic components.

Symbol	Parameter	Value	Unit
L/2	Inductance	82	µH
I_{ACrms}	Inductor current (rms)	32.7	A
A_e	Core cross effective section	2.29×10^{-4}	m^2
K	Parameter for core loss density	1.055	
α	Parameter for core loss density	1.988	
β	Parameter for core loss density	33.1	
N	Winding turns	22	
NC	Number of stacked cores	2	
V_e	Core effective volume	2.86×10^{-5}	m^3
A_L	Effective inductance per square turn	85	nH/T^2
DCR	DC resistance	1.63	mΩ

2.4. Design of the DC Capacitor

By applying the specifications from Table 3, the result is C = 5.9 mF, which can be achieved by connecting 22 pieces of Chemicon EKMM451VSN271MA35S electrolytic capacitors of 450 V, 270 µF in parallel. The resulting capacitance is 5.94 mF with an RMS given by

$$I_{Crms} = \frac{P}{\eta}\sqrt{\frac{8\sqrt{2}}{3\pi V_{AC}V_{DC}} - \frac{1}{{V_{DC}}^2}} \tag{8}$$

Table 3. Capacitor design parameters.

Symbol	Parameter	Value	Unit
C	Total capacitance	5.94	mF
I_{Crms}	Inductor current (rms)	19.6	A
ESR	Total capacitor ESR	45	mΩ

Table 3 resumes the main data of the capacitor design.

For each of the 22 capacitors, the current would be 0.89 A, which is below the rated current of 1.28 A specified by the manufacturer. This results in a design with a voltage safety factor of 1.125 and a current safety factor of 1.438.

2.5. Selection of Transistors

Modern AC–DC converters typically use two types of transistors: silicon IGBTs and silicon carbide (SiC) MOSFETs. While silicon IGBTs have traditionally been the most common, SiC MOSFETs have gained significant popularity due to their numerous performance advantages and steadily decreasing costs. SiC MOSFETs provide excellent thermal conductivity, allowing for more efficient heat dissipation and stable operating temperatures at the device level. This advantage makes them ideal for reducing overall system size, improving efficiency, and potentially lowering system costs [24]. Following these considerations for the converter design, the C3M0040120K SiC MOSFET was chosen.

The root mean square (rms) value of the current through the transistor can be calculated with

$$I_{Qrms} = \sqrt{\frac{{I_{ACrms}}^2}{2} + \frac{{\Delta I_{AC}}^2}{6}} \tag{9}$$

Table 4 shows the main parameters of this transistor.

Table 4. Transistor design parameters.

Symbol	Parameter	Value	Unit
$R_{DS(on)}$	Drain-source on-state resistance	40	mΩ
V_{DS}	Drain-source voltage	1200	V
I_D	DC continuous drain current	48	A
I_{Qrms}	Calculated rms current	23.2	A
C_{OSS}	Output capacitance	129	pF
Q_{RR}	Reverse recovery charge	478	nC
I_{SD}	Inverse current test reference	40	A
V_F	Diode forward voltage	4.5	V
t_d	Switching dead time	150	ns
V_{GSon}	On-state gate voltage	15	V
V_{GSoff}	Off-state gate voltage	−4	V
Q_G	Total gate charge	118	nC
R_{thJC}	Thermal resist. junction-case	0.46	K/W
R_{thCH}	Thermal resist. case-heatsink	0.2	K/W

2.6. Inductors Power Loss Analysis

The conduction loss in the inductors is due to the DC resistance (DCR) of the winding, resulting in a corresponding power loss, calculated as

$$P_{LR} = {I_{ACrms}}^2 DCR \tag{10}$$

The calculation of the core loss is too complex, but it can be approximated using the equation of Steinmetz

$$P_{LC} = K(2f_S)^{\alpha} \Delta B^{\beta} V_e \tag{11}$$

where the parameters K, α, and β of the magnetic material, along with the total effective magnetic material volume V_e, are provided by the magnetic core manufacturer. By applying Faraday's law and considering its impact on inductor current, ΔB can be expressed in terms of inductance. Assuming a minor variation in L as the inductor current changes, the following equation can be used

$$\Delta B = \frac{L \Delta I_{AC}}{NNC\, A_e} \tag{12}$$

2.7. Capacitor Power Loss Analysis

In a capacitor, power losses occur due to series resistance, current leakage, and dielectric loss. In our case, with the use of electrolytic capacitors, the power loss calculation can be simplified by considering only the losses due to equivalent series resistance (ESR), resulting in:

$$P_{CR} = {I_{Crms}}^2 ESR \tag{13}$$

where I_{Crms} is the rms value of the capacitor currents given by Equation (8).

2.8. Transistors Power Loss Analysis

A power loss analysis of the SPBR has been conducted, accounting for all contributions from conduction and switching losses of the transistors, including losses due to inductances and capacitors. Only minimal losses from connections, sensors, and control circuits have been excluded.

The full bridge consists of four switches, each using a single transistor. To calculate the conduction power loss of the transistors, Equation (10) must be applied.

$$P_{QC} = {I_{Qrms}}^2 R_{DSon} \tag{14}$$

The switching power loss of the transistor must be in consideration both turn-on and turn-off switching losses using the next equation

$$P_{QS} = (E_{OFF} + E_{ON}) f \tag{15}$$

where E_{ON} and E_{OFF} are, respectively, the accumulated turn-on and turn-off energies in a mains cycle. E_{OFF} is calculated using the graphs provided by the manufacturer using the following polynomial function [27].

$$E_{OFF} = \sum_{i=0}^{f_S/2f} a(I_S(i) + \Delta I_{AC})^2 + b(I_S(i) + \Delta I_{AC}) + c \tag{16}$$

where a, b, and c take the values of Table 5 and $I_S(i)$ is the transistor current in the different turn-off transitions

$$I_S(i) = \sqrt{2} I_{AC} \sin\left(2\pi \frac{f}{f_S} i\right) \tag{17}$$

Table 5. Transistor parameters for switching losses calculation.

Symbol	Parameter	Value	Unit
a	E_{OFF} first coefficient	50	nJ/A^2
b	E_{OFF} second coefficient	−1.0	μJ/A
c	E_{OFF} constant term	35	μJ
d	E_{ON} first coefficient	25	nJ/A^2
e	E_{ON} second coefficient	3.05	μJ/A
g	E_{ON} constant term	72.5	μJ

Analogously, the accumulated switching energy in turn-on can be calculate with

$$E_{ON} = \sum_{i=0}^{f_S/2f} d(I_S(i) - \Delta I_{AC})^2 + e(I_S(i) - \Delta I_{AC}) + g \tag{18}$$

where the new coefficients d, e, and g are also found in Table 5.

The loss generated because of the charge and discharge of the output capacitances C_{OSS} of the MOSFETs is calculated with

$$P_{COSS} = \frac{C_{OSS} {V_{DC}}^2 f_S}{2} \tag{19}$$

If a MOSFET is turned-on when the body diode of the opposite MOSFET in the same inverter arm is conducting, a reverse recovery loss is generated. This loss is determined by the following equation

$$P_{RR} = Q_{RR} V_{DC} f_S \frac{I_{ACrms}\sqrt{2}}{\pi} \frac{1}{I_{SD}} \tag{20}$$

where Q_{RR} is the diode reverse recovery charge measured at the inverse current test reference I_{SD}.

The dead time corresponds to the portion of the cycle where no transistor is switched on to prevent a potential short circuit caused by the simultaneous conduction of the transistors in the same leg of the bridge. During this time, the diodes conduct the current, and therefore, the losses are determined by the forward voltage V_F of the diodes. In the dead time the loss P_{DT} is calculated using

$$P_{DT} = 2\, V_F \frac{I_{ACrms}\sqrt{2}}{\pi} t_d f_S \tag{21}$$

where t_d is the switching dead time that is imposed by the control circuit.

The power loss caused by charging and discharging of the gate of the MOSFET from minimum gate voltage V_{GSoff} to maximum gate voltage V_{GSon} and back with a gate total charge Q_G is

$$P_G = 2\left(V_{GSon} - V_{GSoff}\right) Q_G f_S \tag{22}$$

Finally, the total power loss of each converter transistor is given by

$$P_Q = P_{QC} + P_{QS} + P_{COSS} + P_{RR} + P_{DT} + P_G \tag{23}$$

2.9. Total Power Loss and Efficiency Calculations

The total power loss of the converter operating in any mode is given by

$$P_{TOT} = 4P_Q + P_{CR} + 2(P_{LR} + P_{LC}) \tag{24}$$

Consequently, the efficiency is

$$\eta = 1 - \frac{P_{TOT}}{P} \tag{25}$$

2.10. Thermal Design

With the power losses determined, the thermal design of the transistors can proceed. The maximum transistor junction temperature can be calculated with the following equation:

$$T_J = T_A + P_Q(R_{thJC} + R_{thCH}) + 4P_Q\,R_{thHA} \tag{26}$$

Setting the maximum T_J at 136 °C and the ambient temperature T_A at 40 °C as design limits, a maximum R_{thHA} value of 0.75 K/W is obtained, allowing for the selection of a heatsink similar to the model SK 121. Table 6 summarizes the parameters and results obtained in the thermal design.

Table 6. Parameters for thermal design.

Symbol	Parameter	Value	Unit
T_A	Ambient temperature	40	°C
T_{Jmax}	SiC MOSFET junction temp.	136	°C
R_{thHA}	Thermal resist. heatsink-ambient	0.75	K/W
HS	Heatsink SK 121	125	mm

2.11. Control Design

The simplified control scheme of the proposed SPBR is shown in Figure 4. It employs a unipolar modulation (UPWM) technique. This method utilizes two sinusoidal modulating waves, Vsin and its inverted, which have identical magnitude and frequency but are 180 degrees out of phase. These modulating waves are compared within the "SPWM Modulator" block with a common triangular carrier wave operating at the switching frequency, fs, to generate two gating signals, VG1 and VG4 for the upper switches Q1 and Q4, along with complementary signals VG2 and VG3 for the lower switches Q2 and Q3, respectively. A key feature of this scheme is that the upper two switches do not switch simultaneously, distinguishing it from bipolar pulse width modulation (BPWM), where all four switches operate in unison. The inverter output voltage, Vab (illustrated in Figure 3), alternates between zero and +Vdc during the positive half-cycle, and between zero and −Vdc during the negative half-cycle of the fundamental frequency. This behavior characterizes the unipolar modulation technique.

The sinusoidal reference Vsin is generated by the "Phase Regulator" block, which adjusts the phase of a voltage reference derived from the grid voltage to ensure zero phase difference between the current and voltage on the AC side of the converter. This phase alignment is measured by the "Phase Detector" block. The amplitude of the reference signal is controlled by the "Amplitude Regulator" block, which selects the output of the DC voltage regulator in rectifier mode or the output of the DC current regulator in inverter mode. The unipolar switched inverter provides reduced switching losses and generates lower electromagnetic interference (EMI). This makes it more efficient than the bipolar switching scheme, as it effectively doubles the output harmonics' switching frequency, thereby reducing the amplitude of high-frequency current ripple.

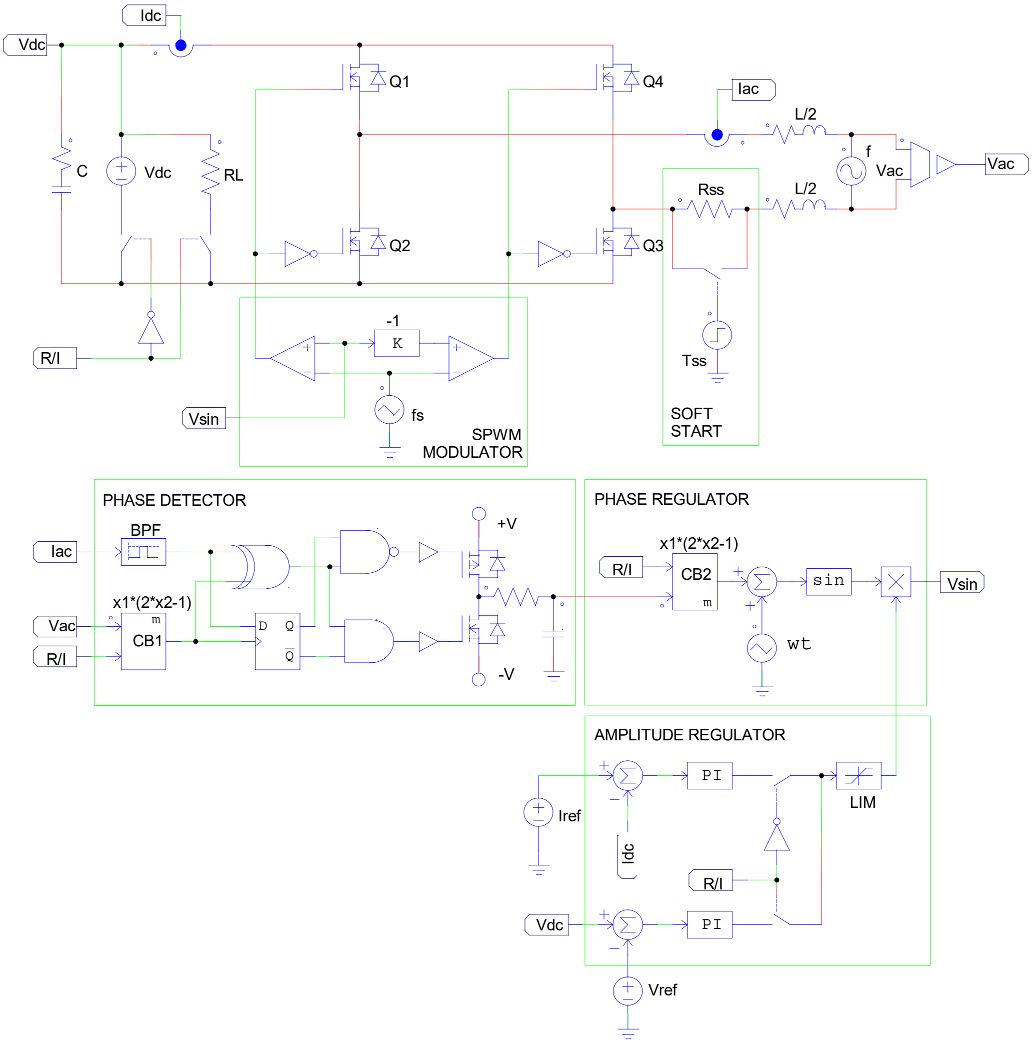

Figure 4. Schematic of the SPBR control.

When the SPBR operates as a boost converter in rectifier mode, the control system cannot limit the capacitor charging current until the voltage reaches the grid voltage peak. To address this, a "Soft Start" auxiliary current control circuit is required.

As the circuit must function bidirectionally, the converter control must seamlessly transition between rectifier and inverter modes with minimal adjustments, ideally in an automatic manner. The R/I signal facilitates this by automatically configuring the control: in rectifier mode (R/I = H), it sets the polarity of the reference signal in the "Phase Detector" and "Phase Regulator" blocks accordingly and selects the voltage feedback for the "Amplitude Regulation" block. In inverter mode (R/I = L), the polarity is reversed, and current feedback is used instead. To simplify the control design, dead time generation has been intentionally excluded from this scheme.

3. Results Analysis and Discussion

3.1. Calculated Results

Table 7 presents the calculated results from the power loss analysis of the converter at full power.

Table 7. Transistor design results.

Symbol	Parameter	Value	Unit
P_{QC}	Transistor conduction loss	21.6	W
P_{QS}	Transistor switching loss	2.4	W
P_{RR}	Diode reverse recovery loss	1.4	W
P_{DT}	Diode dead time loss	0.4	W
P_{COSS}	Output capacitance loss	0.2	W
P_G	Gate charge loss	0.1	W
P_Q	SiC MOSFET total losses	26.1	W
T_J	SiC MOSFET junction temp.	136	°C
P_{RC}	Total capacitor loss	17.5	W
P_{LR}	Inductor L/2 conduction loss	1.8	W
P_{LC}	Inductor L/2 core loss	0.6	W
P_{TOT}	SPBR total losses	132	W
η	SPBR efficiency	98.2	%

In Figure 5 all of the converter power losses have been represented as a function of the input power. It can be seen that the most important loss corresponds to the power conduction losses of the transistors. It is also observed that the powers related to the switching frequency are balanced. All of this justifies the importance of the choice of the transistor and the working frequency.

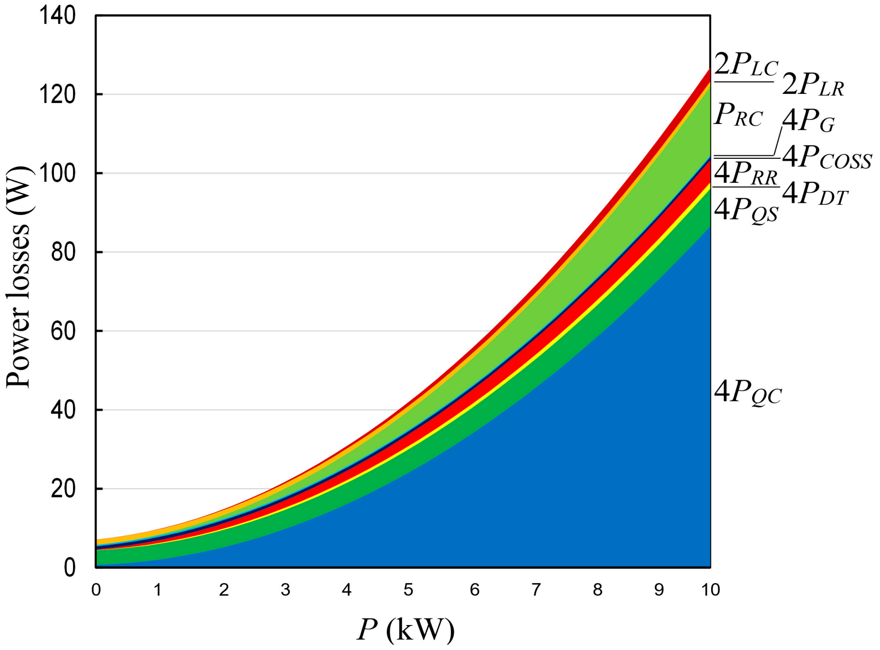

Figure 5. Calculated power losses of the converter.

Figure 6 presents the converter efficiency obtained from previous calculations. From Figures 5 and 6, it can be observed that when the output power is low, the power losses, while small in absolute terms, are significant relative to the output power. This explains the converter's low efficiency at low output power. As the output power increases, this effect diminishes until it reaches approximately 2 kW, where efficiency is maximized, exceeding

99%. Beyond this point, the power losses increase more rapidly than the output power, causing the efficiency to decrease, reaching 98.3% at maximum output power.

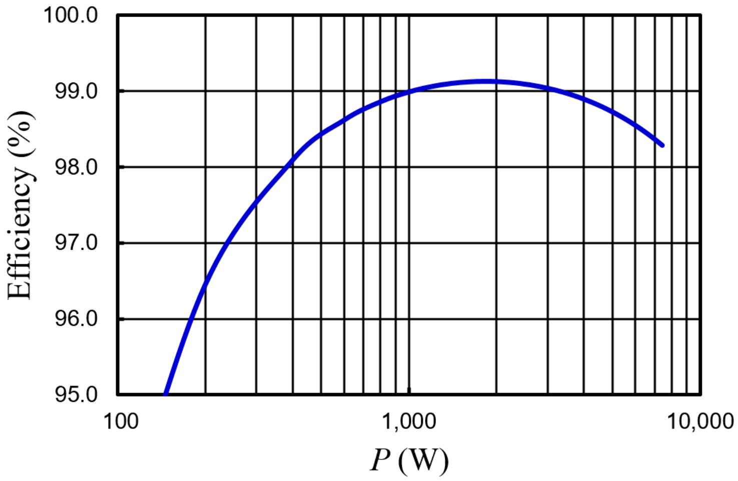

Figure 6. Calculated efficiency of the converter.

3.2. Experimental Results

This subsection presents the experimental results from testing a 7.4 kW SPBR converter operating under the specifications outlined in Table 1. The component values used in the circuit were those derived in previous sections. For experimental validation, a test setup was built, consisting of the elements included in Table 8.

Table 8. Elements of the experimental setup.

Label	Element
A	Full bridge with four C3M0040120K SiC MOSFETs with FPGA control and heatsink
B	AC side inductor composed of two pieces of 82 µH
C	A DC capacitor made by 22 pieces of 270 µF in parallel
D	Regenerative bidirectional programmable DC power supply
E	Mains (230 V, 50 Hz)
F	Digital storage oscilloscope (DSO) and probes
G	Power analyser

The DC side is connected to the IT6012C-800-50 bidirectional laboratory power supply that acts like electronic load in rectifier mode or like voltage supply in inverter mode. The AC side is connected to the mains. Figure 7 shows a picture of the test bed used to obtain the following experimental results. The alphabetical labels refer to the elements in Table 8.

Figure 8 illustrates the experimental efficiency measurements for both inverter mode and rectifier mode, regulating power up to 7.4 kW. The results for the two operating modes were highly similar. However, discrepancies between the experimental and calculated results were observed. These differences may be attributed to the modeling approach used, unaccounted losses from other elements (such as conductors, connections, parasitic components, voltage and current sensors, etc.), and the measurement process itself. The calculated and experimental efficiency of the SPBR converter is shown as a function of AC active power in rectifier mode and DC power in inverter mode. Solid lines and marked symbols indicate experimental measurements, while dashed lines represent calculated predictions.

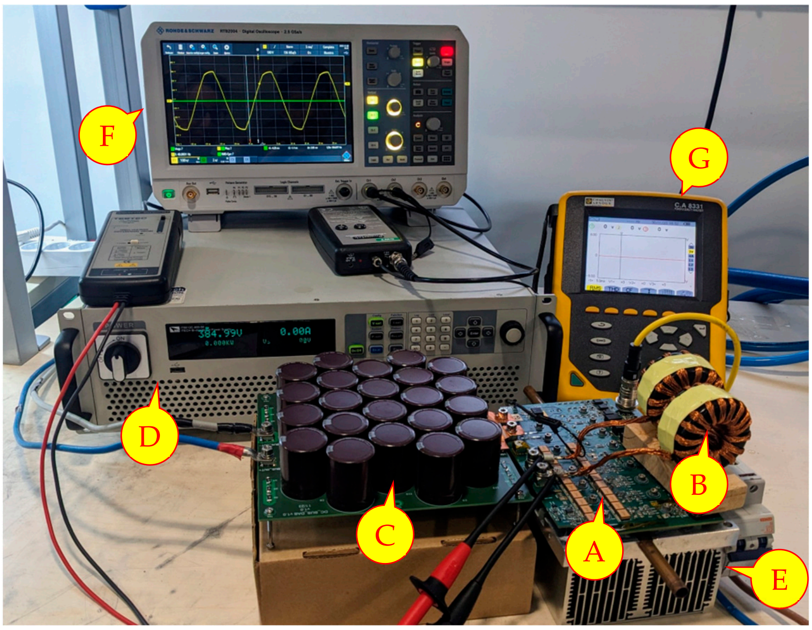

Figure 7. SPBR test bed.

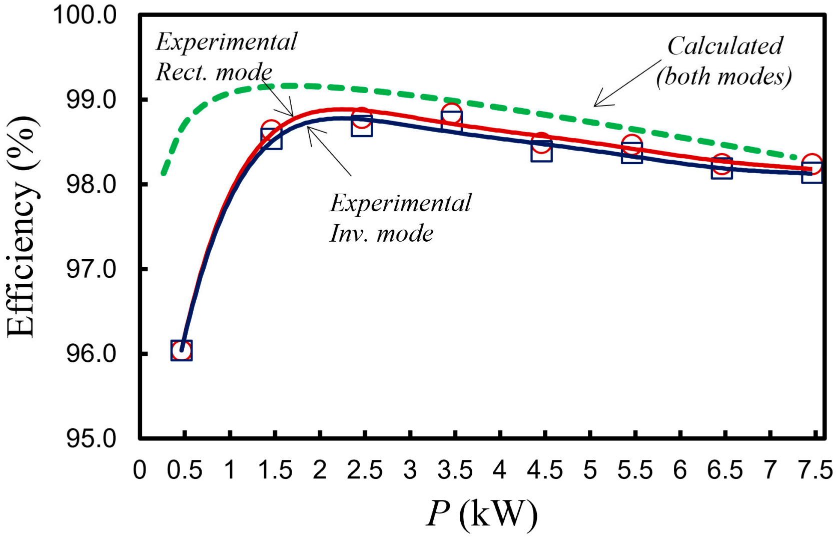

Figure 8. The calculated and experimental efficiency of the SPBR converter.

Finally, Figure 9 display waveforms captured by digital oscilloscope for the SPBR converter operating in rectifier and inverter mode at full power with 400 V at the DC side and 230 Vrms in AC side. Chanel C1 (dark blue) is the mains voltage VAC (100 V/div), C2 (magenta) is the mains current IAC (20 A/div), C3 (light blue) is the bridge voltage Vab (100 V/div), and C4 (brown) is the DC voltage VDC (100 V/div). The time base is 5 ms/div. The switching frequency is 20 kHz. The measured power factor is 1.0 and the THD is less than 7%.

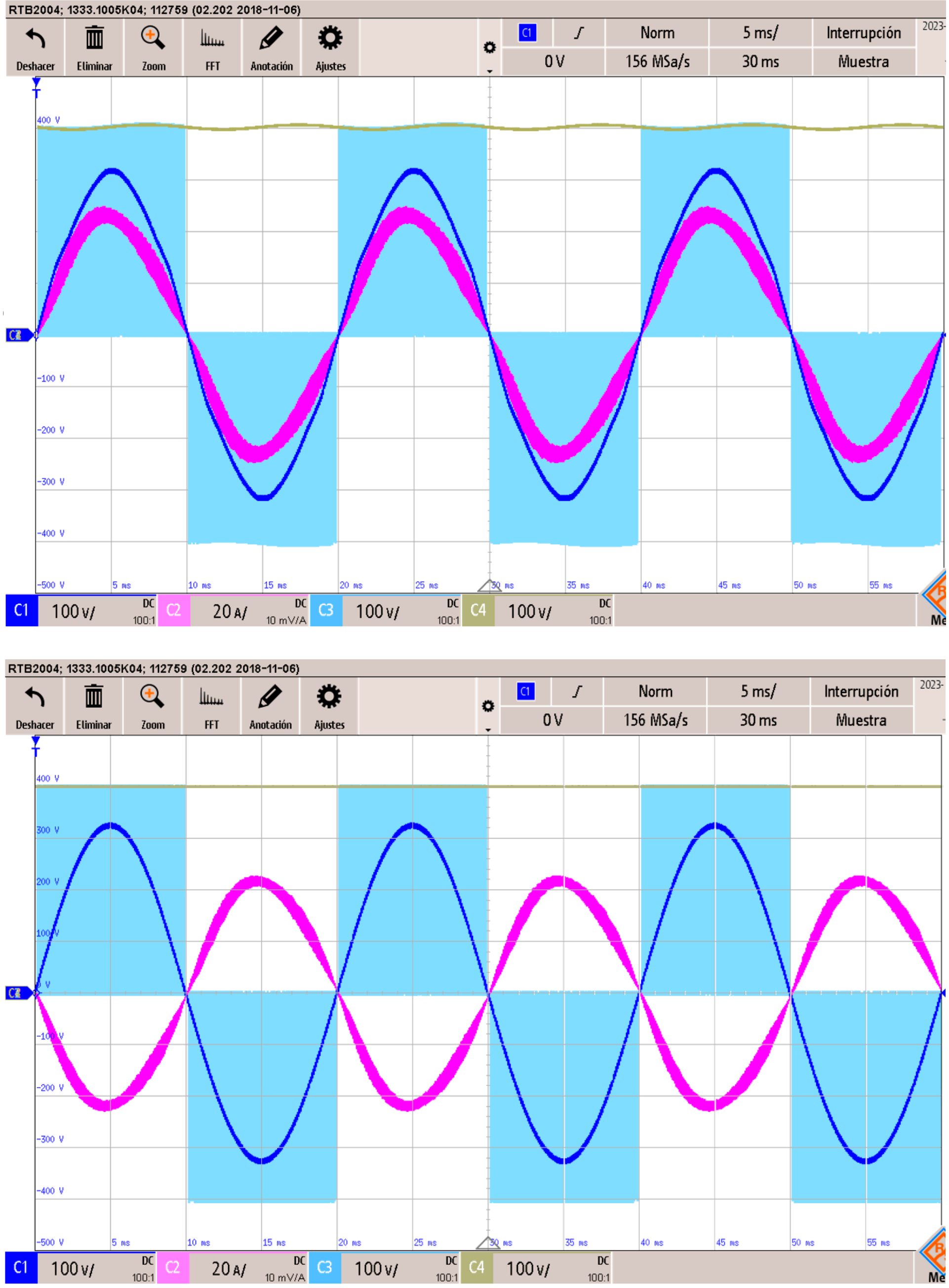

Figure 9. Experimental waveforms of the SPBR in rectifier mode (**top**) and inverter mode (**bottom**).

4. Conclusions

The power stage of the single-phase bidirectional rectifier (SPBR), used for the bidirectional AC–DC converters in HEMS applications, was fully designed in this work. The working conditions of the converter have been determined by a thorough examination of its components that are designed and evaluated.

To verify the viability of the design, a complete analysis of power losses was developed, making it possible to accurately design the parts and estimate the converter's efficiency since all power losses have been correctly calculated. All of this has determined that the SPBR converter is an effective solution. The feasibility of this design has been verified with the construction and testing of a 7.4 kW converter using SiC MOSFET transistors where an efficiency close to 98% was achieved.

Currently, there are many topologies applicable for the design of a bidirectional AC/DC converter. Although the selected topology is neither the most sophisticated nor the one offering the best performance in terms of energy efficiency or dynamic response, the presented Single-Phase Bidirectional Rectifier can be considered a simple solution with few active components. Therefore, it is robust and highly reliable, achieving an effective, low-cost converter perfectly suited for HEMS applications.

Author Contributions: Conceptualization and methodology, V.E.; software, J.L.B.; validation, J.J.; formal analysis, V.E.; resources, V.E.; data curation, J.L.B.; writing, editing and visualization V.E.; supervision, V.E.; project administration and funding acquisition, V.E. All authors have read and agreed to the published version of the manuscript.

Funding: This research received no external funding.

Data Availability Statement: The data presented in this study are available on request from the corresponding author. The data are not publicly available due to privacy restrictions.

Conflicts of Interest: The authors declare no conflicts of interest.

Abbreviations

AC	Alternating Current
AWG	American Wire Gauge
BDC	Bidirectional DC–DC Converter
BPWM	Bipolar Pulse Width Modulation
DAB	Dual Active Bridge
DC	Direct Current
DC-BUS	Intermediate DC-Bus
DCR	DC Resistance
DSO	Digital Storage Oscilloscope
ESS	Energy Storage Systems
EMI	Electromagnetic Interference
ESR	Equivalent Series Resistance
EV	Electric Vehicle
FPGA	Field-Programmable Gate Array
GaN	Gallium Nitride
HCC	Hysteresis Current Control
HESM	Home Energy Management Systems
HPWM	Hybrid Modulation Pulse Width Modulation
IGBT	Isolated Gate Bipolar Transistor
LVG	Low-Voltage Grid
MOSFET	Metal-Oxide-Semiconductor Field-Effect Transistor
MPPT	Maximum Power Point Tracking
PEV	Plug-in Electric Vehicle
PF	Power Factor
PFC	Power Factor Correction
PWM	Pulse Width Modulation
PV	Photovoltaic
RES	Renewable Energy Sources
Si	Silicon
SiC	Silicon Carbide
SM	Smart Meter
SPBR	Single-Phase Bidirectional Rectifier
SPWM	Sine Pulse Inverter Width Modulation
THD	Total Harmonic Distortion
UPWM	Unipolar Pulse Width Modulation
VSI	Voltage Source Inverter

References

1. Motta, L.L.; Ferreira, L.C.B.C.; Cabral, T.W.; Lemes, D.A.M.; Cardoso, G.d.S.; Borchardt, A.; Cardieri, P.; Fraidenraich, G.; de Lima, E.R.; Neto, F.B.; et al. General Overview and Proof of Concept of a Smart Home Energy Management System Architecture. *Electronics* **2023**, *12*, 4453. [CrossRef]
2. Palensky, P.; Dietrich, D. Demand side management: Demand response, intelligent energy systems, and smart loads. *IEEE Trans. Ind. Inform.* **2011**, *7*, 381–388. [CrossRef]
3. Europe Home Energy Management System Market Size & Share Analysis—Growth Trends & Forecasts (2024–2029). Available online: https://www.mordorintelligence.com/industry-reports/europe-home-energy-management-system-market (accessed on 18 November 2024).
4. Wei, G.; Chi, M.; Liu, Z.W.; Ge, M.; Li, C.; Liu, X. Deep Reinforcement Learning for Real-Time Energy Management in Smart Home. *IEEE Syst. J.* **2023**, *17*, 2489–2499. [CrossRef]
5. DiOrio, N.; Denholm, P.; Hobbs, W.B. A model for evaluating the configuration and dispatch of PV plus battery power plants. *Appl. Energy* **2020**, *262*, 114465. [CrossRef]
6. Guo, R.; Meunier, S.; Protopapadaki, C.; Saelens, D. A review of European low-voltage distribution networks. *Renew. Sustain. Energy Rev.* **2023**, *173*, 113056. [CrossRef]
7. Zhao, B.; Song, Q.; Liu, W.; Sun, Y. Overview of Dual-Active-Bridge Isolated Bidirectional DC–DC Converter for High-Frequency-Link Power-Conversion System. *IEEE Trans. Power Electron.* **2014**, *29*, 4091–4106. [CrossRef]
8. Esteve, V.; Bellido, J.L.; Jordán, J.; Dede, E.J. Improving the Efficiency of an Isolated Bidirectional Dual Active Bridge DC–DC Converter Using Variable Frequency. *Electronics* **2024**, *13*, 294. [CrossRef]
9. Li, B.; Huang, S.; Chen, X. Performance Improvement for Two-Stage Single-Phase Grid-Connected Converters Using a Fast DC Bus Control Scheme and a Novel Synchronous Frame Current Controller. *Energies* **2017**, *10*, 389. [CrossRef]
10. Peng, T.; Yang, P.; Dan, H.; Wang, H.; Han, H.; Yang, J.; Wang, H.; Dong, H.; Wheeler, P. A Single-Phase Bidirectional AC/DC Converter for V2G Applications. *Energies* **2017**, *10*, 881. [CrossRef]
11. Pannawan, A.; Kaewchum, T.; Saeseiw, C.; Pachanapan, P.; Hinkkanen, M.; Somkun, S. Design and Implementation of Single-Phase Grid-Connected Low-Voltage Battery Inverter for Residential Applications. *Electronics* **2024**, *13*, 1014. [CrossRef]
12. Lo Franco, F.; Morandi, A.; Raboni, P.; Grandi, G. Efficiency Comparison of DC and AC Coupling Solutions for Large-Scale PV+BESS Power Plants. *Energies* **2021**, *14*, 4823. [CrossRef]
13. Ahmed, M.; Harbi, I.; Kennel, R.; Heldwein, M.L.; Rodríguez, J.; Abdelrahem, M. Performance Evaluation of PV Model Based Maximum Power Point Tracking Techniques. *Electronics* **2022**, *11*, 2563. [CrossRef]
14. Kim, H.S.; Ryu, M.H.; Baek, J.W.; Jung, J.H. High-Efficiency Isolated Bidirectional AC–DC Converter for a DC Distribution System. *IEEE Trans. Power Electron.* **2012**, *28*, 1642–1654. [CrossRef]
15. Singh, B.; Singh, B.N.; Chandra, A.; Al-Haddad, K.; Pandey, A.; Kothari, D.P. A review of single-phase improved power quality AC-DC converters. *IEEE Trans. Ind. Electron.* **2003**, *50*, 962–981. [CrossRef]
16. Mohan, N.; Undeland, T.M.; Robbins, W.P. *Power Electronics Converters, Applications, and Design*; Wiley: New Delhi, India, 2003.
17. Salmon, J.; Wang, L.; Noor, N.; Krieger, A.W. A carrier-based unipolar PWM current controller that minimizes the PWM-cycle average current error using internal feedback of the PWM signals. *IEEE Trans. Power Electron.* **2007**, *22*, 1708–1718. [CrossRef]
18. Li, R.T.; Chung, H.S.H.; Lau, W.H.; Zhou, B. Use of hybrid PWM and passive resonant snubber for a grid-connected CSI. *IEEE Trans. Power Electron.* **2010**, *25*, 298–309. [CrossRef]
19. Shukla, A.; Ghosh, A.; Joshi, A. Hysteresis modulation of multilevel inverters. *IEEE Trans. Power Electron.* **2011**, *26*, 1396–1409. [CrossRef]
20. Liao, Y.-H. A Novel Reduced Switching Loss Bidirectional AC/DC Converter PWM Strategy with Feedforward Control for Grid-Tied Microgrid Systems. *IEEE Trans. Power Electron.* **2014**, *29*, 1500–1513. [CrossRef]
21. Su, M.; Wu, S.; Dan, H.; Xu, J.; Sun, Y.; Wang, H.; Liu, Y.; Xiong, W.; Liang, X. A Natural Bidirectional Isolated Single-Phase AC/DC Converter with Wide Output Voltage Range for Aging Test Application in Electric Vehicle. *IEEE J. Emerg. Sel. Top. Power Electron.* **2021**, *9*, 3489–3500. [CrossRef]
22. Du, Y.; Bhat, A.K. Analysis and Design of a High-Frequency Isolated Dual-Tank LCL Resonant AC–DC Converter. *IEEE Trans. Ind. Appl.* **2016**, *52*, 1566–1576.
23. Stupar, A.; Friedli, T.; Minibock, J.; Kolar, J.W. Towards a 99% efficiency three-phase buck-type PFC rectifier for 400-V dc distribution systems. *IEEE Trans. Power Electron.* **2012**, *27*, 1732–1744. [CrossRef]
24. Esteve, V.; Bellido, J.L.; Jordán, J. Optimal Design of a Single-Phase Bidirectional Rectifier. *Energies* **2024**, *17*, 1280. [CrossRef]
25. Niu, S.; Zhao, Q.; Niu, S.; Jian, L. A Comprehensive Investigation of Thermal Risks in Wireless EV Chargers Considering Spatial Misalignment from a Dynamic Perspective. *IEEE J. Emerg. Sel. Top. Ind. Electron.* **2024**, *5*, 1560–1571. [CrossRef]

26. Niu, S.; Lyu, R.; Lyu, J.; Chau, K.T.; Liu, W.; Jian, L. Optimal Resonant Condition for Maximum Output Power in Tightly Coupled WPT Systems Considering Harmonics. *IEEE Trans. Power Electron.* **2025**, *40*, 152–156. [CrossRef]
27. Esteve, V.; Jordán, J.; Dede, E.J.; Martinez, P.J.; Ferrara, K.J.; Bellido, J.L. Comparative analysis and improved design of LLC inverters for induction heating. *IET Power Electron.* **2023**, *16*, 1754–1764. [CrossRef]